Institute of Condensed Matter and Nanosciences
Division of Bio and Soft Matter

Development of novel Polymer-based Cathodes and Electrolytes for High Performance Batteries

Fadoi Boujioui

Jury members:

Prof. Jean-François Gohy (UCL), Supervisor
Prof. Jacques Devaux (UCL), Chairman
Prof. Charles-André Fustin (UCL)
Prof. Dominique Hourdet (ESPCI)
Prof. David Mecerreyes (POLYMAT)
Prof. Evelyne van Ruymbeke (UCL)

Thesis submitted in fulfillment of
the degree of Doctor in Sciences

Louvain-la-Neuve 2018

Acknowledgements

Although we are at the beginning of the manuscript, I write these few lines while I am at the end of my thesis.

My thanks go to my promotor Jean-François for giving me the opportunity to work on this multidisciplinary subject, as vast as enriching. Thank you for giving me freedom and for trusting me during these 4 years.

I also thank the jury members, Jacques Devaux, Charles-André Fustin, Dominique Hourdet, David Mecerreyes and Evelyne van Ruymbeke, for the interest they showed in my work. Thank you for sharing your intellectual rigor in reading my manuscript. Your remarks and advices enlightened me a lot.

Thank you Charles-André for always answering to my scientific questions. I laughed a lot during the lunch breaks with your sense of humor, as well as that of Jean-François and Alexandru.

I would like to address a special thanks to Evelyne. You helped me a lot with your support and your advice. I shared excellent moments with you and your team, who considered me as one of team member.

I would like to express my gratitude to those who contributed to the project. First of all, thanks to Flanco and Olivier without whom I could not have taken up some experimental challenges. Thanks for your involvements and your advices. Thanks to Tobias for the ESR measurements, which were not easy to realize with my samples. Thanks to Jürgen for his expertise in the installation of MALS detector. Thanks to Pascal and Colette for their thoughtful remarks concerning the microscopy characterizations. I also thank my intern Helen who contributed to the chapter 4 in a good mood. I wish you to success in your future PhD student's life in Germany.

Of course, I do not forget all the others with whom I worked during my thesis and with whom I lived good and unforgettable moments during a PhD student's life, whether they are scientists or not and permanent or not, the collaborators and my colleagues. To all, I address my sincere thanks. It was a pleasure to work with you.

To finish, I want to particularly thank my family and my friends who always supported me. You are always there for me. I would not have been able to accomplish this thesis without you.

Tell me and I forget, Teach me and I may remember,
Involve me and I learn.
Benjamin Franklin

Nothing in life is to be feared, it is only to be understood.
Now is the time to understand more, so that we may fear less.
Marie Curie

One never notices what has been done,
One can only see what remains to be done.
Marie Curie

Do it otherwise, you will regret it.
My mother

Table of contents

List of symbols

Ah	Ampere-hour
ATRP	atom transfer radical polymerization
AzPMA	3-Azidopropyl methacrylate
C, I	Current
Cp	Practical (or experimental) capacity
CRP	Controlled radical polymerization
CTA	Chain Transfer Agents
Cu	Copper
CuAAC	Copper-catalyzed Cycloaddition of Azides and Alkynes
CV	Cyclic Voltammetry
cyCA	cyclic Carbonate Acrylate
cyCB	cyclic Carbonate
cyCMA	cyclic Carbonate Methacrylate
Đ	Dispersity
DEC	Diethyl Carbonate
DP	Degree of Polymerization
DSC	Differential Scanning Calorimetry
E	Specific energy
E_a	Activation Energy
EC	Ethylene Carbonate
EIS	Electrochemical Impedance Spectroscopy
*E*p	Peak potential
ESR	Electron Spin Resonance
F	Faraday constant
f	Frequency
FAES	Flow-Assisted Electrochemical Systems
FTIR	Fourier Transform Infrared spectroscopy
G’	Storage modulus
G’’	Loss modulus
GPE	Gel Polymer Electrolyte
IL	Ionic Liquid
Ip	Peak current

IPA	Isopropanol
Li	Lithium
LiB	Lithium Battery
$LiClO_4$	Lithium perchlorate
$LiPF_6$	Lithium hexafluorophosphate
LITFSI	Lithium bis(trifluoromethanesulfonyl)imide
M, Mn	Molar mass
MAF	2-Trifluoromethyl acrylic acid
n	Number of charge carrier
nBA	nButyl Acrylate
NMP	Nitroxide-Mediated radical Polymerization
NMR	Nuclear Magnetic Resonance
ORB	Organic Radical Battery
P	Specific power
Pa	Pascal
PBIB	Propargyl 2-bromoisobuyrate
PEO	Poly(ethylene oxide)
PISA	Polymerization Induced Self-Assembly
PMA	Propargyl methacrylate
PMDETA	*N*,*N*,*N*',*N*',*N*''-pentamethyldiethylenetriamine
POEGMA	Poly(oligo(ethylene glycol) methyl ether methacrylate)
PS	Polystyrene
PTMA	Poly(2,2,6,6-tetramethylpiperidinyloxy-4-yl methacrylate)
PVDF	Poly(vinylidene fluoride)
Q	Specific (or Theoretical) capacity
RAFT	Reversible Addition-Fragmentation chain Transfer
RDRP	Reversible-Deactivation Radical Polymerization
RFB	Redox Flow Battery
SARA	Supplemental Activator and Reducing Agent
SEC	Size Exclusion Chromatography
SEI	Solid Electrode-Electrolyte Interphase
SET-LRP	Single-Electron Transfer Living Radical Polymerization
SPE	Solid Polymer Electrolyte
TEM	Transmission Electron Microscopy
TEMPO	2,2,6,6-tetramethylpiperidinyloxyl
T_g	Glass Transition Temperature

t_{Li^+}	Lithium Transference Number
T_m	Melting temperature
TMPM	2,2,6,6-tetramethylpiperidin-4-yl methacrylate
V	Volt
VFT	Volgel-Fulcher-Tamman
Wh	Watt-hour
η	Viscosity
η*	Complex viscosity
γ	Shear strain
ΔE	Potential difference
σ	Conductivity
ω	Angular frequency
v	Scan rate

General introduction

For several years, the climate change (also known as global warming) is one of the major concerns of humans. Scientists maintain that it is due primarily to the use of fossil fuels releasing greenhouse gases. In order to fight against this issue, the European Union (EU) Council adopted in 2008 the "European plan on the energy and climate change".[1] This plan consists in three proposals known as "20-20-20 targets" by 2020. The EU has to reduce by 20% the greenhouse gases, to improve by 20% the energy efficiency and to increase by 20% the share of renewable energy. Thus, the production and storage of clean, inexpensive and portable energies in the aim of relieving the depletion of natural resources need to be implemented by different energy management strategies. This is where energy storage systems, such as batteries and supercapacitors, are expected.

In general, the electrochemical storage of the energy can be achieved through non-rechargeable (single use or primary batteries) or rechargeable (secondary batteries and supercapacitors) systems. These devices have been developed because of problems encountered with energy conversion systems, also known as fuel cells. In fact, in addition to continually requiring fuels (such as hydrogen and oxygen), a significant loss of energy occurs from its conversion to its distribution. Meanwhile, the batteries and supercapacitors directly convert electrical energy from chemicals stored inside.

All these systems are usually composed of two electrodes (respectively called anode and cathode) separated by an inert membrane (called separator) and put in contact with an electrolyte. However, these systems display different mechanisms of energy storage allowing them to deliver different performances. Their performances are usually depicted in a so-called Ragone diagram (Fig.1), which compares them according to the specific power (P) and the specific energy (E), which can be stored and delivered. The specific energy refers to the cell autonomy (in $Wh.kg^{-1}$ or $Wh.L^{-1}$), whereas the specific power refers to the power output (in $W.kg^{-1}$ or $W.L^{-1}$).

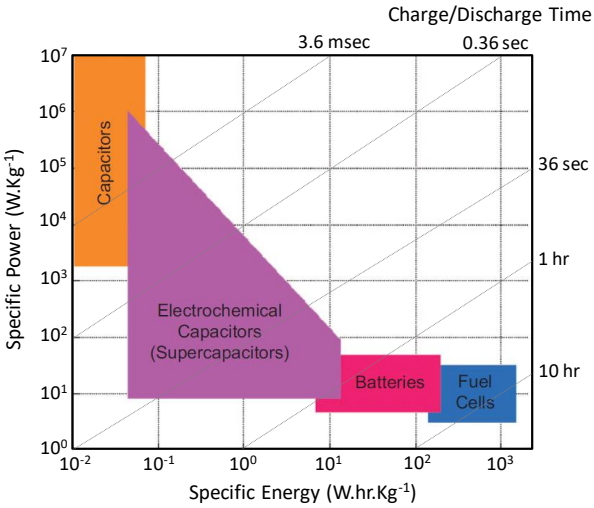

Figure 1. Ragone plot showing specific power versus specific energy for various energy storage/conversion devices.[2]

Batteries store/deliver energy through redox reactions in the bulk of the electrode materials (faradic processes) allowing the storage/delivery of high amounts of energy over long times (Fig.2a). In contrast, supercapacitors store the energy at the surface of the electrode materials.[3] They are categorized into two main groups: the electrochemical double-layer capacitors (EDLCs) and the pseudocapacitors. EDLCs store/deliver the energy arising from accumulation/separation of ions at the electrode/electrolyte interface. Those electrostatic reactions (capacitive processes) occur quickly generating high specific power for the device. However, they do not allow the device to store large amounts of energy since they are limited on the surface of the electrodes (Fig. 2b). While for pseudocapacitors reversible redox reactions occur at the electrode surfaces. In the latter case, the storage of energy is thus achieved from faradic-capacitive processes, also known as pseudocapacitive processes.[4]

Despite the ongoing progress, the development of safer, cheaper, portable with lightweight and small size, having sufficient autonomy but also a high power and fast charging, electrical storage systems is still a challenge, which is currently the topic of intense investigations both at the academic and industrial levels.

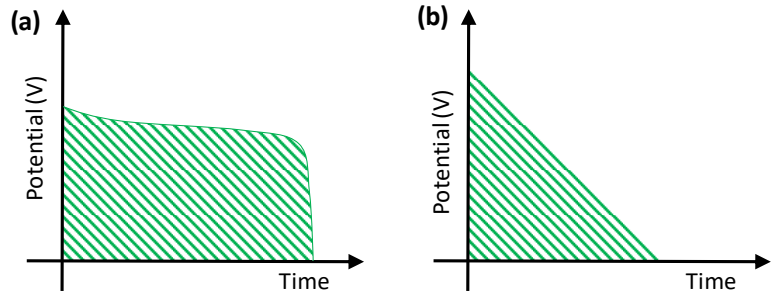

Figure 2. Discharge curve of **(a)** faradic and **(b)** capacitive devices.

In this manuscript, we discuss about the development of polymer-based components, which could be able to increase the performances and to improve the safety of lithium batteries. This manuscript is divided into four main parts. Chapter 1 is devoted to a state of the art on lithium-ion batteries in which the concepts required for the understanding of the next chapters will be briefly introduced. The main focus of this thesis is the development of simple and effective synthetic strategies to develop polymeric materials exhibiting enhanced ionic conductivities. This will in turn allow accelerated transfer of lithium ions into the different compartment of the battery and exploitation of the unique fast redox reactions exhibited by organic battery materials. To illustrate this concept, chapters 2 and 3 are dedicated to the development of gel-like cathode active materials from pseudocapacitive polymer networks and ionic liquid components. The gel-like character of the polymeric cathode material as well as the presence of ionic liquid crosslinking units will facilitate the transfer of ions within the cathode materials and will allow to fully exploit the fast redox reaction kinetics of the polymeric materials. Beside electrode materials, an important ionic conductivity is of course wanted in the electrolyte compartment of the battery. Chapters 4 and 5 focus on the development of solid polymer electrolytes based on cyclic ethylene carbonates with the study of their physico-chemical and electrochemical properties. Compared to classical poly(ethylene oxide)-based solid polymer electrolytes, cyclic ethylene carbonate-based systems are promising since they exhibit a weak interaction with lithium ions and a high dielectric constant facilitating thus both ion dissociation and transport. Finally, chapter 6 describes the development of cathode active materials in suspension, which consist of

pseudocapacitive polymer based nano-objects, for application in flow-assisted electrochemical systems. In this last chapter, the challenge will be to design micellar nano-objects in which the redox-active polymer is incorporated into the micellar core but is still accessible for redox reaction in the electrochemical cell. Localizing the redox polymer into the micellar core will allow us to maximize the amount of redox active polymer while keeping a low viscosity of the micellar solution.

1 'Limiting Global Climate Change to 2 degrees Celsius' by European Commission, *http://europa.eu/rapid/press-release_MEMO-07-16_en.htm*, 2007.
2 P. J. Hall and E. J. Bain, *Energy Policy*, 2008, **36**, 4352–4355.
3 F. Béguin and E. Frackowiak, *Supercapacitors: Materials, Systems, and Applications*, 2013.
4 T. Brousse, D. Belanger and J. W. Long, *J. Electrochem. Soc.*, 2015, **162**, A5185–A5189.

Chapter 1: State of the art

Table of contents

1.1 Batteries

1.1.1 Faradic energy storage

The storage process in batteries is achieved by faradic reactions. Faradic systems involve oxidation-reduction (redox) reactions of the materials constituting the electrodes. The difference of electrochemical potentials between the two electrodes ($\Delta E_{Cell} = E_{cathode} - E_{anode}$) involves exchanges of electrons and ions that allow the conversion of chemical energy into electrical energy via redox reactions (Fig. 1). In the case of rechargeable batteries, the materials can reversibly oxidize and reduce a certain number of times (this concept is called the cyclability). While for primary batteries, the redox reactions are irreversible preventing the charge of the cell to occur.

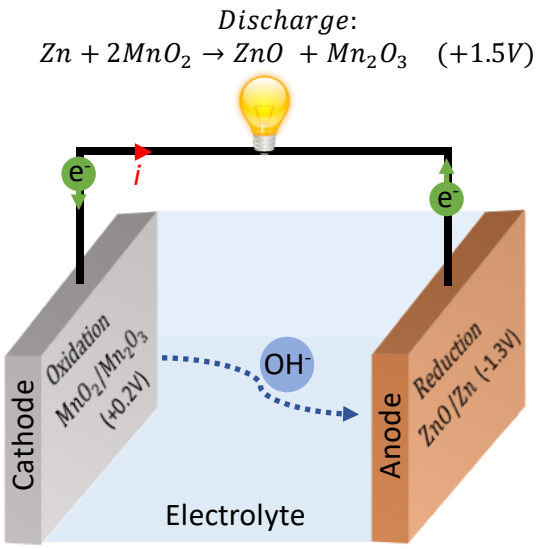

Figure 1. Discharge reaction of the primary battery alkaline.

According to Faraday's law[1] (equation 1), the amount of energy stored/delivered from an active material (cathode or anode active material) depends on its molar mass but also on the number of electrons exchanged during the electrochemical reactions. In fact, this law allows

to obtain the theoretical specific capacity Q (in $Ah.g^{-1}$), corresponding to the amount of electricity delivered during a complete discharge of the system at a defined time.

$$Q = \frac{n\,F}{3600\,M} \qquad (1)$$

Where n is the number of charge carrier (e^- or ion), F is the Faraday constant (96500 $C.mol^{-1}$), M is the molar mass of the active material (in $g.mol^{-1}$) and 3600 is the conversion factor between Coulomb (C) and Ampere-hour (Ah). It is also possible to know the duration (t in hour) of a complete charge (or discharge) at defined applied current (I or C in Ampere A) and at defined capacity (Q in Ah), according to equation 2.

$$Q = t * I \qquad (2)$$

In the case of batteries, the redox reactions take place in the entire volume of their electrodes. Therefore, contrary to supercapacitors, batteries store a large amount of charge carriers, leading to a high specific energy E. However, this latter does not depend solely on the amount of ions displaced within the structure of the electrode materials (whose the number is proportional to that of the electrons). The specific energy E of the battery (in $Wh.kg^{-1}$) also depends on its delivered maximum capacity Q (in $Ah.kg^{-1}$) and on its operating potential ΔE (or cell voltage in Volt) as expressed in equation 3. Therefore, the nature of the involved redox couples as well as the molar mass of the active material also influence the energy E of the battery. However, the transport of electrons as well as the diffusion of the ions in the electrode materials limit the kinetics of these redox reactions, curbing the density power of batteries. In fact, the power P (in $W.kg^{-1}$) is the ability to supply the energy E (in $Wh.kg^{-1}$) in a given time (t in hour) as expressed in equation 4.

$$E = \Delta E * Q_{max} \qquad (3)$$

$$P = {}^{E}/_{t} \qquad (4)$$

Therefore, the three most important criteria are the operating voltage (ΔE), the quantity of energy (specific capacity in $Ah.kg^{-1}$ or $Ah.L^{-1}$) or energy density in $Wh.kg^{-1}$ or $Wh.L^{-1}$) and the electrical power density ($W.kg^{-1}$ or $W.L^{-1}$) that the battery has to supply to a given apparatus.

1.1.2 History of batteries

The technology of secondary batteries has made significant progress in terms of power, energy, lifetime, cost, hazard and weight/volume (Fig. 2 and Fig. 3). The lead acid battery was the first rechargeable battery, invented in 1859. Despite a cell potential of 2 Volts, its chemical composition makes it heavy and toxic with a low theoretical capacity Q (260 $mAh.g^{-1}$) and a short lifetime (below 500 cycles). Then, it was considered unsuitable for portable electronic devices. The batteries based on nickel cathodes were invented thereafter, in 1899. At this period, they were considered to have long lifetimes (*ca.* 500 cycles) and to be lighter with better specific energies thanks to their high capacities. However, they cause high self-discharge and their low cell potential of 1.2 V requires stacked cells to increase the voltage.

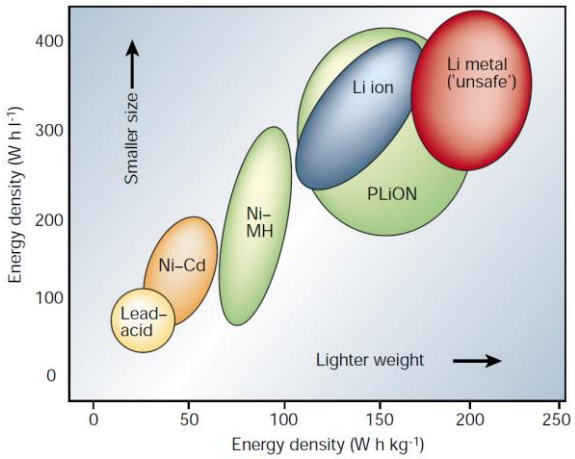

Figure 2. Different battery technologies classified according to their gravimetric and volumetric energy density.[2]

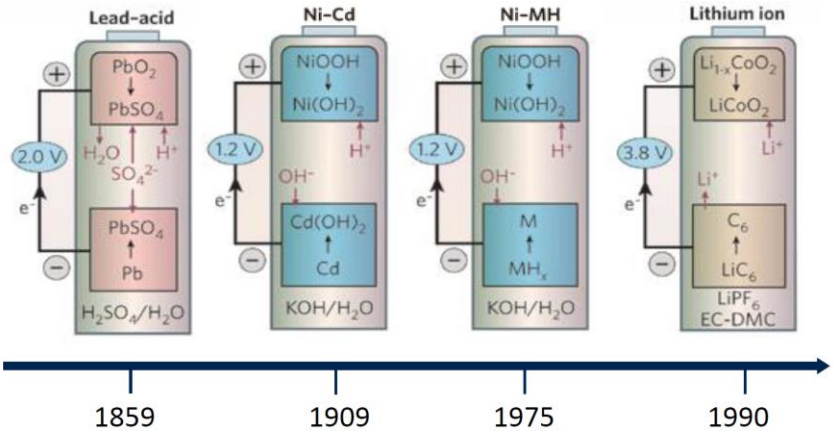

Figure 3. Different batteries and their corresponding electrochemical reactions.[3]

In the 70's, scientists had the idea to use lithium as anode in order to increase the potential ΔE and the capacity Q. In fact, lithium is the lightest solid element with a molar mass of 6.94 $g.mol^{-1}$ and the most reductive element with a redox potential as low as -3.04 V vs ENH. Thus, the voltage and the capacity of cells increase until 5V and 3860 $mAh.g^{-1}$, respectively. With a lithium metal foil as anode and a non-aqueous liquid electrolyte (because lithium reacts intensely with water), lithium batteries present high gravimetric and volumetric energy densities reaching 400 $Wh.l^{-1}$ and 240 $Wh.Kg^{-1}$ respectively (Fig. 2). However, Li may react continuously with the liquid organic electrolytes inhibiting the formation of a stable solid electrolyte interface (SEI) between the Li anode and the electrolyte. After a few charge/discharge cycles, Li-metal batteries become unsafe, prohibiting their commercialization. In a liquid organic electrolyte, the anode lithium metal leads to the formation of dendrites on the surface of the electrode during charging, generating an internal short circuit during cycling or even an explosion (Fig. 4). Therefore, the development of new electrodes and electrolytes was necessary. Two alternatives were proposed in order to solve this safety problem. In the Lithium-ion technology, the lithium metal anode was replaced with a intercalation anode compound, leading to a first commercialization by Sony in 1991.[4] The second alternative was to replace the liquid electrolyte by a

polymer electrolyte.[5] Lithium Metal Polymer batteries (LMP®) were thus commercialized and integrated in Bluecar® by Bolloré.

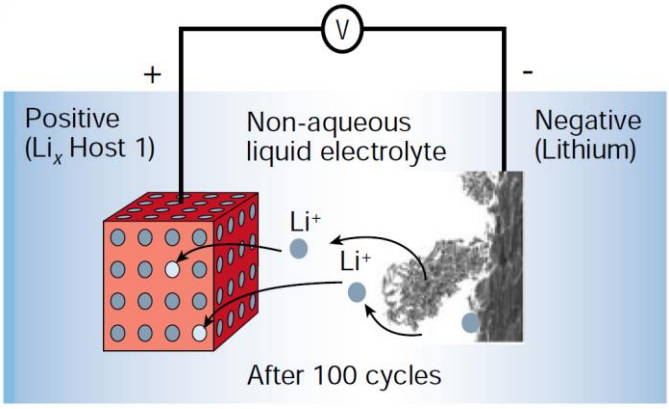

Figure 4. Rechargeable Lithium-metal battery with SEM image of dendrite growth at the Li surface.[2]

1.1.3 Operating process of lithium batteries

For all the batteries based on lithium (LiBs), the operating process remains the same. During the discharge of lithium-ion batteries, the components of the anode oxidize, releasing electrons e^- in the external circuit and lithium ions Li^+ via the electrolyte (Fig. 5). The latter transit to the cathode where reduction takes place by inserting lithium ions into it and consuming the electrons. The electric current I is thereby generated in the circuit. During the charge of batteries, the reverse process takes place. The cathode oxidizes and the lithium ions (which disinsert from the host) as well as the electrons return to where they came from, that is to say the anode. Therefore, the batteries operate on a chemical process of intercalation/deintercalation of Li^+ ions, which is considered softer than break/mend of the chemical bonds in the electrodes of lead-acid batteries (Fig. 3). For a good performance of batteries, it is thus necessary to consider both the structure of electrodes (which will host the ions) as well as their electronic bands, which is further influenced by the nature of the electrolyte. Thereafter, a thorough study is carried out on the cathode and electrolyte.

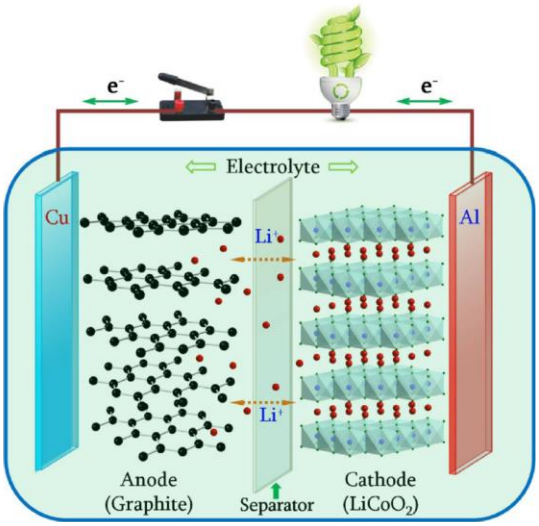

Figure 5. Configuration of rechargeable Lithium-ion battery.[1]

1.2 Cathode active materials

1.2.1 Generality

The active components of cathode active materials play a major role in the performance of batteries. In order to be used, they have to fulfill some key requirements, which are listed below.[6]

(1) They should have a high chemical potential $E_{cathode}$ (V vs Li/Li^+) to maximize the electrochemical potential of the cell.

(2) They should insert/extract a large amount of lithium within their structure in order to maximize the cell capacity.

(3) Their structures should not change during the insertion/extraction process for good cycle life.

(4) They should be good electronic and ionic conductors in order to reduce the polarization loss and the charge/discharge time, thus improving the power density.

(5) They should be thermally and chemically stable over a wide voltage range.

(6) They should be inexpensive, safe and environment-friendly.

The most used cathode active materials in lithium batteries are redox active metals with crystalline intercalation structures, enabling

the insertion/deintercalation of Li^+ ions. Three main common structures of cathode materials exist, layer metal oxide with the general formula $LiMO_2$ (e.g $LiCoO_2$ in Fig. 6a), spinel metal oxide with the general formula LiM_2O_4 (e.g $LiMn_2O_4$ in Fig. 6b) and olivine metal phosphate with the general formula $LiMPO_4$ (e.g $LiFePO_4$ in Fig. 6c).

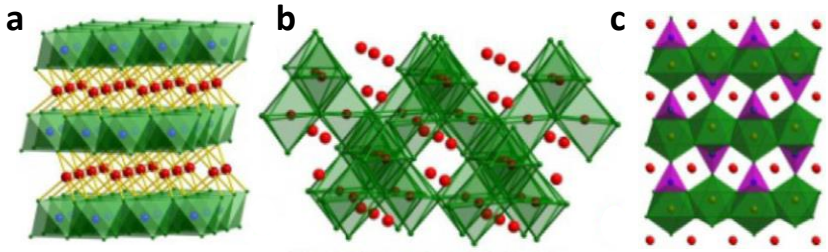

Figure 6. Three common structures used in lithium batteries: **(a)** layered $LiCoO_2$, **(b)** spinel $LiMn_2O_4$ and **(c)** olivine $LiFePO_4$.[1]

The layered and spinel metal oxide structures contain high-oxidized redox couples, which allow the cells to reach high potentials up to 4V (Fig. 7). However, during the discharge of batteries based on these cathode materials, overheating problems and oxygen degassing occur because of the instability of their reducing species. According to safety conditions, olivine $LiFePO_4$ is considered as the best solution, however it generates lower density than the metal oxides. Despite a good capacity of 170 mAh/g, it has a low potential of 3.4 V vs Li/Li^+. Furthermore, these inorganic cathode materials are from non-renewable natural resources and are not environment-friendly because their productions consume high energy and their recycling is still a problem.

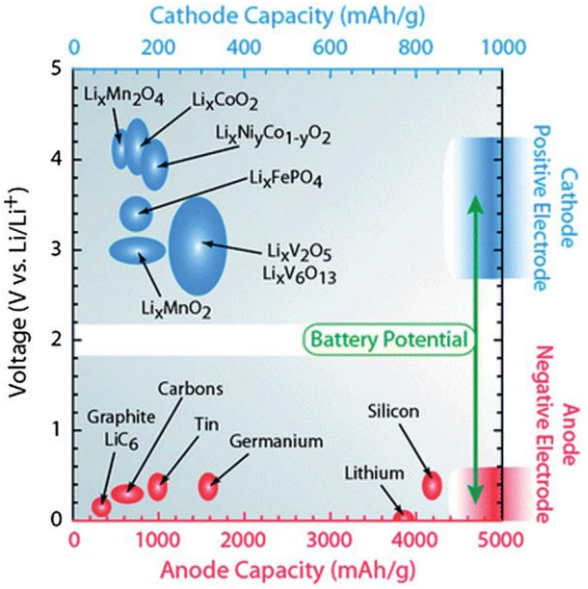

Figure 7. Redox potentials and capacities of anode and cathode materials used in lithium batteries.[7]

1.2.2 Redox active polymers

Redox polymers are a class of active materials containing groups that can be reversibly oxidized/reduced upon electrochemical stimuli. These redox active moieties can be integrated either in the polymer main-chain or as polymer side chains. They can be either organic or inorganic/organometallic type. Moreover, various polymer topologies can be synthesized by playing on the compositions and functionalities. Thus, redox polymers seem to be an ideal alternative to the usual inorganic cathode materials described previously. In fact, it is possible for the cathode to fulfill all the requirements listed above, by replacing the crystalline structure of inorganic compounds with the flexible and modular structure of redox polymers.

Three main families of organic redox polymers for batteries exist: organosulfurs, carbonyls and organic radicals.[8,9] Fig. 8 summarizes the performance of cells based on these organic redox compounds.[10]

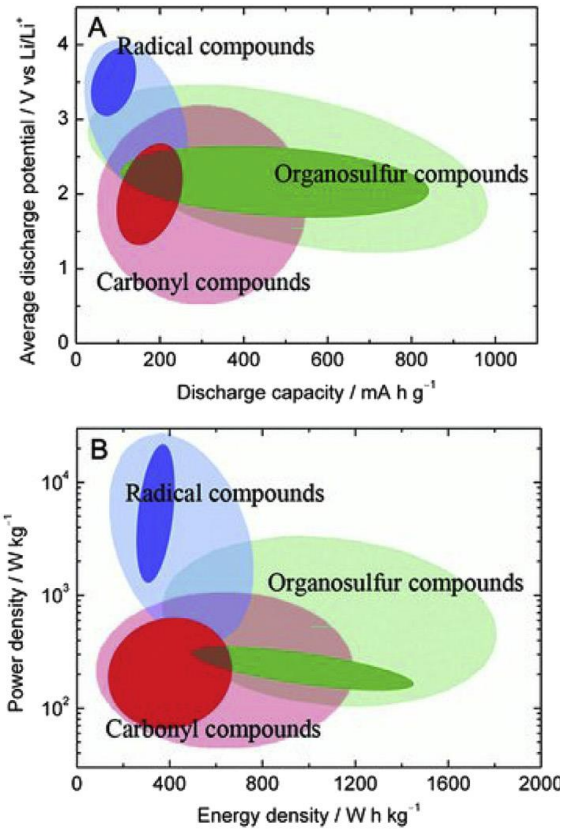

Figure 8. Comparison of the cell performance based on organosulfur (green), radical (blue), and carbonyl compounds (red). **(a)** Plot of potential versus capacity and **(b)** plot of power density versus energy density.[10]

➢ The organosulfur polymers based batteries exhibit great energy densities (Fig. 8) thanks to the high theoretical capacity of the element sulfur (ca. 1678 mAh/g). These polymers contain either disulfide or thioether compounds. The redox mechanism of disulfide polymers consists in the scission and formation of disulfides bonds (Fig. 9a). However, this redox reaction is slow, leading to a low power density (Fig. 8). Contrariwise, the batteries based on thioether polymers store and deliver electric energy via the oxidation/reduction process of the thioether cation/thioether redox couple (Fig. 9b). It was reported that they display better performances than disulfide polymers based batteries. However, the switching between low conducting (thioether)

and high conducting (thioether cation) states leads to the discharge voltage drop of the battery over cycling. Fig 9c shows examples of organosulfur polymer structures.

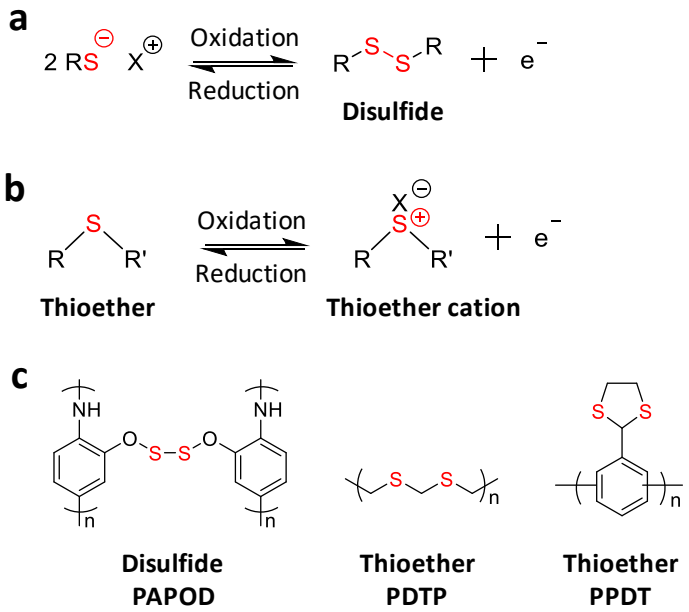

Figure 9. Mechanism of charge/discharge process of **(a)** disulfide polymer and **(b)** thioether polymer. **(c)** Examples of organosulfur polymer, poly[bis(2-aminophenyloxy)disulfide] (PAPOD left), poly(2,4-dithiopentanylene) (PDTP middle) and poly(2-phenyl-1,3-dithiolane) (PPDT right).

➢ The carbonyl polymers are composed of carbonyl compounds, which reduce into radical anions upon electrochemical stimuli (Fig. 10a). In order to undergo a stable reversible redox process, these carbonyl compounds are stabilized with appropriate R groups. The most investigated carbonyl polymers are polyquinone (such as poly[1,4-anthraquinone] in Fig. 10b) and polyimide (such as poly[pyromellitimido-1,4-phenylene] in Fig. 10c). Contrary to polyimides, polyquinones have a better redox potential of ca. 3 V vs Li/Li^+ (against 2 V vs Li/Li^+ for polyimides). However, their synthesis is difficult due to their instability.

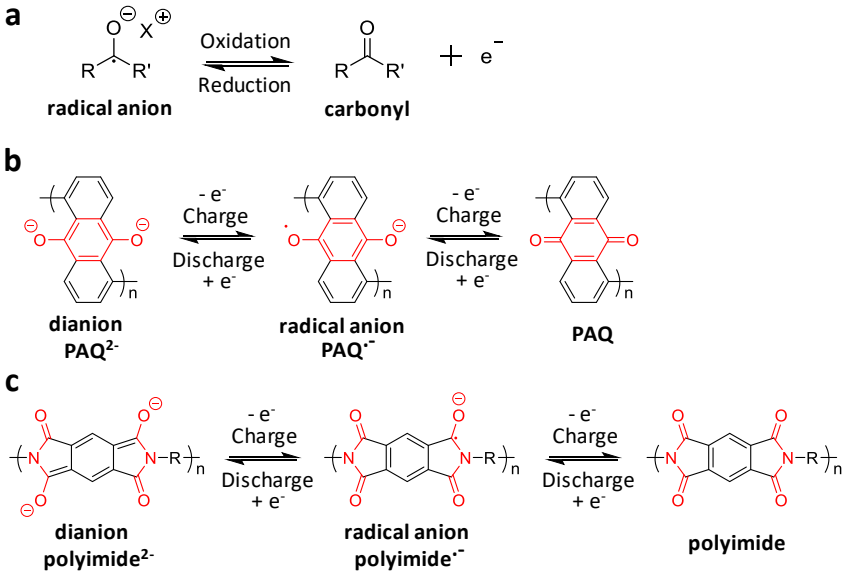

Figure 10. Mechanism of charge/discharge process of **(a)** carbonyl compounds, **(b)** poly[1,5-anthraquinone] (PAQ) and **(c)** poly[pyromellitimido-1,4- phenylene].

➢ The organic radical polymer based batteries (also known as organic radical batteries ORBs) attracted great interest during the past decade. Their active materials consist of polymers bearing stable organic radical pendant groups such as nitroxyl, hydrazyl and phenoxy radicals (Fig. 11). Moreover, nitroxides have the ability to behave both as an oxidant and as a reducer. Therefore, they can be used as active materials for cathodes and anodes. Moreover, the nitroxyl radicals are often classified as "pseudocapacitive" components because of their ultra-fast redox reaction (10^{-1} cm.s^{-1}),[11] allowing ORBs to support high power density (Fig. 8).

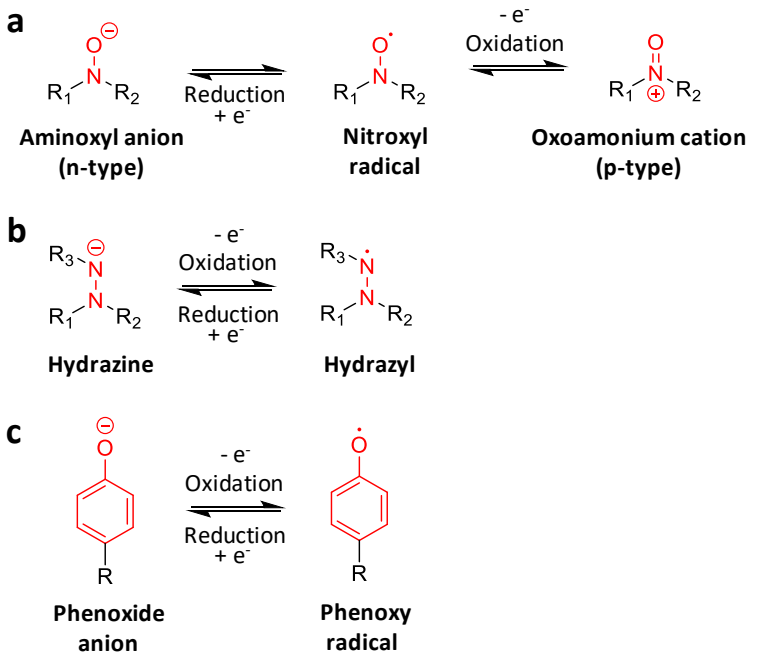

Figure 11. Mechanism of charge/discharge process of **(a)** nitroxyl radical, **(b)** hydrazyl radical and **(c)** phenoxy radical.

Various structures bearing nitroxide were developed and tested in ORBs (Fig. 12). According to the previously described equation 1, the charge storage capacity of nitroxide polymers depends on the number of charge carriers stored per unit of repetition (generally equal to 1) but also depends on the molar mass of the monomer. Therefore, the theoretical capacity increases when the molar mass of the monomer decreases. The 2,2,6,6-tetramethylpiperidinyloxyl (TEMPO) group remains the most studied because (1) it is the easiest to synthesize and (2) its nitroxide group is stable and robust thanks to the steric hindrance around the radical. Thus, it offers the best balance between the theoretical capacity (111 mAh/g) and the redox potential (0.7 V vs Ag/AgCl or 3.6 V vs Li/Li^+) when it is used in ORBs. Moreover, a change in the stability of the nitroxide leads to a shift of the potential.

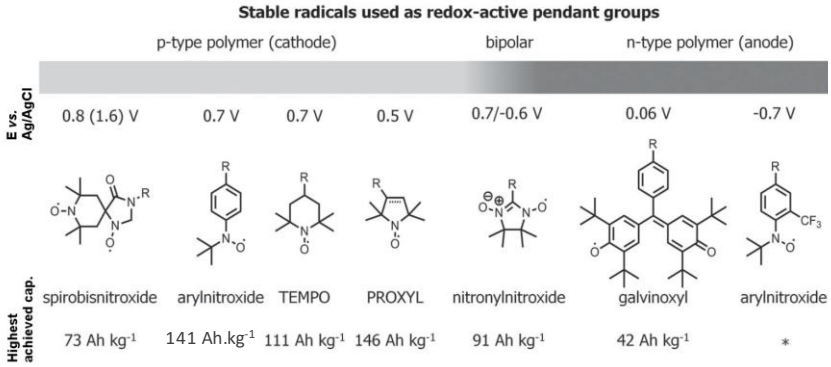

Figure 12. Variety of stable radicals with their potential vs Ag/AgCl and capacity (*: no battery was built).[12]

1.2.3 Organic radical batteries (ORBs)

Nakahara et al. reported[13] the first ORB based on a stable nitroxyl polyradical, poly(2,2,6,6-tetramethylpiperidinyloxy-4-yl methacrylate) (PTMA) bearing TEMPO groups (Fig. 13). This ORB consists in a Lithium metal anode, $LiPF_6$ salt in EC/DEC as electrolyte, and a cathode involving PTMA/graphite/binder (at 10/80/10 wt. %). PTMA was easily obtained by free radical polymerization of its amine-precursor followed by the oxidation of the amine into nitroxyde radical (Fig. 13a). Afterward, it was mixed with graphite as electrical conductor and PFE as binder. This ORB demonstrated a stable and reversible redox process with a voltage of 3.6 V vs Li/Li^+ (Fig. 13b), which is better than commercial Li-ion batteries employing $LiFePO_4$ (3.4 V vs Li/Li^+). This makes PTMA a good alternative for Li-ion batteries. However, the capacity was measured to reach 77 mAh/g. Although it corresponds to 70% of the theoretical capacity of the PTMA (which is 111 mAh/g), this value remains low compared to the inorganic cathode materials of conventional Li-ion batteries (150-170 mAh/g). Based on this initial result, several investigations were further conducted about the use of nitroxyl polyradical as cathode active material.

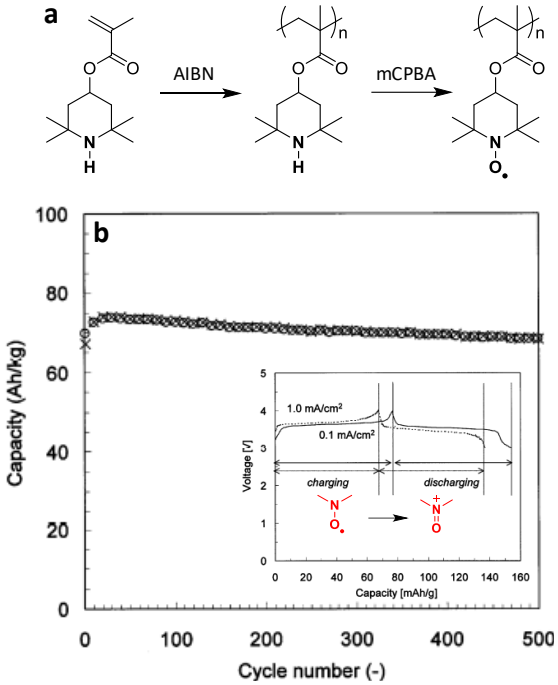

Figure 13. (a) Synthesis of poly(2,2,6,6tetramethylpiperidinyloxy-4-yl methacrylate) (PTMA) and **(b)** Charge-discharge cycles performance of organic radical battery using PTMA as cathode active material.[13]

Nishide et al. investigated completely organic polymer based rechargeable batteries (Fig. 14a). Nitroxyl radicals, such as the poly(TEMPO substituted norbornene) (Fig. 14b) and the poly(nitronylnitroxylstyrene) (Fig. 10c), were used as cathode active materials, whereas the phenoxy radical (Fig. 14d), which can only reduce into the phenoxide anion, was used as anode active material.[14] Furthermore, poly(nitronylnitroxylstyrene) was used both as cathode and anode active material.[15]

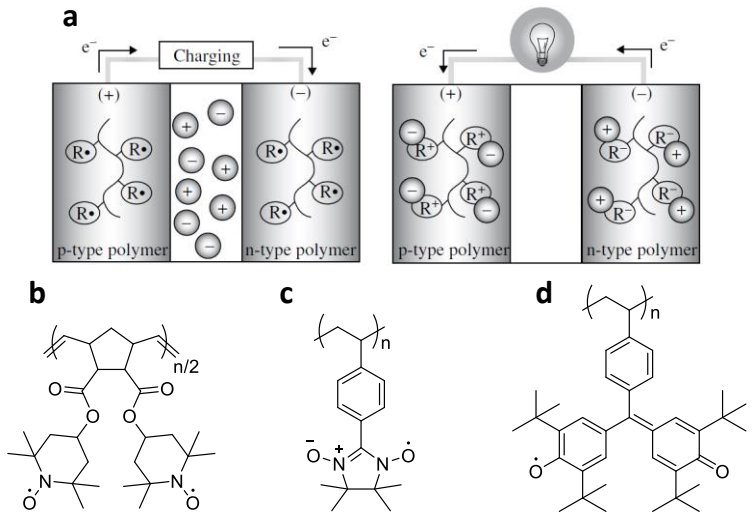

Figure 14. (a) Configuration of the complete organic radical polymer based rechargeable battery. **(b - c)** nitroxyl radical polymer used as cathode active materials and **(d)** galvanoxyl radical polymer used as anode active material.[14,15,16]

Vlad et al. reported[17] an hybrid electrochemical storage device with PTMA/$LiFePO_4$ mixture (1/1 capacity ratio) as cathode active material (Fig. 15). They demonstrated that the individual properties of the two components (organic radical and inorganic) are in synergy and that an internal electron transfer could occur between the organic and the inorganic component during the charging process. Therefore, the electrochemical device is able to store rapidly electricity with the ultra-fast electron transfer of the PTMA (generating high power density) but also able to store a large amount of electricity (generating high energy density).

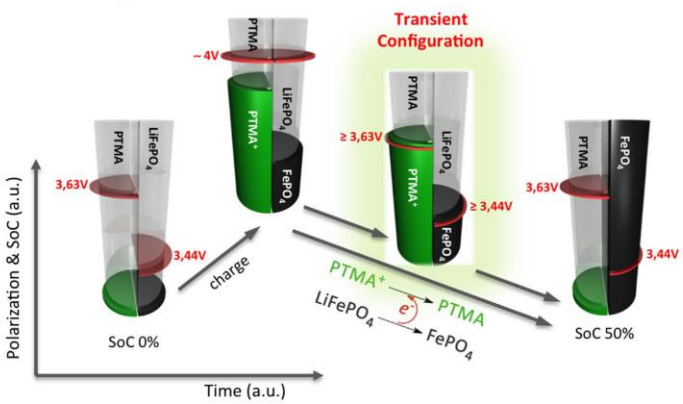

Figure 15. Schematic representation of the fast charge - relaxation process. The green and black half-cylinders are indicative of the stored charge respectively in PTMA and $LiFePO_4$. The relative position of the red disk indicates the polarization of the constituents in the hybrid electrode.[17]

Armand et al. reported[18] a polymer binder based on PEDOT electrical conducting backbones with PTMA redox active pendant groups (Fig. 16a). The synergy between the properties of two components allows the battery to have a good cycling stability and a fast charge/discharge in reducing the amount of carbon additive, which is required to improve the electrical conductivity (Fig. 16b).

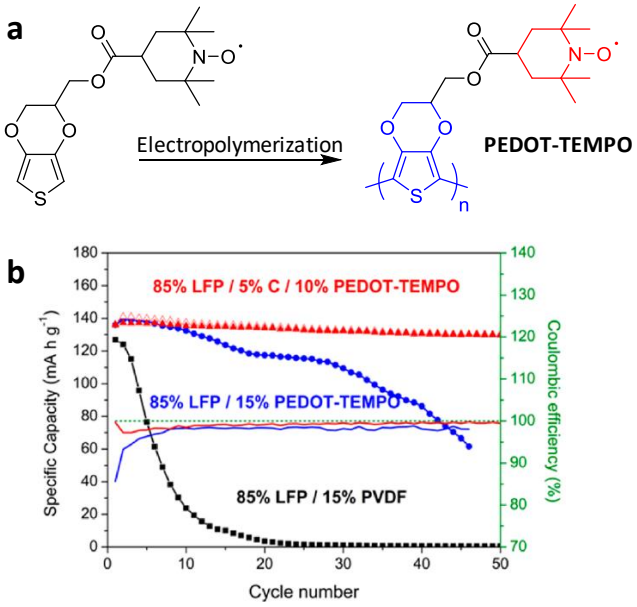

Figure 16. (a) Electrochemical polymerization of the PEDOT-TEMPO and **(b)** Cell performance of $LiFePO_4$ cathodes based battery with different compositions.[18]

1.3 Development of non-aqueous electrolytes

1.3.1 Generality

The main role of the electrolyte is to transport ions from one electrode to the other electrode. Therefore, the choice of the electrolytes is very important because their physicochemical properties influence the electrochemical performances of batteries. These electrolytes have to fulfill a set of requirements, listed below.[19]

(1) They should be good ionic conductors (up to 10^{-4} $S.cm^{-1}$ at room temperature) to facilitate the transport of ions.

(2) They should be electrical insulators (below 10^{-10} $S.cm^{-1}$) to prevent self-discharge or short-circuit of the device.

(3) They should be thermally stable (from -150°C to 300°C) and electrochemical stable (0V to 5V vs Li/Li^+) to prevent their degradations from taking place in the range of working temperature and potential window.

(4) They should be compatible with the electrode materials, forming stable electrode-electrolyte interphase (SEI). The SEI is a layer obtained from degradation (or reaction) of a limited amount of electrolyte components with a limited amount of electrode materials, allowing a protection of the electrodes-electrolyte interface from further decomposition and facilitating the transport of Li^+ cations between electrodes and electrolyte.

Contrary to the aqueous electrolytes, the main advantages of non-aqueous electrolytes are their wider electrochemical stability window as well as their wider temperature range of operation. The liquid electrolytes, usually used in commercial lithium batteries, consist of lithium salts dissolved in polar aprotic solvents. However, other kinds of non-aqueous electrolytes were developed. Here we will only discuss about organic liquids (i.e carbonate-based liquids and ionic liquids) and solid polymer electrolytes.

1.3.2 Conventional liquid electrolytes

1.3.2.1 Lithium Salts

In addition to the requirements listed previously, the lithium salts dissolved in the electrolytes should easily dissociate and be able to flow through the device with high mobility especially for lithium ions, which should have a lithium transference number t_{Li^+} close to 1 (see chapter 3 for more details about t_{Li^+}). In general, a salt is directly dissociated and solvated in polar solvents (Fig 17 a). However, in the case of lithium salts, the Li^+ ion is a hard Lewis acid. Therefore, complex anions with well-delocalized negative charge were used so that the lithium salts easily dissociate (Fig. 17 b1) and that the solvent easily solvates the Li^+ ions (Fig 17 b2).

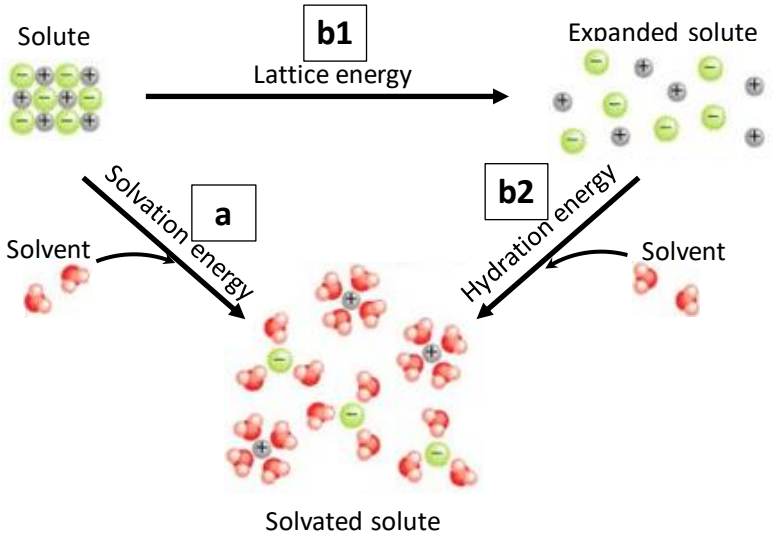

Figure 17. Solvation process of a solute.

Fig. 18 summarizes the most employed lithium salts in lithium batteries.[20] Known as anions of superacids, the anions are simple X^- anions (e.g. F^-) complexed with strong Lewis acid (e.g. PF_5) to weaken their connection with Li^+ ions (LiX bond). The lithium perchlorate salt ($LiClO_4$) presents a good solubility and a good ionic conductivity. However, the chlorine (VII), which is a strong oxidant, reacts violently with most organic oxidant under certain conditions. Although, the $LiClO_4$ is unsafe in the batteries at high current and at high temperature, it is frequently used in laboratory because it is economical and easy to handle.[20] Despite its high ionic conductivity, the lithium hexafluorophosphate salt ($LiPF_6$) can easily decompose into LiF, PF_5 and HF at high temperature/voltage and in contact with water. LiF forms a solid layer, which increases the resistance of the device, whereas PF_5 is a strong Lewis acid responsible of the decomposition of carbonate-based solvents. Contrary to $LiPF_6$, lithium hexafluoroarsenate ($LiAsF_6$) has a better ionic conductivity and a better resistance to humidity. However, the non-toxic arsenic As (V) can lead to toxic elements such as As (III) and As (0) after degradation. Lithium tetrafluoroborate ($LiBF_4$) is more stable and less toxic than the previous salts, but it presents low ionic conductivity. In addition to being stable, lithium bis(trifluoromethanesulfonyl)imide salt (LiTFSI) is a much

better choice than $LiPF_6$. However, it is responsible for aluminum corrosion from 4.4 V vs. Li/Li^+ which limits its use in 4V batteries. None of these lithium salts meets thus all the required criteria. Currently, the commercial electrolytes are based on $LiPF_6$ salt because it offers the best balance between advantages and drawbacks.

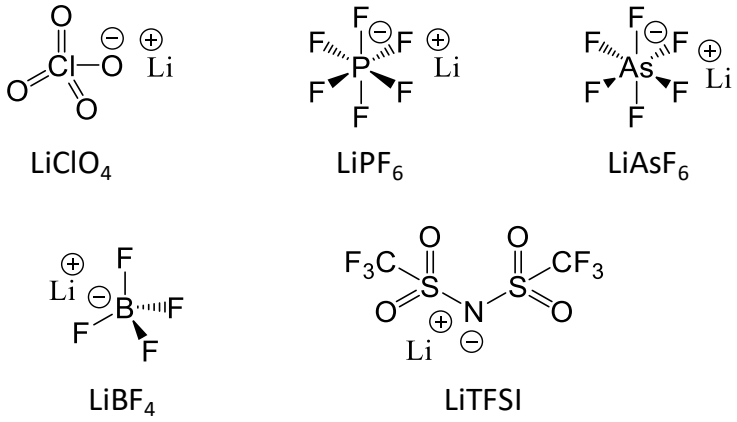

Figure 18. The structures of some lithium salts.[20]

1.3.2.2 Polar aprotic solvents

In addition to the requirements listed previously, the solvents should have low viscosity and high dielectric constant to promote dissociation of the lithium salts. Therefore, the solvents used in non-aqueous electrolytes are bearing polar groups such as carbonyl (C=O), nitrile (N≡O), sulfonyl (S=O) and ether (-O-). However, it is often necessary to mix several solvents (also known as addition of co-solvents or additives) in order to fulfill these requirements. [21,22,23,24] Currently, the commercial electrolytes are based on solution mixtures of linear alkyl carbonates and cyclic alkyl carbonates (Fig. 19 and Table 1). This is due to the fact that cyclic carbonates exhibit a high dielectric constant but also a high viscosity, whereas the linear carbonates are less viscous but are characterized by a lower dielectric constant.[25] The propylene carbonate (PC) based electrolyte was the first to be used in commercial lithium ion batteries for its wide range of working temperature (between -49°C to 242°C), its stability against oxidation and its dielectric constant of 65. Subsequently, PC was replaced by

ethylene carbonate (EC) because of its higher dielectric constant of 90 and its ability to produce a more stable SEI leading to high rate capacity. However, it is still used as co-solvent because of its high melting point (36°C), rendering it useless as ambient-temperature electrolyte. In order to improve the intrinsic properties of cyclic carbonates, EC was further functionalized. Indeed, it was reported that the substitution of the hydrogen at the 4th or 5th position of the ethylene carbonate cycle (Fig. 19) by an alkyl chain as for butylene carbonate (BC in Fig. 19), has an influence on the intrinsic properties of the electrolytes.[26] In this respect, BC exhibits stability in wider temperature and electrochemical potential ranges than EC (Table 1). However, the grafted alkyl substituent chain increases the viscosity and decreases the dielectric constant (Table 1), decreasing the ionic conductivity. Subsequently, the hydrogen at the 4th or 5th position of the ethylene carbonate cycle was substituted with fluorine-containing electron withdrawing groups (Fig. 19). It was reported that fluoroethylene carbonate (FEC) promotes the solvation of Li^+ ions thanks to its fluorine group.[27] Moreover, it presents a low viscosity as well as a low melting point. Finally, the decomposition of FEC leads to a better conductive and stable SEI film,[28,29] improving the battery performances. Firstly reported by McMillan et al.[30] as an alternative solvent for lithium-ion batteries, FEC is an emerging solvent for commercial properties.

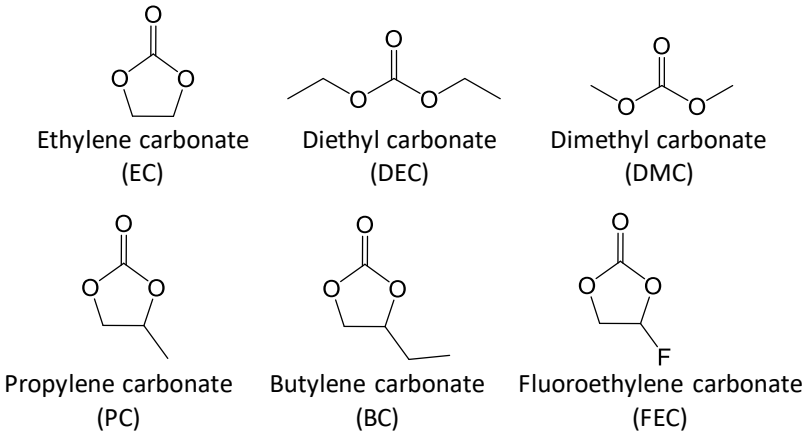

Figure 19. The structures of carbonate solvents.[25]

Solvents	Melting point (°C)	Boiling point (°C)	Viscosity (mPa.s)	Dielectric constant ε
EC	36	248	1.9 (40°C)	90 (40°C)
PC	-49	242	2.5	65
BC	-53	240	3.2	53
DEC	-74	126	0.75	2.8
DMC	5	91	0.59	3.1

Table 1. The intrinsic properties of carbonate solvents.[25]

In order to improve the properties of electrolytes, numerous researches were realized on organic solvents containing sulfur, phosphorus and boron elements, in addition to the fluorine element previously discussed.[31] The development of new lithium salts was also explored with these same elements. However, the operating mechanism of these functional groups and their influence on the properties of the devices remain to be investigated in more details. Moreover, despite all the acquired properties, these polar organic liquid electrolytes remain flammable and bad ionic conductor compared to aqueous electrolytes. Many research groups try to develop non-aqueous electrolytes safer and more ionic conducting such as ionic liquid electrolytes or solid polymer electrolytes discussed thereafter.

1.3.3 Ionic liquid electrolytes

Ionic liquids (ILs) are another class of liquid electrolytes. They are defined as salts with a melting temperature below 100°C.[32] In general, ILs are composed of organic cations and organic/inorganic anions. Both of them (cation and anion) are bulky with asymmetric shapes in order to delocalize charge and to decrease the lattice energy of the salt, reducing its melting temperature and increasing the mobility of charges (Fig. 17).[33] Fig. 20 shows some well-known ILs. According to cation-anion combinations and the substitution of their groups,[34] it is possible

to obtain ILs with variable physicochemical properties. Therefore, their properties can be adjusted to suit requirements.[35] ILs are thus used for many applications in various fields[32,36,37] such as catalysis, engineering, pharmaceutic and electrochemistry.

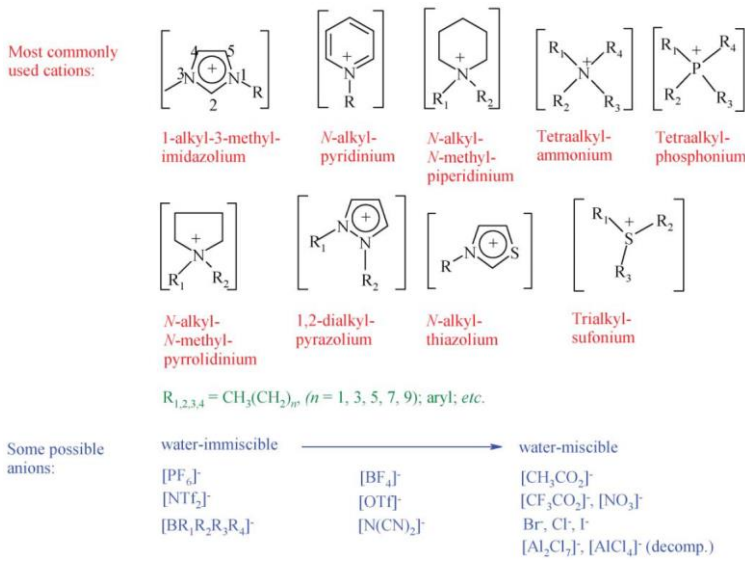

Figure 20. Structures of usual cations and anions forming ILs.[36]

Moreover, these ILs exhibit interesting properties, which allow them to be promising candidates for lithium batteries. In fact, they are nonflammable and nonvolatile due to their low vapor pressure as well as their high thermal and chemical stabilities. However, despite they exhibit excellent ionic conductivity (from 10^{-4} to 10^{-2} $S.cm^{-1}$), it does not exceed the conductivity of the standard electrolytes. This is because their ionic conductivity is obviously related to the density of ions and their dissociated state, which both influence the viscosity of the medium.[38] In general, it is preferable to use less viscous ILs in order to increase the ionic conductivity. It was reported that anions with highly delocalized charges (such as $TFSI^-$) decrease the viscosity of ILs. In fact, for a same 1-butyl-3-methylimidazolium cation, the viscosity decreases in the following order: [39]

$$Cl^- > PF_6^- > BF_4^- > NO_3^- > TFSI^-$$

While, the small size of anions increases the ion mobility. In fact, it was reported that for a same TFSI anion, the viscosity decreases in the following order: [40]

$$\text{Ammonium}^{+} > \text{Pyrrolidinium}^{+} > \text{Piperidinium}^{+} > \text{Imidazolium}^{+}$$

The imidazolium ring is small and planar due to the conjugated double bonds, contrary to the tetrahedral structure of the tetraalkyl-ammonium.

According to the Walden law (equation 5)[41,42] the ionic conductivity of ILs is closely related to their viscosity. The latter allows assessing the ionic behavior of ILs by coupling the fluidity (inverse of the viscosity η) to the ionic mobility (or molar conductivity Λ) (Fig. 21). The ionic liquids are compared to the ideal electrolyte solution (red dashed line in Fig. 21) where ions are completely dissociated, typically an aqueous solution of KCl (1M). Below this "ideal" line, ILs are classified as "poor". This means that the ions are associated and close together, leading to a high vapor pressure. Conversely, above this line, ILs are classified as "superionic" because the ions are decoupled, generating a low vapor pressure. This is usually the case of poly(ionic liquid)s also known as polyelectrolytes (see 1.3.4 Polymer electrolytes).

$$\Lambda . \eta = \text{constant} = \text{Walden product} \qquad (5)$$

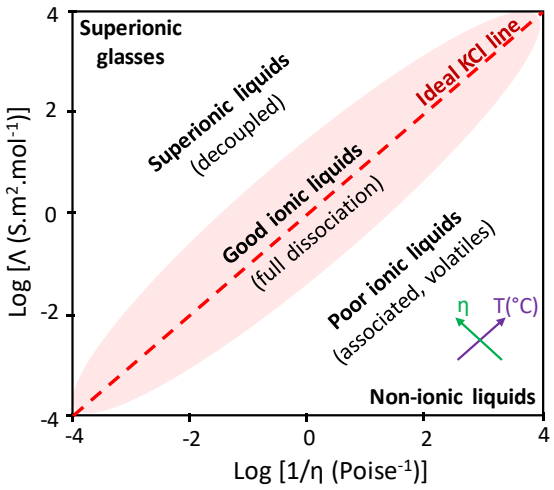

Figure 21. Walden plot Log (fluidity) versus Log (molar conductivity).

Although some ILs have high ionic conductivity, it is not sufficient to use them alone as electrolytes. In fact, the addition of lithium salts is necessary to ensure Li^+ transport between the electrodes where it is dissociated from its counter-ion. However, when lithium salts are added to ILs, the viscosity increases for two reasons. Firstly, Li^+ ions have large solvation shells coming from bulky ILs. Therefore, Li^+ ions migrate slowly because of their solvation shell, leading to a low Li^+ transport number. Secondly, lithium salts form neutral ion-pairs (or aggregates) with ILs. Therefore, the ions do not contribute to the ionic conductivity due to their associated state.[43]

Facing these problems, mixtures of ionic liquids and lithium salts were widely studied to be used as electrolytes for lithium batteries. Currently, several approaches are exploring ways to get around those issues. The first approach is to use ILs only as additive, in addition to another electrolyte. In fact, nowadays ILs are not used pure in commercial batteries. However, for some cases, they are used for high temperature applications due to their ability to make the batteries fireproof (Fig. 22a).[44] Recently, ILs were functionalized with redox groups to increase the energy of supercapacitors (Fig. 22b).[45] ILs are also used as plasticizers by being trapped in an organic/inorganic solid and flexible membrane in order to form a separator (also known as ionogel) whose the structure does not change depending on the temperature (Fig. 22c).[46,47] The other approach consists in polymerizing ILs in order to decouple ions (such as superionic liquids in Fig. 21) and thus to promote Li^+ migration by hopping mechanism with the motion of chains based on ILs (see 1.3.4 Polymer electrolytes).

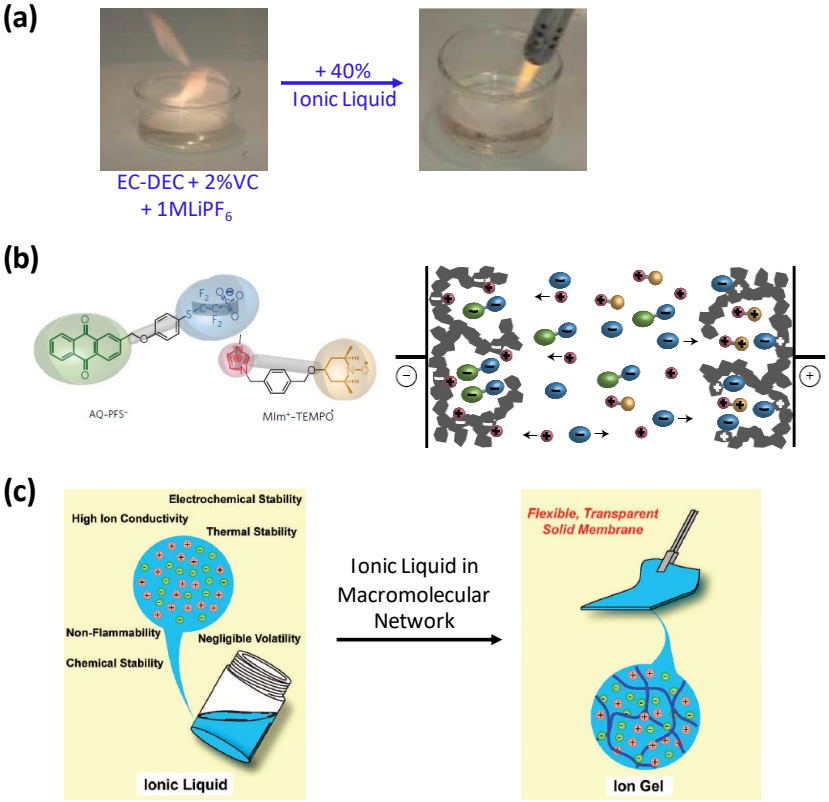

Figure 22. (a) Flammability test on usual liquid electrolyte without and with EMI-TFSI ionic liquid.[44] **(b)** Capacitor based on the biredox IL electrolyte comprising a perfluorosulfonate anion bearing anthraquinone ($AQ–PFS^-$) and a methyl imidazolium cation bearing TEMPO ($MIm^+–TEMPO^{\cdot}$).[45] **(c)** Preparation of ionogels.[47]

1.3.4 Solid polymer electrolytes

Generally, two main polymer electrolytes can be distinguished. The first is the gel polymer electrolyte (GPE), which is based on liquid electrolyte (lithium salt with solvent) trapped in a non-conductor solid polymer matrix. The liquid electrolyte is the only ionic conductor, allowing GPE to exhibit high ionic conductivity (up to 10^{-2} $S.cm^{-1}$) comparable to that of liquid electrolyte. However, the disadvantages related to the safety are similar to liquid electrolytes. The second is the

solid polymer electrolyte (SPE), which is based on lithium salts dissolved in a dry polar polymer matrix.

The dry SPEs attract great attention because they are considered as a safer alternative to liquid electrolytes. As discussed previously, these SPEs were developed in order to prevent leakage/dendrites problems of lithium-metal batteries. Their adjustable mechanical strength and plasticity are the main advantages, which allow SPEs to be used in flexible batteries. Of course, the polymer is selected according to two factors in order to be used in SPE. Firstly, the polymer has to possess functional polar groups able to solvate ions. Secondly, the chains as well as their polar groups have to be in movement to facilitate the mobility of ions. It means that the structure of the polymer does not have to hinder the segmental motion of chains and thus the motion of ions.[48]

The polymers widely used as matrix in SPEs are often semi-crystalline polymers with electro-donating groups, which coordinate Li^+ cations. The first studied SPE is the crystalline poly(ethylene oxide) (PEO) but other polymers were investigated later such as poly(vinylidene fluoride) (PVDF), poly(propylene oxide) (PPO), poly(methyl methacrylate) (PMMA), poly(3-caprolactone) (PCL) and poly(vinylpyrrolidone) (PVP). In addition to be thermally/chemically stable, their relatively high dielectric constants allow these polymers to dissolve the salts by forming solvation shell around Li^+ with their electro-donor atoms. However, these semi-crystalline polymers based SPEs exhibit ionic conductivity lower than 10^{-5} $S.cm^{-1}$ at room temperature because of their high degree of crystallinity, which hinders their ability to conduct ions. In fact, it was reported[49] that below the melting temperature (Tm), the motions of polymer chains facilitate the conduction of ions in the amorphous regions (Fig. 23a), whereas the crystalline regions slow down (or prevent) the diffusion of ions (Fig. 23b).

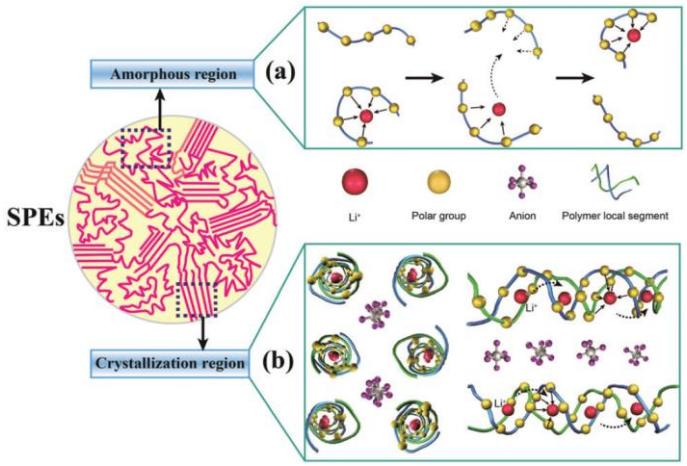

Figure 23. Two types of ion conduction mechanism in solid polymer electrolytes (SPEs).[49]

Several approaches were investigated in order to understand the relationships between the structure of materials and their conductive properties. Shi and Vincent reported[50] the effect of molecular weight on ionic mobility in polymer electrolytes. They demonstrated the existence of a critical molar mass (Mn*) to distinguish two modes of polymer conduction (equal to 5000 g/mol for PEO). Linear low molar mass polymers in the molten state (Mn < Mn* and T > Tm) have a better mobility and can easily diffuse because they do not have any constraint, following the Rouse model. Since Li^+ cations are complexed by the PEO chains, the ionic diffusion (or migration) is then dictated by the polymeric chain motion. In contrast, high molar mass polymers (Mn > Mn*) do not have significant effect on the diffusion of cation because the chain motions are slowed down by topological constraints. The reptation process of the chains occurs, which takes longer times. Therefore, the motion of the cations is hampered, resulting in a negligible conductivity.

Devaux et al. reported[51] the effect of the molar mass and end groups on the mechanism of ion transport in PEO/LiTFSI complexes. They demonstrated that polar OH end groups strongly interact with the ions and the chains backbones by hydrogen bonds. The formation of these transient crosslinking limits the mobility of ions and increases the viscosity of the electrolyte (Fig. 24). Conversely, the use of the CH_3 end

groups, which generate high free volume, do not affect the mobility of ions. Thus, the use of polar OH end groups decrease the ionic conductivity values contrary to CH_3 end groups. They also demonstrated that the influence of end groups on the ionic conductivity and viscosity of PEO electrolytes only takes place for low molar mass polymer and their influence decreases when molar mass of the polymer increases (Fig. 24). Thus, they verified the theory of Shi and Vincent discussed previously, which is the short chains lead to a good motion of ions because they have a better mobility, while for long chains the conductivity decreases until to reach a constant. However, they concluded that for high molar mass polymers, the ion transport mechanism is the jump from one coordination site to another one and is not influenced by the reptation of PEO chains. Whereas, their transport is ensured by low molar mass polymers according to the vehicular mechanism.

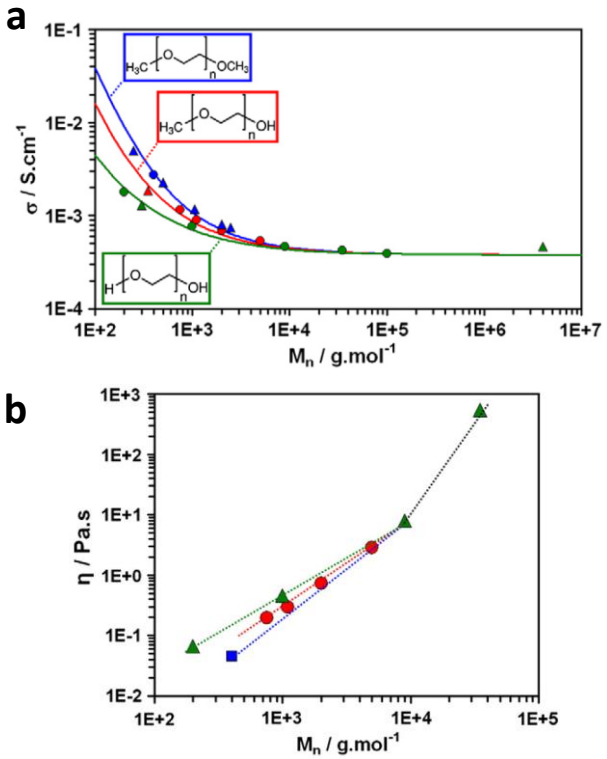

Figure 24. Isothermal variation at 60°C of **(a)** the ionic conductivity and **(b)** the viscosity versus molar mass Mn of the PEG (green), PEGM (red) and PEGDM (blue).

In 2005, Kanamura et al. reported[52,53] a SPE based on PS-*b*-POEGMA-*b*-PS triblock copolymers loaded with $LiClO_4$ in molar ratio EO:Li of 20, which exhibits a high ionic conductivity of 10^{-4} $S.cm^{-1}$ at room temperature and a tensile strength of 3MPa (Fig. 25). The conductor central block, shaped like "flexible comb", consists in short poly(oligo(ethylene glycol) methyl ether methacrylate) (POEGMA 1000 g/mol) with long PEO pendant chains to promote the ionic conductivity. While, the polystyrene blocks allow improving the mechanical strength.

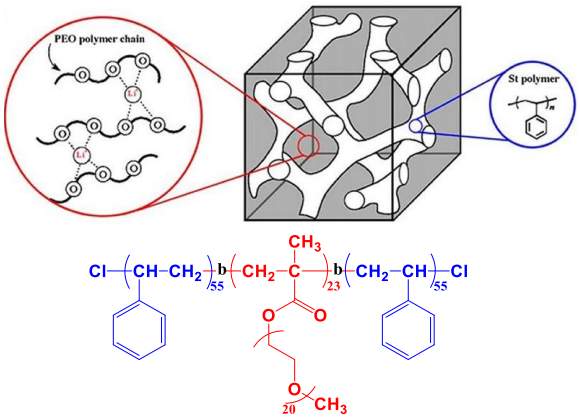

Figure 25. SPE based on bicontinous nanostructure-controlled PS-*b*-POEGMA-*b*-PS triblock copolymers obtained with over 80% POEGMA content. [52,53]

Gohy et al. developed[54] solid diblock copolymer electrolytes based on PS and POEGMA (Fig. 26). They demonstrated that a minor polystyrene block is sufficient to give a mechanical strength to the POEGMA block without hindering the ion conduction, which attains 0.01 mS/cm at room temperature.

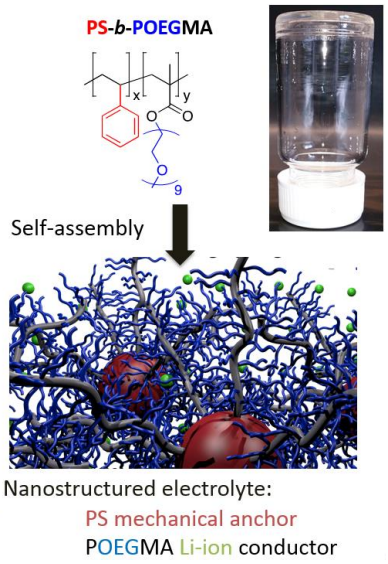

Figure 26. Chemically anchored liquid-PEO based block copolymer electrolytes.[54]

Following this, Bouchet et al. investigated[55] the influence of the morphology and periodicity of microphase separated nanostructures on the ionic conductivity for the SPE based on PS-*b*-PEO-*b*-PS loaded with LiTFSI salt at EO:Li molar ratio of 20 (Fig. 27). The morphology is determined by the variation of the volume fraction of the two blocks of the copolymers, whereas the periodicity is determined by the variation of the molar mass of the copolymers. They observed that the ionic conductivity decreases when longer PS blocks are added to the same short PEO central block (Fig. 27 a). While for the structures having the same PEO content but different molar masses the ionic conductivity remains approximatively the same (Fig. 27 b). They concluded that only the conductor block content influences the ionic conductivity because the increase of this block decreases the ratio of "dead zone", which affects the conductivity (Fig. 27 c).

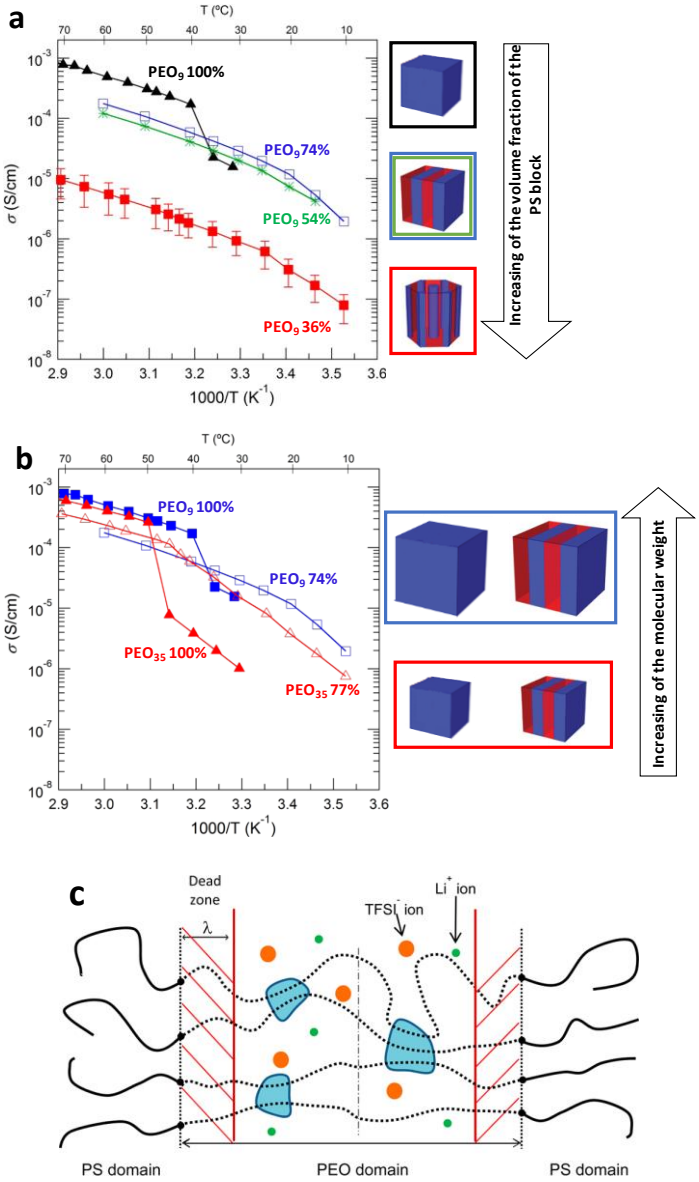

Figure 27. Conductivities versus temperature for triblock copolymer electrolytes (PS-PEO-PS) **(a)** with same length of PEO central block (9 kg/mol) but different lengths of PS block and **(b)** at different molar masses (9 and 35 kg/mol) containing approximatively 75wt% PEO. **(c)** Schematic representation of the microstructured block copolymer electrolyte (PS-PEO-PS). The hatched red areas show the zone devoid of ionic transport, and the blue areas are PEO crystallites.[55]

Bouchet et al. reported[56] the effect of the nature of the conductor block on ionic mobility in SPE. They replaced[56] the polystyrene (PS) blocks by polyanionic (PSTFSILi) blocks (Fig. 28) in order to improve the diffusion of Li^+. They demonstrated that anionic pendant groups promote the Li^+ transport number, which is estimated up to 0.85. Moreover, they observed that P(STFSILi)-PEO-P(STFSILi) triblocks exhibit better mechanical strength than PS-PEO-PS triblocks. However, the use of polyanions hindered the mobility of anions, leading to a low ionic conductivity of 10^{-5} $S.cm^{-1}$ at 60 °C. In fact, the anions are linked by covalent bonds, decreasing their mobility.[57]

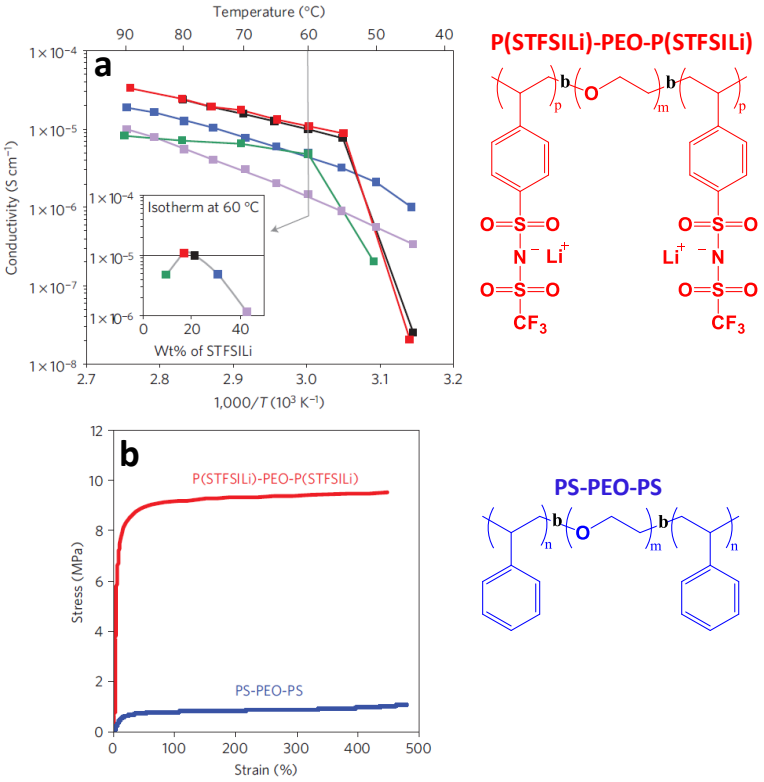

Figure 28. (a) Ionic conductivity depending of the temperature and of the content in PSTFSILi block (in wt%). **(b)** Tensile tests at 40°C for PS-PEO-PS (in blue) and for PSTFSILi-PEO-PSTFSILi (in red) with a PEO block of 35 kg/mol; PS blocks of 2 x 6 kg/mol (corresponding to 25 wt%) and PSTFSILi blocks of 2 x 7.8 kg/mol (corresponding to 31 wt%).[56]

1.4 Flow batteries

Flow batteries are another type of rechargeable batteries where the active materials are not stored within the electrodes as the usual solid-state systems but in external tanks that are called catholyte and anolyte (Fig. 29). These external tanks are composed of 5 to 20 wt. % of active storing materials, contrary to the electrode films used in usual batteries for which the composition is in active materials is higher than 80 wt. %. Thus, the active materials, that are dissolved (or in suspension) in electrolyte solutions, flow from outside of the cell to the inside of the electrodes.[58] The pumping of the active materials through the main cell allows the latter to be fueled continuously, generating electrical energy.

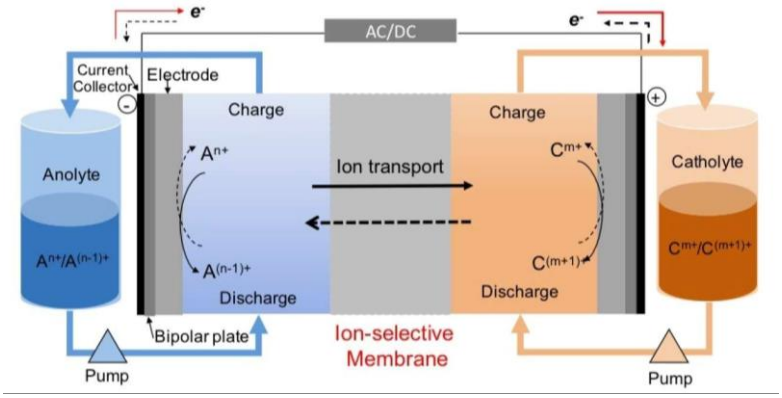

Figure 29. Configuration of flow battery. [59]

In these flow batteries, the energy and power are independent variables.[60] In fact, the energy is related to the concentration and the size of the external tanks. While the power is related to the composition and the size of the electrodes. Even if these batteries work with a flow system, they remain batteries where no physical transfer of active materials should take place across the separator. Therefore, the anolyte and catholyte components must not mix, to avoid an abrupt discharge of the battery (or short circuit). In most common aqueous redox flow batteries (RFB), small molecules of vanadium complexes are used as active materials. With a Nafion ion exchange membrane as separator, the vanadium complexes can not cross though the membrane pores due

to the electrostatic repulsion. Unfortunately, this system is unfavorable in nonaqueous media because the vanadium is poorly soluble and the Nafion membrane becomes a poor ionic conductor.[61]

Thus, a new concept of size exclusion of nanomaterials in RFBs was implemented (Fig. 30). This consists of developing and using active materials with sizes equal to or higher than the pore sizes of the membrane. A quantitative exclusion for $r_{particle}/r_{pore} \approx 0.6$ has even been predicted.[62] Moore, Lopez and al.[63] studied the impact of redox-active poly(vinylbenzyl ethylviologen) molecular weight on the electrochemical properties and transport across porous separators in nonaqueous solvents. They demonstrated that the transport across porous separators of lithium salts increased significantly by changing the active materials from small molecules to redox-active polymers. Moreover, they confirmed that the polymers can be completely rejected from crossing over a porous membrane with high $r_{polymer}/r_{pore}$ values (>0.6). Unfortunately, the redox active polymers having higher molecular weight display low limiting current.

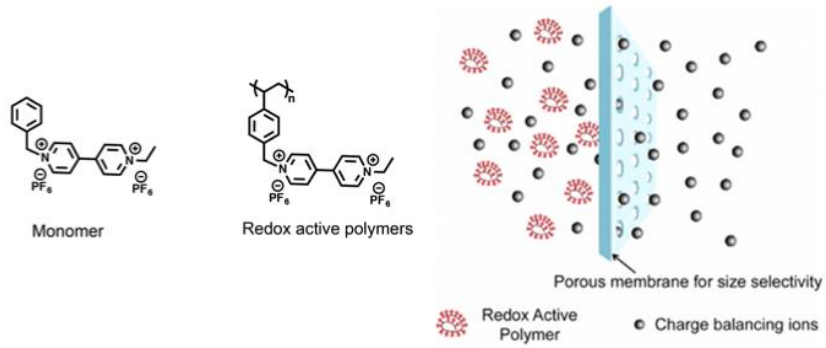

Figure 30. (Left) Chemical structure of the vinylbenzyl ethylviologen monomer and polymer redox active. **(Right)** Illustration of transport of charges across porous separators.[63]

1.5 Objective of the thesis

Batteries are electrochemical energy storage systems. They have the capacity to store and to deliver electrical energy thanks to chemical reactions that take place within their electrodes. Over the years, batteries have rapidly evolved according to the environmental, economic and societal demands. They became lighter, smaller and more autonomous with high specific energy. However, one of the main drawbacks of batteries is their limited power delivery and charging time, which are due to the slow charge transfer and ion diffusion processes occurring in the bulk electrode materials. The other drawback of batteries is the safety issue, as far as the liquid electrolyte is concerned. In fact, the fast charge of batteries causes accelerated degradation of their constituents, increasing the heat production, which can lead to fire and explosion hazards. Furthermore, the batteries remain expensive because of their manufacturing method but also because of the limited supply of the raw materials. Different strategies have been examined to overcome these problems by playing on the active materials of the cathodes and on the electrolytes. Unfortunately, only compromises were considered until now, because it is difficult to fulfill all the requirements in a single material.

The aim of the thesis is to develop new polymer-based components for cathode and electrolyte, easy to synthesize, safer and able to improve the performances of batteries. Investigations will be conducted on the understanding and the finding of an adequate correlation between the structure of the proposed materials and their electrochemical properties. In this thesis, we will design polymeric materials with enhanced ionic conductivity for different types of batteries. In fact, the improvement of the ionic conductivity of batteries could facilitate the charge transfers within batteries, allowing them to charge quickly and handle high power. This motivation to develop these types of materials lies in the constantly increasing demand for more efficient batteries. In this respect, our research is clearly related to requirements form the battery market.

The first part reports on the development of hybrid ionic conducting and electro-active polymer gels as cathode active materials for organic radical batteries (ORBs). We will focus on the development of cathodes

for ORBs based on two main components, the redox-active PTMA and ionic liquid triazolium. The redox-active PTMA is known as pseudo-capacitive component, which generates ultra-fast electron transfer process. This latter allows a rapid charge of the battery. In order to improve the ionic conductivity, we decided to incorporate the ionic triazolium component. It will be used as crosslinking nodes in order to prevent the dissolution of PTMA in the organic electrolyte, which leads to a drop of the performance of batteries. Therefore, these cathode active materials will consist of redox active polymer chains based on PTMA cross-linked together by ionic liquid triazolium nodes. Thus, fast ion-exchange reactions in electrodes are considered in the electrodes based on pseudo-capacitive redox polymer and ionic liquid triazolium, as the systems we designed in chapters 2 and 3. This further allows obtaining batteries able to deliver high power when needed (e.g. for application in power tools). Firstly, in chapter 2, the synthesis of PTMA gels in one-pot by a combination of Cu(0)-mediated radical polymerization and copper-catalyzed cycloaddition of azides and alkynes (CuAAC click chemistry) will be investigated. Secondly, in chapter 3, the effect of the nature of crosslinking nodes as well as the crosslinking ratio on the performances of batteries will be studied.

In the second part, we will try to improve the ionic conductivity by developing solid polymer electrolytes (SPEs) based on cyclic ethylene carbonate (EC) groups. The idea is to use EC as pendant groups in order to facilitate the jump or vehicular mechanism of ions from one pendant group to another one. Thus, motion of ions within the electrolyte could be enhanced, leading to a swift charge of the battery. Moreover, EC groups have high dielectric constant, which enables the dissociation of salts. Thus, high amount of lithium salts could be incorporated, increasing the ionic conductivity values. The migration of ions will not be hindered by any complexation of EC groups as for the case of PEO electrolyte. In addition, contrary to the linear alkyl carbonates, the cyclic ethylene carbonate based electrolytes could form stable interfaces with electrodes (also known as SEI). Thus, the SPEs investigated in chapters 4 and 5 were envisaged in order to exhibit high ionic conductivity at room temperature, as required for application in the so-called solid lithium metal polymer batteries, which are currently intensively investigated for use in the electric vehicles. In chapter 4, studies will be conducted on fluorinated semi-crystalline copolymers

based on EC pendant groups in order to bring a mechanical resistance to the solid polymer electrolyte. The EC groups are functionalized with fluorinated groups and copolymerized with poly(vinylidene fluoride) (PVDF) semi-crystalline. An easy synthesis of this copolymer was carried out by Ameduri et al. PVDF is used as binder or as separator in Li-battery due to its good mechanical properties. Contrary to common hydrophobic polymers such as polystyrene, PVDF is composed of fluorinated groups, which are known to better dissolve salts than hydrophobic polymers. Thus, the SPE crystalline phases generated by the PDVF could also contribute to the mobility of ions. Conversely, in chapter 5, studies will be conducted on amorphous copolymers composed on EC and n-butyl acrylate (*n*BA). They will be easily synthesized by controlled radical polymerization (*i.e.* RAFT). Here, the PVDF semi-crystalline groups are replaced by low Tg P*n*BA chains so that the flexibility of the chains facilitates the mobility of the ions.

Finally, the third part (or chapter 6) reports the development of PTMA redox active polymer based nano-objects as cathode active materials in suspension for aqueous flow battery. Thus, hydrophobic PTMA will be copolymerized in order to be dispersed in water. For this, an economical synthesis will be employed. The polymerization induced self-assembly (PISA) will be used in order to form the amphiphilic nano-objects simultaneously in the same reaction medium that of the copolymerization of the second PTMA hydrophobic block. However, as discussed previously (1.4 flow batteries), the structure and the size of the nano-objects influence the diffusion of these active materials within the flow battery and therefore the electrochemical properties of cells. That why in chapter 6, intrinsic parameters (such as nature of hydrophilic blocks, molar mass of the block copolymer and hydrophilic fraction *p*) will be modified in order to found an ideal composition of amphiphilic nano-objects based redox active PTMA, improving the performances of the flow battery. Moreover, we will try to control the viscosity of these organic catholytes in order to be intensively developed to store the energy produced by intermittent sources like windmills and photovoltaic panels.

Bibliography

1 C. Liu, Z. G. Neale and G. Cao, *Mater. Today*, 2016, **19**, 109–123.
2 J. M. Tarascon and M. Armand, *Nature*, 2001, **414**, 359–367.
3 M. Armand and J. M. Tarascon, *Nature*, 2008, **451**, 652–657.
4 J. Chen, *Materials (Basel).*, 2013, **6**, 156–183.
5 M. S. Whittingham, *Chem. Rev.*, 2004, **104**, 4271–4301.
6 A. Manthiram and T. Muraliganth, in *Handbook of Battery Materials*, Wiley-VCH., 2011, pp. 343–375.
7 M. Osiak, H. Geaney, E. Armstrong and C. O'Dwyer, *J. Mater. Chem. A*, 2014, **2**, 9433–9460.
8 S. Muench, A. Wild, C. Friebe, B. Häupler, T. Janoschka and U. S. Schubert, *Chem. Rev.*, 2016, **116**, 9438–9484.
9 N. Casado, G. Hernández, H. Sardon and D. Mecerreyes, *Prog. Polym. Sci.*, 2016, **52**, 107–135.
10 D. R. Nevers, F. R. Brushett and D. R. Wheeler, *J. Power Sources*, 2017, **352**, 226–244.
11 H. Nishide, S. Iwasa, Y. J. Pu, T. Suga, K. Nakahara and M. Satoh, *Electrochim. Acta*, 2004, **50**, 827–831.
12 T. Janoschka, M. D. Hager and U. S. Schubert, *Adv. Mater.*, 2012, **24**, 6397–6409.
13 K. Nakahara, S. Iwasa, M. Satoh, Y. Morioka, J. Iriyama, M. Suguro and E. Hasegawa, *Chem. Phys. Lett.*, 2002, **359**, 351–354.
14 T. Suga, H. Ohshiro, S. Sugita, K. Oyaizu and H. Nishide, *Adv. Mater.*, 2009, **21**, 1627–1630.
15 T. Suga, S. Sugita, H. Ohshiro, K. Oyaizu and H. Nishide, *Adv. Mater.*, 2011, **23**, 751–754.
16 T. Suga, Y.-J. Pu, S. Kasatori and H. Nishide, *Macromolecules*, 2007, **40**, 3167–3173.
17 A. Vlad, N. Singh, J. Rolland, S. Melinte, P. M. Ajayan and J. F. Gohy, *Sci. Rep.*, 2014, **4**, 1–7.
18 N. Casado, G. Hernández, A. Veloso, S. Devaraj, D. Mecerreyes and M. Armand, *ACS Macro Lett.*, 2016, **5**, 59–64.
19 Q. Li, J. Chen, L. Fan, X. Kong and Y. Lu, *Green Energy Environ.*, 2016, **1**, 18–42.
20 K. Xu, *Chem. Rev.*, 2004, **104**, 4303.
21 A. Laheäär, H. Kurig, A. Jänes and E. Lust, *Electrochim. Acta*, 2009, **54**, 4587–4594.
22 E. Perricone, M. Chamas, L. Cointeaux, J. C. Leprêtre, P. Judeinstein, P. Azais, F. Béguin and F. Alloin, *Electrochim. Acta*, 2013, **93**, 1–7.
23 A. Jänes and E. Lust, *J. Electroanal. Chem.*, 2006, **588**, 285–295.
24 A. Janes, J. Eskusson, T. Thomberg and E. Lust, *J. Electrochem. Soc.*, 2014, **161**, A1284–A1290.
25 M. S. Ding, K. Xu, S. Zhang and T. R. Jow, *J. Electrochem. Soc.*,

2001, **148**, A299.
26 K. Chiba, T. Ueda, Y. Yamaguchi, Y. Oki, F. Saiki and K. Naoi, *J. Electrochem. Soc.*, 2011, **158**, A1320.
27 T. Böttcher, N. Kalinovich, O. Kazakova, M. Ponomarenko, K. Vlasov, M. Winter and G. V. Röschenthaler, *Novel Fluorinated Solvents and Additives for Lithium-Ion Batteries*, Elsevier, 2015.
28 Y. Lee, J. Lee, H. Kim, K. Kang and N. S. Choi, *J. Power Sources*, 2016, **320**, 49–58.
29 A. L. Michan, B. S. Parimalam, M. Leskes, R. N. Kerber, T. Yoon, C. P. Grey and B. L. Lucht, *Chem. Mater.*, 2016, **28**, 8149–8159.
30 R. McMillan, H. Slegr, Z. X. Shu and W. Wang, *J. Power Sources*, 1999, **81**–**82**, 20–26.
31 W. Zhao, Y. Ji, Z. Zhang, M. Lin, Z. Wu, X. Zheng, Q. Li and Y. Yang, *Curr. Opin. Electrochem.*, 2017, **6**, 84–91.
32 J. F. Brennecke and E. J. Maginn, *AIChE J.*, 2001, **47**, 2384–2389.
33 H. L. Ngo, K. LeCompte, L. Hargens and A. B. McEwen, *Thermochim. Acta*, 2000, **357**–**358**, 97–102.
34 B. Baek, S. Lee and C. Jung, *Int. J. Electrochem. Sci.*, 2011, **6**, 6220–6234.
35 H. Tokuda, K. Ishii, A. Bin, H. Susan, S. Tsuzuki, K. Hayamizu and M. Watanabe, 2006, 2833–2839.
36 N. V. Plechkova and K. R. Seddon, *Chem. Soc. Rev.*, 2008, **37**, 123–150.
37 M. Armand, F. Endres, D. R. MacFarlane, H. Ohno and B. Scrosati, *Nat. Mater.*, 2009, **8**, 621–629.
38 A. M. O. Mahony, D. S. Silvester, L. Aldous, C. Hardacre and R. G. Compton, *Engineering*, 2008, 2884–2891.
39 H. Olivier-Bourbigou and L. Magna, *J. Mol. Catal. A Chem.*, 2002, **182**–**183**, 419–437.
40 I. Osada, H. De Vries, B. Scrosati and S. Passerini, *Angew. Chemie - Int. Ed.*, 2016, **55**, 500–513.
41 M. Yoshizawa, W. Xu and C. A. Angell, *J. Am. Chem. Soc.*, 2003, **125**, 15411–15419.
42 C. Austen Angell, Y. Ansari and Z. Zhao, *Faraday Discuss.*, 2012, **154**, 9–27.
43 S. Tsuzuki, K. Hayamizu and S. Seki, *J. Phys. Chem. B*, 2010, **114**, 16329–16336.
44 A. Guerfi, M. Dontigny, P. Charest, M. Petitclerc, M. Lagacé, A. Vijh and K. Zaghib, *J. Power Sources*, 2010, **195**, 845–852.
45 E. Mourad, L. Coustan, P. Lannelongue, D. Zigah, A. Mehdi, A. Vioux, S. A. Freunberger, F. Favier and O. Fontaine, *Nat. Mater.*, 2016, **1**.
46 J. Le Bideau, L. Viau and A. Vioux, *Chem. Soc. Rev.*, 2011, **40**, 907–925.
47 T. Ueki, M. Watanabe and W. Masayoshi, *Macromolecules*, 2008, **41**, 3739–3749.

48 S. B. Aziz, T. J. Woo, M. F. Z. Kadir and H. M. Ahmed, *J. Sci. Adv. Mater. Devices*, 2018, **3**, 1–17.
49 R. Chen, W. Qu, X. Guo, L. Li and F. Wu, *Mater. Horizons*, 2016, **3**, 487–516.
50 J. Shi and C. A. Vincent, *Solid State Ionics*, 1993, **60**, 11–17.
51 D. Devaux, R. Bouchet, D. Glé and R. Denoyel, *Solid State Ionics*, 2012, **227**, 119–127.
52 T. Niitani, M. Shimada, K. Kawamura and K. Kanamura, *J. Power Sources*, 2005, **146**, 386–390.
53 T. Niitani, M. Shimada, K. Kawamura, K. Dokko, Y.-H. Rho and K. Kanamura, *Electrochem. Solid-State Lett.*, 2005, **8**, A385.
54 J. Rolland, J. Brassinne, J.-P. Bourgeois, E. Poggi, A. Vlad and J.-F. Gohy, *J. Mater. Chem. A*, 2014, **2**, 11839–11846.
55 R. Bouchet, T. N. T. Phan, E. Beaudoin, D. Devaux, P. Davidson, D. Bertin and R. Denoyel, *Macromolecules*, 2014, **47**, 2659–2665.
56 R. Bouchet, S. Maria, R. Meziane, A. Aboulaich, L. Lienafa, J. P. Bonnet, T. N. T. Phan, D. Bertin, D. Gigmes, D. Devaux, R. Denoyel and M. Armand, *Nat. Mater.*, 2013, **12**, 452–457.
57 H. Ohno, *Macromol. Symp.*, 2007, **249**–**250**, 551–556.
58 A. Z. Weber, M. M. Mench, J. P. Meyers, P. N. Ross, J. T. Gostick and Q. Liu, *J. Appli. Electrochem.*, 2011, **41**, 1137–1164.
59 https://www.imperial.ac.uk/song-group/research/batteries-for-energy-storage
60 K. B. Hatzell, M. Boota and Y. Gogotsi, *Chem. Soc. Rev.*, 2015, **44**, 8664–8687.
61 L. Su, R.M. Darling, K.G. Gallagher, W. Xie, J.L. Thelen, A.F. Badel, J.L. Barton, K.J. Cheng, N.P. Balsara, J.S. Moore, F.R. Brushett, *J. Electrochem. Soc*., 2016, **163**, A5253−A5262.
62 E. F. Casassa, *J. Polym. Sci., Part B: Polym. Lett.* 1967, **5**, 773−778.
63 G. Nagarjuna, J. Hui, K. Cheng, T. Lichtenstein, M. Shen, J. S. Moore, J. R. Lopez, *J. Am. Chem. Soc.,* 2014, **136**, 16309−16316.

Chapter 2:

One-pot synthesis of redox-active polymer gels via copper-mediated radical polymerization and click chemistry

Table of contents

2.1 Introduction

Amongst the different redox-active polymer materials investigated so far,[1] poly(2,2,6,6-tetramethylpiperidinyloxy-4-yl methacrylate) (PTMA) has been widely used. Due to its stable and robust nitroxide radicals lateral groups,[2] PTMA supports a high rate performance with an ultra-fast electron-transfer process of 10^{-1} cm/s,[3] a reversible redox process of 3.6 V *vs.* Li/Li^{+}[4] and a cycling stability exceeding 1000 cycles.

Nevertheless, the performances of PTMA based cathodes are often hindered by the poor conductivity of the PTMA and by its intrinsic solubility in standard battery electrolytes. Many research groups have provided strategies to avoid solubilization of this active material and to increase its conduction properties. For example, PTMA was polymerized with polystyrene to form insoluble frozen micelles,[5] however the addition of a dead component such as styrene affects cathode performances. It was subsequently grafted on insoluble and conducting carbon nanotube (CNT),[6] unfortunately CNTs are difficult to manipulate, disrupting the cathode fabrication process.

Ideally, the strategy should end up with a material that combines insolubility in battery electrolytes while allowing a good ionic conductivity in the bulk of the cathode. Interestingly those prerequisites can be met by gel materials, the network being able to provide structural integrity while an adequate swelling in the electrolyte solution can support a fast ionic flux. Gels have long been known as ideal candidates for many technological applications,[7,8] due to their adjustable mechanical properties. They vary mostly depending on the nature of the cross-linking nodes (or/and backbones), which could generate covalent[9] or physical[10] bonds but also depending on the cross-linking density.

The strategy developed in this thesis is to synthesize PTMA gels with triazolium crosslinking nodes mimicking ionic liquids (ILs). Thus, PTMA chains will be immobilized in a three-dimensional network. In addition to maintain the network, the ionic groups could improve the ionic diffusion and reduce the hazard risks related to the commercial electrolyte. In order to facilitate the manufacturing process, a one-pot and controlled synthesis of the gel will be approached in this chapter 2,

while the influence of the triazolium ionic liquid crosslinking nodes will be investigated in chapter 3.

The "click" chemistry is a set of coupling reactions[11,12,13] introduced by Sharpless *et al*.[14] It is mainly used to produce polymers with complex topologies.[15] Amongst these coupling reactions, the 1-3 dipolar cycloaddition involving azides and alkynes has raised interest of the scientific community and has become the most popular of this class. The azide-alkyne has proved to be a particularly powerful coupling reaction. Moreover, the cycloaddition reaction catalyzed by Cu^{I} (CuAAC) is efficient and regioselective[16,17] because it yields only the 1,4-disubstituted 1,2,3-triazole at room temperature (Fig.1).

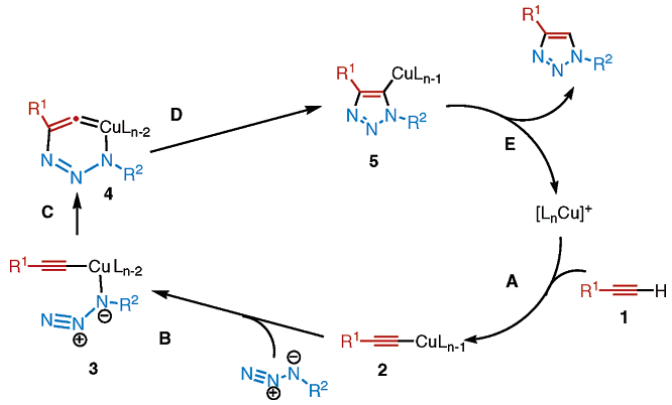

Figure 1. Mechanism of copper(I) catalyzed azide–alkyne cycloaddition.[16]

Controlled radical polymerization (CRP) (or reversible-deactivation radical polymerization (RDRP)) is known to enable access to well-defined polymer materials. Over the last years, those techniques have been widely employed to prepare polymers with complex topologies by using polyfunctional initiators or monomers combined with click chemistry. Indeed, numerous examples of CRP combined with click chemistry have already been reported such as clickable block copolymers synthesis via RAFT[18] and azide-alkyne cycloaddition on miktoarm star terpolymers synthetized via NMP.[19] However, among the various CRP techniques, ATRP combined to CuAAC[20,21] is the most widely employed given the benefit of using the same catalyst for both involved synthetic processes.

More recently, a new RDRP technique has emerged, namely the copper(0)-mediated reversible-deactivation radical polymerization. This technique was first introduced by Matyjaszweski *et al.*,[22] to which major contributions reported by Percec *et al.*[23,24] and Haddleton *et al.*[25,26] have brought further developments. It is an attractive technique because of its ability to synthesize well-defined polymers at lower temperatures along with high chain-end fidelity. Indeed, it is possible to reach a total monomer conversion without observing transfer and termination mechanisms. Moreover, all the problems related to the instability of Cu(I) are suppressed. In fact, this variant of atom transfer radical polymerization (ATRP) consists in using a mixture of Cu(0)/Cu(II) instead of Cu(I), which is usually used in ATRP as the main activator. According to the role of the Cu(0), two types of Cu(0)-mediated radical polymerization exist. The Cu(0) is either used as the supplemental activator of the Cu(I) and reducing agent of Cu(II) in ATRP (SARA-ATRP in Fig. 2a) or used as exclusive activator in the single-electron transfer living radical polymerization (SET-LRP in Fig. 2b).[27,28] In the SARA-ATRP, the Cu(I) activates the growth of polymer chains and oxidizes into Cu(II). Thereafter, the main part of Cu(II) reduces into Cu(I), thus forming dormant chains, whereas the remaining part of Cu(II) comproportionates with Cu(0) to form more Cu(I). In the SET-LRP, it is the Cu(0) which activates the growth of polymer chains. The resulting Cu(I) disproportionates into Cu(0) and Cu(II). While, the Cu(0) continues to activate the growth of polymer chains, the Cu(II) deactivates the growth of polymer chains.

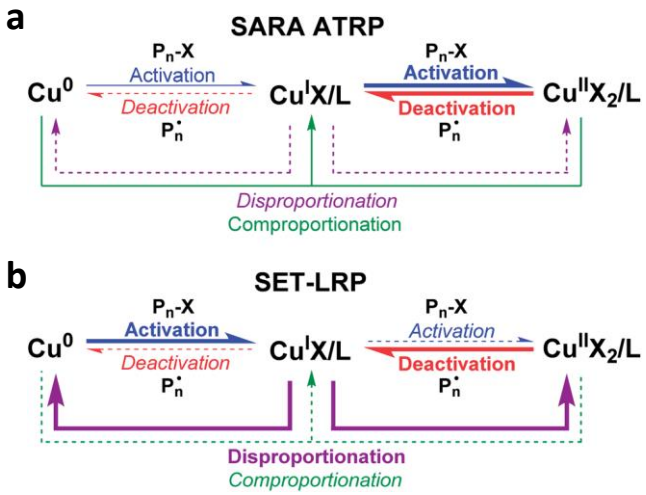

Figure 2. The mechanism of **(a)** SARA ATRP and **(b)** SET-LRP. Bold arrows indicate major reactions contributing to the polymerization process. Solid arrows indicate supplemental reactions. Dashed arrows indicate minor reactions that can be neglected.[27]

The objective of this chapter is to immobilize PTMA chains in a three-dimensional network in order to avoid their solubilisation in commercial electrolytes and to generate shortens the lifespan and the overall performance of the battery. Thus, we will explore the Cu(0)-mediated RDRP in conjunction with the CuAAC to prepare PTMPM networks in one pot (Fig.3). The polymerization of 2,2,6,6-tetramethylpiperidin-4-yl methacrylate (TMPM) with an azide functionalized monomer (3-Azidopropyl methacrylate or AzPMA) by Cu(0)-mediated RDRP have already been investigated.[29,30] After the oxidation process, the nitroxide moieties displayed a stable and a reversible redox process by voltammetry cyclic. Here, our strategy is based on the synthesis of PTMPM chains simultaneously with the formation of 1,4-disubstituted 1,2,3-triazole crosslinking points by using a propargyl functionalized initiator (PBIB) and a second co-monomer adding an azide functionality (AzPMA) to the chain as sticking group. A detailed investigation of this simultaneous one-pot synthesis is presented in the following. The measurements related to the Figs. 9, 10, 11 and 12, have been realized and interpreted by Dr. Olivier Bertrand. The oxidation of PTMPM finally yields redox-active PTMA

gels and their electrochemical performances are analyzed and detailed. The electron spin resonance (ESR) spectroscopy measurements were kindly carried out by the Dr. Tobias Janoschka from the team of prof. Schubert in Jena University in Germany.

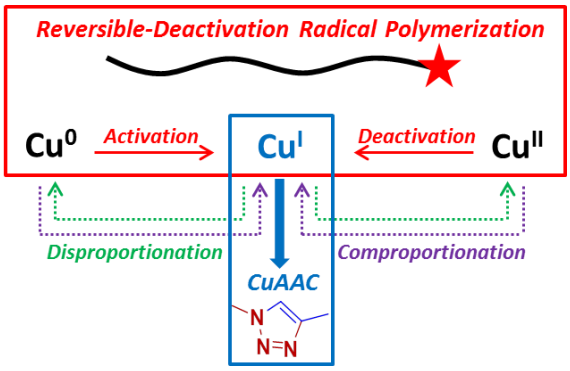

Figure 3. Strategy developed in chapter 2: the Cu(0)-mediated RDRP (in red square) realized simultaneously with the CuAAC click chemistry (in blue square) by using an equilibrium of copper generated by disproportionation and comproportionation.

2.2 The one-pot synthesis of the precursor gel

2.2.1 Synthesis

The synthesis of the PTMPM gel was carried out in two steps. In a first step, the synthesis was realized with 5 cm of Cu(0) wire and [$CuBr_2$]/[PMDETA] = 0.05/0.12 molar ratio in isopropanol (IPA) (60 wt. %) at 40 °C (Fig. 4). Two different molar ratios of [PBIB]/[TMPM]/[AzPMA] were employed, 1/5/2 and 1/23/2. In a second step, a third co-monomer [PMA] = 1 molar ratio in IPA was added after a given time. Thereafter, the viscosity increased until the formation of a gel (Fig. 4). This second step consists in forming a gel as homogeneous as possible by avoiding the azide/alkyne ratio of 2/2 at the beginning.

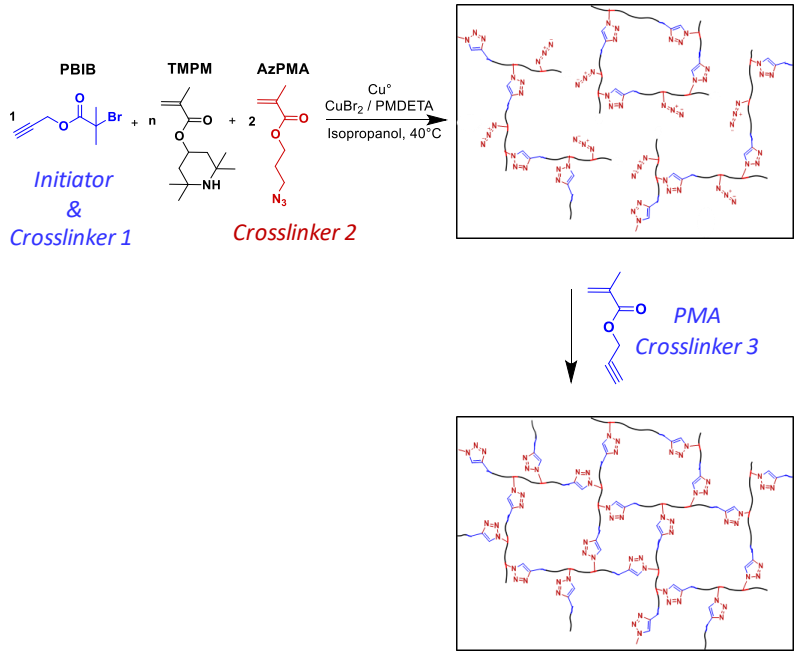

Figure 4. One-step synthesis for the formation of the PTMA networks.

2.2.2 Chain extension due to the coupling reaction

Regarding the first step of the process, samples of the polymerization mixture were withdrawn and subjected to ^{1}H-NMR and SEC analyses in order to monitor the reaction as well as to determine the end of the first step process before adding the PMA co-monomer. The results were compared to an homopolymer reference like the EBIB-P(TMPM$_{18}$-*r*-AzPMA$_2$) copolymer realized in the same conditions but also to AzPMA-c-PMA crosslinking nodes (Fig.6). All samples were collected via a cannula under inert conditions.

For both polymers with experimental ratios PBIB-P(TMPM$_5$-*r*-AzPMA$_2$) and PBIB-P(TMPM$_{23}$-*r*-AzPMA$_2$), the absence of vinyl peaks (at 5.5 and 6.1 ppm in Fig 5) in the crude samples indicates a full consumption of the monomers after 18 h of polymerization.

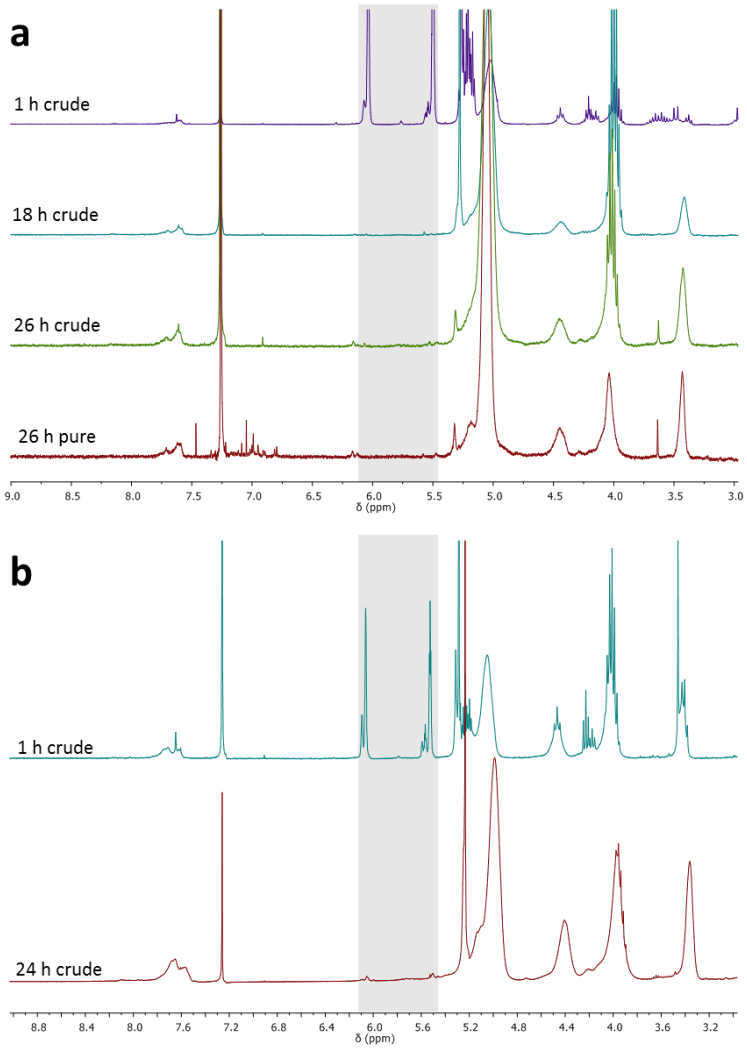

Figure 5. Evolution of ^{1}H NMR spectra in $CDCl_3$ versus polymerization time before adding end chain PMA for **(a)** PBIB-P(TMPM$_{23}$-*r*-AzPMA$_2$) and **(b)** PBIB-P(TMPM$_5$-*r*-AzPMA$_2$).

Moreover, the visualization of the alkyne α-proton peak (d_1 at 4.7 ppm in Fig. 6) and the azide α-proton peak (c_1 at 3.52 ppm in Fig. 6) shifting toward deshielded areas (d_2 at 5.32 ppm and c_2 at 4.45 ppm respectively in Fig. 6), from the beginning of the polymerization, confirms the azide-alkyne coupling into triazoles (Fig. 6). The characteristic proton of the triazole ring (e_2) is also observed at 7.63

ppm, but its intensity is influenced by the presence of copper in contrast to the intensity of other click reaction characteristic peaks as triazole ring γ-proton peak (b_2), which grows as a function of the polymerization time (Fig. 5a). For both targeted compositions, unreacted azide functions of the AzPMA units are still present in the medium when full consumption of the TMPM monomer is achieved (> 24 h) as shown by the representative ^{1}H-NMR spectrum (Fig. 6 middle). This is easily explained by the excess ratio of alkyne:azide functions (1:2).

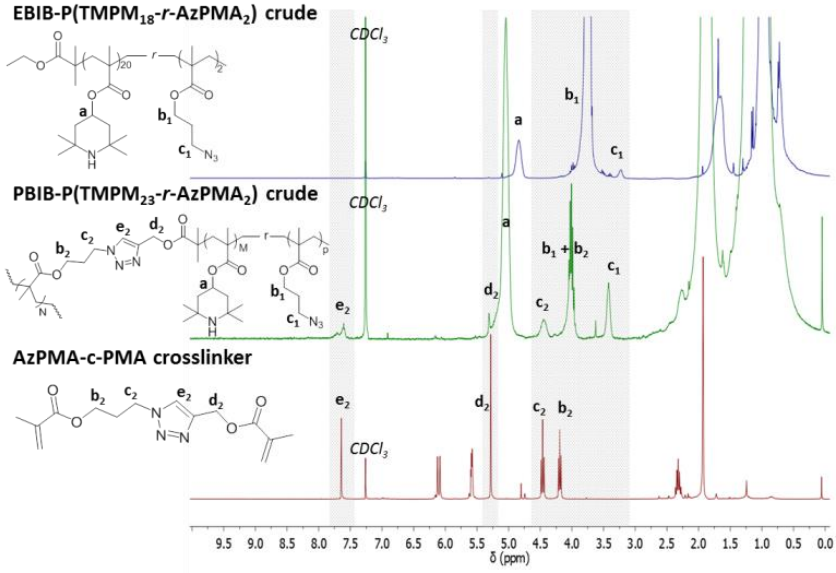

Figure 6. ^{1}H-NMR spectra of PBIB-P($TMPM_{23}$-*r*-$AzPMA_2$) before adding end chain PMA **(middle)**, EBIB-P($TMPM_{18}$-r-$AzPMA_2$) **(top)** and AzPMA-c-PMA crosslinker **(bottom)** measured in $CDCl_3$.

In addition to NMR spectroscopy, SEC measurements were also performed (Fig. 7). Of course, the obtained results are relative to polystyrene. A shift toward higher molar mass population is observed as a function of time for PBIB-P($TMPM_{23}$-*r*-$AzPMA_2$), but also for PBIB-P($TMPM_5$-*r*-$AzPMA_2$). Moreover, the increase of $Đ$ is also observed for both materials. It clearly demonstrates the chain extension due to the crosslinking process. From 26 h of polymerization, the increase of the molar mass and the progression of peak shape stop, indicating that the CuAAC process has come to an end. The same trend

has also been observed after 24 h for the synthesis of the PBIB-P(TMPM$_5$-*r*-AzPMA$_2$).

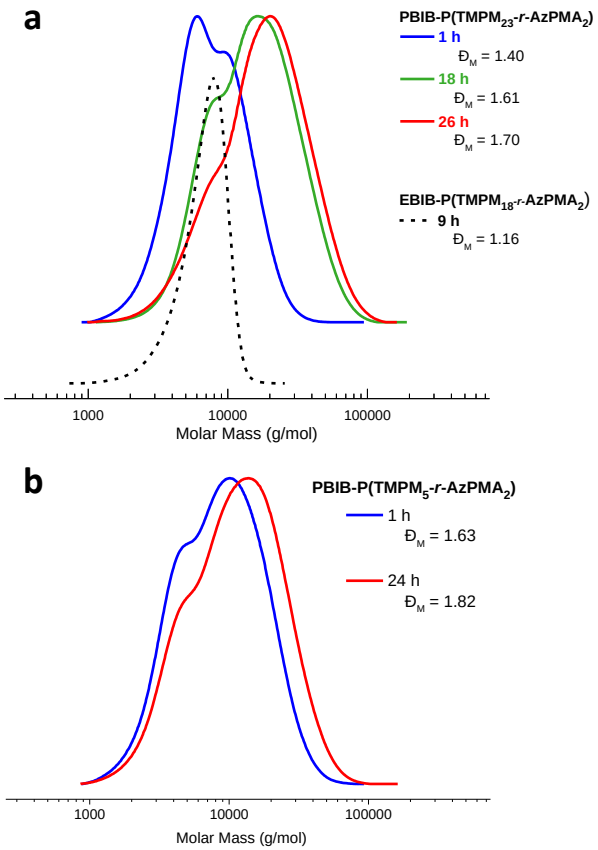

Figure 7. Evolution of SEC curves with polymerization time before adding PMA. **(a)** is PBIB-P(TMPM$_{23}$-r-AzPMA$_2$) and **(b)** is PBIB-P(TMPM$_5$-r-AzPMA$_2$). For the sake of comparison, the EBIB-P(TMPM$_{20}$-r-AzPMA$_2$) reference sample is shown (dotted line).

2.2.3 Efficiency of the coupling reaction

The efficiency of the coupling reaction between azide and alkyne functions was studied by Fourier Transform Infrared spectroscopy (FTIR). As illustrated in Fig. 8 for the AzPMA monomer the azide functions are evidenced by an absorption peak at 2100 cm^{-1}. At the end of the first step, the FTIR spectrum of P(TMPM$_{23}$-*r*-AzPMA$_2$) displays

the azide absorption band as expected from the 1:2 alkyne:azide ratio. Indeed, while switching the EBIB initiator to a PBIB (one bearing an alkyne group), the relative signal of the azide has significantly decreased. This signal being concentration dependent, it illustrates the further conversion of the azide groups related to the alkyne:azide ratio. By increasing the number of alkyne functions after adding PMA comonomer in the second step, no signal for the presence of azide functions is observed. The complete disappearance of the azide band at 2100 cm^{-1} confirms the quantitative coupling between the alkyne functions of the PMA pending groups and the remaining azide groups of the P(TMPM-*r*-AzPMA).

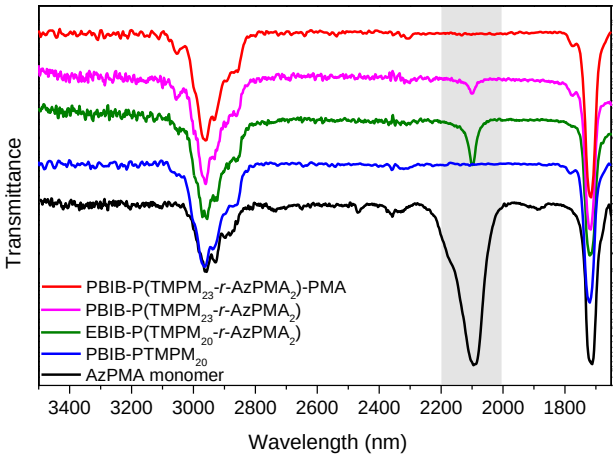

Figure 8. Overlay of FTIR spectra.

The PBIB-P($TMPM_{23}$-*r*-$AzPMA_2$) and PBIB-P($TMPM_5$-*r*-$AzPMA_2$) samples were observed as free-flowing solutions before turning into gels upon addition of the PMA co-monomer. The formation of a gel was evidenced by the inverted tube test as illustrated in Fig. 9. By recording linear oscillatory frequency sweeps, the viscoelastic properties of the materials were probed under different time scales. As shown in Fig. 9, the storage (G') and loss (G'') moduli were measured as a function of frequency (f) for PBIB-P($TMPM_{23}$-*r*-$AzPMA_2$)-PMA (further abbreviated as DP23 for clarity) and PBIB-P($TMPM_5$-*r*-$AzPMA_2$)-PMA (further abbreviated as DP5 for clarity), for which only the number of repeating units of TMPM monomers (M) is varying

between each triazole cross-linking node (N). To avoid spoiling the network by removing the copper species, the rheological measurements were realized on crude samples with the presence of copper.

Dynamic mechanical spectroscopy (Fig. 9a) reveals that before PMA addition, the materials are viscoelastic liquids, as indicated by the domination of loss modulus G'' over the whole frequency range but also the presence of a crossover frequency (fc ≥ 10 Hz). If the material behaves liquid-like and flows on long timescales (low frequencies), the values of G' and G" get closer as the frequency increases. At frequencies beyond fc (short timescale), the material answer is supposed to be dominated by elasticity due to transient entanglements between chains. In this context, DP23 shows higher moduli than DP5, which can be logically ascribed to the difference in chain length.

In contrast, after adding PMA, plateaus are observed for G' and G'' values. The storage modulus G' dominates (Fig. 9b) with a plateau value between 10^3 and 10^4 Pa, defined as the plateau modulus (G_0). These observations are consistent with the solid-like elastic nature of the formed gels. Moreover, the materials do not relax at low frequencies, reflecting well the permanent network. It is known that the G_0 value increases with the cross-linking density until they reach a maximum. In our case, the gap between G_0(DP23) and G_0(DP5) is not clearly emphasized, meaning that the maximum value of G_0 has been reached for these systems.

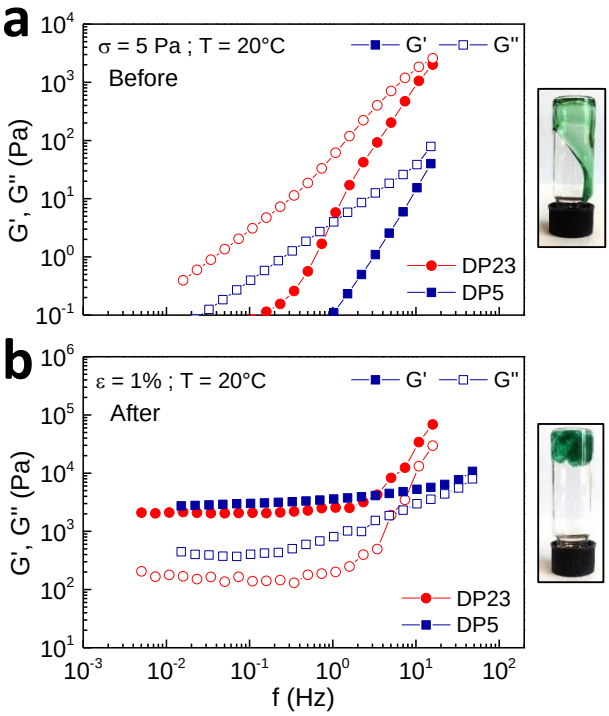

Figure 9. Frequency sweep and picture of PBIB-P(TMPM$_5$-*r*-AzPMA$_2$) and of PBIB-P(TMPM$_{23}$-*r*-AzPMA$_2$) **(a)** before and **(b)** after addition of PMA end chain (40wt% of polymer, 0.4g/ml).

As demonstrated below, the first step of this one-pot synthesis has yielded the desired functional polymers, P(TMPM$_5$-*r*-AzPMA$_2$) and P(TMPM$_{23}$-*r*-AzPMA$_2$) thanks to the efficient simultaneous CuAAC and RDRP processes. The difunctional initiator (PBIB) has been able to ensure on the one hand the initiation of PTMPM chains by Cu(0)-mediated RDRP, and on the other hand the formation of 1,2,3-triazoles crosslinks by CuAAC with the AzPMA comonomer. Moreover, as full conversion of the reactants was achieved during the first step, the system undergoes a uniform gelation process by addition of the PMA co-monomer. Those observations confirm the retention of chain-end fidelity and the presence of Cu^I species in the medium, catalyzing the coupling process, as reported in the literature.[31,32]

2.2.4 The equilibrium between coppers

As stated in the introduction, the mechanism of Cu(0)-mediated RDRP is still under debate. The use of Cu° as the activator and the low temperature used in our synthesis would suggest a SET-LRP mechanism. However, the possibility to realize the CuAAC during the polymerization suggests that a significant concentration of Cu^{I} is present in the system and thus SARA-ATRP is probably operating during this synthesis. To address this issue, we decided to study the disproportionation and comproportionation of copper in our system by UV-Vis spectroscopy. The experiments were realized in sealed quartz cuvettes, under the same conditions as the polymerization without CuAAC and with a constant concentration in copper.

In the case of the disproportionation experiment, degassed solutions of PMDETA/IPA with and without TMPM have been added to the quartz cuvette containing Cu^{I}. The solutions were then stirred at 25 °C under argon atmosphere and the absorbance spectra were recorded after 0, 5, 10, 15, 30, 60, 90 and 120 minutes. Fig. 10 presents the evolution with time of the absorbance of CuBr/PMDETA in the TMPM/IPA solution (60 wt.% of IPA). An increase of the absorbance with time is monitored, indicating dissolution of CuBr in the medium and formation of CuBr/PMDETA complex. Moreover, this increase in the absorbance is concomitant to a shift of the λ_{max} toward higher wavelength.

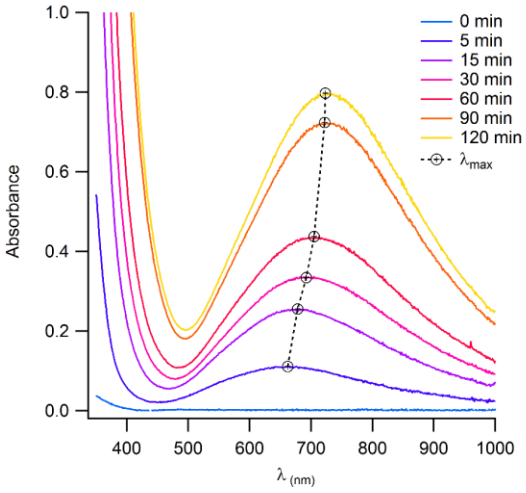

Figure 10. Evolution of the absorbance with time of a solution of CuBr/PMDETA/TMPM/IPA.

Fig.11 shows the evolution of the λ_{max} during the disproportionation experiment in solution of TMPM/IPA (black dotted line with circular markers) and IPA (red dotted line with circular markers). We can notice that the λ_{max} of the solution increases with time from 662 to 723 nm and reaches the value of a solution of $CuBr_2$/PMDETA (solid line) after 2 h. This phenomenon was also observed for the disproportionation experiment realized in pure IPA (red curve) with an increase from 665 to 744 nm. This evolution of the λ_{max} indicates that the CuBr/PMDETA complex is not stable in solution and that Cu^{I} disproportionates into Cu° and Cu^{II}, pointing out towards a SET-LRP mechanism.

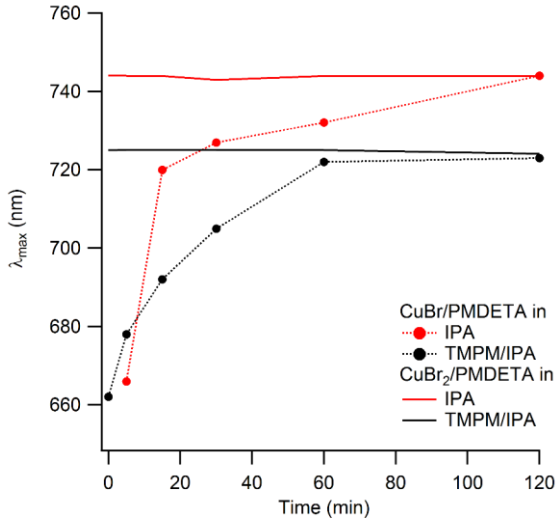

Figure 11. Evolution of the λ_{max} of the solution of CuBr/PMDETA with disproportionation time.

However, macroscopic observation of those solutions (Fig 12a) seems to be in contradiction with the UV-Vis results of Fig.10. Indeed, solutions of CuBr/PMDETA in IPA are blue while $CuBr_2$/PMDETA in IPA gives a green solution. This observation seems to indicate that the disproportionation of CuBr is limited or inexistent in the considered medium and thus that the SARA-ATRP mechanism has to be considered. However, the difference in the solution coloration can be attributed to the extent of the disproportionation degree. Indeed, the comparison of the UV-Vis spectrum of the solution of disproportionated Cu^{I} with the spectrum of a $CuBr_2$/PMDETA solution

in the polymerization mixture (Fig. 12b) indicates that the disproportionation of the Cu^{I} species is not quantitative since the intensity of the absorption band in the area between 500 and 700 nm is higher than the same area for the solution of $CuBr_2$/PMDETA.

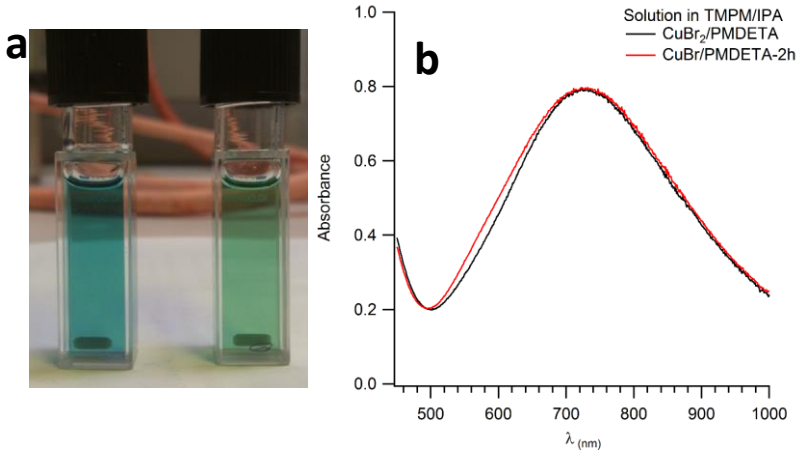

Figure 12: (a) Coloration of solutions of CuBr/PMDETA (left) and Cu(0)/$CuBr_2$/PMDETA (right) in IPA stirred for 5h. **(b)** Overlay of the UV-Vis spectra of a solution of $CuBr_2$/PMDETA (black curve) and a disproportionate solution of CuBr/PMDETA (red curve) in TMPM/IPA.

The comproportionation experiment was realized by the addition of an activated Cu° wire to a degassed solution of $CuBr_2$/PMDETA/TMPM/IPA in a sealed quartz cuvette. The solution was stirred at 25 °C under argon atmosphere and the absorbance spectra were recorded after 0, 5, 10, 15, 30, 60, 90 and 120 minutes. In this case, only an increase of the absorbance is monitored with time (Fig.13). The variation of λ_{max} as noted in the case of the disproportionation experiment is not observed here. However, the overlaid spectra of the solution of the comproportionation experiment stirred for 2 h to a solution of $CuBr_2$/PMDETA revealed that an increase of the absorbance is observed between 500 and 700 nm, similarly to the disproportionation experiment.

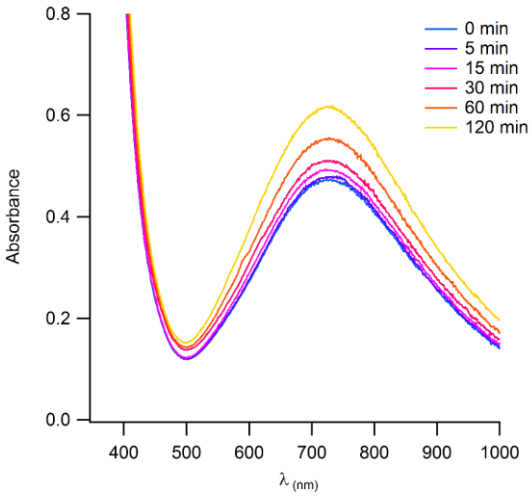

Figure 13: Evolution of the absorbance with time of solution of Cu(0)/$CuBr_2$/PMDETA/TMPM/IPA.

These two experiments tend to demonstrate that the disproportionation and comproportionation of copper are two concomitant events and that the copper species reach equilibrium, with a non-negligible amount of Cu°, CuBr and $CuBr_2$ in the polymerization medium without initiator.[33] To try to discriminate between the two mechanisms, we realized the polymerization of TMPM/AzPMA in the presence of PBIB as initiator but without $CuBr_2$. These conditions would allow monitoring the polymerization with a suppressed comproportionation phenomenon. If a SARA-ATRP is considered, the polymerization upon these conditions should display the following characteristics: i) The initiation is rapid but a long induction period is observed, since the activation by Cu° is limited and slow and that a sufficient amount of Cu^I should be produced to observe the activation. ii) The control over the polymerization is poor since the deactivating Cu^{II} species are obtained after two "initiation" steps. iii) The CuAAC reaction should be quick as soon as a sufficient amount of Cu^I is present in the medium. If a SET-LRP mechanism is considered, the polymerization should present different characteristics: i) The initiation is rapid and no induction period is observed, since the Cu° is the activator. ii) The polymerization should be controlled, since the rapid disproportionation of the Cu^I into Cu° and Cu^{II} leads to a sufficient amount of deactivator ($CuBr_2$) in the polymerization medium.[34] iii) The

click efficiency should slowly increase since the Cu^{I} species are not stable long enough to catalyze the CuAAC reaction. Table 1 presents the summary of the characteristics expected for the polymerization of TMPM/AzPMA without $CuBr_2$ added to the polymerization medium in the case of a SET-LRP or SARA-ATRP mechanism.

	SET-LRP	**SARA-ATRP**
Initiation	Rapid	Induction period
Polymerisation	Good control	Poor control
CuAAC	Slow	Rapid and induction period

Table 1. Characteristics expected for the polymerization of TMPM/AzPMA without $CuBr_2$ added to the polymerization medium in the case of a SET-LRP or SARA-ATRP mechanism.

Fig.14a presents the kinetic experiment of the polymerization of TMPM/AzPMA without $CuBr_2$ in the polymerization medium, the red squares account for the semi-logarithmic plot of conversion as determined by ^{1}H NMR *vs.* time, whereas the blue squares display the CuAAC efficiency as determined by ^{1}H NMR. In the semi-logarithmic plot, no induction period is observed indicating that the primary activator is the Cu° wire and, thus, a SET-LRP mechanism. We can also observe that the semi-logarithmic plot of conversion increases linearly indicating a "controlled polymerisation" with a constant propagation of radicals. However, the controlled behavior of the polymerization is questioned upon SEC analysis. Fig.14b presents an overlay of the SEC chromatograms of the samples synthesized with and without $CuBr_2$ in the polymerization medium. The SEC trace corresponding to the polymerization without $CuBr_2$ is badly defined with a large molar mass distribution ($Đ$ = 2.59) in comparison to the SEC trace of the sample polymerized in presence of $CuBr_2$ ($Đ$ = 1.61). Moreover, for 18 h of polymerization, only a small fraction of TMPM has polymerized in the experiment without $CuBr_2$, whereas at the same time, a full consumption of monomers has been observed in the experiment with $CuBr_2$ (Fig. 14c). These observations indicate that an insufficient amount of $CuBr_2$ is generated in the medium, because the disproportionation of Cu^{I} in the medium is minimal as in SARA-ATRP.

In the plot of the click efficiency *vs.* time, the reaction is observed to be very rapid, since 82% of the alkyne and azide functions are coupled after 2h and 98% of efficiency are monitored after 20h. It indicates that disproportionation of Cu^{I} is not fast enough (or non-existent) since Cu^{I} participates to the CuAAC.

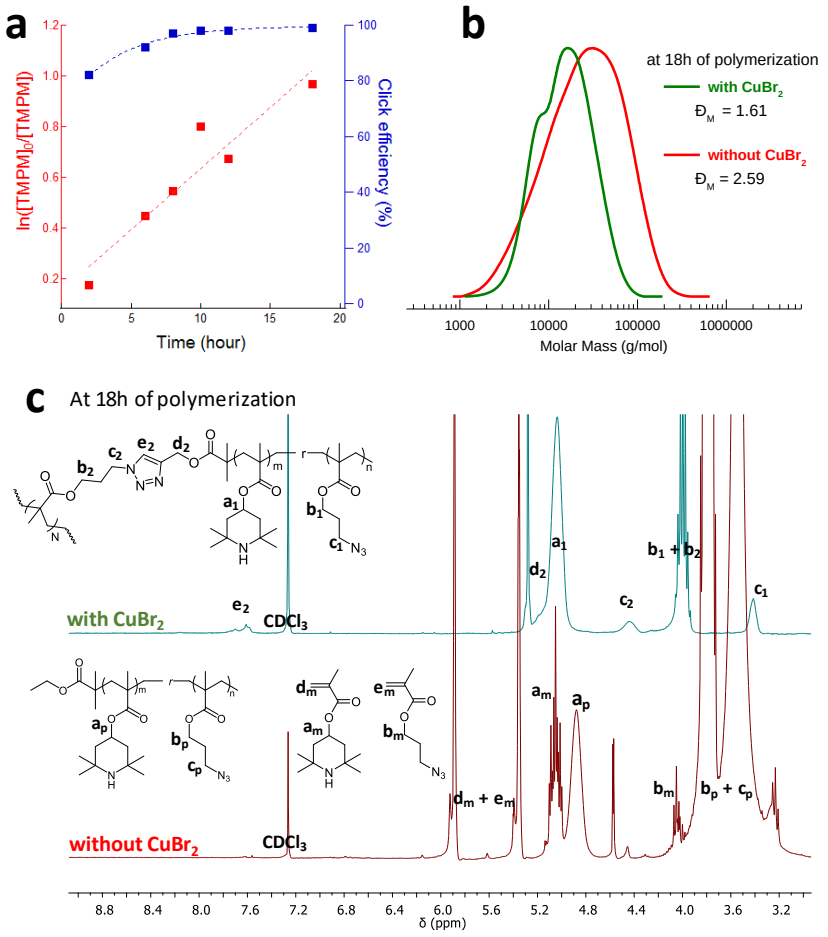

Figure 14: (a) Semi-logarithmic plot of conversion *vs.* time (red) and evolution of the CuAAC efficiency *vs.* time (blue) for the polymerization of Cu°/PBIB/TMPM/AzPMA (5cm/1/23/2) without $CuBr_2$ in the polymerization medium. **(b)** GPC chromatogram and **(c)** ^{1}H NMR spectra of Cu°/PBIB/TMPM/AzPMA (5cm/1/23/2) at 18 hours of polymerization with $CuBr_2$ (green) and without $CuBr_2$ (red).

The polymerization without $CuBr_2$ did not allow discriminating between the two postulated polymerization mechanisms. Indeed, the absence of an induction period suggests a SET-LRP mechanism, whereas the poor control over the polymerization and the good click efficiency suggest a SARA-ATRP mechanism. In fact, this experiment clearly demonstrates that the Cu^I generated via the polymerization initiation is sufficient to obtain a high degree of click efficiency. However, this experiment also demonstrates that $CuBr_2$ is required in the polymerization medium, i) to have a controlled behavior of the polymerization, which is needed to have a good control over the lattice parameter of the gels and ii) to allow an equilibrium between the copper species, which is needed to have a comproportionation (and/or disproportionation).

2.3 The electrochemical performance

2.3.1 Oxidation of PTMPM into redox-active PTMA

The PTMPM gel was grinded in order to facilitate the copper removal and the oxidation step with selective solvents. It is necessary to remove the copper from the PTMPM network because after oxidation, the copper could influence the electrochemical measurements. It was oxidized with H_2O_2 in the presence of Na_2WO_4 at 60 °C in methanol to obtain PTMA (Fig. 15). The conversion of the amine groups to nitroxides through reaction with Na_2WO_4/H_2O_2 endows mild oxidation conditions. It was demonstrated that the oxidation did not lead to the decomposition of the polymer and did not affect the azide function.[29] UV-Vis spectroscopy is generally a simple way to determine the amount of PTMPM secondary amines converted into PTMA nitroxide radical.

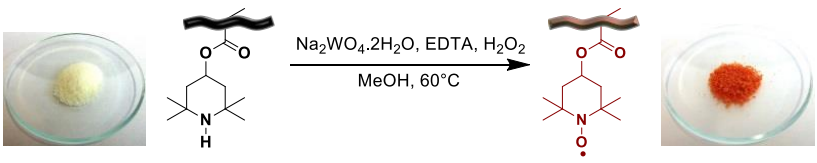

Figure 15. Oxidation reaction of PTMPM into redox-active PTMA.

The experiment was carried out with different concentrations of polymer and overlaid on the calibration curve obtained using a TEMPO-tBu derivative (Fig. 16). The oxidation yield for PBIB-P(TMPM$_{23}$-*r*-AzPMA$_2$)-PMA and PBIB-P(TMPM$_5$-*r*-AzPMA$_2$)-PMA was found to be *ca.* 94% and *ca.* 87% respectively. These values are in perfect agreement with the results obtained by electron spin resonance (ESR) spectroscopy, which is another way to determine the oxidation degree of PTMA. In this respect, oxidation yield determined by ESR for PBIB-P(TMPM$_{23}$-*r*-AzPMA$_2$)-PMA and PBIB-P(TMPM$_5$-*r*-AzPMA$_2$)-PMA was found to be *ca.* 93% and *ca.* 88% respectively. The obtained oxidation degrees can be explained by the network density of the investigated materials. The oxidation yield of DP23 is somewhat higher due to a slightly less dense network (as observed in mechanical tests), allowing the secondary amines to be more accessible for oxidation.

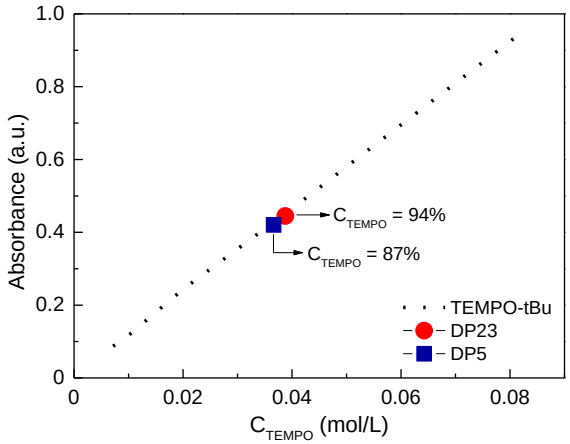

Figure 16. UV-Vis spectrum of PBIB-P(TMPM$_{25}$-*r*-AzPMA$_2$)-PMA (DP25) and PBIB-P(TMPM$_5$-*r*-AzPMA$_2$)-PMA (DP5) oxidized and concentrated to 10 g/L.

2.3.2 Cyclic voltammetry

Cyclic voltammetry measurements (CV) were firstly performed to confirm the redox properties of PTMA gels. This technique consists in varying the potential E of the working electrode (i.e. cathode) linearly versus time in cyclical phases. The current I exhibited from the working electrode is plotted versus the applied potential, forming the cyclic voltammogram. Here, the applied potential is swept between 3V and 4V vs Li/Li^+ at a scan rate of 0.1 mV/s. In this respect, Fig. 17 shows a reversible redox process (or charge/discharge process) around 3.6 V *vs.* Li/Li^+ ascribed to the oxidation of the nitroxide radicals into oxoammonium cations.

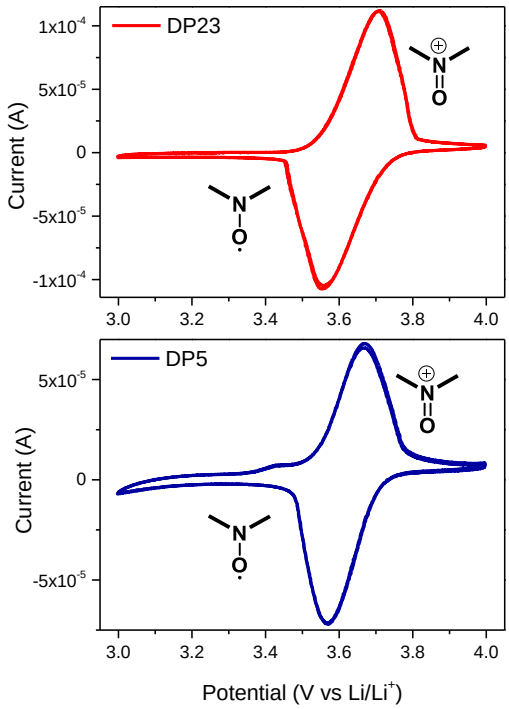

Figure 17. Cyclic voltammetry of PBIB-P($TMPM_{23}$-*r*-$AzPMA_2$)-PMA (DP23 in red on the **top**) and PBIB-P($TMPM_5$-*r*-$AzPMA_2$)-PMA (DP5 in blue on the **bottom**) electrodes in half-cell configuration with lithium as counter electrode at 0.1 mV/s (2 cycles are depicted for each electrode).

2.3.3 Galvanostatic charge/discharge cycling

The electrochemical performances of the synthesized materials were also evaluated by galvanostatic cycling in half-cell configuration. This technique measures the amount of electric charges stored/delivered per gram of active material during complete charge/discharge of the half-cell (i.e practical capacity Cp in mAh/g), over a range potential. The capacity Cp is measured by applying time t and electric current C, i.e current-rate (or C-rate) which is relative to the theoretical capacity Q of the cell (*see the equation 2 in chapter 1*). Here, the 1C-rate was estimated at 80 mAh of active material and the potential range is comprised between 2.9 and 4.2 V *vs.* Li/Li^+. This means that the cell will be completely discharged (or charged) in 1 hour by imposed theoretical current C of 80 mA.

The first three cycles were performed at low current-rate of 0.1C-rate (meaning a complete charge or discharge of the cell in 10 hours at theoretical current of 80 mA). Subsequent cycling was performed at 1C-rate (Figs. 18 and 19). During the first charge cycle, nitroxide groups but also remaining secondary amines are oxidized. However, only the oxoammonium groups can be reversibly reduced, whereas impurities cause irreversible redox processes and first cycle capacity loss. Thus, the first cycle efficiency performed at low current-rate can be associated to the amount of active nitroxide groups present and thus to the yield of the chemical oxidation. Fig.18 shows a first cycle efficiency of 84% for DP5, which is close to the oxidation yield obtained by UV-Vis and ESR spectroscopy (87%). For DP23 the first cycle efficiency is only 65% due to a high charge value. However, after some cycles, charge equilibrates with discharge and the practical specific capacity is maintained at 85 to 90% of the theoretical value (which is 111 mAh/g for the PTMA). We can postulate the presence of impurities (non-oxidized amines or chains released from the network and migrating in the electrolyte) contained in the sample, which have been eliminated during the first charge.

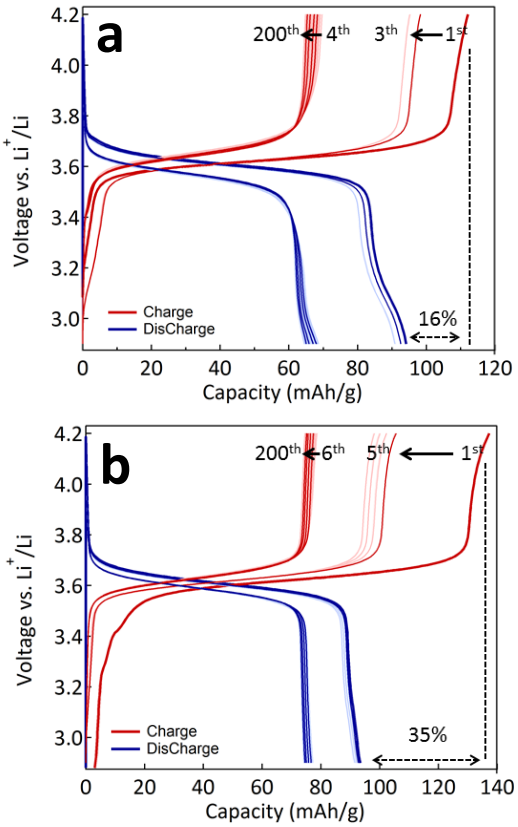

Figure 18: Charge-discharge performance for **(a)** PBIB-P(TMPM$_5$-*r*-AzPMA$_2$)-PMA (DP5) and **(b)** PBIB-P(TMPM$_{23}$-*r*-AzPMA$_2$)-PMA (DP23) with 30/60/10 of PTMA/SC45/Binder at C/10 and C rate.

When cycled at constant current of 1C-rate (80 mAh), the cells exhibit relatively good practical capacities values of *ca.* 78 mAh/g (for DP23) and *ca.* 66 mAh/g (for DP5). After 200 cycles, the cells display only *ca.* 10% capacity loss with a plateau around 3.6 V *vs.* Li/Li$^+$ being held throughout the cycling (Fig. 19). Moreover, a difference of less than 10% in capacity is observed between the DP23 and DP5 electrodes, which is in perfect correlation with the oxidation yields obtained from UV-Vis and ESR experiments.

The power performances were evaluated for both materials (Fig.20). The cells show good capacity retention when operated at high rates, confirming the excellent stability for PTMA-containing

electrodes when exposed to high current loads. The gap in capacity values between the two electrodes is still maintained at *ca.* 10%. At this stage, we observe DP23 electrode having better capacities than DP5 electrode.

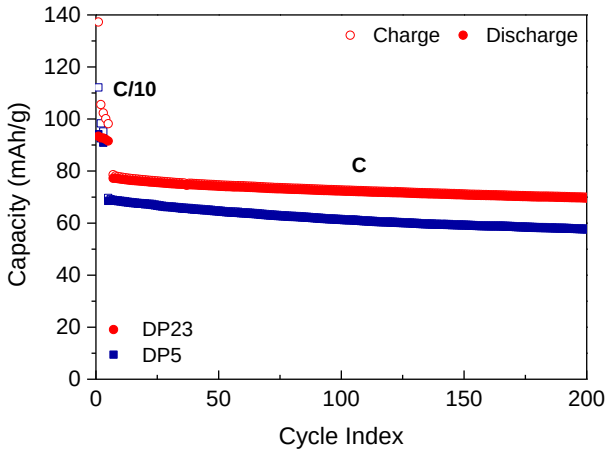

Figure 19. Specific capacity *vs.* cycle number for PBIB-P(TMPM$_{23}$-*r*-AzPMA$_2$)-PMA (DP23 in red) and PBIB-P(TMPM$_5$-*r*-AzPMA$_2$)-PMA (DP5 in blue) electrodes cycled in half-cell configuration with lithium as counter electrode.

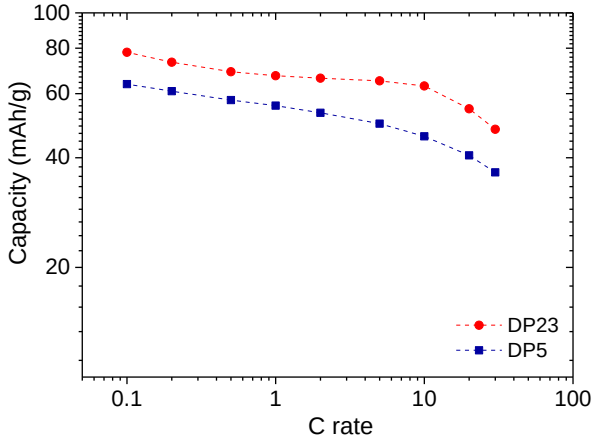

Figure 20. The rate performance of PBIB-P(TMPM$_{23}$-*r*-AzPMA$_2$)-PMA (DP23 in red) and PBIB-P(TMPM$_5$-*r*-AzPMA$_2$)-PMA (DP5 in blue) at variable currents (symmetrical charge – discharge conditions).

2.4 Conclusion

The one-pot RDRP-CuAAC synthesis of redox-active gels from a ‘‘clickable’’ initiator (PBIB) and accordingly reactive comonomers (AzPMA and PMA) is a promising way for the development of new organic radical battery materials based on polymers bearing TEMPO. In this chapter, we have investigated in details the fate of copper species acting as catalysts for both RDRP and CuAAC processes. We observed that an equilibrium between copper allowed the synthesis of gels. However, as far as the RDRP process is concerned, our investigations did not allow us to discriminate between the SARA-ATRP and SET-LRP processes. The obtained gels have been fully characterized and present good electrochemical property, paving the way for their use as active cathode materials in organic radical batteries. Moreover, the power performances of our gels are excellent due to the good accessibility of the electroactive TEMPO groups and their fast redox reaction kinetics. We also highlighted the fact that the oxidation degree of the PTMA had an influence on the electrochemical performances. Unfortunately, despite that the one-pot RDRP-CuAAC synthesis is a promising way, it must be improved in order to minimize the amount of copper. In fact, it remains difficult to eliminate Cu(II), which is partly complexed by triazole rings and which can affect the cells performances. Thus in chapter 3, the gels will be synthesized by free radical polymerization, so that the interpretation of the results will not be influenced by the presence of residual copper or uncrosslinked pendant chains.

2.5 Experimental section

- Materials

Triethylamine (TEA, 99%, Aldrich) was distilled over CaH_2 under an argon atmosphere. Immediately before use, a copper wire (diameter = 0.25 mm) was washed in hydrochloric acid for 10 min, rinsed thoroughly with milliQ water and dried with acetone. Porous polyethylene membranes (Celgard), lithium metal foils (99.9% Alfa Aesar), conductive carbon black (Super C45, MTI), electrolyte consisting of a mix of ethylene carbonate (EC) and diethyl carbonate (DEC) 1:1 v:v with 1 M of lithium hexafluorophosphate ($LiPF_6$) purchased from Solvionic (99.9%), coin-cells spare parts acquired from X2Labware, Kynarflex binder from Arkema (poly(vinylidene fluoride)-*co*-hexafluoropropylene, PVDF-*co*-HFP), isopropanol (IPA, 99%, Acros), 2-bromoisobutyryl bromide (98%, Aldrich), 3-bromoropropanol (98%, TCI), sodium azide (99.9%, Acros), methacryloyl chloride (97%, contains ~200 ppm MEHQ), 2,2,6,6-tetramethylpiperidin-4-yl methacrylate (TMPM, TCI), *N*,*N*,*N*',*N*',*N*"-pentamethyldiethylenetriamine (PMDETA, 98%, Aldrich) and $CuBr_2$ (99+%, Acros) were used as received.

- Instrumentation

1H NMR. Proton nuclear magnetic resonance (^{1}H NMR) spectra were acquired either on a 300 MHz Bruker Avance II or on a 500 MHz Bruker Avance II in deuterated chloroform ($CDCl_3$).

Infrared (FTIR). Spectra were recorded with a Shimadzu FTIR-8400S spectrometer. The samples were deposited as a thin film on a ZnSe prism for ATR measurements.

UV-Visible. The samples were finely milled with a mortar, dispersed in CH_2Cl_2 and put into quartz cuvettes. The studies were carried out in a Varian Cary 50 UV-Vis spectrophotometer with emission scans recorded from 250 to 1000 nm.

SEC. Average molar masses (Mn and Mw) and dispersities (Đ) were measured on an Agilent size exclusion chromatography (SEC) system equipped with an Agilent 1100/1200 pump (25 °C; eluent: chloroform/triethylamine/isopropanol (94/4/2); flow rate: 1 mL/min), an Agilent differential refractometer and two PSS SDV columns (Beads 10 µm; porosity of column 1: 10000 A; porosity of column 2: 1000 A). The calibration was performed using polystyrene standards. Therefore, the Mn, Mw and Đ are obtained in polystyrene equivalent.

Rheological measurements. Rheology experiments were performed on a Kinexus Ultra (Malvern Instruments) rheometer equipped with a heat exchanger and plate-plate steel geometry (8 mm diameter). Oscillatory measurements were carried out in the linear regime (either at strain control of 1% or at stress control of 5 Pa) with a gap adjusted between 350 and 450 µm and temperature fixed at 20 °C.

Electron Spin Resonance (ESR). ESR experiments were carried out on an EMXmicro CW-EPR spectrometer (EMX micro EMM-6/1/9-VT control unit, ER 070 magnet, EMX premium ER04 X-band microwave bridge equipped with EMX standard resonator, EMX080 power unit) by Bruker Corporation. Powdered samples were investigated at room temperature and the data handling was done on the Bruker Xenon software package, version 1.1b86. The SpinCount™ software module was used for quantitative measurements (average of three measurements).

Electrochemical measurements. Charge/discharge tests were performed using an ARBIN Instrument Battery Tester (BT-2043). The electrochemical impedance spectroscopy (EIS) and cyclic voltammetry (CV) tests were carried out using a Parstat 3000. The EIS measurements were performed over a frequency range of 1 MHz to 10 mHz, on the cells after 200 charge–discharge cycles. The CV measurements were performed at a scan rate of 0.1 mV/s. The electrodes were tested in half-cell configuration with lithium metal foil as counter and reference electrodes and porous polyethylene membrane as separator (Fig.21). The used electrolyte was 1 M of lithium hexafluorophosphate ($LiPF_6$) in ethylene carbonate (EC) and diethyl carbonate (DEC) (1:1, v:v). All coin-cells were assembled under argon atmosphere (<0.1 ppm H2O, <0.1 ppm O2) in an Inert Lab glovebox.

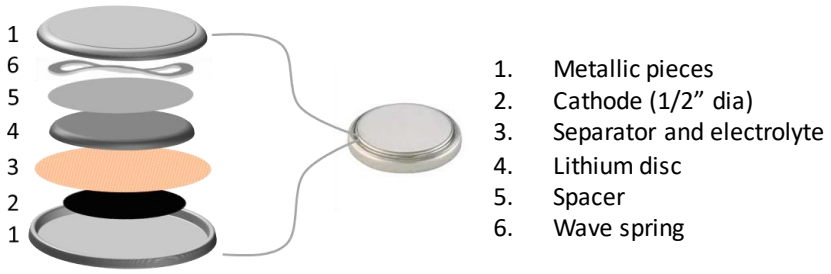

Figure 21. Half-cell configuration.

Electrode preparation. The cathodes were prepared by blending the active material PTMA/carbon SC45/PVDF-*co*-HFP binder at 5 wt. % in NMP (30/60/10). The ingredients were mixed uniformly with a ball mill at room temperature before casting on an aluminum foil using a doctor blade instrument. The wet slurries obtained with thicknesses controlled at 200 μm were dried at 70 °C and cut in circular disks of ½ inches diameter to be used as cathodes. The active material loading was typically varying from 0.5 to 1.5 mg/cm^2.

- Synthesis

Propargyl 2-bromoisobuyrate (PBIB).[35] Into a 250 mL round-bottom flask, propargyl alcohol (3 g, 53 mmol) and TEA (5.9 g, 59 mmol) were dissolved in CH_2Cl_2 (50 mL) and cooled to 0 °C for 30 minutes. Afterwards, a solution of 2-bromoisobutyrylbromide (13.5 g, 59 mmol) in CH_2Cl_2 (20 mL) was added dropwise slowly into the flask. The mixture was left at 0 °C for 1 h and then at room temperature for 16 h. The formed salt was removed by washing the mixture with distilled water (70 mL) three times. The organic layer was dried over anhydrous $MgSO_4$ and the solvent was evaporated under reduced pressure. The solution was purified by a silica gel column (hexane/ethyl acetate, 94/6) to obtain a colorless product (8.5 g, 77%).
^{1}H-NMR (300 MHz, $CDCl_3$), δ (ppm): 4.71 (d, 2H, C**H**$_2$O), 2.49 (t, 1H, C**H**≡C), 1.90 (s, 6H, Br(C**H**$_3$)$_2$C).
^{13}C-NMR (300 MHz, $CDCl_3$), δ (ppm): 171 (1C, C_{quat}-**C**O_2), 77 (1C, HC≡**C**-CH_2), 76 (1C, H**C**≡C), 55 (1C, ≡C-**C**H_2-O-), 52.5 (1C, Br-**C$_{quat}$**), 31 (2C, (**C**H_3)$_2$-C_{quat}).

3-Azidopropyl methacrylate (AzPMA). AzPMA was synthesized as previously described.[29]
^{1}H-NMR (300 MHz, $CDCl_3$), δ (ppm): 6.11 (m, 1H, C=CH**H**), 5.58 (m, 1H, C=C**H**H), 4.24 (t, 2H, C**H**$_2$-O), 3.52 (t, 2H, C**H**$_2$-N_3) and 1.91-2.02 (m, 5H, overlapping C**H**$_3$-C and C-C**H**$_2$-C).
^{13}C-NMR (300 MHz, $CDCl_3$), δ (ppm): 167 (1C, C-**C**O_2), 136 (1C, **C**=CH_2), 125 (1C, H_2**C**=C), 62.7 (1C, H_2C-**C**-O), 46 (1C, N_3-**C**H_2), 29.5 (1C, H_2C-**C**H_2-CH_2), 17.9 (**C**H3-C).
IR spectrum (neat liquid on a ZnSe prism): 2100 cm^{-1} (ν_{N3}) and 1721 cm^{-1} ($\nu_{C=O}$).

Propargyl methacrylate (PMA).[36] In a 250 mL round-bottom flask, a solution of propargyl alcohol (11 mL, 185 mmol) and TEA (27 mL, 203 mmol) in CH_2Cl_2 (90 mL) was cooled in an ice-water bath. A solution of methacryloyl chloride (20 mL, 203 mmol) in CH_2Cl_2 (25 mL) was added dropwise over a period of 1 hour and the mixture was then stirred at room temperature overnight. The triethylammonium chloride salt was filtered and the mixture was extracted with an aqueous solution of hydrochloric acid (0.1 M), a saturated solution of $NaHCO_3$, and water. The organic phase was dried over $MgSO_4$. The crude product was purified by silica gel column (hexane/ethyl acetate, 9/1) to afford a colorless oil.
^{1}H-NMR (300 MHz, $CDCl_3$) δ (ppm): 6.14 (m, 1H, C=C**H**H), 5.61 (m, 1H, C=CH**H**), 4.73 (s, 2H, OC**H**$_2$), 2.46 (m, 1H, C≡C**H**), 1.94 (m, 3H, C-C**H**$_3$).
^{13}C-NMR (300 MHz, $CDCl_3$), δ (ppm): 167 (1C, C-**C**O_2), 137 (1C, **C**=CH_2), 124 (1C, H_2**C**=C), 77 (1C, HC≡**C**-CH_2), 76 (1C, H**C**≡C), 52 (1C, ≡C-**C**H_2-O-), 17.9 (**C**H3-C).

Typical procedure of gelation: PBIB-P(TMPM$_{23}$-*r*-AzPMA$_2$)-PMA (PTMPM$_{23}$ gel). In a Schlenk tube, a solution of TMPM (2 g, 9.4 mmol), AzPMA (145 µL, 0.94 mmol), IPA (4.7 mL, 60 wt%), PBIB (63 µL; 0.47 mmol; 1 eq.), and 260 µL of a solution of CuBr2/PMDETA (0.05/0.12 eq) in IPA (Ccu= 20 g/L) was degassed three times by freeze-pump-thaw cycling. Under argon flux, a magnetic bar with 5 cm of activated Cu° wire was introduced. The solution was then degassed by two freeze pump-thaw cycles and filled with argon before it was stirred in an oil bath at 40 °C for 26 hours. After that, PMA (59 µL; 0.47 mmol ; 1 eq.) dissolved in IPA (100 µL) was degassed by

argon bubbling and added dropwise to the Schlenk tube. The mixture was left at 40 °C overnight. The gel formed was roughly grinded in a solution of PMDETA/EDTA in methanol and dialyzed with methanol until disappearance of the green/blue copper (ca. three days). A pale yellow solid was obtained after removing the solvent.

Oxidation of the PTMPM gel. Into a 250 mL round-bottom flask equipped with a condenser, the PTMPM gel (1.2 g, 5.1 mmol of amine functions, 1 eq.), $Na_2WO_4 \times 2H_2O$ (420 mg, 1.3 mmol, 0.25 eq.) and EDTA (285 mg, 0.76 mmol, 0.15 eq.) were dissolved in methanol (120 mL). The solution was stirred at 60 °C for 10 minutes and H_2O_2 (6.6 mL, 110 mmol, 15 eq.) was added dropwise over 15 h. The solution was then stirred at 60 °C for a total of 48 h. The mixture was concentrated under reduced pressure and the solid was filtered. Afterwards, it was washed three times with distilled water, three times with methanol and dried in vacuum at 40 °C overnight. An orange solid was finally obtained.

Bibliography

1 S. Muench, A. Wild, C. Friebe, B. Häupler, T. Janoschka and U. S. Schubert, *Chem. Rev.*, 2016, **116**, 9438–9484.

2 R. Gracia and D. Mecerreyes, *Polym. Chem.*, 2013, **4**, 2206–2214.

3 T. Suga, Y. J. Pu, K. Oyaizu and H. Nishide, *Bull. Chem. Soc. Jpn*, 2004, **77**, 2203–2204.

4 K. Nakahara, S. Iwasa, M. Satoh, Y. Morioka, J. Iriyama, M. Suguro and E. Hasegawa, *Chem. Phys. Lett.*, 2002, **359**, 351–354.

5 G. Hauffman, a. Vlad, T. Janoschka, U. S. Schubert and J.-F. Gohy, *J. Mater. Chem. A*, 2015, **3**, 19575–19581.

6 B. Ernould, M. Devos, J.-P. Bourgeois, J. Rolland, A. Vlad and J.-F. Gohy, *J. Mater. Chem. A*, 2015, **3**, 8832–8839.

7 C. M. Kirschner and K. S. Anseth, *Acta Mater.*, 2013, **61**, 931–944.

8 N. Annabi, A. Tamayol, J. A. Uquillas, M. Akbari, L. E. Bertassoni, C. Cha, G. Camci-Unal, M. R. Dokmeci, N. a. Peppas and A. Khademhosseini, *Adv. Mater.*, 2014, **26**, 85–124.

9 G. Deng, C. Tang, F. Li, H. Jiang and Y. Chen, *Macromolecules*, 2010, **43**, 1191–1194.

10 C. Tsitsilianis, *Soft Matter*, 2010, **6**, 2372.

11 M. A. Tasdelen, *Polym. Chem.*, 2011, **2**, 2133–2145.

12 R. E. Parker and N. S. Isaacs, *Chem. Rev.*, 1959, **59**, 737–799.

13 C. E. Hoyle and C. N. Bowman, *Angew. Chem. Int. Ed. Engl.*, 2010, **49**, 1540–1573.

14 H. C. Kolb, M. G. Finn and K. B. Sharpless, *Angew. Chemie - Int. Ed.*, 2001, 40, 2004–2021.

15 K. Kempe, A. Krieg, C. R. Becer and U. S. Schubert, *Chem. Soc. Rev.*, 2012, **41**, 176–91.

16 V. V. Rostovtsev, L. G. Green, V. V. Fokin and K. B. Sharpless, *Angew. Chem.*, 2002, **114**, 2708–2711.

17 C. W. Tornøe, C. Christensen and M. Meldal, *J. Org. Chem*, 2002, **67**, 3057–3064.

18 D. Quémener, T. P. Davis, C. Barner-Kowollik and M. H. Stenzel, *Chem. Commun.*, 2006, **48**, 5051–5053.

19 O. Altintas, B. Yankul, G. Hizal and U. Tunca, *J. Polym. Sci. Part A Polym. Chem.*, 2007, **45**, 3588–3598.

20 P. L. Golas and K. Matyjaszewski, *QSAR Comb. Sci.*, 2007, **26**, 1116–1134.

21 J. Geng, J. Lindqvist, G. Mantovani and D. M. Haddleton, *Angew. Chem. Int. Ed. Engl.*, 2008, **47**, 4180–4183.
22 K. Matyjaszewski, S. Coca, S. G. Gaynor, M. L. Wei and B. E. Woodworth, *Macromolecules*, 1997, **30**, 7348–7350.
23 V. Percec, B. Barboiu and M. Van Der Sluis, *Macromolecules*, 1998, **31**, 4053–4056.
24 V. Percec, T. Guliashvili, J. S. Ladislaw, A. Wistrand, A. Stjerndahl, M. J. Sienkowska, M. J. Monteiro and S. Sahoo, *J. Am. Chem. Soc.*, 2006, **128**, 14156–14165.
25 G. R. Jones, Z. Li, A. Anastasaki, D. J. Lloyd, P. Wilson, Q. Zhang and D. M. Haddleton, *Macromolecules*, 2016, **49**, 483–489.
26 C. Waldron, Q. Zhang, Z. Li, V. Nikolaou, G. Nurumbetov, J. Godfrey, R. McHale, G. Yilmaz, R. K. Randev, M. Girault, K. McEwan, D. M. Haddleton, M. Droesbeke, A. J. Haddleton, P. Wilson, A. Simula, J. Collins, D. J. Lloyd, J. A. Burns, C. Summers, C. Houben, A. Anastasaki, M. Li, C. R. Becer, J. K. Kiviaho and N. Risangud, *Polym. Chem.*, 2014, **5**, 57–61.
27 D. Konkolewicz, Y. Wang, P. Krys, M. Zhong, A. a. Isse, A. Gennaro and K. Matyjaszewski, *Polym. Chem.*, 2014, **5**, 4409.
28 N. Zhang, S. Samanta, B. Rosen and V. Percec, *Chem. Rev.*, 2014, **114**, 5848–5958.
29 O. Bertrand, B. Ernould, F. Boujioui, A. Vlad and J.-F. Gohy, *Polym. Chem.*, 2015, **6**, 6067–6072.
30 O. Bertrand, A. Vlad, R. Hoogenboom and J. F. Gohy, *Polym. Chem.*, 2016, **7**, 1088–1095.
31 S. Díez-González, *Catal. Sci. Technol.*, 2011, **1**, 166–178.
32 J. E. Hein and V. V Fokin, *Chem. Soc. Rev.*, 2010, **39**, 1302–1315.
33 F. Alsubaie, A. Anastasaki, V. Nikolaou, A. Simula, G. Nurumbetov, P. Wilson, K. Kempe and D. M. Haddleton, *Macromolecules*, 2015, **48**, 5517–5525.
34 G. Lligadas and V. Percec, *J. Polym. Sci., Part A Polym. Chem.*, 2008, **46**, 6880–6895.
35 Q. H. Zhou, J. K. Zheng, Z. Shen, X. H. Fan, X. F. Chen and Q. F. Zhou, *Macromolecules*, 2010, **43**, 5637–5646.
36 J. Geng, G. Mantovani, L. Tao, J. Nicolas, G. Chen, R. Wallis, D. A. Mitchell, B. R. G. Johnson, S. D. Evans and D. M. Haddleton, *J. Am. Chem. Soc.*, 2007, **129**, 15156–15163.

Chapter 3:
Ionic conducting and redox-active polymer gels as cathode active materials for organic radical batteries

Table of contents

3.1 Introduction

Ionic liquids (ILs) have been proposed as potentially safe electrolytes because of their non-flammability, low vapor pressure and high thermal/chemical stability. Moreover, according to the type of counter-ions and of substituent groups, their physicochemical properties can be adjusted to suit requirements.[1,2] Due to these outstanding properties, ILs are used in various applications[3,4,5] such as organocatalyst, electrochemistry and biotechnology.

In the past decade, ILs have been introduced into polymeric structures as repetition units, leading to an class of polyelectrolytes called poly(ionic liquid)s (PILs).[6,7,8] The various existing PILs are classified according to their preparation method (Fig. 1).

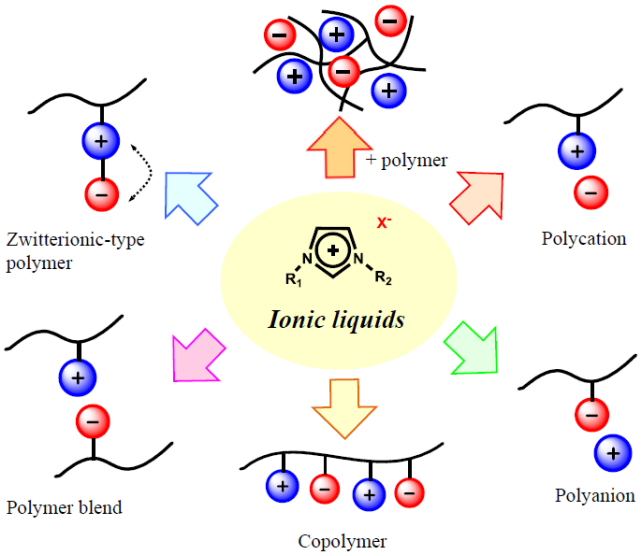

Figure 1. The different manners to prepare PILS.[8]

Recently, an European project (named renaissance-ITN) was dedicated to the development of innovative poly(ionic liquid)s for energy and environmental applications.[9] Mecerreyes et al. reported[10] that the properties of ionic liquids are usually preserved when used as ion-gels. These ion-gels were investigated as polymer electrolyte for supercapacitors by Marcilla et al.[11,12] They found that the pyrrolidinium

cation formed the most electrochemically stable electrolyte because of the combination of cyclic aliphatic cations and imide anions. Mercerreyes, Gerbaldi et al. investigated[13] PILs as single-ion conducting polymer electrolyte for lithium metal polymer battery. Detrembleur et al. developed[14] a hybrid electrochemical energy storage (EES) system based on a poly(catechol-*random*-anionic sulfonate). The catechol generates the electroactive ortho-quinones by the redox activity and the anionic sulfonate was introduced in order to enhance Li^+ ion mobility. This combination allowed boosting the performance of EES system. They also developed[15] homopolymeric systems as antifouling, which combine catechol/pyrogallol with cationic imidazolium as repeating units. Conversely, Mecerreyes et al. developed[16] a poly(ionic liquid)s (*i.e* poly(diallyldimethylammonium chloride)) with redox-active molecules as counter anions (*i.e.* nitroxide-TEMPO and anthraquinone) through an easy anion exchange reaction. Electrode of lithium battery based on these active materials, displayed excellent capacity and stable cycle life.

Among the various classes of ILs, imidazolium-based salts represent the most prominent and widely used as subclass of N-heterocyclic cations.[17] However, one important limitation of using imidazolium salts is their decomposition into N-heterocyclic carbenes under strongly basic conditions, because of the high acidity of their C-H bond[18] (carbon 2 in Fig. 2a). 1,2,3-triazolium salts do not have highly acidic C-H bonds between two nitrogen atoms (Fig. 2b).

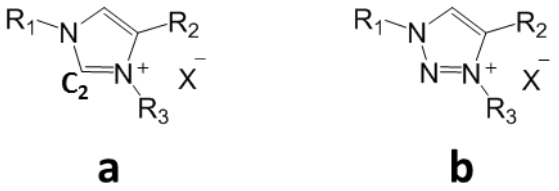

Figure 2. General structure of **(a)** imidazolium salt and **(b)** 1,2,3-triazolium salt.

Even though, 1,2,3-triazolium salts were reported in 1887,[19] their ionic liquid properties were not investigated, neglecting them as ionic liquids until recently. In fact, since the development of the copper-catalyzed azide-alkyne cycloaddition (CuAAC), 1,2,3-triazolium

became the most popular ionic liquids.[20,21] The physical and ionic conducting properties of main-chain and side-chain 1,2,3-triazolium-based poly(ionic liquid)s have been reported by Drockenmuller and coworkers,[22] to the point of becoming a pioneer of poly(1,2,3-triazolium). Subsequently, Garcia et al. investigated[23] 1,2,3-triazolium based polymer as antimicrobial.

The objective of this chapter is to use the triazolium in order to improve the motion of ions within the cathode based on PTMA active materials. The triazolium is used because it is easily obtained by the copper-catalyzed azide-alkyne cycloaddition (CuAAC), but also because this strategy was not investigated before. Here, we explore the influence of the triazolium cation as crosslinking node in the PTMA three-dimensional network on the electrochemical performances (Fig. 3). The triazolium will be used as crosslinking nodes in order to prevent the dissolution of PTMA in the organic electrolyte, which leads to a drop of the performance of batteries. The synthesis of gels has been detailed. The influence of the nature of the counter-ions as well as the amount of triazolium nodes were investigated by conductivity measurements and galvanostatic analyses.

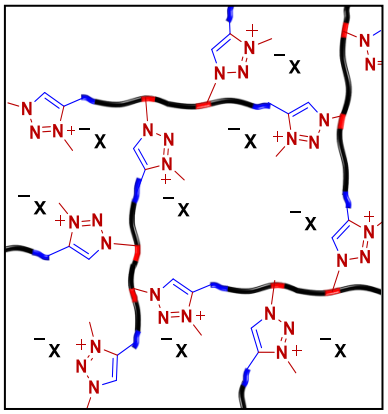

Figure 3. PTMA three-dimensional network with triazolium cation as crosslinking node.

3.2 Synthesis of ionic - redox gels

3.2.1 Synthesis of ionic liquid crosslinking nodes

The 1,4-disubstituted 1,2,3-triazole crosslinking agent (**1** in Fig. 4) was synthesized by the copper(I)-catalyzed alkyne-azide cycloaddition (CuAAC) reaction of 3-azidopropyl methacrylate (AzPMA) with propargyl methacrylate (PMA) catalyzed by Cu(I). According to NMR results (Triazole in Fig. 5), the absence of characteristic peaks of azide and alkyne groups in the reaction product points towards a complete CuAAC reaction. Moreover, the observation of narrow peaks and the presence of vinyl peaks (in the crude samples after the removal of the copper) indicate that the use of dichloromethane at low temperature has prevented the polymerization of methacrylate groups.

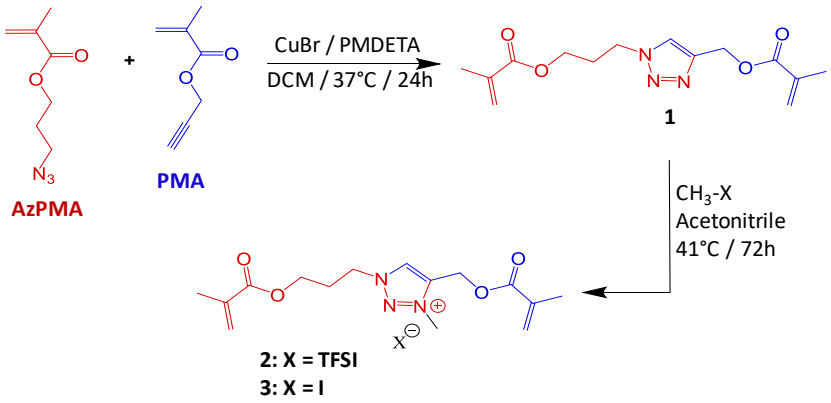

Figure 4. Synthesis of triazole **(1)**, triazolium^{+}/TFSI^{-} **(2)** and triazolium^{+}/I^{-} crosslinker **(3)**.

The 1,2,3-triazole group of **1** was further alkylated using methyl bis[(trifluoromethyl)sulfonyl]imide and methyl iodide to provide ionic triazolium crosslinking nodes (**2** and **3,** respectively in the Fig.4). In order to allow a good solubilization of charged species and therefore to promote the quaternization of the 1,2,3-triazole into 1,2,3-triazolium, a polar aprotic solvent, namely acetonitrile, was used. This reaction leads to a complete quaternization of the triazole group (Fig. 5) as indicated

by the shift toward deshielded area of the characteristic triazole ring proton (f from 8.21 to 9.05 ppm) and by the appearance of a methyl group onto the triazole ring (j at 4.31 ppm).

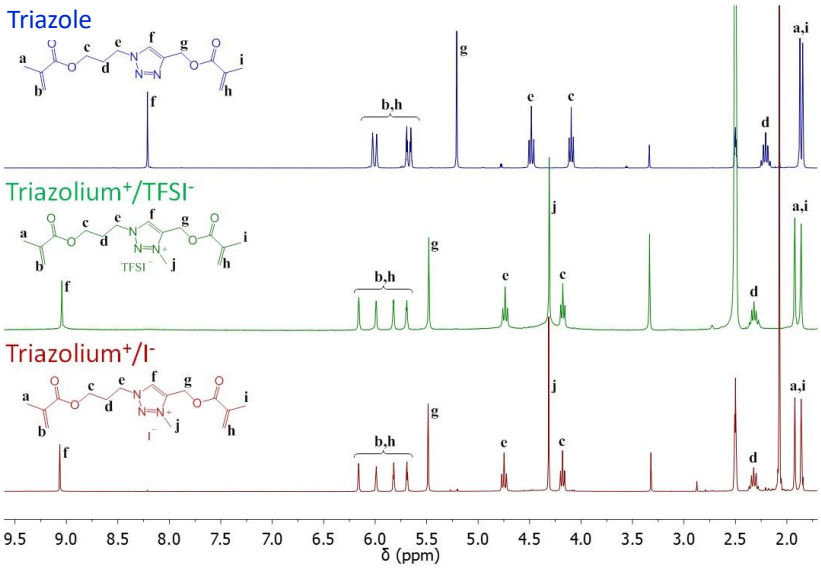

Figure 5. ^{1}H NMR spectrum in DMSO-d_6 of triazole (on the top in blue), triazolium^{+}/TFSI^{-} (on the middle in green) and triazolium^{+}/I^{-} (on the bottom in red) crosslinking nodes.

3.2.2 Synthesis of gels

The synthesis of the PTMA gels was carried out via free radical polymerization using 2,2,6,6-tetramethylpiperidin-4-yl methacrylate (TMPM) as monomer, 1,4-disubstituted 1,2,3-triazole/triazolium as crosslinking agent (**1**, **2** and **3** of the Fig.4) and AIBN as initiator (Fig. 6). After complete gelification and purification, the three PTMPM gels (triazole, triazolium^{+}/TFSI^{-} and triazolium^{+}/I^{-}) were oxidized into PTMA gels with Na_2WO_4/H_2O_2 at 60 °C (**4**, **5** and **6** in Fig.6). This mild oxidation reaction condition is known to convert until 99% of PTMPM secondary amines into nitroxide moieties without leading to decomposition of the polymer or network.[24,25] Moreover, the results studied below will also prove that this oxidation has no impact on the triazole and triazolium crosslinking nodes of PTMA networks.

However, the last network named triazolium^{+}/PF_6^{-} (**7**) was obtained by anion exchange of triazolium^{+}/I^{-} network with $LiPF_6$ salt dissociated in acetonitrile. This reaction was realized under controlled atmosphere, after the oxidation of the PTMPM, to minimize or prevent the PF_6^{-} anion degradation.

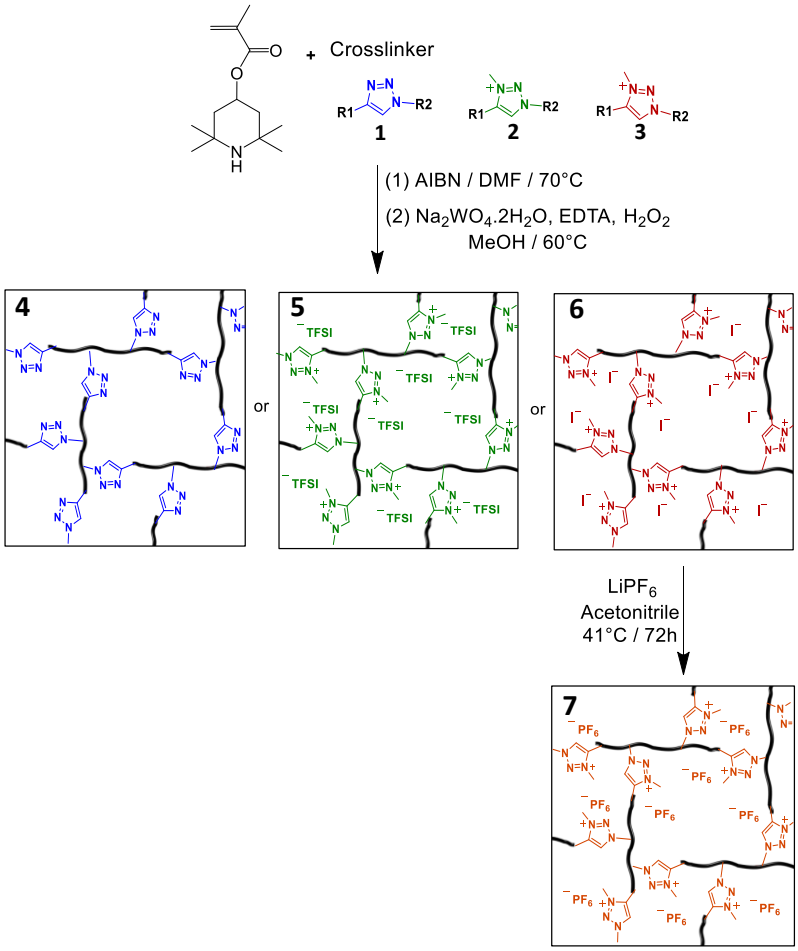

Figure 6. Synthesis of PTMA gels with different crosslinkers, **(4)** triazole gel, **(5)** triazolium^{+}/$TFSI^{-}$ gel, **(6)** triazolium^{+}/I^{-} gel and **(7)** triazolium^{+}/PF_6^{-} gel.

These four types of systems were synthesized with three different crosslinking degrees (A, B and C) summarized in the Table1. For these three cases, the triazole gel is our reference sample.

Crosslinking type	$\frac{[Crosslinking\ agent]}{[Monomer]}$	**mol. % crosslinking agent**
A	0.006	0.6
B	0.025	2.4
C	0.1	9

Table 1. Summary of three different crosslinking degrees.

3.3 Influence of the nature of the crosslinking nodes

To investigate the influence of the nature of crosslinking nodes, the four systems (**4**, **5**, **6** and **7** in Fig.6) crosslinked at 2.4 mol. % were investigated (crosslinking type B of the Table 1).

3.3.1 Conductivity measurements without added salts

Electrochemical impedance spectroscopy (EIS) consists in applying an alternating electric field (needed to generate an accumulation of charge carriers at sample-electrolyte interfaces) over a frequency range and to measure the resistance of charge carriers. In our case, the EIS measurements have been performed at an AC voltage field of 5 mV on the four networks sandwiched between two blocking stainless steel electrodes in a Swagelok cell (Fig.19 in experimental part).

The EIS measurements have been conducted on dry PTMA networks with a 270 µm thickness, giving unfortunately no signal. However, Boudouris et al.[26] performed similar analysis on thin film of linear PTMA in the solid state and they found a conductivity of *ca.* $1x10^{-6}$ S cm^{-1}. Based on their work, we assume that the motion of

PTMA chains is hindered by the presence of crosslinking nodes. The networks were therefore studied in their swollen state, with ethylene carbonate (EC)/diethyl carbonate (DEC) solvent mixture (1/1 vol/vol) (see experimental part for details on the swelling process). Frequently employed as commercial electrolytes, EC and DEC are here used as plasticizers to promote the mobility of charge carriers[27] by diffusing into the polymer network, thus increasing the free volume. They are good solvents for PTMA chains as demonstrated by the solvent content reached at the equilibrium by the gels obtained by swelling the investigated PTMA networks in EC/DEC 1/1 vol/vol (Table 2). Indeed, a solvent content of c.a. 83 wt. % has been noted for the gel prepared from the neutral PTMA network containing triazole crosslinker and a value as high as 95 wt. % for the gel containing charged crosslinking. As the triazole gel is not charged, it will be used as a reference. Thus, although the presence of ionic sites enables the PTMA gel to incorporate more solvent, the solvent content was kept constant (i.e *ca.* 83 wt. % of solvent corresponding to the solvent content of the triazole gel) for the EIS measurement of the four networks.

Gels	**SC (*wt%*) [a]**	**Anion Volume (Å^3)**[28]
Triazole (reference)	83	-
Triazolium$^+$/I$^-$	86	34.31
Triazolium$^+$/PF_6^-	93	72.61
Triazolium$^+$/TFSI$^-$	95	147.65

$a.\ Solvent\ Content\ (wt\%) = [(W_{swollen} - W_{dry})/W_{swollen}] * 100$

Table 2. Maximum EC/DEC solvent content (SC) for the investigated gels and the volume of TFSI$^-$, I$^-$ and PF_6^- anions in angstrom (Å^3).

Fig. 7a shows the conductivity (σ) of the investigated gels at ambient temperature. These conductivities were calculated using the following equation 1:

$$\sigma = L/(R_b.A) \qquad (1)$$

Where R_b is resistance obtained from Nyquist diagram in Fig.7b, L is the width and A is the area of the sample in contact with the electrodes. Our reference sample, the triazole gel (in blue) displays a conductivity of $2.4x10^{-6}$ S/cm. A similar value has been previously obtained for long chains of PTMA spin coated onto an ITO substrate.[26] For this system, the charge carriers are electrons belonging to nitroxide radical groups of PTMA. Thus, this electrical conductivity value is associated to the electron hopping mechanism along the PTMA chains facilitated by the liquid mixture of EC/DEC in which the PTMA chains are swollen. When the neutral triazole crosslinking nodes are replaced by charged triazolium$^+$/X$^-$ ones, the conductivity increases. The presence of counter-anions associated to the triazolium groups opens the possibility to observe ion mobility and thus provides ionic conductivity in addition to the electrical one generated by PTMA. The increase of conductivities follows the counter-anions order:

I^- ($7.4x10^{-6}$ S/cm) < PF_6^- ($1.7x10^{-5}$ S/cm) < $TFSI^-$ ($3.2x10^{-5}$ S/cm)

This is similar to the trend noted for swelling ratios and inversely related to the size of the anions (Table 2). Indeed, it has been reported that bulky anions generate an important charge delocalization enhancing the dissociation of triazolium$^+$/X$^-$ ions and thus increasing the mobility of the counter-anions.[29]

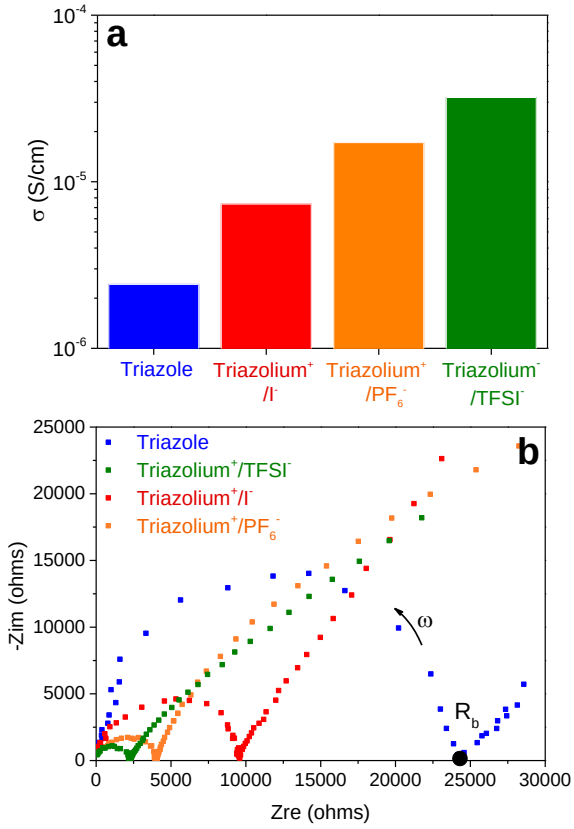

Figure 7. (a) Conductivity values and **(b)** Nyquist diagram of each gel comprising 2.4 mol. % of crosslinker and swollen with EC/DEC (1/1). The measurements were carried out at ambient temperature, on cells composed of Stainless Steel|PTMA gel|Stainless Steel. The triazole (in blue) is the reference.

The conductivities (σ) of the gels were then measured at variable temperature and plotted in Fig.8. For all investigated gels, the plots of ln (σ) versus 1000/T follow linear regression, indicating an Arrhenius behavior (eq. 2).

$$\sigma = A.exp(-E_a/R.T) \qquad (2)$$

Where A is a pre-exponential constant, E_a is the activation energy for conduction, R is the universal gas constant (8.314 $J.mol^{-1}.K^{-1}$) and T is the temperature.

This Arrhenius behavior can be explained by the fact that in those experiments, the temperatures of measurement are always lower than the glass temperature of the PTMA which is estimated to be around 170°C in bulk.[26,30] Moreover, the investigated gels can be seen as solid polymers interpenetrated by liquid, considering them as "semi-solid hybrid systems".[31] Thus, compared to linear chains, the segmental relaxation of the crosslinked chains in our systems is frozen, allowing the secondary relaxation (corresponding to the side chain group motion) to be the principal process.

Arrhenius fit of data gives activation energy (Ea) of 12.2 kJ/mol for the triazole gel reference (Fig. 8), which can be attributed to the thermally activated electron hopping of TEMPO groups with the help of solvent. The E_a of the triazolium$^+$/TFSI$^-$ gel is identical to that of the neutral triazole gel, which is the reference sample. In contrast, the E_a increases if the counter-ion is replaced by I^- (17.1 kJ/mol). This observation is in agreement with our previous results. In fact, among the three used counter ions, the iodine anion is the smallest and is thus more strongly associated to the triazolium cation, influencing the energy barrier of the PTMA gel. In contrast, the TFSI$^-$ anion is more mobile due to its weak association with the triazolium cation and has therefore no effect on the E_a of the PTMA gel.

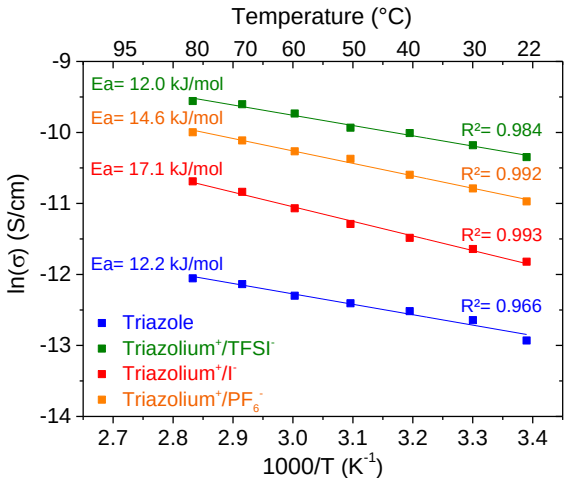

Figure 8. Temperature-dependent conductivity of each gel swollen with EC/DEC (1/1) and comprising 2.4 mol. % of crosslinker. The cells are composed of Stainless Steel|PTMA gel|Stainless Steel. The triazole (in blue) is the reference.

3.3.2 Ionic mobility with added salts

This time, the gels were studied in the presence of lithium salts. The four networks have been therefore swollen with commercial electrolytes, such as LiTFSI (1M) in EC/DEC (1/1) and $LiPF_6$ (1M) in EC/DEC (1/1). The solvent content of the gels was also kept constant here.

The swollen gels have again been sandwiched between two stainless steel electrodes and EIS measurements have been performed. Fig. 9a and 9b show Nyquist diagrams of swollen gels with $LiPF_6$ and LiTFSI electrolytes, respectively. The obtained resistance values are much lower than those obtained previously in Fig. 7b, as a result of the addition of lithium salts. In fact, the resistance is estimated at 35 and 40 ohms for triazole gels swollen with $LiPF_6$ and LiTFSI in EC/DEC electrolytes respectively, while it reaches $34.8x10^3$ ohms for the same network swollen with only EC/DEC (Fig. 8b). Moreover, the charged gels continue to exhibit better results than the reference (i.e. triazole gel), due to the nature of the counter-ion belonging to the network. Although, the resistance value of the triazolium$^+$/PF_6^- swollen gel with $LiPF_6$/EC/DEC electrolyte is slightly lower than these of the gel swollen with LiTFSI EC/DEC electrolyte, the other charged gels keep the same trend as previously obtained, whatever the used solvent, i.e:

$$R_b(\text{triazolium}^+/I^-) > R_b(\text{triazolium}^+/TFSI^-) > R_b(\text{triazole})$$

We hypothesize that the presence of different counter-ions in the medium does not disturb the conductivity.

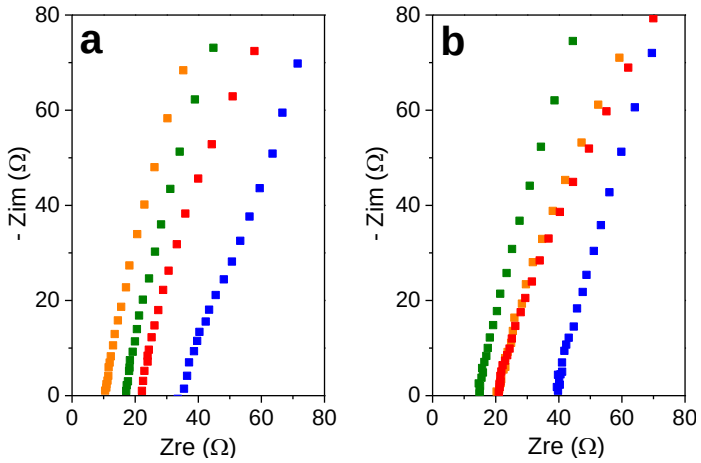

Figure 9. Nyquist diagram of triazole gel (the reference in blue), triazolium$^+$/TFSI$^-$ gel (in green), triazolium$^+$/I$^-$ gel (in red) and triazolium$^+$/PF_6^- (in orange). The gels are swollen with **(a)** $LiPF_6$ (1M) in EC/DEC (1/1) and **(b)** LiTFSI (1M) in EC/DEC (1/1). The cells are composed of Stainless Steel|PTMA gel|Stainless Steel.

The previously determined ionic mobility includes the contributions of both cations and anions movements. However, as described in chapter 1, only the Li^+ cations cross electrode interphases and participate in the intercalation process. The "steady-state current approach" developed by Bruce-Evans-Vincent[32] is then employed to study the mobility of lithium cations within the networks. The swollen gels are sandwiched between two non-blocking lithium foils electrodes and a direct electric field (d.c. voltage of 5 mV in our case) is applied on the cell in order to polarize the lithium electrodes. At the positively polarized electrode, the Li is oxidized into Li^+, which is reduced into Li at the negatively polarized electrode. Thus at t = 0, both cations and anions migrate under the d.c. voltage field, contributing to the ionic current. A steady state equilibrium is reached when only Li^+ cations, which are not blocked by the electrodes, contribute to the ionic current (Fig.10). The ratio of steady state current on initial current leads to the lithium transference number ($t_{Li^+} = I_{ss}/I_0$). However, Bruce-Evans-Vincent noticed that the polarization of the cell leads to an increase of the resistance, corresponding to the increase of the passivation layer at the surface of metallic lithium (also known as SEI). Thus, they reported that EIS measurements have to be conducted before and after the

polarization in order to take into account the influence of the passivation layer, which is a consequence of the reaction electrolyte - lithium foil (insets of Fig.10). The combination of the d.c. voltage polarization and a.c. voltage impedance measurements (Fig.10) leads to the lithium ion transference numbers (t_{Li^+}) of both gels, by using Bruce-Evans-Vincent equation (3):[32]

$$t_{Li+} = \frac{I_{ss}(\Delta V - I_0 R_0)}{I_0(\Delta V - I_{ss} R_{ss})} \qquad (3)$$

Where I_0 and I_{ss} are the initial and steady state currents obtained during the polarization, R_0 and R_{ss} are the resistances measured before (initial state) and after (steady-state) the polarization is applied and ΔV is the d.c. potential bias.

The transference numbers measurements were carried out on triazole (Fig.10a) and triazolium$^+$/PF_6^- (Fig.10b) swollen gels with $LiPF_6$ (1M) in EC/DEC (1/1). Since PTMA is a weak intrinsic electrical conductor, celgard separators soaked with $LiPF_6$ electrolyte were placed between lithium foils and the PTMA gels. The t_{Li^+} is estimated at 0.60 for the triazolium$^+$/PF_6^- gel and at 0.46 for the triazole gel. The mobility of lithium ions is thus facilitated in the charged PTMA network.

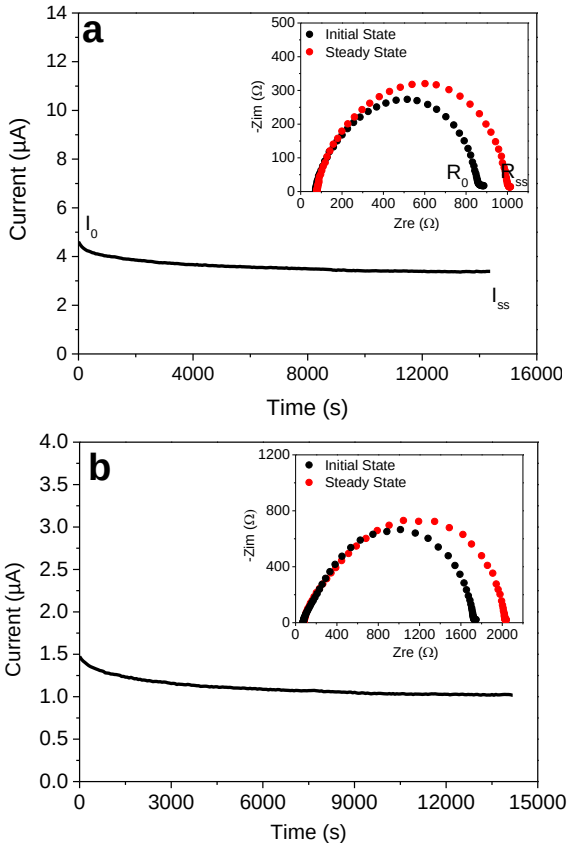

Figure 10. Time-dependence response of d.c. polarization for **(a)** Li|celgard|triazole gel with $LiPF_6$-EC:DEC electrolyte|celgard|Li (corresponding to the reference) and **(b)** Li|celgard|triazolium$^+$/PF_6^- gel with $LiPF_6$-EC:DEC electrolyte|celgard|Li symmetric cell configuration at an applied d.c. bias of 5 mV and at 40°C. The inset shows the impedance spectra of the initial and steady states of the cell with a.c. bias of 5mV.

3.3.3 Electrochemical performances

The electrochemical performances of gels swollen in electrolytes have been evaluated by galvanostatic charge/discharge cycling in half-cell configuration with lithium as counter electrode and over the voltage range from 3.0V to 4.2V *vs.* Li/Li$^+$. The crosslinking degree of the four investigated gels enables homogeneous dispersion with carbon SC45 and PVDF-co-HFP in NMP with 30/60/10 wt proportion. The LiTFSI

electrolyte was only used for the triazolium$^+$/TFSI$^-$ gel while the $LiPF_6$/EC/DEC electrolyte was utilized for the three other gels.

Firstly, charge-discharge cycles have been performed at a constant current of 1C corresponding to a current density of 100 mA/g (Fig. 11a). After *ca.* 200 cycles, the cells display relatively stable capacities, with a loss of less than 1% of the initial capacity for the triazole gel, followed by *ca.* 8% loss for the triazolium$^+$/I$^-$ and triazolium$^+$/PF_6^- gels and finally a 13% capacity fading for the triazolium$^+$/TFSI$^-$ gel. When the cells are cycled at variable currents ranging from C/10 to 2C (Fig. 11b), the four gels retain *ca.* 88% of their initial capacity.

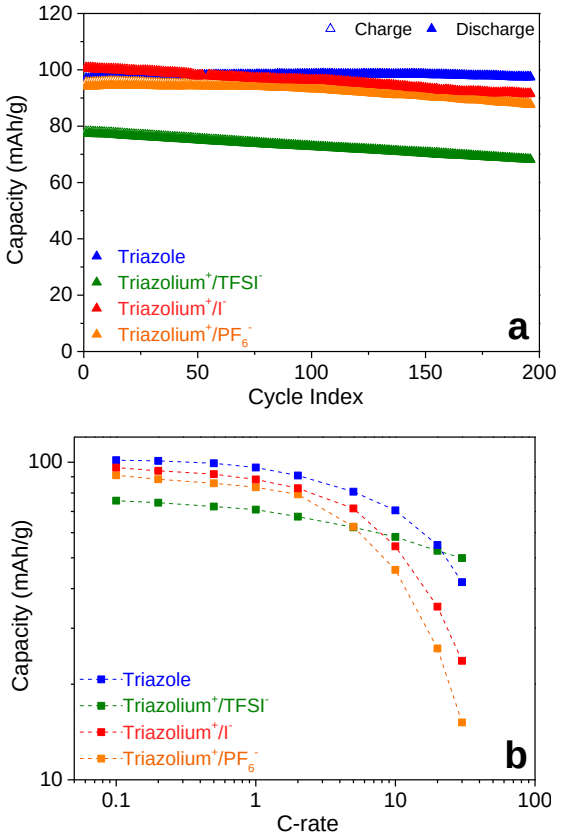

Figure 11. (a) Cycling stability at 1C (being 100 mA/g) and **(b)** C-rate performance at variable currents of PTMA gels comprising 2.4 mol. % of crosslinker. The electrodes were cycled in half-cell configuration with lithium as counter electrode and with PTMA/SC45/CMC/PVDF-co-HFP (30/60/10 wt. %) as cathode. The triazole (in blue) is the reference.

In both experiments (*i.e.* at cycling rates of 1C), we observe that the capacity of gels follows the opposite trend to that of conductivity:

$TFSI^-$ (71 mAh/g) < PF_6^- (83 mAh/g) < I^- (88 mAh/g) < triazole (96 mAh/g).

Although the oxidation process of PTMPM into PTMA was realized in the same condition for all investigated samples, we should not exclude the fact that the type and size of charged crosslinking nodes can influence the oxidation degree of the nitroxide radical groups and then cell capacities (as demonstrated in chapter 2). Fig. 12 shows the capacity retentions of gels obtained at variable C-rates normalized with the respect to the oxidation degrees and to the capacity obtained at C/10. We can observe that the PTMA gel comprising $triazolium^+/TFSI^-$ crosslinking nodes exhibits better and more stable capacity retention than the other gels, even when the cells are cycled quickly (beyond 2C). To understand these results, the potential is plotted versus the capacity (Fig.14).

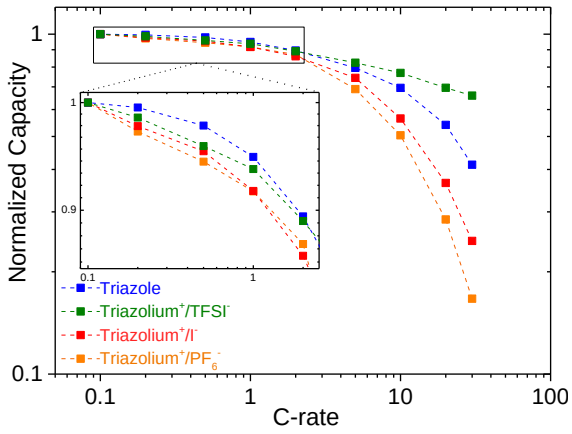

Figure 12. Comparison of PTMA gels comprising different crosslinking nodes (2.4 mol. % of crosslinker) according to their normalized capacities at variable C-rates. The triazole (in blue) is the reference.

With the potential-capacity curve, it is possible to observe the phenomena which contribute to the loss of the capacity. Three types of polarization loss exist: activation, ohmic and concentration polarizations (Fig.13). At low current, the activation polarization loss occurs, which is associated to the electrochemical reaction rate, *i.e.* the charge transfer kinetics. In the medium current range, the ohmic polarization is observed that is related to the ionic and electronic resistance (or conduction) of the electrolyte and the electrode. It is often related to the nature and concentration of the salts and used solvents. At the end of cycle, the concentration polarization occurs. Particularly observed at high C-rate, this loss is attributable to the depletion of the concentration of active species, i.e. mass transfer limitation. This latter polarization is common in the process of charging/discharging cells.

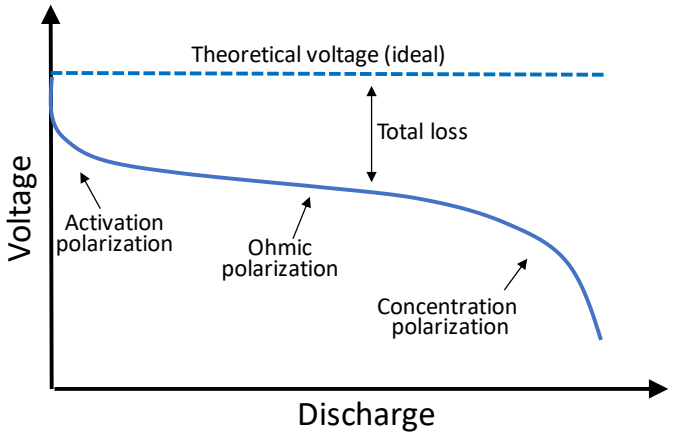

Figure 13. Typical discharge curve of battery showing the influence of various types of polarization.[33]

In our case, the triazolium$^+$/TFSI$^-$ gel is, among the investigated charged gels, the only one what keeps a stable plateau around 3.6V *vs.* Li/Li$^+$ without any polarization effect (Fig. 14b). This can prove that the presence of triazolium$^+$ cation does not hamper the Li$^+$ insertion in the cathode because of electrostatic repulsion. In contrast, the triazolium$^+$/I$^-$ gel displays important activation and ohmic polarization starting from C/5 (Fig. 14c). Thus, we must not exclude the effect of the charged crosslinker nodes during the charge-discharge cycling. In fact, during the discharge of the cell, the anions are supposed to move from the cathode to the anode. The presence of immobilized counter-

anions X^- in the cathode can therefore provoke a polarization behavior. The polarization effect is more pronounced for the triazolium$^+$/I^- gel. As described previously, this result can be due to a strong ionic interaction between triazolium$^+$ and I^-, preventing iodine anions to exit the cathode. Whereas the $TFSI^-$ is less associated to triazolium$^+$ and then more mobile. Concerning the triazolium$^+$/I^- gel (Fig. 14d), only the ohmic polarization is observed, which could be explained by the degradation of the PF_6^- counter-anions.

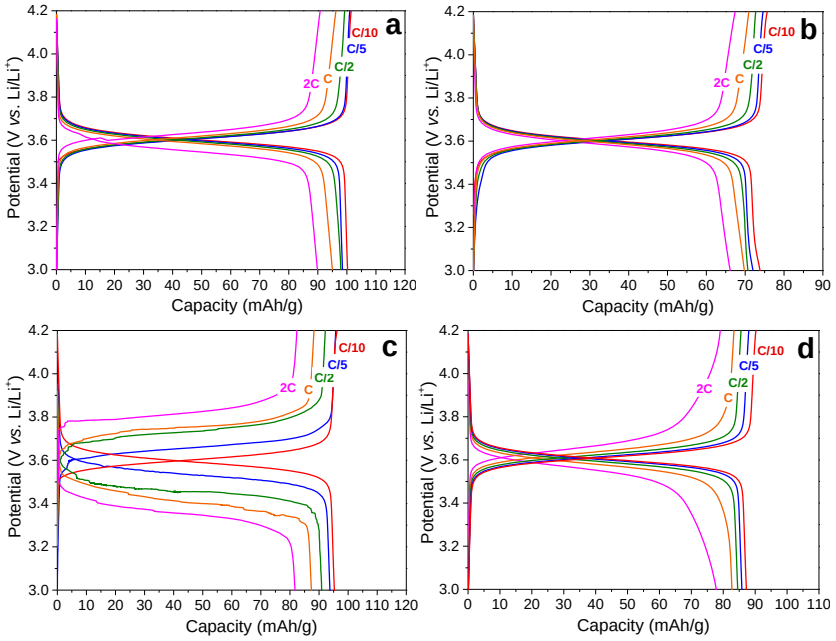

Figure 14. Potential-capacity curves at variable C-rates for **(a)** triazole gel (corresponding to the reference), **(b)** triazolium$^+$/$TFSI^-$ gel, **(c)** triazolium$^+$/I^- gel and **(d)** triazolium$^+$/PF_6^- gel (at 2.4 mol. % of crosslinker). The electrodes were cycled in half-cell configuration with lithium as counter electrode and with PTMA/SC45/PVDF-co-HFP (at 30/60/10 wt. % in NMP) as cathode.

3.4 The influence of crosslinking degree

The effect of the crosslinking degree on the conductivity and galvanostatic measurements was also studied by varying the concentration of crosslinker in each investigated gel, i.e. 0.6 mol. %, 2.4 mol. % and 9 mol. %.

3.4.1 Conductivity measurements

For each set of cross-linked system, the solvent content is fixed based on the maximum swelling of their respective neutral triazole reference gel. Thus, all the gels crosslinked at 0.6 mol. %, 2.4 mol. % and 9 mol. % are swollen with 93 wt. %, 83 wt. % and 87 wt. % of solvent respectively.

Fig.15 shows the conductivity of four PTMA networks swollen with EC/DEC solvent as a function of the crosslinker concentration (in mol. %). Whatever the amount of crosslinker, the conductivity values follow the same trend as previously:

$$\sigma_{triazole} < \sigma_{triazolium^+/I^-} < \sigma_{triazolium^+/PF6^-} < \sigma_{triazolium^+/TFSI^-}$$

We can also observe that all gels reach a limit of conductivity around $1x10^{-5}$ S/cm when the crosslinker concentration approaches zero. This conductivity value can correspond to the maximum value reached by a PTMA gel swollen with a maximum amount of EC/DEC solvent.

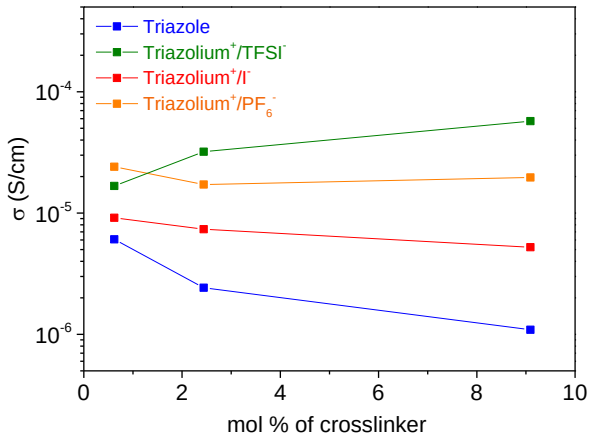

Figure 15. Conductivity values of each gel as a function of the molar percentage (mol %) of crosslinker. The cells are composed of Stainless Steel|PTMA gel swollen with EC:DEC (1:1)|Stainless Steel. The triazole (in blue) is used as reference.

The conductivity of the triazole gel decreases with increasing amount of crosslinker. In fact, the gel comprising 0.6 mol. % of triazole crosslinker displays a conductivity value of 6.1×10^{-6} S/cm while 1×10^{-6} S/cm is measured for a concentration of 9 mol. %. A slightly cross-linked gel swells more in solvents and its side groups are more mobile, leading to a better conductivity. For the charged gels such as the triazolium$^+$/TFSI$^-$ gel, an opposite effect is observed. Indeed, this gel comprising 9 mol. % of triazolium$^+$/TFSI$^-$ crosslinker has a better conductivity than the less cross-linked counterparts reaching 5.7×10^{-5} S/cm. A large amount of triazolium$^+$/TFSI$^-$ crosslinker thus improves the conductivity of the PTMA gel even though this latter is highly cross-linked and swells less with solvents. A similar trend is observed with the increase of the temperature (Fig. 16).

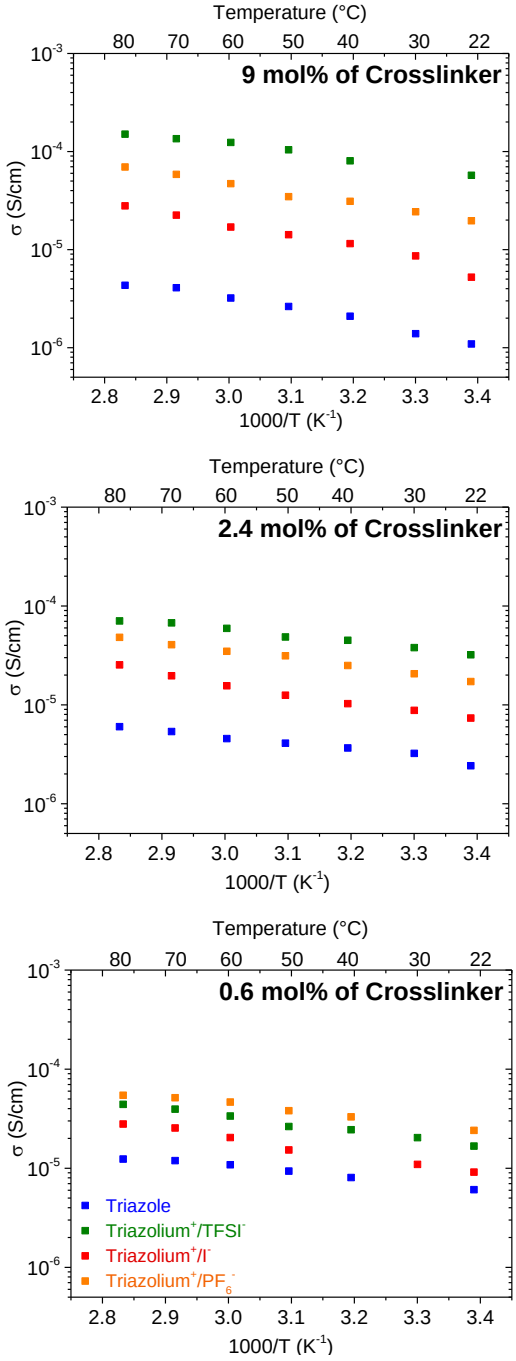

Figure 16. Temperature dependence of the ionic conductivity for PTMA gels comprising 9 mol. %, 2.4 mol. % and 0.6 mol. % of crosslinker. The triazole (in blue) is the reference.

The activation energies of all the investigated gels, obtained from the Arrhenius equation, increase with the crosslinker concentration (Fig. 17). For the triazole gel, a 92% increase in the value of the E_a is noted when the amount of crosslinker varies from 0.6 to 9 mol. %. This influence on the energetic barrier can be explained by the poor solvent swelling and the poor mobility of the side groups of the PTMA chains. This increase is less pronounced with the presence of charged crosslinkers with 17% and 30% increase in the E_a for triazolium$^+$/TFSI$^-$ and triazolium$^+$/PF_6^- gels, respectively. This result confirms the previously made hypothesis.

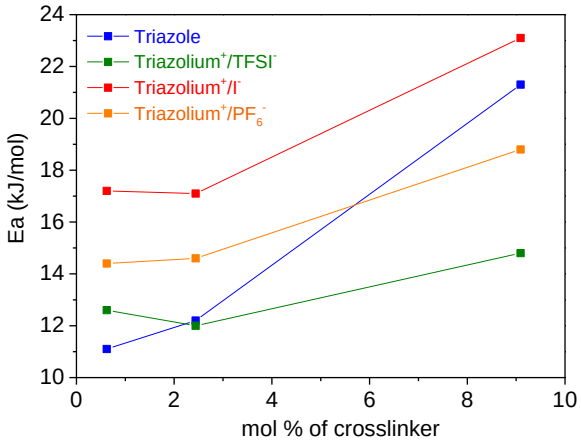

Figure 17. The plot of activation energy (E_a) versus crosslinker concentration (in mol. %).

3.4.2 Electrochemical performances

The PTMA gels comprising 2.4 mol. % and 9 mol. % of crosslinker were compared according to their capacity retentions at variable C-rates (Fig. 18). Their capacities were also normalized with respect to the oxidation degree and to the capacity obtained at C/10. Only the triazolium$^+$/TFSI$^-$ gel exhibits superior rate capabilities when it is more crosslinked (*i.e.* 9 mol. %). Whereas, the triazole, triazolium$^+$/I$^-$ and triazolium$^+$/PF_6^- gels (Fig. 18a, c and d, respectively) have a more pronounced capacity drop when they are crosslinked at 9 mol. %. This observation is in correlation with the observation achieved about the conductivity in Fig. 14.

In fact, the conductivity of the triazolium$^+$/TFSI$^-$ gel increases when the crosslinking degree increases from 2.4 to 9 mol. %, leading to an upgrade of C-rate performances. Whereas, the conductivity of triazole and triazolium$^+$/I$^-$ decreases with C-rate performances. Concerning the triazolium$^+$/PF_6^- gel, the capacity drops more than the triazolium$^+$/I$^-$ gel (Fig. 18), while it exhibits better conductivity that the latter (Fig.15). This could be due to the degradation of the counter-ion during the ion-exchange process.

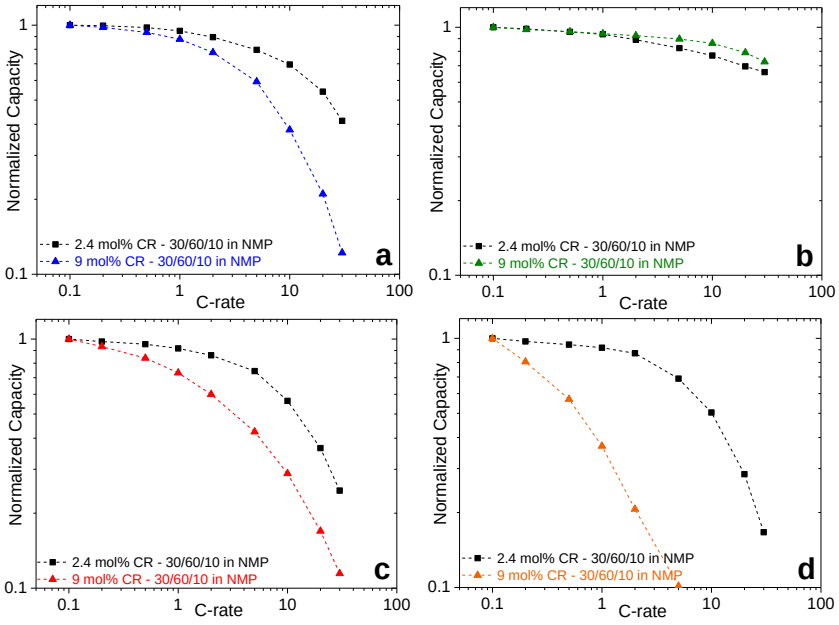

Figure 18. Comparison of PTMA gels, comprising 2.4 mol. % and 9 mol. % of crosslinker, according to their normalized capacities at variable C-rates. **(a)** triazole gel, **(b)** triazolium$^+$/TFSI$^-$ gel, **(c)** triazolium$^+$/I$^-$ gel and **(d)** triazolium$^+$/PF_6^- gel. The capacities are normalized with respect to the oxidation degree and to the capacity obtained at C/10. The electrodes were cycled in half-cell configuration with lithium as counter electrode and with PTMA/SC45/PVDF-co-HFP (at 30/60/10 wt. % in NMP) as cathode.

The variation of the crosslinking degree can also influence the elaboration of the slurry. In fact, the PTMA gels comprising 0.6 mol. % of crosslinker highly swell in NMP, hampering the slurry preparation. They were therefore dispersed in water with SC45 carbon, CMC and SBR (45/45/7/3 wt. %) because the PTMA gels collapse in water due to the bad polymer/solvent interaction, enabling a good grinding and dispersion. As observed previously, the PTMA gels comprising 9 mol. % of crosslinker have no problem of overswelling in NMP. However, in order to compare the results of PTMA gels crosslinked at 0.6 mol. %, the PTMA gels crosslinked at 9 mol. % were also dispersed in water. Unfortunately, the obtained results are not in correlation with all the observations achieved in this chapter. A poor contact between the active material and the carbon could take place during the slurry processing in water because of the significant crosslinking of the network accentuated by the collapse of the gel in water for the PTMA gels comprising 9 mol. % of crosslinker. Moreover, the amphiphilicity of the IL components[34] could also disrupt the electrochemical performance results.

3.5 Conclusion

We demonstrated that the conductivity and electrochemical performances of PTMA gel are improved by the incorporation within the three-dimensional network of charged groups mimicking ILs as crosslinking nodes. However, we showed that the choice of the counter-anions as well as the quantity of ILs are very important for the proper functioning of the battery based on PTMA gel cathode. Among the investigated counter-ions (*i.e.* $TFSI^-$, I^- and PF_6^-), the PTMA gels containing $triazolium^+/TFSI^-$ crosslinking nodes exhibited high conductivities and capacity retentions, even at high C-rates. Moreover, the addition of a high amount of $triazolium^+/TFSI^-$ crosslinking node had no harmful effect on the performance of PTMA gels as active materials for cathodes, contrary to other crosslinking nodes.

Unfortunately, the use of organic liquid electrolyte jeopardizes the safety of batteries. That why, in the next chapter, the improve of the ionic conductivity of solid polymer electrolyte (without organic solvent) will be investigated.

3.6 Experimental section

- Materials

All reagents were used as received. 2,2,6,6-tetramethylpiperidin-4-yl methacrylate (TMPM, TCI). CuBr (99+%, Acros). Ethylenediaminetetraacetic acid (EDTA, 99%), hydrogen peroxide solution (H_2O_2, 30% w/w), sodium tungstate dihydrate (>99%), N,N,N',N",N"-pentamethyldiethylenetriamine (PMDETA, 98%), ethylene carbonate (EC, >99%) diethyl carbonate (DEC, >99%), lithium hexafluorophosphate ($LiPF_6$, battery grade, >99.99%), bis(trifluoromethane)sulfonimide lithium salt (LiTFSI), methyl iodide (ICH_3, >99%), *N*-methyl bis[(trifluoromethyl)sulfonyl]imide (CH_3TFSI, >90%) were purchased from Aldrich.

- Instrumentation

Proton nuclear magnetic resonance. 1H NMR spectra were acquired on a 300 MHz Bruker Avance II in DMSO-d_6 or $CDCl_3$.

Samples preparation. The gels powder were pressed in pellet-shaped under 5 tons for few minutes to obtained a thickness between 200 to 250 µm. The pellets were deposited on stainless steel electrodes and solvent was added drop-by-drop until reach a swollen state of gels. This allowed the gel to swell until the equilibrium was reached. The thickness was kept constant with a 270 µm thick PTFE spacer between two stainless steel electrodes into the Swagelok cell (Fig.19). For the transference number measurements, the swelling of the networks as well as the assembly of Swagelok cells were carried out in an argon glove box. All the cells rest 24h before each measurement.

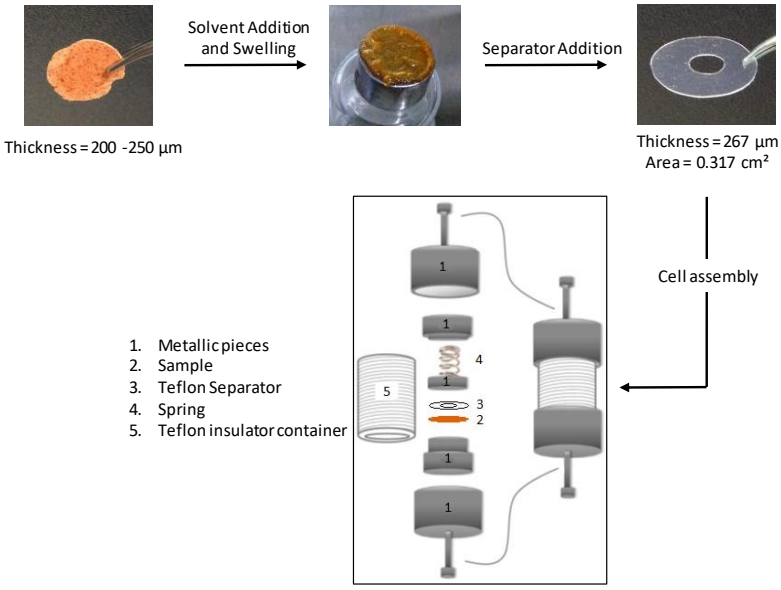

Figure 19. Sample preparation and Swagelok cell assembly for EIS measurements.

Electrochemical impedance spectroscopy (EIS) measurements were performed using a Parstat 4000 apparatus over a frequency range of 1 MHz to 10 mHz and with an amplitude AC excitation voltage of 5 mV. The temperature dependence measurements were carried out from 25 to 80°C by gradually increasing the temperature by steps of 10°C with an equilibration time of 1 h between each step.

Transference number measurements were carried out using Li|celgard|swollen gel|celgard|Li symmetric cells assembled in an argon glove box. The d.c polarization measurements were performed on an Arbin Instrument battery tester BT-2043 with a d.c. bias of 5 mV. The electrochemical impedance spectroscopy (EIS) measurements were performed on Parstat 4000 with an a.c. bias of 5 mV.

Electrodes preparation. Two different ways were used. (1) The cathodes were prepared by blending the active material PTMA/carbon SC45/PVDF-*co*-HFP binder at 5 wt.% in NMP (30/60/10). And (2) the cathodes were prepared by blending the active material PTMA/carbon SC45/CMC-SBR binder at 4 wt.% in water (45/45/7-3). For the two cases, the ingredients were mixed uniformly with a ball mill at room

temperature before casting on an aluminum foil using a doctor blade instrument. The wet slurries obtained with thicknesses controlled at 200 µm were dried at 70 °C and cut in circular disks of ½ inches diameter to be used as cathodes. The active material loading was typically comprised between 1.5 and 2.0 mg/cm^2.

Galvanostatic measurements. Charge/discharge tests were performed using an ARBIN Instrument Battery Tester (BT-2043). The electrodes were tested in half-cell configuration with porous polyethylene membrane as separator and lithium metal foil as counter and reference electrodes. The electrolyte used for the triazole, triazolium$^+$/I$^-$ gel and triazolium$^+$/PF_6^- gel, was $LiPF_6$ (1M) in EC/DEC (1:1, v:v). For the triazolium$^+$/TFSI$^-$ gel, the electrolyte used was LiTFSI (1M) in EC/DEC (1:1, v:v). All coin-cells were assembled under argon atmosphere (<0.1 ppm H_2O, <0.1 ppm O_2) in an Inert Lab glovebox. The cells was cycled over the voltage range from 3.0V and 4.2V *vs.* Li/Li$^+$.

- Synthesis

3-azidopropyl methacrylate (AzPMA) was synthesized as previously described.[35]

Propargyl methacrylate (PMA) was synthesized following a procedure reported earlier.[36]

1,2,3-triazole cross-linkers. Into a 50 ml round-bottom flask, PMA (500 mg, 4 mmol), AzPMA (680 mg, 4 mmol) and PMDETA (50 µl, 0.06 mmol) were dissolved in dichloromethane (25 mL, 95 wt%). The solution was bubbled with argon flux during 20min and CuBr (20 mg, 0.03mmol) was added. The mixture was stirred at room temperature for 1h before heated at 37°C for 24h. The green solution was stirred under open air for 30min and passed through neutral alumina column. The solvent was evaporated to give yellow viscous solid (0.98 g, 84 %).
^{1}H-NMR (300 MHz, DMSO-d_6), δ (ppm): 8.21 (s, 1H, N-C**H**-C_{quat}), 6.0 (m, 2H, 2*C=CH**H**), 5.6 (m, 2H, 2*C=C**H**H), 5.22 (s, 2H, C_{quat}-C**H_2**-O), 4.49 (t, 2H, N-C**H_2**), 4.10 (t, 2H, O-C**H_2**-CH_2), 2.21 (m, 2H, H_2C-C**H_2**-CH_2), 1.87 (m, 6H, 2*C**H_3**-C).
^{13}C-NMR (300 MHz, DMSO-d_6), δ (ppm): 166.4 (2C, 2*C-**C**O_2), 141,8 (1C, **C_{quat}**-N), 135.6 (2C, 2***C**=CH_2), 126 (2C, C=**C**H_2), 124.8 (1C, N-

CH-C_{quat}), 61.6 1C, H_2C-**C**H2-O), 57.6 (1C, C_{quat}-**C**H_2-O), 46.7 (1C, N-**C**H_2), 28.7 (1C, H_2C-**C**H_2-CH_2), 17.9 (1C, 2*H_3**C**-C).

Quaternization of 1,2,3-triazole cross-linkers.

(i) Triazolium $^+$ ***/ TFSI***$^-$. 1,2,3-triazole cross-linkers (600 mg, 2.05 mmol) and *N* methyl bis[(trifluoromethyl)sulfonyl]imide (841 mg, 2.85 mmol) were mixed in Acetonitrile (1 mL) and heated for 72 hours at 41 °C. The crude compound was precipitated in diethyl ether and filtered on 0.22 µm PTFE filter. The yellow solid obtained was dried in vacuum at 40°C (1.08 g, 90 %).

(ii) Triazolium $^+$***/I***$^-$. 1,2,3-triazole cross-linkers (260 mg, 0.887 mmol) and methyl iodide (1.26 mg, 8.87 mmol) were mixed in Acetonitrile (1 mL) and heated for 72 hours at 41 °C. The crude compound was precipitated in diethyl ether and filtered on 0.22 µm PTFE filter. The yellow solid obtained was dried in vacuum at 40°C (360 mg, 93%).

^{1}H-NMR (300 MHz, DMSO-d_6), δ (TMS, ppm): 9.05 (s, 1H, N-C**H**=C), 6.10 (d, 2H, C**H$_2$**=C), 5.70 (d, 2H, C**H$_2$**=C), 5.48 (s, 2H, C-C**H$_2$**-O), 4.74 (t, 2H, CH_2-C**H$_2$**-N), 4.31 (s, 3H, N-C**H$_3$**), 4.18 (t, 2H, O-C**H$_2$**-CH_2), 2.32 (quin, 2H, CH_2-C**H$_2$**-CH_2), 1.93 (d, 6H, 2*C**H$_3$**-C).

^{13}C-NMR (300 MHz, DMSO-d_6), δ (TMS, ppm): 166.3 (d, 2***C**=O), 138.6 (s, C=**C**-CH_2), 135.6 (d, 2***C**=CH_2), 130.6 (s, **C**H_2=C), 127.6 (s, **C**H_2=C), 126.1 (s, N-**C**H_2=C), 61.2 (s, C-**C**H_2-O), 53.9 (s, O-**C**H_2-CH_2), 50.7 (s, CH_2-**C**H_2-N), 38.3 (s, N-**C**H_3), 27.7 (s, CH_2-**C**H_2-CH_2), 17.9 (s, 2***C**H_3-C).

General procedure for the gelation (PTMPM gel). In a Schlenk flask, TMPM (4 g, 17.7 mmol, 20 eq.) and triazole cross-linker (0.130 g; 0.444 mmol ; 0.5 eq) diluted in DMF (20 wt. %) were heated at 70°C and bubbled with argon flux. Thereafter, a solution of AIBN (0.030 g; 0.182 mmol; 0.2 eq. or 1% of reactants) in degassed DMF was added in the schlenk. The mixture was stirred at 70°C overnight. The gel formed was swollen in DCM and filtered on 0.5µm PTFE filter. Then, the gel was dried in vacuum at 40°C. Once the polymer network dry, it is ground to be oxidized.

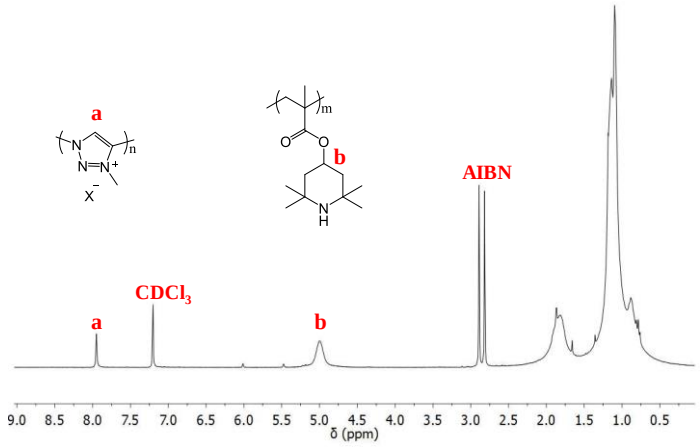

Figure 20. ^{1}H NMR spectrum in $CDCl_3$ of the crude PTMA gel.

General procedure for the oxidation of PTMPM gel into PTMA gel was realized following a procedure reported earlier in chapter 2.[25]

Anion exchange of triazolium $^{+}/I^{-}$ PTMA gel into triazolium $^{+}/PF_6^{-}$ PTMA gel. Triazolium $^{+}/I^{-}$ based PTMA gel (0.50 g, 0.097 mmol) was swollen with acetonitrile (3mL) and the medium was bubbled with argon. Lithium hexafluorophosphate (0.026 mg, 0.174 mmol) was dissolved in acetonitrile (1 mL) in an argon glove box and added to the PTMA gel solution. Then, the medium was heated for 78 hours at 40 °C. The product was added to 50 ml of methanol and following by filtration on 0.22 µm PVDF filter. The gel was dried in vacuum at 40°C.

Bibliography

1 B. Baek, S. Lee and C. Jung, *Int. J. Electrochem. Sci.*, 2011, **6**, 6220–6234.

2 H. Tokuda, K. Ishii, A. Bin, H. Susan, S. Tsuzuki, K. Hayamizu and M. Watanabe, 2006, 2833–2839.

3 M. Armand, F. Endres, D. R. MacFarlane, H. Ohno and B. Scrosati, *Nat. Mater.*, 2009, **8**, 621–629.

4 J. F. Brennecke and E. J. Maginn, *AIChE J.*, 2001, **47**, 2384–2389.

5 N. V. Plechkova and K. R. Seddon, *Chem. Soc. Rev.*, 2008, **37**, 123–150.

6 J. Yuan, D. Mecerreyes and M. Antonietti, *Prog. Polym. Sci.*, 2013, **38**, 1009–1036.

7 D. Mecerreyes, *Prog. Polym. Sci.*, 2011, **36**, 1629–1648.

8 N. Nishimura and H. Ohno, *Polymer (Guildf).*, 2014, **55**, 3289–3297.

9 F. N. Ajjan, M. Ambrogi, G. A. Tiruye, D. Cordella, A. M. Fernandes, K. Grygiel, M. Isik, N. Patil, L. Porcarelli, G. Rocasalbas, G. Vendramientto, E. Zeglio, M. Antonietti, C. Detrembleur, O. Inganäs, C. Jérôme, R. Marcilla, D. Mecerreyes, M. Moreno, D. Taton, N. Solin and J. Yuan, *Polym. Int.*, 2017, **66**, 1119–1128.

10 A. S. Shaplov, R. Marcilla and D. Mecerreyes, *Electrochim. Acta*, 2015, 175, 18–34.

11 G. A. Tiruye, D. Munoz-Torrero, J. Palma, M. Anderson and R. Marcilla, *J. Power Sources*, 2015, **279**, 472–480.

12 G. A. Tiruye, D. Muñoz-Torrero, J. Palma, M. Anderson and R. Marcilla, *J. Power Sources*, 2016, **326**, 560–568.

13 L. Porcarelli, A. S. Shaplov, F. Bella, J. R. Nair, D. Mecerreyes and C. Gerbaldi, *ACS Energy Lett.*, 2016, **1**, 678–682.

14 N. Patil, A. Aqil, F. Ouhib, S. Admassie, O. Inganäs, C. Jérôme and C. Detrembleur, *Adv. Mater.*, 2017, **29**, 1–9.

15 N. Patil, D. Cordella, A. Aqil, A. Debuigne, S. Admassie, C. Jérôme and C. Detrembleur, *Macromolecules*, 2016, **49**, 7676–7691.

16 G. Hernández, M. Işik, D. Mantione, A. Pendashteh, P. Navalpotro, D. Shanmukaraj, R. Marcilla and D. Mecerreyes, *J. Mater. Chem. A*, 2017, **5**, 16231–16240.

17 M. D. Green and T. E. Long, *Polym. Rev.*, 2009, **49**, 291–314.

18 Z. Yacob and J. Liebscher, in *Ionic Liquids - Classes and Properties*, 2011, pp. 1–23.

19 T. Zincke and A. T. Lawson, *Ber. Dtsch. Chem. Ges.*, 1887, **20**,

1176–1183.
20 Z. Yacob and J. Liebscher, *Top Heterocycl Chem*, 2015, **40**, 167–210.
21 Y. Jeong and J. S. Ryu, *J. Org. Chem.*, 2010, **75**, 4183–4191.
22 M. Obadia and E. Drockenmuller, *Chem. Commun.*, 2016, **52**, 2433–2450.
23 R. Tejero, D. López, F. López-Fabal, J. L. Gómez-Garcés and M. Fernández-García, *Biomacromolecules*, 2015, **16**, 1844–1854.
24 R. Noyori, M. Aoki and K. Sato, *Chem. Commun.*, 2003, **3**, 1977–1986.
25 F. Boujioui, O. Bertrand, B. Ernould, J. Brassinne, T. Janoschka, U. S. Schubert, A. Vlad and J.-F. Gohy, *Polym. Chem.*, 2017, **8**, 441–450.
26 L. Rostro, A. G. Baradwaj and B. W. Boudouris, *ACS Appl. Mater. Interfaces*, 2013, **5**, 9896–9901.
27 M. C. Smart, B. V. Ratnakumar and S. Sumurampudi, *J. Electrochem. Soc.*, 1999, **146**, 486.
28 A. S. Fisher, M. B. Khalid, M. Widstrom and P. Kofinas, *J. Electrochem. Soc.*, 2012, **159**, A592.
29 M. M. Obadia, B. P. Mudraboyina, A. Serghei, T. N. T. Phan, D. Gigmes and E. Drockenmuller, *ACS Macro Lett.*, 2014, **3**, 658–662.
30 H. A. López-Penña, L. S. Hernández-Munñoz, B. A. Frontana-Uribe, F. J. González, I. González, C. Frontana and J. Cardoso, *J. Phys. Chem. B*, 2012, **116**, 5542–5550.
31 A. Kumar and D. Saikia, in *Specialty Polymers Materials and Applications*, 2007, p. 440.
32 J. Evans, C. A. Vincent and P. G. Bruce, *Polymer (Guildf).*, 1987, **28**, 2324–2328.
33 M. Winter and R. J. Brodd, *Chem. Rev.*, 2004, **104**, 4245–4269.
34 Y.-S. Ye, J. Rick and B.-J. Hwang, *J. Mater. Chem. A*, 2013, **1**, 2719–2743.
35 O. Bertrand, B. Ernould, F. Boujioui, A. Vlad and J.-F. Gohy, *Polym. Chem.*, 2015, **6**, 6067–6072.
36 J. Geng, G. Mantovani, L. Tao, J. Nicolas, G. Chen, R. Wallis, D. A. Mitchell, B. R. G. Johnson, S. D. Evans and D. M. Haddleton, *J. Am. Chem. Soc.*, 2007, **129**, 15156–15163.

Chapter 4:
Solid polymer electrolytes from a fluorinated copolymer bearing cyclic carbonate pendant groups

Table of contents

4.1 Introduction

The development of safe, cheap and efficient batteries has become a necessity in our modern society. This implies an increase in energy density for batteries and the related development of new chemistries for both the active electrode materials and the electrolyte.[1,2,3] As far as the electrolyte is concerned, there is a need for replacing the current technologies based on liquid or gel electrolytes due to safety issues. Indeed, the formation of irregular metallic lithium electrodeposits during the recharge, which results in dendrites and explosion hazards, cannot be avoided whenever organic solvents are used.[4,5,6]

Nowadays, solid-state electrolytes are considered as an appropriate alternative to mitigate safety issues. The advantages of solid-state electrolytes compared to organic liquid-based electrolytes are (i) safety, (ii) the possibility of increasing energy density (if the used solid electrolyte can enable the use of a lithium metal anode), and (iii) potentially improving cycling, lifetime or rate performance. However, the problems faced by all-solid-state cells are considerable as detailed in recent reviews.[7,8,9] One of the greatest challenges is the development of a solid-state electrolyte combining high ionic conductivity and suitable mechanical properties.

Two major classes of solid-state electrolytes are the focus of research, namely ceramic and solid polymer electrolytes (SPEs).[10,11] On the one hand, ceramic electrolytes, and more particularly sulfide-based electrolytes, have the advantages of exhibiting similar (and sometimes higher) ionic conductivities compared to those of liquid electrolytes at room temperature. Unfortunately, they are characterized by typical mechanical properties, which prevent them from keeping good contact with the electrodes during cycling. On the other hand, SPEs display the typical mechanical properties of polymers that allow good contacts with the electrodes but are still characterized by low ionic conductivities at room temperature (*ca.* 10^{-4} S/cm for the best systems). Moreover, SPEs are generally based on poly(ethylene oxide) (PEO) mixed with a lithium salt. The use of those systems is hampered by three issues: (i) the partial crystallization of PEO leading to slow diffusion of lithium ions in the crystalline areas, (ii) the unsatisfactory mechanical properties of PEO/Li^+ SPEs requiring the addition of fillers or other polymer blocks

as reinforcing agents,[12] and (iii) the motion of lithium ions carrying only a fraction of the overall ionic current (low transference number).[13] Finally, recent studies have reported a combination of both types of solid electrolytes and have designed hybrid solid electrolytes in which ceramic electrolytes are embedded in SPEs.[14] Those efforts rely on the formation of a continuous network of ceramic (nano)particles in the SPE matrix. Although this last approach seems to be promising, a critical issue arises from the control of the SPE/(nano)particles interface in those hybrid systems, stemming for the development of novel types of SPEs.

This chapter focusses on a new class of SPE based on a poly(vinylidene fluoride-co-(2-oxo-1,3-dioxolan-4-yl)methyl 2-(trifluoromethyl)acrylate) copolymer, abbreviated as poly(VDF-co-MAF-cyCB) (Fig. 1a). PVDF is a polymer widely used in Li-battery as binder or as separator due to its chemical inertness and its good mechanical properties. It has been often copolymerized with hexafluoropropylene (HFP) in order to control its crystallinity[15] and to be used in gel polymer electrolytes.[16] Moreover, fluorinated polymers are particularly interesting because of their good dielectric constant promoting ion-dissociation, as demonstrated by studies on SPEs prepared from poly(VDF-co-HFP) $LiCF_3SO_3$[17] or Li bis(trifluoromethanesulfonyl)imide.[18] Nevertheless, due to the lack of coordinating atoms for Li ions, Li salts crystallization is often observed in those SPEs, that can be suppressed by using a fluorophilic anion in the used Li salt.[19] Recently, Ameduri et al. reported[20] the synthesis of poly(vinylidenefluoride-*co*-trioxa-3,6,9-decyl-2-trifluoromethacrylate) copolymers, poly(VDF-*co*-MAFTEG) (Fig. 1b), with the aim to functionalize PVDF membranes with polar TEG units to be used as gel polymer electrolytes with the presence of an ionic liquid electrolyte. The obtained results demonstrated the success of this approach with the formation of gel electrolytes exhibiting ionic conductivities above 0.2 mS/cm at room temperature, which is close to the values of the pure ionic liquid (1–2 mS/cm). Nevertheless, silica nanoparticles were added to the gel electrolyte in order to guarantee good mechanical properties to the accordingly obtained gels. Moreover, the poly(VDF-*co*-MAFTEG) copolymer could not be used as SPE due to the low amount of MAFTEG units in the copolymer and the associated low content of coordinating oxygen for lithium ions (only 3 ethylene oxide units in

each MAFTEG). The present research aims at replacing the MAFTEG units by MAF-cyCB ones that could also result in a better mobility for lithium ions and accordingly in enhanced ionic conductivity. As far as MAF-cyCB units are concerned, those are analogues of the very well-known cyclic carbonates-based liquid electrolytes. The incorporation of cyclic carbonates into polymer architecture seems to be a promising approach towards high performance SPEs, as recently reviewed by Brandell and co-authors.[21] Indeed, carbonate functional groups present high dipolar moment and dielectric constant enabling them to dissociate many types of salts.[22] They are found especially in five-membered cyclic form into commercial liquid electrolytes composition as ethylene carbonate and propylene carbonate.

The objective of this chapter is to increase the ionic conductivity by developing semi-crystalline polymer electrolytes based on cyclic ethylene carbonate (EC) as pendant groups and fluorinated backbones. The EC groups, by dissociating the salts with their high dielectric constant, could facilitate the motion of ions from one electrode to the other electrode and lead to a swift charge of the battery. Compared to polyethylene oxide (POE), the complexation of Li^+ ions could be avoided even at high concentration in salts. Moreover, a stable interface with electrode (also known as SEI) could be formed by using EC groups instead of the linear alkyl carbonates. Here, we investigate the mechanical and electrochemical properties of poly(VDF-co-MAF-cyCB) copolymer at different content of lithium salts. The copolymer was synthesized by Ameduri et al. from the Institute Charles Gerhardt at Montpellier and the rheology measurements were kindly realized by Dr Flanco Zhuge.

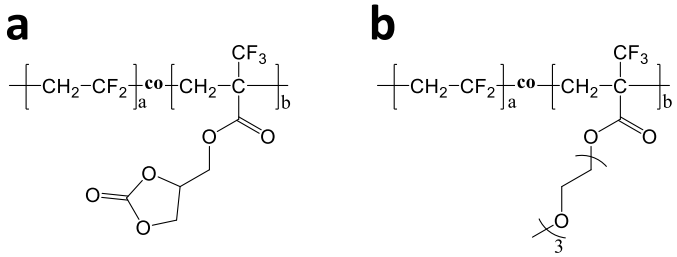

Figure 1. Structure of **(a)** poly(VDF-co-MAF-cyCB) and **(b)** poly(VDF-*co*-MAFTEG).

4.2 Synthesis of SPEs

The poly(VDF-*co*-MAF-cyCB) copolymer was synthesized via a conventional radical copolymerization of VDF with MAF-cyCB, a fluorinated methacrylate bearing a cyclic carbonate group as side-chain. The synthesis of the MAF-cyCB monomer was achieved by the esterification reaction of 2-trifluoromethyl acrylic acid (MAF) with glycerol carbonate (Fig. 2). First, MAF was modified into 2-(trifluoromethyl)acryloyl chloride (MAF-COCl) using thionyl chloride (step A).[23] Then, the esterification reaction of MAF-COCl with glycerol carbonate led to MAF-cyCB, in 85% yield (step B, see NMR spectrum in Fig. 15 in Experimental section). Similar to MAF and other MAF-esters,[23,24,25] the homopolymerization MAF-cyCB failed under radical initiation.

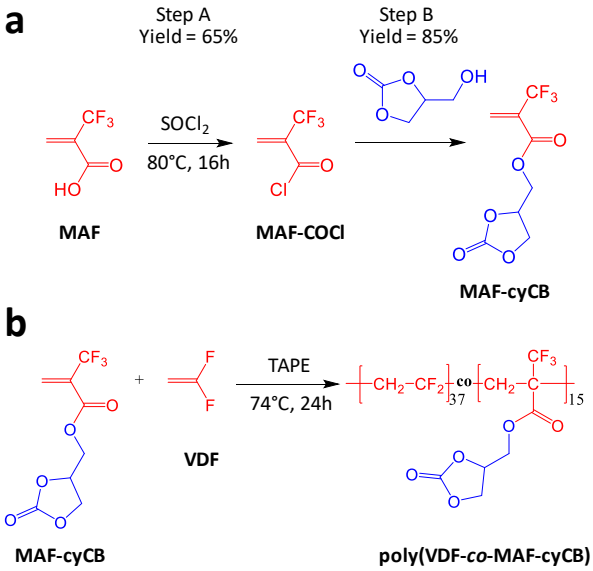

Figure 2. (a) Synthesis of (2-oxo-1,3-dioxolan-4-yl)methyl 2-(trifluoromethyl)acrylate (MAF-cyCB). **(b)** Radical copolymerization of VDF with MAF-cyCB initiated by *tert*-amyl peroxy-2-ethylhexanoate (TAPE).

The copolymerization of VDF with MAF-cyCB was initiated radically by *tert*-amyl peroxy-2-ethylhexanoate (TAPE) at 74 °C in dimethyl carbonate (DMC) in a high pressure autoclave since VDF is a gas. In the course of the polymerization, an initial increase in pressure up to 37 bars with the increase in temperature was noted, followed by a decrease in pressure when the temperature reached 70 °C. This is explained by the dissociation of the initiator at this temperature that released radicals enabling the copolymerization to start. Then, the consumption of the monomers led to the decrease of the pressure down to 24 bars. After 16 hours, the pressure was 10 bars justifying the reactivity of VDF and, after opening the autoclave and purification, the copolymerization reached 60% yield. The obtained poly(VDF-*co*-MAF-cyCB) random copolymer presents an average content of 28 mol% (corresponding to 59 wt%) of MAF-cyCB units as determined by NMR (^{1}H NMR spectrum in Fig. 16 and ^{19}F NMR in Fig. 17 in Experimental section), a molar mass (M_n) of 6,500 g/mol and a dispersity ($Đ$) of 1.67 as determined by SEC (in PS equivalent). SPEs were finally prepared by mixing the poly(VDF-*co*-MAF-cyCB) copolymer with various amounts of $LiClO_4$.

The distribution of comonomers was recently studied in similar terpolymers containing VDF, trifluoroethylene (TrFE) and MAF monomers.[26] The batch polymerization generates a heterogeneity in the composition of chains. In fact, according to Ameduri et al.,[26] MAF reacts quickly and preferentially with VDF until its complete conversion, followed by the homopolymerization and copolymerization of unreacted VDF with TrFE. The absence of NMR signals corresponding of the MAF-TrFE indicates that poly(MAF-*co*-TrFE) segments were not obtained during the batch polymerization. Thus, poly(VDF-*co*-MAF) segments are thus first obtained during the polymerization followed by pure poly(VDF) segment and poly(VDF-co-TrFE) segments. The remaining VDF units are then polymerized leading to a (quasi) pure poly(VDF) segment at the end of the polymer chain. One can assume that the same situation prevails for the copolymer investigated here. The actual microstructure of the copolymer could be thus described as a poly(VDF-*co*-MAF-cyCB) segments linked to a poly(VDF) block, although this copolymer will be named poly(VDF-*co*-MAF-cyCB) in the following. In fact, MAF-cyCB

reacts until its complete conversion with VDF, followed by the homopolymerization of the remaining VDF.

4.3 Study of the morphology

Before measuring the electrochemical characteristics of the studied SPEs, it is worth determining their morphology. The results obtained in this section could help to understand the ionic conductivities results studied below.

First, structural information about the investigated SPEs can be obtained by differential scanning calorimetry (DSC) experiments. The DSC thermograms of the SPEs (Fig. 3) reveal two typical transitions, i.e. a glass transition (T_g) and a melting peak (T_m). The melting transition has been attributed to PVDF segments since the corresponding PVDF polymer is semi-crystalline. For the pure poly(VDF-*co*-MAF-cyCB) copolymer without added salt, a T_m of 147 °C has been noted and a degree of crystallinity of 22% has been calculated using equation 1.

$$Degree\ of\ crystallinity\ (\chi) = \frac{\Delta H_m}{(\Delta H_c).(wt\%\ PVDF)} \qquad (1)$$

Where ΔH_c (104.6 J g^{-1}) corresponds to the melting enthalpy of 100% crystalline PVDF,[27,28] ΔH_m corresponds to the experimental melting enthalpy obtained by DSC (Fig. 3) and wt.% is the mass percent composition of PVDF corresponding to 41 wt.%.

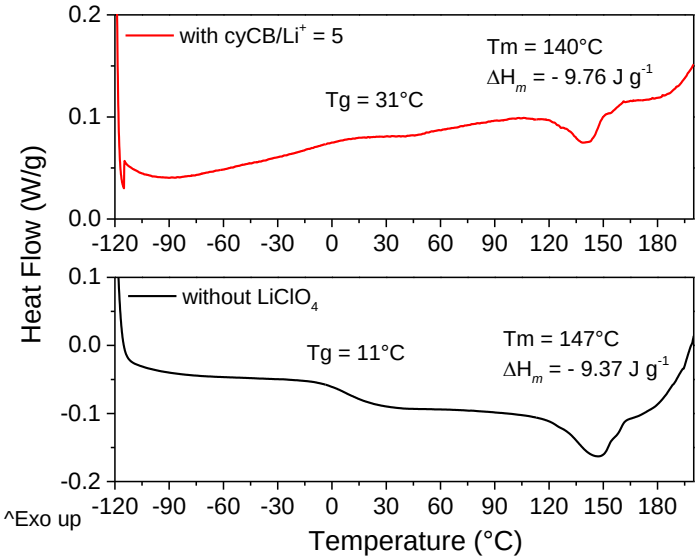

Figure 3. DSC thermograms of poly(VDF-*co*-MAF-cyCB) with and without salt in the second heating cycle.

These values are significantly lower compared to those of pure PVDF, for which a T_m of 177°C and a degree of crystallinity of 50% are commonly observed.[29] The T_g of pure PVDF is reported[29] to be around -40 °C while the T_g for the poly(MAF-cyCB) is not available since this homopolymer cannot be synthesized by radical polymerization. The T_g measured for the poly(VDF-*co*-MAF-cyCB) copolymer investigated here is 11 °C. This value is substantially higher than for pure PVDF.

These observations can be understood on the basis of the microstructure of the copolymer discussed in the section above. Indeed, the copolymer chains are consisting of a poly(VDF-*co*-MAF-cyCB) segment followed by a pure PVDF sequence. Actually, the presence of both the trifluoromethyl and cyclocarbonate side groups imparts some bulkiness of the MAF-cyCB units. Therefore, we believe that crystallization is hampered in the MAF-cyCB units. Moreover, MAF-cyCB units are believed to increase substantially the value of the *T*g. In contrast, crystallization can be observed in the small amount of pure PVDF segments. On the basis of these considerations, we propose a microphase separated morphology in which PVDF crystalline domains are embedded in an amorphous matrix of poly(VDF-*co*-MAF-cyCB)

segments (see Fig. 4). This picture is confirmed whenever the effect of the addition of salt is investigated. Indeed, addition of $LiClO_4$ does not affect T_m nor the degree of crystallinity in the SPE while it substantially increases the T_g. As a typical example, the T_g rises up to 31 °C for copolymer electrolyte with cyCB/Li^+ = 5 (Fig. 3). This result points out towards a morphology where the mechanical properties are controlled by crystalline PVDF nanodomains and where ionic conductivity would be ensured by the amorphous poly(VDF-*co*-MAF-cyCB) matrix with dissolved $LiClO_4$.

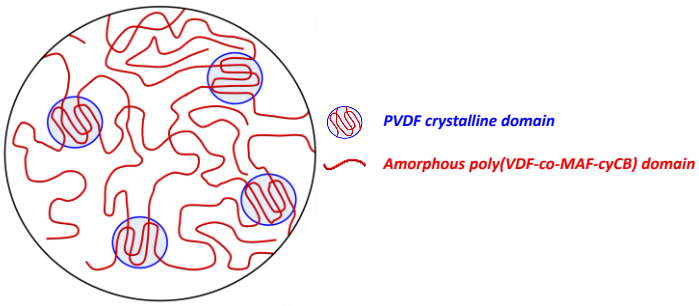

Figure 4. Sketch of the microstructure of the poly(VDF-co-MAF-cyCB) copolymer.

This picture is further confirmed by AFM measurements on the poly(VDF-*co*-MAF-cyCB) SPEs. Indeed, the AFM images (Fig. 5) reveal a nano-structured morphology for the SPEs. The nanosized features observed in Fig. 5 (left) for the pure poly(VDF-*co*-MAF-cyCB) copolymer are attributed to the PVDF crystalline-rich phase and to the amorphous poly(VDF-*co*-MAF-cyCB) domains. Addition of salt tends to increase the size of the nano-structured features (Fig. 5 right). The added salt is indeed expected to be incorporated in the amorphous poly(VDF-*co*-MAF-cyCB) zones to form an ionically conducting phase. Indeed, the added lithium ions can act as transient cross-linkers between poly(VDF-*co*-MAF-cyCB) domains, reducing segmental motion of amorphous chains (as evidenced by an increase in T_g) and enhancing microphase-separation. AFM phase contrast images (data not shown) were blurry and did not allow obtaining further identification of a hard crystalline phase and a soft amorphous phase. This is the reason why a detailed analysis of the mechanical properties of the SPEs is detailed in the next section.

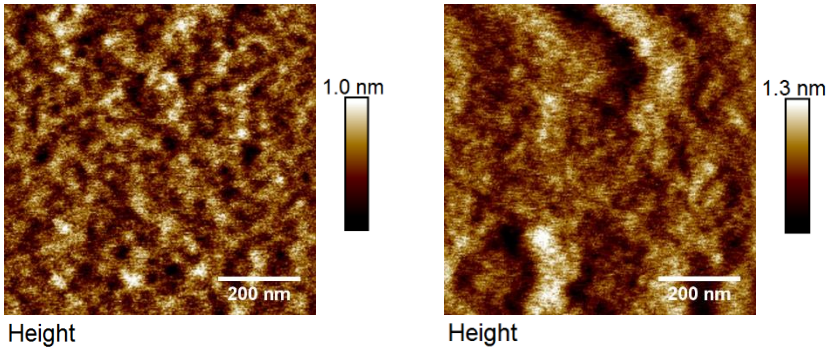

Figure 5. AFM images (height contrast) of poly(VDF-co-MAF-cyCB) copolymer without $LiClO_4$ **(left)** and with added $LiClO_4$ with cyCB/Li^+ = 5 **(right)**.

4.4 Mechanical properties of SPEs

The mechanical properties of the SPEs were studied by oscillatory shear rheology. Initially, frequency sweep measurements were performed at 25 °C. The materials act as elastic solids in which the storage modulus G' remains always higher than the loss modulus G'' for all the SPEs with or without $LiClO_4$ as reported in Fig. 6.

The terminal regime is absent within the measurement range meaning that the materials do not dynamically flow. This elastic solid behavior is attributed to the phase separation within the poly(VDF-*co*-MAF-cyCB) copolymer as discussed in the above section. Hence, the investigated SPEs are composed of a hard phase which is originating from the crystallization of PVDF and an amorphous one from poly(VDF-*co*-MAF-cyCB) segments. The PVDF hard phases act as physical cross-linkers surrounded by the amorphous phase and these cross-linkers allow the formation of a network that prevents the material from flowing.

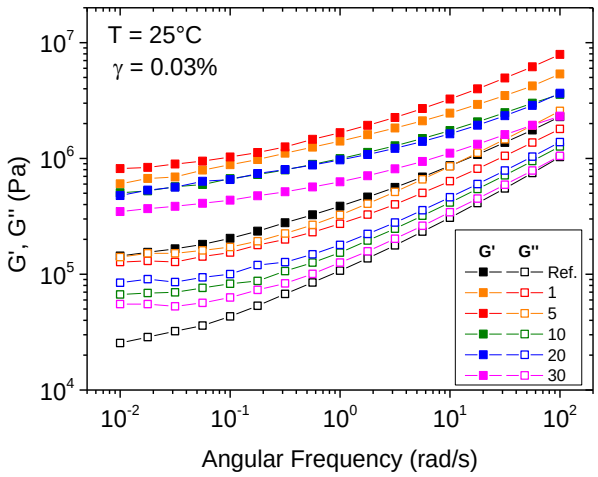

Figure 6. Frequency sweeps displaying the influence of the salt concentration on the SPEs at T = 25 °C. The storage modulus G′ is represented by filled symbols and the loss modulus G″ by unfilled symbols. The reference black curves represent the poly(VDF-co-MAF-cyCB) copolymer without any $LiClO_4$ and the colored curves represent the polymer mixed with different salt amounts. The numbers indicated in the insert correspond to the cyCB/Li^+ ratio.

The addition of salts within the polymeric matrix tends to increase this phase separation where the lithium salts are dissolved in the amorphous phase of the polymer to reduce at maximum the surface contact with the crystalline PVDF domains. This increase in phase separation is confirmed in oscillatory shear measurements for which the elasticity of the SPEs raises when the salt concentration increases (except when the cyCB/Li^+ ratio is equal to one, which will be explained below). For instance, for a fixed angular frequency, e.g. ω = 1 rad/s, the storage modulus G' values of the reference copolymer along with SPEs are reported and compared in Fig. 7.

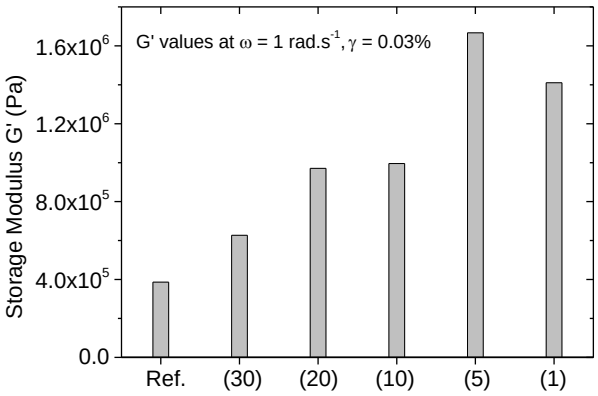

Figure 7. Storage modulus G' values at angular frequency ω = 1 rad/s for different poly(VDF-*co*-MAF-cyCB) copolymers with and without $LiClO_4$ obtained through frequency sweep measurements at T = 25 °C and γ = 0.03%.

The reference sample displays a G' of 3.86 x 10^5 Pa that is increased by 62% up to one order of magnitude depending on the amount of added lithium ions. There is no significant difference in mechanical properties between the SPEs with cyCB/Li^+ = 10 and cyCB/Li^+ = 20 (Fig. 7). But, when the concentration of salt raises up to cyCB/Li^+ = 5, a storage modulus G' as high as 1.67 x 10^6 Pa is observed (Fig. 7). As mentioned above, the increase in moduli upon addition of lithium salt could be attributed to an enhanced phase separation between the hard crystalline PVDF and the soft poly(VDF-*co*-MAF-cyCB) phases and to a reduced segmental motion of amorphous poly(VDF-*co*-MAF-cyCB) segments since lithium ions are expected to behave as transient cross-linkers between MAF-cyCB units. When the cyCB/Li^+ ratio reaches 1, G' decreases to a value slightly lower than the one at cyCB/Li^+ = 5 but significantly higher than that assessed for the reference copolymer without any added salt (Fig. 7). We hypothesize that the salt concentration has reached a saturation level at cyCB/Li^+ = 1 and that the excess of salt is not dissolved in poly(VDF-*co*-MAF-cyCB) amorphous phase and forms salt clusters compromising mechanical properties. This result also indicates that it is useless to further investigate SPEs with cyCB/Li^+ ratio as low as 1.

Furthermore, the evolution of complex viscosity is also an interesting mechanical feature to investigate as shown in Fig. 8. Typically, all the studied systems display a shear-thinning behavior as the complex viscosities of the materials with salt decrease by three orders of magnitude when the shear rate varies from 0.003 to 3 s^{-1}. The high viscosities of these systems, e.g. 14.6 MPa.s for the reference and 82.9 MPa.s for cyCB/Li^+ = 5 at low shear rate, clearly indicate that the materials behave as a solid in which the elasticity and the stiffness of the sample both increase upon addition of lithium salts.

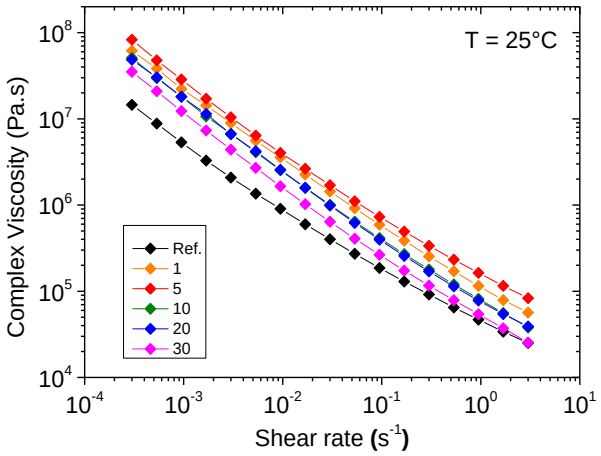

Figure 8. Complex viscosity vs shear rate showing the influence of the added salt at T = 25 °C. The reference black curve represents the poly(VDF-*co*-MAF-cyCB) copolymer without any added salt and the colored curves represent this polymer mixed with different salt amounts. The numbers indicated in the insert correspond to the cyCB/Li^+ ratio.

4.5 Ionic conductivity measurements

The SPEs consisting of poly(VDF-*co*-MAF-cyCB) copolymer loaded with various $LiClO_4$ amounts were studied by electrochemical impedance spectroscopy (EIS). Fig. 10 plots the ionic conductivity (σ) of the SPEs versus their lithium salt ($LiClO_4$) loading, at ambient temperature.

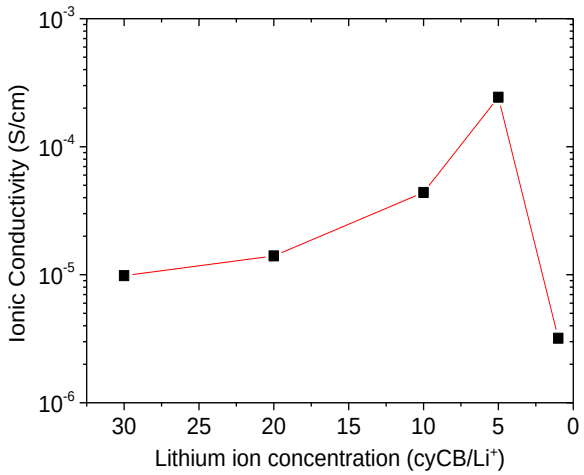

Figure 9. Ionic conductivity vs. Lithium salt concentration (expressed as the cyCB/Li^+ ratio) at 22°C.

The ionic conductivity increases when the amount of lithium salt incorporated into the polymer increases up to cyCB/Li^+ equals to 5. An ionic conductivity value in the range of 2 x 10^{-4} S/cm is noted at room temperature for the cyCB/Li^+ = 5. This value is quite interesting and renders our materials promising for possible application as SPE for Li-ion batteries. This ratio of 5 is much higher than those observed at room temperature for classical PEO-based SPEs.[30] These observations could be easily understood with the following equation (2):[31]

$$\sigma = n_i \, q_i \, \mu_i \qquad (2)$$

Where σ is the ionic conductivity, i is the type of ions, n_i is the concentration of charge carriers, q_i is the charge of electron and μ_i is the mobility of ions.

In fact, the ionic conductivity measurements depend on the concentration but also on the mobility of the charge carriers in the matrix. In the case of PEO-based SPEs, the high amount of salt decreases the ionic conductivity values due to the complexation of salts by ethylene oxide groups leading to an increase of the viscosity. This explains why for these systems, the maximal fraction of incorporating salts is around 0.04 (corresponding to EO/Li^+ ratio of 25). In our case, the maximal fraction reached is 0.20 (corresponding to cyCB/Li^+ ratio

of 5) because the cyCB units as well as the fluorinated groups have a high dielectric constant allowing them to dissolve the salts. However, thereafter for the highest salt concentration (cyCB/Li^+ equals to 1), a drop in conductivity is noted (Fig. 9), meaning that the mobility of ions is reduced for high salt loading. Indeed, at high salt concentrations, free ions could recombine into aggregates or ions pairs, which do not contribute to the conductivity anymore.[32,33,34] This observation is consistent with the rheological characterization performed in the above section where a decrease in G' has been noted for a cyCB/Li^+ ratio of 1 due to the possible formation of ionic clusters at high salt loading.

The ionic conductivities for the SPEs with different cyCB/Li^+ molar ratios increase with temperature, as shown in Fig. 10. This increase of ionic conductivity is attributed to an enhanced mobility of the polymer segments and charge carriers when the temperature increase. Competing values above 10^{-3} S/cm are reached at 80 °C for the sample with a cyCB/Li^+ ratio of 5. We also observe that the plot Ln(σ) versus 1000/T is nonlinear, indicating a Volgel-Fulcher-Tamman (VFT) behavior. This model predicts relation between the mobility of ions and the segmental relaxation of polymer from the following equation (3):

$$\sigma = \sigma_0 T^{-\frac{1}{2}} \exp\left[-\frac{E_a}{k_B(T-T_0)}\right] \qquad (2)$$

Where σ_0 is pre-exponential factor, E_a is the activation energy for ionic conduction (in eV or $kJ.mol^{-1}$) corresponding to the energy required for ion hopping, k_B is the Boltzmann constant ($1.38x10^{-23}$ $J.K^{-1}$), T is the temperature (in Kelvin) and T_0 corresponds to 10-50 K below the T_g of the polymer. The activation energies (E_a), obtained by tracing $Ln(\sigma.T^{1/2})$ versus $1000/(T-T_0)$ (Fig. 11), are relatively low indicating an easy ion hopping. In addition to having high dielectric constant cyCB units, which dissolve the ions species, the segmental motion of polymer backbones involves ions transport process, which improves the ions mobility. Moreover, we also observe that the E_a decreases when the salt concentration increases. This observation is in correlation with the equation (2). In fact, the dispersion of a high amount of a $LiClO_4$ salt with a low lattice energy in polymer matrix comprising high dielectric constant cyCB units leads to excellent ionic conductivity values.[31]

Because of its interesting values, the SPE obtained from a cyCB/Li^+ ratio of 5 was selected for further electrochemical characterizations.

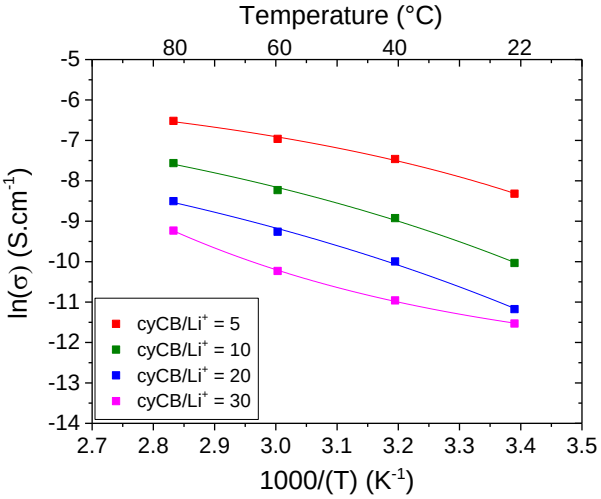

Figure 10. Temperature dependence of the ionic conductivity for the investigated SPEs.

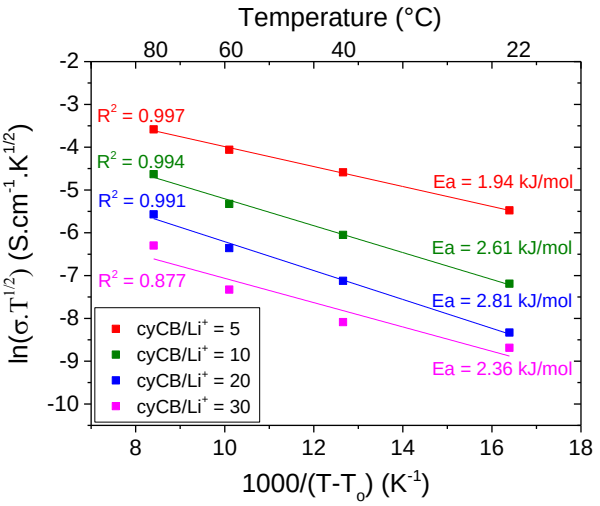

Figure 11. Temperature dependence of the ionic conductivity for the investigated SPEs using VFT model.

4.6 Electrochemical stability

The electrochemical stability window of the SPE with cyCB/Li^+ = 5 was investigated by linear sweep voltammetry between 0.5 V and 6 V vs Li/Li^+ at a scan rate of 0.5 mV/s (Fig. 12). The studied cell consisted in a sandwiched SPE film between a stainless steel working electrode and a Li-metal anode playing the role of reference electrode. The polymer appears to be electrochemically stable from 1.4 V to 4.9 V vs Li/Li^+. This electrochemical window allows the poly(VDF-*co*-MAF-cyCB)/$LiClO_4$ SPEs to be compatible with e.g. Li-ion batteries based on lithium titanate anodes.

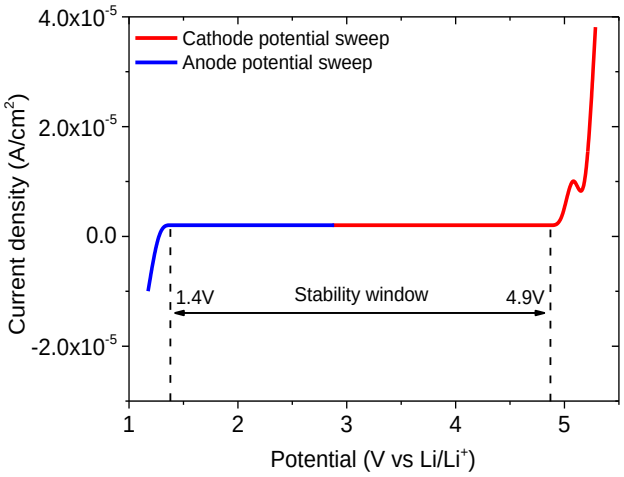

Figure 12. Linear sweep voltammetry curves of polymer electrolyte with cyCB/Li^+ = 5. The scan rate is 0.5 mV/s.

Below 1.4 V and above 4.9 V, reactions of degradation occur. The cathodic peaks at potentials above 5 V are mainly attributed to the decomposition of the $LiClO_4$ and oxidative corrosion of stainless steel working electrode. For potentials below 1.4 V vs. Li/Li^+, considerable SPE decomposition can be observed which is associated to complex surface reactions between the electrolyte components and the electrode materials (Li-metal in this case). In contact with the Li-metal electrode, the poly(VDF-*co*-MAF-cyCB) segments of the SPE decompose and form a solid-electrolyte interface (SEI).[35] The stability of this SEI was analyzed by galvanostatic cycling measurement on a Li │polymer-

electrolyte | Li symmetrical cell at 40°C. This technique consists in imposing a capacity of 0.2 µAh/cm² so that the lithium strips and plates at the interface with the polymer electrolyte, at a C-rate of 0.1µA/cm². The stripping/plating cycles are studied by the monitoring of the variation of the voltage as a function of time. Fig. 13 shows a stable voltage over a period of 107 hours and at low current density of 0.1µA/cm², indicating an acceptable compatibility between the poly(VDF-*co*-MAF-cyCB)/$LiClO_4$ SPE and the Li-metal electrode, but only at low capacity, which can be due to the instability of the $LiClO_4$.

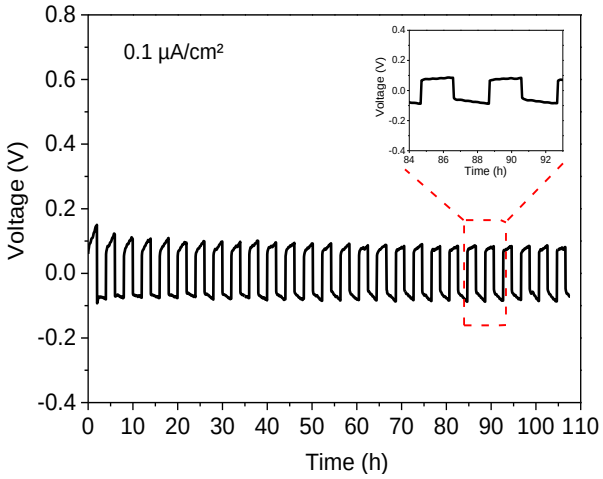

Figure 13. Galvanostatic cycling curve of Li/SPE/Li symmetrical cell at 40°C and at current density of 0.1µA/cm² with charge/discharge cycle time of 4 hours. The inset shows 2 cycles of charge/discharge between 84 and 93 hours.

4.7 Lithium transference number

The lithium ion transference number (t_{Li^+}) is another very important parameter for the characterization of lithium ion battery electrolytes. It represents the fraction of current carried by lithium ions and it should be close to 1. Fig. 14 shows the time-dependence of current flowing through the copolymer electrolyte with cyCB/Li^+ ratio of 5 at 40 °C. The inset in Fig. 14 shows the impedance measurements performed at the initial and steady states. The lithium ion transference number of the

SPE was estimated by using Evans et al.'s equation[36] that combines the d.c. polarization and a.c. impedance techniques. The poly(VDF-*co*-MAF-cyCB) electrolyte displays a high t_{Li^+} of 0.68 at 40 °C compared to the t_{Li^+} values reported for PEO-based SPEs.[30,33,34] This can be explained by a weaker interaction of lithium ions with cyCB units compared to the PEO matrix which displays coordinating feature. Moreover, the high dielectric constant anticipated for the MAF-cyCB matrix allows efficient dissociation and solubilisation of the ions, further enhancing the transport of lithium ions. Finally, the nano-structured morphology of the investigated poly(VDF-*co*-MAF-cyCB)/$LiClO_4$ SPE could also promote ion diffusion in the amorphous phase, as discussed above.

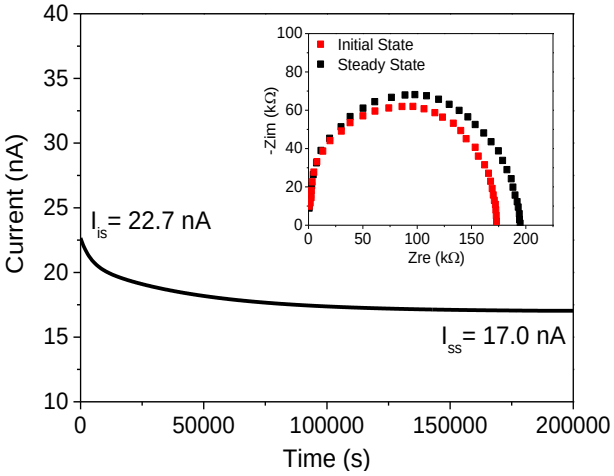

Figure 14. Time-dependence response of dc polarization for a Li|poly(VDF-*co*-MAF-cyCB)/$LiClO_4$|Li symmetric cell configuration at an applied d.c. bias of 10 mV and at 40 °C. The inset shows the impedance spectra of the initial and steady states of the cell with a.c. bias of 10 mV (cyCB/Li^+ = 5).

4.8 Conclusion

In this chapter, we have disclosed a novel fluorinated copolymer bearing cyclic carbonate pendant groups that fulfils the criteria to be used as solid polymer electrolyte after loading with a lithium salt. The interesting features of this system are triggered by the microphase separation between crystalline PVDF and amorphous poly(VDF-*co*-MAF-cyCB) nano-domains. Indeed, the presence of reinforcing crystalline PVDF nano-domains brings decent thermal and mechanical properties with moduli values ranging between 10^5 and 10^6 Pa. The addition of $LiClO_4$ further enhances the mechanical properties up 10^7 Pa at 10^2 rad/s for a poly(VDF-*co*-MAF-cyCB) copolymer with a cyCB/Li^+ ratio of 5. These high shear rates moduli, which are typically observed for elastic solid materials, could mitigate or even prevent the formation of lithium dendrites into batteries. Moreover, the added $LiClO_4$ dissolved in the amorphous poly(VDF-*co*-MAF-cyCB) phase leads to excellent ionic conductivity values. Indeed, amorphous PVDF is known for its ability to dissolve lithium salts. Similarly, the MAF-cyCB counterpart is also capable to dissociate large amounts of lithium salt because of the high dielectric constant of cyclic carbonate unit. The localization of cyclic carbonate moiety as a pendant group to the polymer backbone imparts a good mobility to the system. These positive features are also reflected in the rather high lithium ion transference numbers (0.68 obtained at 40 °C). Unfortunately, the use of $LiClO_4$ salts allows the studied SPE to display a low electrochemical stability window ranging (from 1.4 V to 4.9 V vs Li/Li^+), due to its instability with lithium foil anode. It should be also noted that the addition of salts above a critical threshold leads to the probable formation of ionic clusters inducing a detrimental effect on the mechanical properties as well as on the ionic conductivity features. On the basis of these observations, we believe that poly(VDF-*co*-MAF-cyCB) SPEs are valuable and promising candidates for further use in all-solid-state batteries.

4.9 Experimental section

- Materials

All reagents were used as received unless stated otherwise. 2-Trifluoromethyl acrylic acid (MAF) and vinylidene fluoride (VDF) were kindly offered by Tosoh F-Tech Company and Arkema, respectively. *Tert*-amyl peroxy-2-ethylhexanoate (TAPE, purity 95%) was supplied from AkzoNobel. Glycerol 1,2-carbonate (purity > 90%) was acquired from TCI Europe N.V. ReagentPlus grade dimethyl carbonate (DMC, purity > 99%), dichloromethane (DCM), pyridine, thionyl chloride, laboratory reagent grade methanol and lithium perchlorate ($LiClO_4$, battery grade, 99.99%) were purchased from Sigma-Aldrich. Deuterated chloroform ($CDCl_3$) and dimethyl sulfoxide (DMSO-d_6), used for NMR spectroscopy, were purchased from Eurisotop (purity > 99.8%).

- Instrumentation

Nuclear magnetic resonance (NMR). The compositions and microstructures of the copolymer were determined by ^{1}H and ^{19}F NMR spectroscopy, recorded on a Bruker AC 400 Spectrometer (400 MHz for ^{1}H and 376 MHz for ^{19}F) using DMSO-d_6 or $CDCl_3$ as solvents. Coupling constants and chemical shifts are given in Hertz (Hz) and parts per million (ppm), respectively. The experimental conditions for recording 1H [or 19F] NMR spectra were as follows: flip angle 90 ° [or 30 °], acquisition time 4.5 s [or 0.7 s], pulse delay 2 s [or 5 s], number of scans 32 [or 64], and a pulse width of 5 µs for ^{19}F NMR.

Size exclusion chromatography (SEC). Molecular weight (Mn) and dispersity (Đ) were assessed from size exclusion chromatography (SEC) with triple-detection GPC from Agilent Technologies using a PL0390-0605390 LC light scattering detector with two diffusion angles (15° and 90°), a PL0390-06034 capillary viscometer, and a 390-LC PL0390-0601 refractive index detector and two PL1113-6300 ResiPore 300 × 7.5 mm columns. DMF (containing 0.1 wt % of LiCl) was used as the eluent at a flow rate of 0.8 mL/min and toluene as the flow-

marker. The entire SEC-HPLC system was thermostated at 35 °C. Poly(methyl methacrylate) standards were used for calibrating the SEC instrument and the results were processed using the corresponding Agilent software.

Electrolyte film preparation. The thick electrolyte films were prepared as follows: The poly(VDF-co-MAF-cyCB) was dissolved in acetone (30 wt%) with different molar ratios of LiClO4. Acetone was slowly evaporated at 40 °C. The samples were casted on stainless steel electrodes and dried again overnight in vacuo at 40 °C. The thickness was kept constant with a 270 µm thick PTFE spacer between two stainless steel electrodes into the Swagelok cell.

Differential scanning calorimetry (DSC). DSC measurements were carried out using a Mettler Toledo 822e calorimeter. The samples were analyzed under nitrogen atmosphere in a 40 µL Al pan with an empty Al pan as reference cell. In order to erase their thermal history, the samples were initially heated from 25 °C to 200 °C and cooled down from 200 °C to -120 °C at a heating and a cooling rate of 10 °C/min. The temperature was maintained for 2 min before changing cycle. The samples were then heated from -120 °C to 200 °C at the same heating rate to determine the glass transition temperature (T_g), the melting temperature (T_m) and the melting enthalpy (ΔH_m) using the Stare software.

Atomic force microscopy (AFM). AFM was performed on a multimode scanning probe microscope (Bruker Multimode Nanoscope VIII). AFM imaging was operated in tapping mode using NCL cantilevers (Si, 48 N/m, 276 kHz, Nanosensors) at a scan rate of 1 Hz. The images were processed by Bruker Nanoscope Analysis software. Silicon wafers were washed with acetone and milli-Q water before treated with piranha solution, rinsed in milli-Q water and dried by spin-coating at 2000 rpm. A copolymer solution at 1 wt. % in NMP was spin-coated onto silicon substrates of 1 cm² at rotation rates of 500 rpm, 1000 rpm then 2000 rpm, respectively.

Rheology. Rheological experiments were performed on a MCR 301 (Anton Paar, Germany) rheometer equipped with a convection oven operating under air. Measurements were conducted using 4 mm stainless steel parallel plate geometry. Oscillatory shear measurements

were carried out in linear regime with a strain amplitude γ of 0.03 %. The gap was adjusted between 400 and 550 μm and the temperature was fixed at 25 °C.

Electrochemical impedance spectroscopy (EIS). EIS measurements were performed using a Parstat 4000 apparatus over a frequency range of 1 MHz to 10 mHz and with an amplitude a.c. excitation voltage of 5 mV. The temperature dependence measurements were carried out from 25 °C to 80 °C by gradually increasing the temperature by steps of 10 °C with an equilibration time of 1 h between each step.

Electrochemical stability. The electrochemical stability window was determined on an Arbin Instrument battery tester BT-2043 by the method of the linear voltammetry. The polymer electrolyte (≈ 270 μm) was sandwiched between a stainless steel working electrode and a lithium foil as counter and reference electrode. The Swagelok cell was assembled in an argon glove box and cycled from 0.5 V to 6 V vs. Li/Li^+ at scan rate of 0.5 mV/s.

Transference number. Those measurements were carried out using Li|solid-polymer-electrolyte|Li symmetric cells, thermally equilibrated in oven at the desired temperature for 24 h before measurement. The d.c. polarization measurements were performed on an Arbin Instrument battery tester BT-2043 with a d.c. bias of 10 mV. The EIS measurements were performed on Parstat 4000 with an a.c. bias of 10 mV.

- Synthesis

Synthesis of (2-oxo-1,3-dioxolan-4-yl)methyl 2-(trifluoromethyl)acrylate (MAF-cyCB). 2-Trifluoromethyl acrylic acid (MAF) was converted into 2-(trifluoromethyl)acryloyl chloride (MAF-COCl) using thionyl chloride following a procedure reported elsewhere.[37] Glycerol 1,2-carbonate (25.27 g, 214 mmol) and pyridine (19.0 mL, 235 mmol) were added to dichloromethane (40.0 mL) in a two-necked round bottomed flask equipped with a dropping funnel. The mixture was then cooled to -10 °C in an ice-salt bath while being purged under nitrogen atmosphere for at least 20 min. MAF-COCl (33.96 g, 214 mmol) was transferred to the dropping funnel under N_2 atmosphere

and added slowly into the reaction mixture (over the course of 30 min) while maintaining the flask temperature at -10 °C for another 2 h and finally at room temperature for additional 16 h. After that, the reaction was quenched by adding 8 mL of methanol. The reaction mixture was then washed three times with 40 mL of diluted HCl, once with saturated $NaHCO_3$ solution (until neutral pH) and finally with water. The organic layers were collected and dried over $MgSO_4$, filtered and the solvent was removed under vacuum. MAF-cyCB, obtained in 55% overall yield from MAF as a brownish viscous liquid, was characterized by ^1H and ^{19}F NMR spectroscopy.

^1H NMR (400 MHz, $CDCl_3$, δ ppm, Fig. 15): 3.74 and 4.54 (2m, 2H, $-O-CH_2-CH(O)-C\underline{\mathbf{H}}_2-O-$); 4.29 (m, 2H, $-O-C\underline{\mathbf{H}}_2-CH(O)-CH_2-O-$); 4.96 (m, 1H, $-O-CH_2-C\underline{\mathbf{H}}(O)-CH_2-O-$); 6.47 and 6.72 (2 s, 2H, $\underline{\mathbf{H}}_2C=C(CF_3)(CO_2CH_2-)$.

^{19}F NMR (376 MHz, $CDCl_3$, δ ppm): peak centered at -65.82 (singlet, $-C\underline{\mathbf{F}}_3$).[38,20]

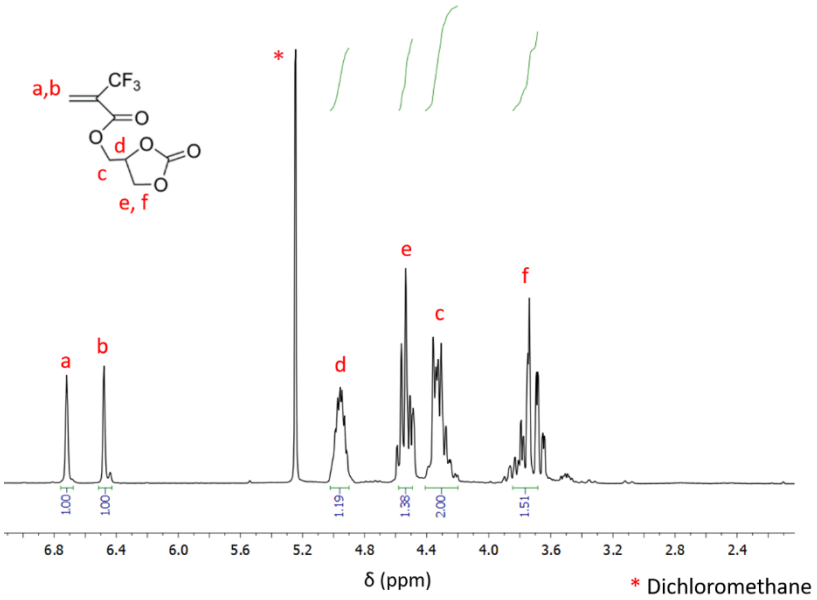

Figure 15. ^1H NMR spectrum of MAF-cyCB (in $CDCl_3$ at 20 °C).

Radical copolymerization of VDF with MAF-cyCB.[37] The copolymerization of VDF with MAF-cyCB was performed in a 100 mL Hastelloy autoclave Parr system (HC 276) equipped with a Bourdon pressure gauge, a mechanical Hastelloy anchor, a rupture disk (3000 PSI), inlet and outlet valves and a Parr electronic controller (for stirring speed and heating control). A solution of TAPE (0.72 g, 3.12 mmol) and MAF-cyCB (5.00 g, 20.83 mmol) prepared in DMC (70 mL) was degassed by N_2 bubbling for 30 min. Before starting the reaction, the autoclave was pressurized with 30 bars of nitrogen to check for any leaks. It was then put under vacuum (40×10^{-3} bar) for 30 min to remove any residual traces of oxygen. The solution was transferred into the autoclave under vacuum through a funnel tightly connected to the introduction valve of the autoclave. The reactor was then cooled in a liquid nitrogen bath, and VDF gas (12 g, 187.5 mmol) was transferred into it under weight control. After this, the vessel was stirred mechanically and gradually heated up to 74 °C, the evolutions of pressure (P_{max} = 37 bar) and temperature being recorded. The reaction was stopped after 16 h (the pressure dropped to 22 bar) by placing the autoclave in an ice bath. The unreacted gaseous monomer was purged off. Then, the autoclave was opened, the solvent and unreacted liquid monomer (if there was any) were completely removed under vacuum. The crude product was then dissolved in acetone and precipitated from cold pentane, centrifuged, and then dried under vacuum (20×10^{-3} bar, 50 °C) for 16 h. The yield of the polymerization was determined by gravimetry (mass of the copolymer obtained/mass of monomers introduced in the reactor) (yield = 60%). The poly(VDF-*co*-MAF-cyCB) copolymer, as a brownish soft material, was characterized by ^{1}H and ^{19}F NMR spectroscopy. The molar fractions of VDF base units in the copolymer were determined from equation (1):

$$mol\%\ VDF = \frac{(\int_{-91}^{-96} CF_2 + \int_{-113}^{-118} CF_2)/2}{(\int_{-91}^{-96} CF_2 + \int_{-113}^{-118} CF_2)/2 + \int_{-66}^{-71} CF_3/3} \times 100 \qquad (1)$$

^{1}H NMR (400 MHz, DMSO-d_6, δ ppm, Fig. 16): 2.15 to 2.40 (m, −$CF_2C\underline{H}_2$−$C\underline{H}_2CF_2$− reverse VDF−VDF tail-to-tail (T-T) dyad addition); 2.70 to 3.20 (m, −$C\underline{H}_2CF_2$−$C\underline{H}_2CF_2$−, normal VDF−VDF head-to-tail (H-T) dyad addition), 2.80 (-$C\underline{H}_2C(CF_3)(CO_2CH_2)$ of MAF-cyCB); 3.73 and 4.60 (2m, 2H, −O−CH_2−CH(O)−$C\underline{H}_2$−O−); 4.30 (m, 2H, −O− O−$C\underline{H}_2$−CH(O)−CH_2−O−); 5.07 (m, 1H, −O−CH_2−$C\underline{H}$(O)−CH_2−O−); 6.05 to 6.45 (small tt, $^{2}J_{HF}$ = 55 Hz , $^{3}J_{HH}$= 4.6 Hz), −CH_2CF_2−$\underline{H}$ end-group originated from the transfer (to solvent or polymer) or from backbiting reaction.[39,40]

^{19}F NMR (376 MHz, DMSO-d_6, δ ppm, Fig. 17): -66 (-$C\underline{F}_3$ of MAF-cyCB in the copolymer), -91.5 to -93 (−$CH_2C\underline{F}_2$−$CH_2C\underline{F}_2$−normal VDF−VDF H-T dyad addition); -93.5 to -95.5 (–$C\underline{F}_2$ of VDF in the alternating VDF–MAF-cyCB dyad); -113.2 (−$CH_2C\underline{F}_2$−CF_2CH_2−CH_2, reverse VDF−VDF H-H dyad addition); -114.8 (dtt, $^{2}J_{HF}$ = 55 Hz, $^{3}J_{HF}$ = 16 Hz and $^{4}J_{FF}$ = 6 Hz, CF_2-$CH_2C\underline{F}_2$-H, chain-end from transfer); -116.5 (−CH_2CF_2−$C\underline{F}_2CH_2$−CH_2, reverse VDF−VDF H-H dyad addition).

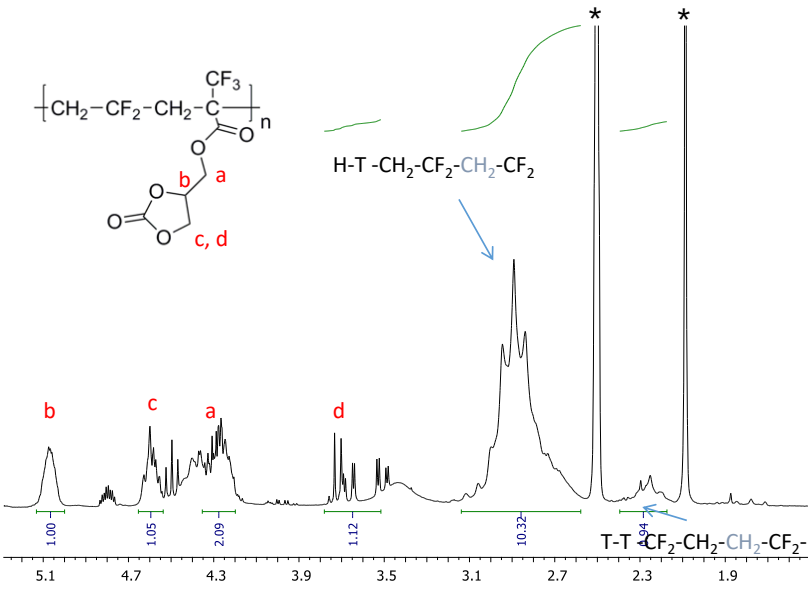

Figure 16. ^{1}H NMR spectrum of poly(VDF-*co*-MAF-cyCB) copolymer (in DMSO-d_6 at 20 °C). *Solvent DMSO signals.

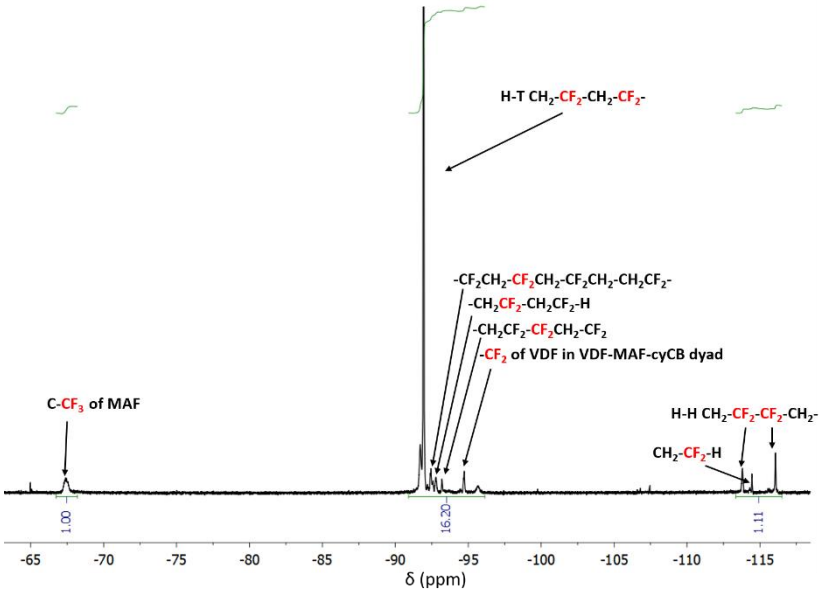

Figure 17. ^{1}H NMR spectrum of MAF-cyCB (in $CDCl_3$ at 20 °C).

Bibliography

1 M. Armand and J. M. Tarascon, *Nature*, 2008, **451**, 652–657.
2 A. Vlad, N. Singh, J. Rolland, S. Melinte, P. M. Ajayan and J. F. Gohy, *Sci. Rep.*, 2014, **4**, 1–7.
3 J. Kim, J. H. Kim and K. Ariga, *Joule*, 2017, **1**, 739–768.
4 J. M. Tarascon and M. Armand, *Nature*, 2001, **414**, 359–367.
5 W. Xu, J. Wang, F. Ding, X. Chen, E. Nasybulin, Y. Zhang and J. G. Zhang, *Energy Environ. Sci*, 2014, **7**, 513–537.
6 M. D. Tikekar, S. Choudhury, Z. Tu and L. A. Archer, *Nat. Energy*, 2016, **1**, 1–7.
7 A. Mauger, M. Armand, C. M. Julien and K. Zaghib, *J. Power Sources*, 2017, **353**, 333–342.
8 J. Janek and W. G. Zeier, *Nat. Energy*, 2016, **1**, 1–4.
9 C. Sun, J. Liu, Y. Gong, D. P. Wilkinson and J. Zhang, *Nano Energy*, 2017, **33**, 363–386.
10 A. Hayashi, K. Noi, A. Sakuda and M. Tatsumisago, *Nat. Commun.*, 2012, **3**, 855–856.
11 Y. Hu and X. Sun, *J. Mater. Chem. A*, 2014, **2**, 10712–10738.
12 A. V. and J.-F. G. J. Rolland, J. Brassinne, J.-P. Bourgeois, E. Poggi, *J. Mater. Chem. A*, 2014, **2**, 11839–11846.
13 W. H. Meyer, *Adv. Mater.*, 1998, **10**, 439–448.
14 S. Zekoll, C. Marriner-Edwards, A. K. O. Hekselman, J. Kasemchainan, C. Kuss, D. E. J. Armstrong, D. Cai, R. J. Wallace, F. H. Richter, J. H. J. Thijssen and P. G. Bruce, *Energy Environ. Sci.*, 2018, **11**, 185–201.
15 J. M. Tarascon, A. S. Gozdz, C. Schmutz, F. Shokoohi and P. C. Warren, *Solid State Ionics*, 1996, **86**–**88**, 49–54.
16 A. M. Stephan, *Eur. Polym. J.*, 2006, **42**, 21–42.
17 S. Ramesh and S. C. Lu, *J. Mol. Struct.*, 2011, **994**, 403–409.
18 S. Ramesh and S. C. Lu, *J. Mol. Liq.*, 2013, **177**, 73–77.
19 E. Cznotka, S. Jeschke, M. Grünebaum and H. D. Wiemhöfer, *Solid State Ionics*, 2016, **292**, 45–51.
20 A. Alaaeddine, J. Vergnaud, J. Rolland, A. Vlad, J.-F. Gohy and B. Ameduri, *Polym. Chem.*, 2015, **6**, 6021–6028.
21 J. Mindemark, M. J. Lacey, T. Bowden and D. Brandell, *Prog. Polym. Sci.*, 2018, **81**, 114–143.
22 K. Xu, *Chem. Rev.*, 2004, **104**, 4303–4417.

23 M. N. Wadekar, Y. R. Patil and B. Ameduri, *Macromolecules*, 2014, **47**, 13–25.

24 R. Souzy, B. Ameduri and B. Boutevin, *Macromol. Chem. Phys.*, 2004, **205**, 476–485.

25 S. Banerjee, V. Ladmiral, A. Debuigne, C. Detrembleur, S. M. W. Rahaman, R. Poli and B. Ameduri, *Macromol. Rapid Commun.*, 2017, **38**, 1–7.

26 T. Soulestin, P. Marcelino Dos Santos Filho, V. Ladmiral, T. Lannuzel, F. Domingues Dos Santos and B. Améduri, *Polym. Chem.*, 2017, **8**, 1017–1027.

27 K. Nakagawa and Y. Ishida, *J. Polym. Sci. Part A-2 Polym. Phys.*, 1973, **11**, 2153–2171.

28 P. Maccone, G. Brinati, V. Arcella, Maccone, G. Brinati and V. Arcella, *Polym. Eng. Sci.*, 2000, **40**, 761–767.

29 M. Benz and W. B. Euler, *J. Appl. Polym. Sci.*, 2003, **89**, 1093–1100.

30 E. Quartarone and P. Mustarelli, *Chem. Soc. Rev.*, 2011, **40**, 2525–2540.

31 S. B. Aziz, T. J. Woo, M. F. Z. Kadir and H. M. Ahmed, *J. Sci. Adv. Mater. Devices*, 2018, **3**, 1–17.

32 and J.-O. L. Pil-Ho Huh, Myung-Geun Choi, Nam Ju Jo, Jin-Kook Lee, *Macromol. Res.*, 2004, **12**, 422–426.

33 M. M. Hiller, M. Joost, H. J. Gores, S. Passerini and H. D. Wiemhöfer, *Electrochim. Acta*, 2013, **114**, 21–29.

34 K. Pożyczka, M. Marzantowicz, J. R. Dygas and F. Krok, *Electrochim. Acta*, 2017, **227**, 127–135.

35 X. J. Wang, H. S. Lee, H. Li, X. Q. Yang and X. J. Huang, *Electrochem. commun.*, 2010, **12**, 386–389.

36 J. Evans, C. A. Vincent and P. G. Bruce, *Polymer*, 1987, **28**, 2324–2328.

37 M. Wehbi, S. Banerjee, A. Mehdi, A. Alaaeddine, A. Hachem and B. Ameduri, *Macromolecules*, 2017, **50**, 9329–9339.

38 Y. Patil and B. Ameduri, *Prog. Polym. Sci.*, 2013, **38**, 703–739.

39 M. Pianca, E. Barchiesi, G. Esposto and S. Radice, *J. Fluor. Chem.*, 1999, **95**, 71–84.

40 S. Banerjee, M. Wehbi, A. Manseri, A. Mehdi, A. Alaaeddine, A. Hachem and B. Ameduri, *ACS Appl. Mater. Interfaces*, 2017, **9**, 6433–6443.

Chapter 5:
Solid polymer electrolytes based on cyclic carbonate acrylate and *n*-butyl acrylate-based copolymers

Table of contents

5.1 Introduction

Improvement of the ionic conductivity of solid polymer electrolytes (SPEs) is an important requirement for the development of safer, flexible and performant energy storage devices. Since poly(ethylene oxide) (PEO) mixed with lithium salts was reported as a promising solid polymer electrolyte, many studies have been realized on the nature and the design of ionically conducting polymers in order to improve the solubility of lithium salts in the polymer matrix and the mobility of lithium ions. In fact, the ion conduction not only depends strongly on the motions of polymer chains (or polymer chain segments) but also on the interactions between the units of the chains and the dissolved salts. For example, the segmental motion of PEO chains that allows the migration of ions, essentially takes place in amorphous regions and is hampered in crystalline domains. Moreover, the electro-donor oxygen atoms trap and coordinate Li^+ cations, inhibiting their displacement and increasing the glass transition temperature (T_g) of the polymer. As a result, solid-state batteries using PEO-based SPEs should be operated above the melting temperature of PEO, typically around 70 °C. Studies are thus being conducted to find alternatives to PEO.

The carbonate functional groups are known to present high dipolar moment and dielectric constant enabling them to dissociate many types of salts.[1] They are found especially as five-membered cyclic form in the composition of commercial liquid electrolytes as ethylene carbonate and propylene carbonate. Carbonates were thus introduced into polymeric architectures in order to provide polymer electrolytes as demonstrated by the early work of Tarascon and co-authors.[2] Contrary to the EO units, the carbonate units show a weak coordination with Li^+ ions.

On the basis of the recent literature, the polymers based on cyclic carbonates were only investigated as gel polymer electrolytes (GPEs) (*i.e.* with the presence of liquid electrolytes), whereas the polymer based on non-cyclic carbonates were investigated as SPEs. Chai et al[3] polymerized vinylene carbonate and obtained a polymer incorporating the cyclic carbonate function in the polymer backbone, reaching an ionic conductivity of 5×10^{-4} S/cm at ambient temperature, good mechanical properties and an electrochemical stability window up to

4.8 V vs Li^+/Li. Cyclic carbonates were also introduced as side-chains in polymer architectures as demonstrated by Lex-Balducci and coworkers[4,5] who copolymerized a cyclic carbonate methacrylate (CCMA) with oligo(ethylene glycol) methyl ether methacrylate (OEGMA) and further studied gel polymer electrolyte obtained by swelling the copolymer in a carbonate-based electrolyte. A non-cyclic poly(propylene carbonate) providing an ionic conductivity of 10^{-4} S/cm at ambient temperature was described by Zhang et al.[6] Tominaga's team reported[7,8] a non-cyclic poly(ethylene carbonate) (PEC) and further developed a hybrid membrane based on porous polyimide matrix, supporting a poly(ethylene carbonate)-based SPE reaching an ionic conductivity of 10^{-5} S/cm at 30 °C. They also proved that the non-cyclic PEC could act as a suitable SPE, exhibiting high lithium transference number (t_{Li+}) and high ionic conductivity that increases with the concentration of salts.

Unfortunately, polycarbonates have higher T_g than polyethers (such as PEO), generating low segmental motion of the chains, which is unfavorable for a good ionic conduction. Tominaga et al. developed[9] a copolymer composed of non-cyclic carbonate and ether units, which was obtained by polymerization of ethylene oxide with CO_2. The poly(EC-EO) presents a low T_g of 1°C, an ionic conductivity of 0.48 mS/cm and a lithium transference number reaching 0.66 at 60°C. They also prove that the presence of EC units prevented the complexation of Li^+ ions by EO units. Mecerreyes et al. synthesized[10] a series of poly(carbonate-ether) by polycondensation of PEO end-capped diol with dimethyl carbonate (DMC) and investigated the influence of the different content of EO units as well as the different content of LiTFSI salts. They found an optimum SPE exhibiting a high ionic conductivity of 3.7 x 10^{-5} S/cm with 30 wt. % of LiTFSI. Besides the presence of PEO groups, the addition of a low amount of LiTFSI salts (below 40 wt. %), decreases the T_g and breaks PEO crystallinity.

We have previously disclosed a semi-crystalline polymer electrolyte based on cyclic carbonate trifluoromethacrylate (MAF-cyCB) and vinylidene fluoride units, which exhibits a great ionic conductivity of 2 x 10^{-4} S/cm at 22°C. Here, the objective is to improve the ionic conductivity by playing with the flexibility of polymer chain electrolytes. In fact, we are assumed that increasing the flexibility of

chains could help the ions to move faster in the SPE. Thus, here we investigate SPEs based on linear amorphous poly(cyclic carbonate acrylate-*r*-*n*butyl acrylate) poly(cyCA-*r*-nBA) (Fig.1). The polymerization of these copolymers by reversible addition-fragmentation chain transfer (RAFT) is detailed below. Moreover, thermal, mechanical and ionic conductivity analyses are carried out in order to understand the effect of the polymer structure on the properties of the accordingly obtained SPEs. The rheology measurements were carried out by the Dr. Flanco Zhuge.

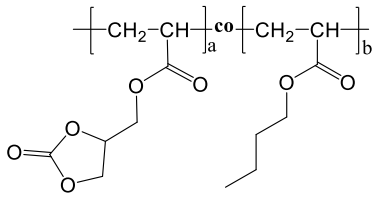

Figure 1. Structure of poly(cyCA-*co*-nBA)

5.2 Synthesis of the SPEs via RAFT polymerization

5.2.1 Synthesis of cyCA monomer

The (2-oxo-1,3-dioxolan-4-yl)methyl acrylate (cyCA) monomer was synthesized in one step (Fig. 2), according to the protocol of Yoshikawa et al.[11] The synthesis was achieved by esterification of 4-(hydroxymethyl)-1,3-dioxolan-2-one with acryloyl chloride, which was base-catalyzed with trimethylamine in dichloromethane. The cyCA monomer was yielded at 53%.

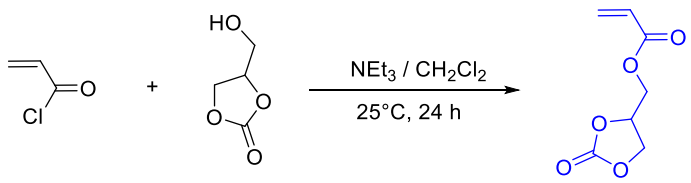

Figure 2. Synthesis of (2-oxo-1,3-dioxolan-4-yl)methyl acrylate monomer (cyCA).

5.2.2 Synthesis of the poly(cyCA) homopolymer

The cyCA was RAFT homopolymerized in order to be used as reference afterward. The polymerization was performed at 70°C in dimethyl sulfoxide (DMSO) at 1mol/L with 2-(dodecylthiocarbonothioylthio)-2-methylpropionic acid (DDMAT) as RAFT chain transfer agent (CTA) and α,α′-azoisobutyronitrile (AIBN) as initiator (Fig. 3). The CTA/initiator ratio was kept at 5.

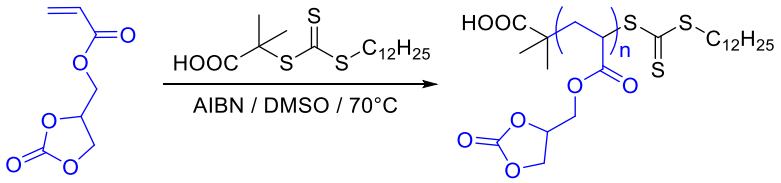

Figure 3. RAFT homopolymerization of (2-oxo-1,3-dioxolan-4-yl)methyl acrylate) [poly(cyCA)].

In order to study the kinetics of the polymerization, samples of the reaction medium were withdrawn and subjected to ^{1}H-NMR and SEC analyses. The initiation of the polymerization is slow and only 23% of conversion are reached after 45 min (Figs. 4 and 5). However, after 125 min of polymerization, the conversion reaches 82%, meaning a relatively fast propagation. Between 30 min and 125 min of polymerization, the evolution of $Ln[M]_0/[M]_t$ is linear with time, which demonstrates that the concentration of the active propagating species remains constant (Fig. 4). Therefore, this indicates that the termination reactions are very low or inexistent. Moreover, the evolution of the molar mass as a function of the conversion is linear, confirming the absence of transfer reactions (Fig. 5). Finally, the dispersity keeps narrow values between 1.10 and 1.13 during the polymerization (Fig. 5).

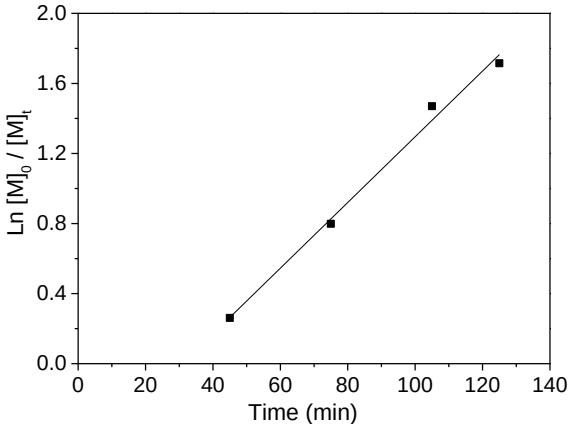

Figure 4. Dependence of $Ln[M]_0/[M]_t$ vs. time.

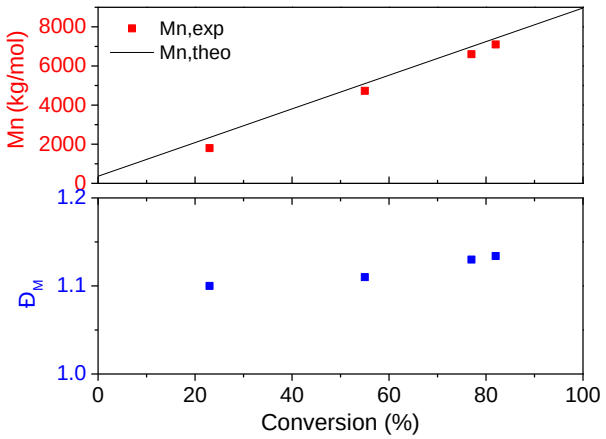

Figure 5. Dependence of M_n and of dispersity ($Đ_M$) vs. conversion.

These results are consistent with SEC curves observed as narrow mono-modal peaks (Fig. 6). The RAFT polymerization of (2-oxo-1,3-dioxolan-4-yl)methyl acrylate is thus considered as a controlled radical polymerization. In this study, the polymerization was stopped at 82% of conversion, yielding the desired $poly(cyCA)_{41}$ homopolymer (Fig. 7).

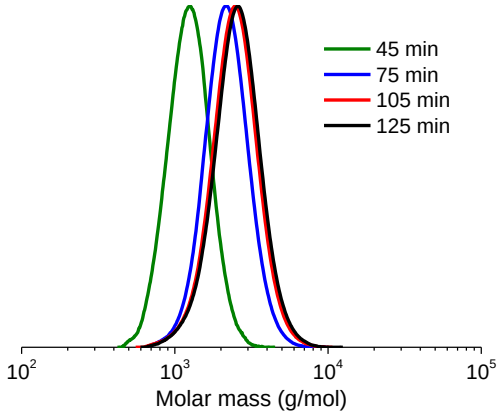

Figure 6. Evolution of the molar mass with polymerization time of poly(cyCA).

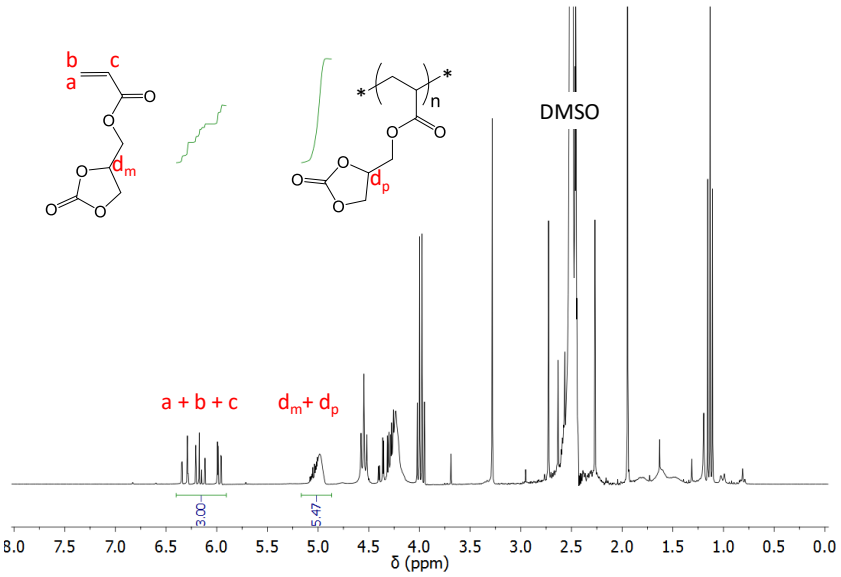

Figure 7. ^{1}H-NMR spectrum (300 MHz, DMSO-d_6, ppm) of the poly(cyCA)$_{41}$ homopolymer.

5.2.3 Synthesis of poly(cyCA$_n$-*r*-nBA$_m$) copolymers

Finally, cyCA was randomly copolymerized with n-butyl acrylate (nBA) (Fig. 8). The RAFT copolymerization was conducted under the same conditions and with the same reagents that for the poly(cyCA)$_{41}$ homopolymer (see above).

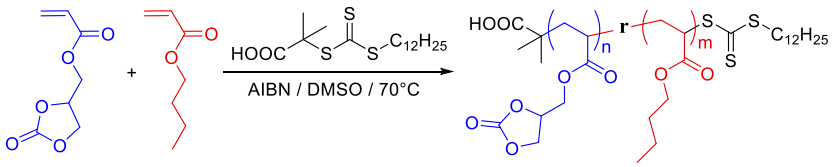

Figure 8. Synthesis of poly(2-oxo-1,3-dioxolan-4-yl)methyl acrylate -*r*- *n*butyl acrylate) via RAFT [poly(cyCA$_n$-*r*-nBA$_m$)].

Three different copolymers with various monomer compositions and various chain lengths were synthesized: poly(cyCA$_{19}$-*r*-nBA$_{35}$), poly(cyCA$_{37}$-*r*-nBA$_{20}$) and poly(cyCA$_{44}$-*r*-nBA$_{71}$), the numbers in subscripts representing the average degree of polymerization of the corresponding monomer as determined by ^{1}H-NMR. The SEC analyses (Fig. 9) show shifting of narrow mono-modal peaks toward higher molar mass, proving that copolymerization did take place. The evolution of molar mass obtained by SEC is in correlation with the trends obtained by NMR. Moreover, the poly(cyCA$_{19}$-*r*-nBA$_{35}$), poly(cyCA$_{37}$-*r*-nBA$_{20}$) and poly(cyCA$_{44}$-*r*-nBA$_{71}$) random copolymers display a dispersity (Đ) of 1.15, 1.18 and 1.23 respectively. We observe that the dispersity increases with the molar mass. In fact, it is possible that the RAFT copolymerization loses its control when high molar masses are targeted.

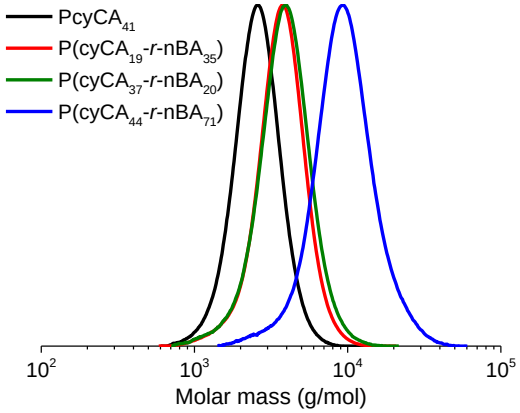

Figure 9. SEC curves superposition of homopolymer and copolymers based on cyCA.

5.2.4 Summary

To summarize, four polymers based on cyCA units were synthesized by RAFT and are reported in Table 1. The poly(cyCA)$_{41}$ homopolymer is used as reference with an average cyCA content of 100 wt. %. The three others are based on a mix of cyCA and nBA monomers. In order to study the influence of the composition in cyCA and nBA on ionic conductivity measurements, two copolymers were synthesized with a similar chain length but a different cyCA content. These are the poly(cyCA$_{19}$-*r*-nBA$_{35}$) and poly(cyCA$_{37}$-*r*-nBA$_{20}$) copolymers which present approximatively the same molar mass, 8200 and 8700 g/mol respectively. However, the poly(cyCA$_{19}$-*r*-nBA$_{35}$) has 42 wt% of cyCA, whereas the poly(cyCA$_{37}$-*r*-nBA$_{20}$) has 71 wt%. On the other hand, to observe the influence of the chain length, two other copolymers display similar cyCA content but different molar masses. In this respect, the poly(cyCA$_{44}$-*r*-nBA$_{71}$) copolymer is comprising 45 wt% of cyCA as the poly(cyCA$_{19}$-*r*-nBA$_{35}$), but it is ca. 2 times longer than the latter.

Sample	cyCA content (wt. %)	Mn,RMN (g/mol)	Đ
$P(cyCA)_{41}$	100	7400	1.13
$P(cyCA_{19}$-*r*-$nBA_{35})$	42	8200	1.15
$P(cyCA_{37}$-*r*-$nBA_{20})$	71	8700	1.18
$P(cyCA_{44}$-*r*-$nBA_{71})$	45	16900	1.24

Table 1. Characteristics of different cyCA based polymers synthesized via RAFT.

5.3 Thermal properties

The glass transition temperatures were measured using differential scanning calorimetry (DSC). The cyclic carbonate acrylate (cyCA) was used instead of cyclic carbonate methacrylate (cyCMA) because for a same chain length, the observed T_g is slightly reduced due to the absence of methyl group in the case of the acrylate. In fact, the T_g of the poly(cyCA) was measured at 68°C, whereas it was obtained at 74°C for the poly(cyCMA).

In the previous chapter, we demonstrated that the addition of salts influences the thermal, mechanical and conductivity properties of solid polymer electrolytes from a fluorinated copolymer bearing cyclic carbonate pendant groups. Here, the nature of the salt is investigated. Thus, DSC measurements were performed on $poly(cyCA)_{41}$ without salt and with two different added salts, $LiClO_4$ and LiTFSI (Fig. 10). These salts are mainly used as dopants by the scientific community in order to study solid polymer electrolytes properties. To be able to compare these results with those obtained in the previous chapter, the cyCA/Li^+ ratio was kept at 5 for both the used salts. We observe that the T_g varies with the addition of salt and that the nature of the anion plays an important role. More precisely, the use of LiTFSI leads to a decrease in the T_g from 68°C to 63°C, while $LiClO_4$ increases it to 81°C. The polymer chains are more mobile in the presence of LiTFSI than $LiClO_4$. Thus, only LiTFSI was considered thereafter.

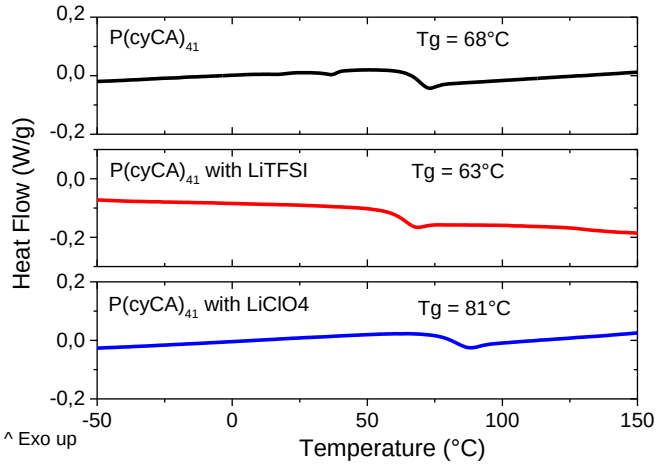

Figure 10. DSC thermograms of poly(cyCA)$_{41}$ without salt, with LiTFSI and with $LiClO_4$ (at cyCA/Li^+ ratio of 5).

The poly(nBA) homopolymer is characterized by a T_g of -54°C. Thus, the addition of nBA monomer sorely decreases the T_g of polymer (Fig. 11). The poly(cyCA$_{19}$-*r*-nBA$_{35}$), which has the same chain length than poly(cyCA$_{37}$-*r*-nBA$_{20}$), displays the lowest T_g. Therefore, the T_g of copolymers decreases from of 26°C to 1°C when the nBA content increases from 29 to 58 wt.%. These observations are in correlation with the fact that the chemical nature of the monomers as well as the composition of the copolymers influence the thermal properties of the materials. The chain length has only a slight impact on the T_g. Indeed, for the copolymers composed of *ca.* 43 wt. % of cyCA, such as poly(cyCA$_{19}$-*r*-nBA$_{35}$) and poly(cyCA$_{44}$-*r*-nBA$_{71}$), the T_g increases only of 5°C despite the chains are ca. 2 times longer for the latter sample.

The addition of LiTFSI (at cyCA/Li^+ molar ratio = 5) lowers the T_g of poly(cyCA$_{37}$-*r*-nBA$_{20}$) from 26°C to 3°C, while the T_g of poly(cyCA$_{19}$-*r*-nBA$_{35}$) increases from 1°C to 12°C. Thus, the presence of a larger cyCA content increases the free volume, allowing the polymer chain segments to move more. The chain length has still not a high impact on the T_g, because the T_g of poly(cyCA$_{44}$-*r*-nBA$_{71}$) increases insignificantly from 6° to 7°C in the presence of LiTFSI.

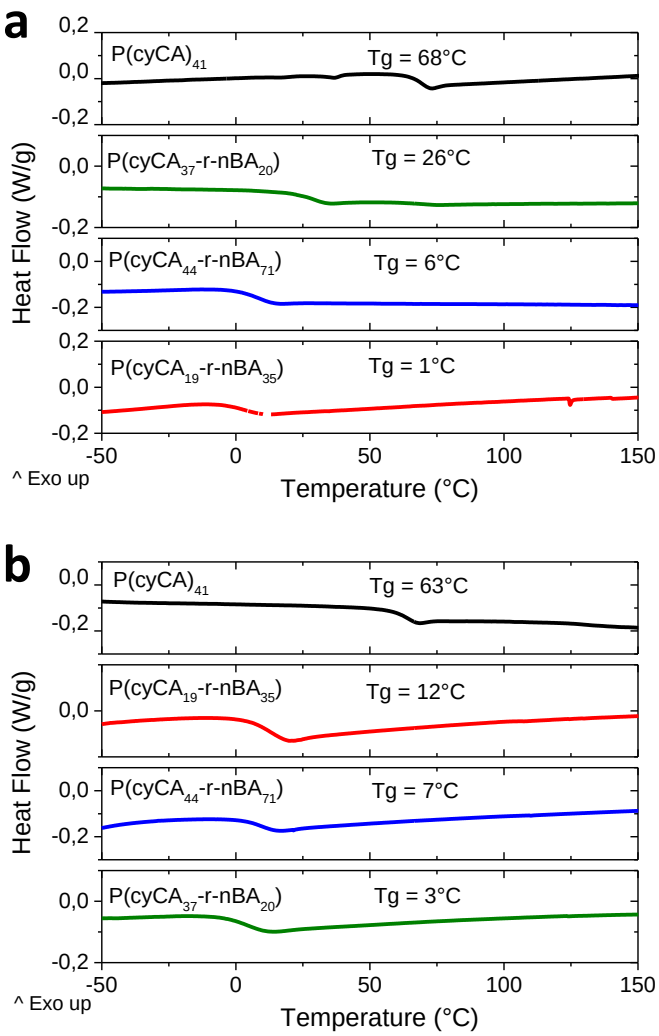

Figure 11. DSC thermograms of homopolymer and copolymers based on cyCA **(a)** without LiTFSI salt and **(b)** with LiTFSI salt (at cyCA/Li^+ molar ratio = 5).

5.4 Mechanical properties

To investigate the linear viscoelastic properties of copolymers containing LiTFSI, shear rheological experiments were performed. Fig. 12 shows the complex viscosity η* (Pa.s) versus angular frequency (rad/s) for the copolymers without and with LiTFSI (cyCA/Li^+ ratio = 5) at 30°C (*i.e.* above their T_g).

The η* of copolymer increases of one decade when the LiTFSI salt is added. Moreover, the flow of the materials is more pronounced with the presence of salts, when the angular frequency increases.

In presence of LiTFSI, at low shear frequency (*i.e.* below *ca.* 10^0 rad/s), the η* of poly(cyCA$_{19}$-*r*-nBA$_{35}$) and poly(cyCA$_{44}$-*r*-nBA$_{71}$) reaches constant values of $1.2x10^5$ and $1.6x10^5$ Pa.s, respectively, corresponding to the maximal resistance that the copolymers exhibit under low deformation. This means that the flow of these copolymers is at rest state because the shear rate approaches zero.[12] The zero shear viscosity of poly(cyCA$_{44}$-*r*-nBA$_{71}$) is higher than that of poly(cyCA$_{19}$-*r*-nBA$_{35}$). This result is in correlation with the fact that the molar mass is a structural parameter influencing the flow behavior of the copolymer. The zero shear viscosity of poly(cyCA$_{37}$-*r*-nBA$_{20}$) is still not observable in the measured angular frequency range. On the contrary, the η* increases toward infinity. Moreover, at a shear frequency of 10^{-2} rad/s, its η* is of $3.2x10^5$ Pa.s, which is higher than those of poly(cyCA$_{19}$-*r*-nBA$_{35}$) and poly(cyCA$_{44}$-*r*-nBA$_{71}$). This can indicate that poly(cyCA$_{37}$-*r*-nBA$_{20}$) has a firm texture compared to the other copolymers, which could be due to a high amount of Li^+-carbonate interactions. At high shear frequency, the three copolymers exhibit shear-thinning flow behavior. The flow of the poly(cyCA$_{37}$-*r*-nBA$_{20}$) is more important than the poly(cyCA$_{44}$-*r*-nBA$_{71}$), which is more important than the poly(cyCA$_{19}$-*r*-nBA$_{35}$). Therefore, the cyCA/Li^+ content has also an influence on the mechanical behavior of the copolymer, which is more important than the molecular weight.

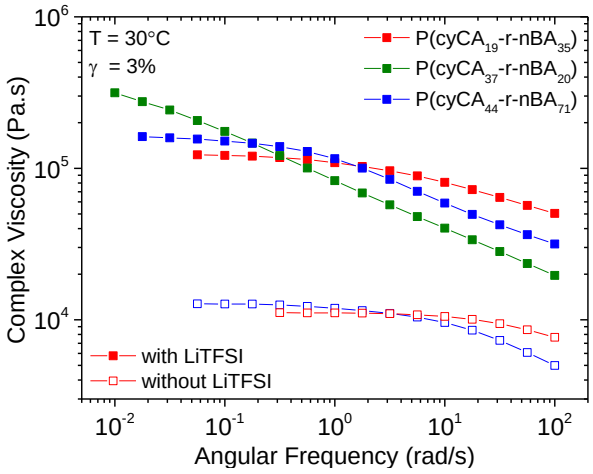

Figure 12. Complex viscosity η* (Pa.s) versus angular frequency (rad/s) for the copolymers with and without LiTFSI (cyCA/Li^+ molar ratio = 5) at 30°C.

5.5 Dependence of the ionic conductivity

All the copolymers mixed with salts at cyCA/Li^+ molar ratio of 5 were subjected to electrochemical impedance spectroscopy (EIS) in order to measure their ionic conductivity. To this aim, the samples were placed between two stainless steel electrodes and the ionic conductivity of samples was measured at various temperatures.

Fig. 13 shows the ionic conductivity versus temperature for three copolymers containing LiTFSI. The ionic conductivity of each copolymers decreases linearly with the inverse of temperature. Over the entire measuring temperature range (*i.e.* from 22°C to 80°C), the poly(cyCA$_{19}$-*r*-nBA$_{35}$) exhibits conductivity values higher than the poly(cyCA$_{44}$-*r*-nBA$_{71}$). At ambient temperature, they display respectively 4.2×10^{-6} S/cm and 8×10^{-8} S/cm. Thus, when the molar mass increases, the ionic conductivity decreases. Concerning the influence of the different amounts of cyCA and nBA units on the ionic conductivity, we hypothesize that the addition of a certain amount of nBA units does slightly increase the conductivity by lowering the T_g of the copolymer. In fact, nBA does not contribute directly to the conductivity because it constitutes as “dead” material due to its low

polarity. Unfortunately, this interpretation is not in correlation with the T_g values obtained for the copolymers loaded with LiTFSI. Although the poly(cyCA$_{37}$-*r*-nBA$_{20}$) and the poly(cyCA$_{19}$-*r*-nBA$_{35}$) contain respectively 71 wt. % and 42 wt. % of cyCA, their conductivities tend to a constant. Thus, as discussed in chapter 1 with the theory of Shi and Vincent, these observations would mean that the conductivity is influenced by the mobility of chains and that the amount of cyCA or nBA groups has no a big influence on the conductivity measurements.

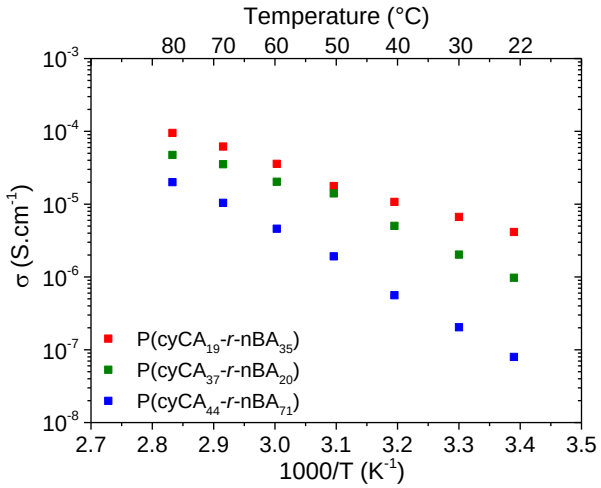

Figure 13. Ionic conductivity versus temperature for copolymers based on cyCA and nBA containing LiTFSI (cyCA/Li^+ ratio = 5).

5.6 Conclusion

In this chapter, we have prepared solid polymer electrolytes (SPEs) based on amorphous random copolymers, which contain cyclic ethylene carbonate (cyCA) and *n*-butyl acrylate (nBA) comonomers. They were easily obtained by controlled radical polymerization (*i.e.* RAFT). Moreover, we demonstrated that the difference in molar mass (*i.e.* Mn of 8200 and 16900 g/mol) of copolymers having the same cyCA and nBA contents, does not have a big influence on the flow behavior and the glass transition temperature (T_g) of the SPEs, maybe because of the small the gap between their Mn. However, this small gap is sufficient to influence the ionic conductivity measurements. Actually, in addition to the local movement of chains, the global movement of chains also affects the conductivity values. Conversely, we observe that the copolymer containing a high amount of cyCA groups exhibits firm texture in presence of salts. Unfortunately, whatever the amount of cyCA in the copolymer, the conductivity values remain approximately the same

5.7 Experimental section

- Materials

All reagents were used as received. Glycerol 1,2-carbonate (>90%) was bought from TCI. Triethylamine (TEA, ≥99 %) and α,α′-azoisobutyronitrile (AIBN, ≥98 %) were purchased from Acros Organics. Acryloyl chloride (≥97 %), *n*-butyl acrylate (nBA, ≥99 %), dimethyl sulfoxide (DMSO, ≥99 %), sodium bicarbonate ($NaHCO_3$, ≥99.7 %), sodium sulfate (Na_2SO_4, ≥99.5 %), lithium perchlorate ($LiClO_4$, battery grade, ≥99.99 %), bis(trifluoromethane)sulfonimide lithium salt (LiTFSI, ≥99.95 %), and 2-dodecylthiocarbonothioylthio-2-methylpropionic acid (DDMAT, ≥98 %) were purchased from Sigma-Aldrich. Dimethyl sulfoxide (DMSO-d_6, >99.8%), used for NMR spectroscopy, was purchased from Euriso-top.

- Instrumentation

Nuclear magnetic resonance (NMR). ^{1}H and ^{13}C NMR spectra were acquired on a Bruker Avance II spectrometer (300MHz or 500 MHz) using DMSO-d_6 as solvent.

Size exclusion chromatography (SEC). Average molar masses (Mn and Mw) and dispersities (Đ) were measured on an Agilent size exclusion chromatography (SEC) system equipped with an Agilent 1200 pump; an Agilent differential refractometer and two PSS Gram columns (1000 and 100 Å). *N*,*N*-dimethylformamide containing 2.5 mM of NH_4PF_6 was used as eluent thermostated at 35 °C with a flow rate of 1 mL/min. The calibration was performed using poly(ethylene glycol) standards. Thus, the M_n, M_w and $Đ$ are in polystyrene equivalent.

Differential scanning calorimetry. DSC measurements were carried out using a Mettler Toledo 822e calorimeter. The samples were analyzed under nitrogen atmosphere in a 40 µL Al pan with an empty Al pan as reference cell. The samples were firstly heated from 25 °C to 200 °C and cooled down from 200 °C to -120 °C at a heating rate of 10 °C/min. The temperature was maintained for 2 min before changing cycle. The samples were then heated from -120 °C to 200 °C at the same heating rate to determine the glass transition temperature (Tg) using the Stare software.

Rheology. Rheological experiments were performed on an Ares (TA Instruments) rheometer equipped with an air/nitrogen convection oven that ensures an accurate temperature control (± 0.1°C). Dynamic mechanical measurements were carried out at given temperatures, using stainless steel 8 mm cone−plate geometries. The cone geometry has an angle of 0.1 rad and a truncation of 31 µm. The sample was equilibrated in the rheometer at 80°C for 30 min. Dynamic frequency sweeps were performed at a deformation amplitude of 3% at 30°C under nitrogen atmosphere and a frequency range of 100 – 0.01 rad/s. All dynamic measurements were performed within the linear viscoelastic region, which was determined from dynamic strain sweep experiments. The equilibration was checked with dynamic time sweep measurements up to 30 min. Normal forces were checked to be relaxed prior any measurement.

Electrolyte film preparation. The thick electrolyte films were prepared as follows: The poly(cyCA-*r*-nBA) and LiTFSI salt were dissolved in acetonitrile. This latter was removed under reduced pressure following by the vacuum at 70°C overnight. The viscous samples were casted on stainless steel electrodes. The thickness was kept constant with a 270 µm thick PTFE spacer placed between two stainless steel electrodes into the Swagelok cell.

Electrochemical impedance spectroscopy. EIS measurements were performed using a Parstat 4000 apparatus over a frequency range of 1 MHz to 10 mHz and with an amplitude a.c. excitation voltage of 5 mV. The temperature dependence measurements were carried out from 22 °C to 40 °C by gradually increasing the temperature by steps of 10 °C with an equilibration time of ca. 1 h between each step.

- Synthesis

Synthesis of (2-oxo-1,3-dioxolan-4-yl)methyl acrylate (cyclic carbonate acrylate or cyCA).[11] Into a 250 mL round-bottom flask, glycerol 1,2-carbonate (10.0 g, 84.68 mmol) and triethylamine (8.74 g, 86.33 mmol) were dissolved in anhydrous DCM (60 mL) and cooled at 0°C under argon atmosphere. A solution of acryloyl chloride (5.11 g, 56.45mmol) in dichloromethane (12.0 mL) was added dropwise into the flask and the mixture was left at 0°C during 1h before reaching the ambient temperature. After 24 h, the mixture was filtered and then washed with 5 % aqueous $NaHCO_3$ followed by distilled water. The organic phase was dried over Na_2SO_4 and the DCM was removed under reduced pressure. After purification by silica gel column chromatography (hexane: ethyl acetate, 3:2) the product was isolated as a colorless liquid (8.43 g, 53 %).
^{1}H-NMR (300 MHz, $CDCl_3$) δ (ppm): 6.35 (dd, 1H, -HC=C**H**H), 6.05 (dd, 1H, -**H**C=CH_2), 5.84 (dd, 1H, -HC=CH**H**), 4.90 (m, 1H, -O-(CH_2)C**H**-CH_2-), 4.52 (t, 1H, -O-C**H**H-CH-), 4.30 (m, 3H, -O-CH**H**-CH- and -CH-C**H_2**-O-).
^{13}C-NMR (300 MHz, CDCl3) δ (ppm):165.3 (1C, -HC-**C**O-O-), 154.5 (1C, -O-**C**O-O-), 132.3 (1C, **C**H_2=CH-), 127.1 (1C, CH_2=**C**H-CO-), 73.9 (1C, -O-(CH_2)**C**H-CH_2-), 66.0 (1C, O-**C**H_2-CH-), 63.1 (1C, -CH-**C**H_2-O).

Homopolymerization of 2-oxo-1,3-dioxolan-4-yl)methyl acrylate [**poly(cyCA]**. In a 25 mL flask CCA (2000 mg, 11.62 mmol, 50 eq.), AIBN (8 mg, 0.05 mmol, 0.2 eq.) and DDMAT (85 mg, 0.23 mmol, 1 eq.) were dissolved in DMSO (11.6 mL). The mixture was purged with argon for 30 minutes and immersed in a preheated oil bath at 70°C. After 125 minutes, the reaction was stopped by cooling in liquid nitrogen and by exposing to air. The polymer was precipitated in ethanol, filtered and washed with ethanol to obtain poly($cyCA)_{31}$. To determine the final conversion and the dispersity, the analysis was performed by GPC and ^{1}H-NMR (in DMSO-d_6).

Typical procedure for the synthesis of poly(2-oxo-1,3-dioxolan-4-yl)methyl acrylate -r- n butyl acrylate) [poly(cyCA$_{37}$-*r*-nBA$_{20}$)]. In a 50 mL flask (2-oxo-1,3-dioxolan-4-yl)methyl acrylate (2000 mg, 11.62 mmol, 50 eq.), n-butyl acrylate (2000 mg, 4.64 mmol, 20 eq.), AIBN (8 mg, 0.05 mmol, 0.2 eq.) and DDMAT (85 mg, 0.23 mmol, 1 eq.) were dissolved in DMSO (16.2 mL). The mixture was purged with argon for 30 minutes and immersed in a preheated oil bath at 70°C. After 90 minutes, the reaction was stopped by cooling with liquid nitrogen following by exposure to air. The polymer was precipitated in water, filtered and washed with water and methanol. To determine the final conversion and the dispersity, the analysis was performed by GPC and ^{1}H-NMR (in DMSO-d$_6$). Poly(cyCA$_{19}$-*r*-nBA$_{35}$), poly(cyCA$_{37}$-*r*-nBA$_{20}$) and poly(cyCA$_{44}$-*r*-nBA$_{71}$) were obtained by using [cyCA]/[nBA]/[DDMAT] ratio equal to 30/40/1, 50/20/1 and 60/80/1 respectively.

Bibliography

1 K. Xu, *Chem. Rev.*, 2004, **104**, 4303.

2 J. H. Golden, B. G. M. Chew, D. B. Zax, F. J. DiSalvo, J. M. J. Fréchet and J. M. Tarascon, *Macromolecules*, 1995, **28**, 3468–3470.

3 J. Chai, Z. Liu, J. Zhang, J. Sun, Z. Tian, Y. Ji, K. Tang, X. Zhou and G. Cui, *ACS Appl. Mater. Interfaces*, 2017, **9**, 17897–17905.

4 S. D. Tillmann, P. Isken and A. Lex-Balducci, *J. Power Sources*, 2014, **271**, 239–244.

5 S. D. Tillmann, P. Isken and A. Lex-Balducci, *J. Phys. Chem. C*, 2015, **119**, 14873–14878.

6 J. Zhang, J. Zhao, L. Yue, Q. Wang, J. Chai, Z. Liu, X. Zhou, H. Li, Y. Guo, G. Cui and L. Chen, *Adv. Energy Mater.*, 2015, **5**, 1–10.

7 K. Kimura, M. Yajima and Y. Tominaga, *Electrochem. commun.*, 2016, **66**, 46–48.

8 Y. Tominaga, V. Nanthana and D. Tohyama, *Polym. J.*, 2012, **44**, 1155–1158.

9 T. Morioka, K. Nakano and Y. Tominaga, *Macromol. Rapid Commun.*, 2017, **38**, 1–5.

10 L. Meabe, T. V. Huynh, N. Lago, H. Sardon, C. Li, L. A. O'Dell, M. Armand, M. Forsyth and D. Mecerreyes, *Electrochim. Acta*, 2018, **264**, 367–375.

11 M. Yoshikawa, N. Hotta, J. Kyoumura, Y. Osagawa and T. Aoki, *Sensors Actuators B Chem.*, 2005, **104**, 282–288.

12 M. Pahl, H. M. Laun and W. Gleissle, *Praktische Rheologie der Kunststoffe und Elastomere*, Düsseldorf, VDI., 1995.

Chapter 6:
Redox-active polymer based nano-objects via polymerization induced self-assembly

Table of contents

6.1 Introduction

Flow-assisted electrochemical systems (FAES) are receiving increasing interest because of their application in various systems including redox flow battery (RFB),[1,2] electrochemical flow capacitor (EFC)[3] and semi-solid flow battery (SSFB).[4] Typically, those systems are used for (grid) energy storage, water deionization, and wastewater treatment. For this type of electrochemical systems, the active species are stored in solution in external tanks and pumped through the main cell to fuel it continuously, thereby generating the energy (Fig. 1). While the energy density is related to the size of the tanks, the power density is determined by the composition of electrodes. The suspension electrodes are called catholytes or anolytes and are composed between 5 and 20 wt. % of active storing material, contrary to the electrode films used in batteries for which the composition is greater than 80 wt. %.[5]

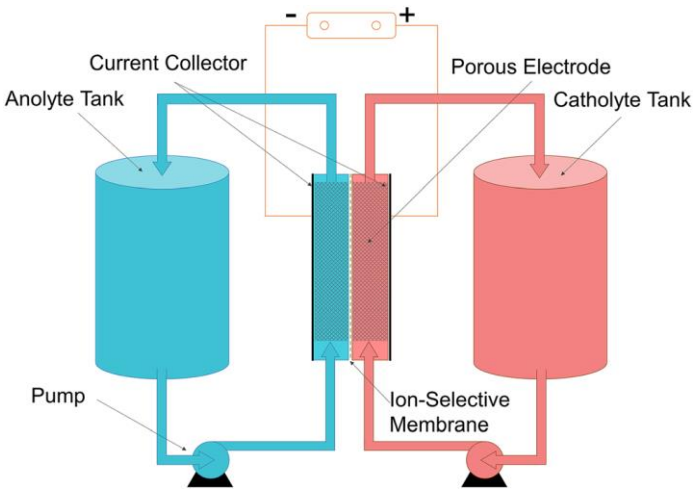

Figure 1. Schematic illustration of a redox flow battery.[6]

Among the different materials used for the preparation of suspension electrodes, redox-active polymers are receiving special interest because their properties can be easily tailored by macromolecular engineering. For example, their solubility can be tuned in various solvents by co-polymerizing with the adequate monomers. Their molar masses, molar masses distribution as well as their

architectures (*i.e.* linear, branched, statistical, block copolymers, etc.) can be easily tuned provided that controlled or living polymerization techniques are used for their synthesis.

Poly(2,2,6,6-tetramethylpiperidinyloxy-4-yl-methacrylate) (PTMA) is considered as an excellent redox-active polymer for application in FAES. Indeed, PTMA is able to undergo stable and reversible redox reactions upon electrochemical stimuli.[7] Moreover, it displays a high power density with an ultra-fast electron-transfer process of 10^{-1} cm.s^{-1}.[8] Thus it is also classified as a pseudo-capacitive component. This allows PTMA to be widely used as cathode materials in organic radical batteries (ORB).[9,10] Schubert et al. have synthesized water-soluble statistical copolymers containing PTMA and hydrophilic comonomers[11] and have studied their electrochemical properties in water based and in organic carbonates based RFBs.[12] While the organic carbonates are widely used due to their good stabilities, the water-based system reveal better performances as well as positive environmental impact. Furthermore, Schubert and coworkers were able to design a full-organic water-based RFB[13] by using water-soluble redox-active polymers as both catholyte and anolyte.

One of the main challenges related to redox-active polymer-based electrodes remains the relatively low concentration of redox-active material that can be dissolved while keeping a viscosity sufficiently low to allow the pumping of the liquid electrode in the main electrochemical cell. Decreasing the molar mass of the polymer is not a valid option since the electroactive polymer should not pass through the semi-permeable membrane located in the main electrochemical cell.[13] One way to allow the dispersion of a high amount of electroactive polymer while not reaching a too high viscosity consists in tethering the redox-active polymer chains in a micellar design. Basically, the redox-active polymer chains could be incorporated into two different compartment of the micellar cargo: the micellar core or the micellar corona. In a previous work, we have designed micellar nano-objects comprising PTMA coronal chains tethered onto a polystyrene (PS) core. Those objects were synthesized from PTMA-*b*-PS diblock copolymers containing a major PTMA block dissolved in carbonate solvents that are selective solvents for the PTMA blocks.[14] The accordingly obtained micelles were successfully tested as catholytes in RFB.[15] Such a design

presents the advantage to allow a good accessibility of the electroactive PTMA chains for redox reaction since they are located in the micellar corona but the disadvantage to be limited to organic solvents for the preparation of the liquid electrode since both PTMA and PS are hydrophobic groups.

The aim of this chapter is to synthesize micellar nano-objects in aqueous medium containing the electroactive PTMA polymer. Our target is to synthesize an amphiphilic block copolymer containing a water-soluble hydrophilic block and a hydrophobic PTMA block. In aqueous medium, such a copolymer is expected to form micellar nano-objects containing a PTMA core and a hydrophilic polymer corona. In order to maximize the amount of PTMA in the system, the composition of our copolymers will be adjusted to target cylindrical micelles rather than spherical ones. Practically, our attention is focused on the so-called polymerization induced self-assembly (PISA) method.[16] This method has indeed emerged as a promising alternative to classical water-based polymerization techniques since it is surfactants-free (the formed copolymer plays indeed the role of surfactant) and it leads to the formation of the micellar nano-objects directly during the synthetic process of the copolymer (Fig. 2).[16]

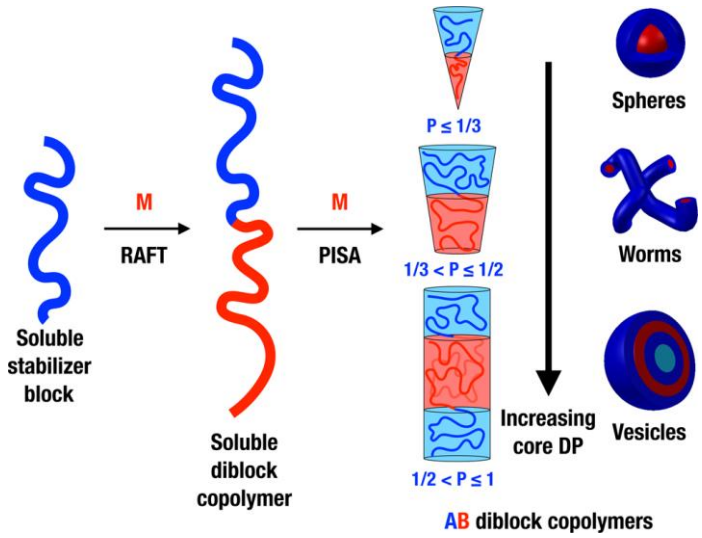

Figure 2. Schematic of the synthesis of diblock copolymer nano-objects via polymerization-induced self-assembly (PISA).[17]

Because it involves the polymerization of both an hydrophobic and an hydrophilic monomer usually in an aqueous medium, the PISA process is a peculiar type of heterogeneous polymerization, also known as emulsion, suspension and dispersion polymerizations.[18] While Charleux et al. mainly reported reversible addition-fragmentation chain transfer (RAFT) aqueous emulsion polymerizations,[19] Armes et al. developed a RAFT aqueous dispersion synthetic route.[20] Moreover, dispersion and emulsion polymerizations are not limited to aqueous media and were also developed in alcohol, alkane and alcohol/water mixture.[17,21,22] In the PISA process based on RAFT polymerization, the macro-chain transfer agents (macro-CTAs) also play the role of stabilizers since it further leads to the formation of an amphiphilic block copolymer. The formation of micellar nanostructures occurs therefore simultaneously during the copolymerization. Indeed, the accordingly formed amphiphilic block copolymers can self-assemble into different structures, such as spherical, cylindrical or vesicles micelles and other complex micelles (Fig. 2), [23] at high concentration and full monomeric conversion rate.[24] These morphologies are influenced by the nature, the composition and the concentration of each blocks (hydrophilic and hydrophobic) as well as the nature of the solvent.[25]

The strategy developed in the present contribution is to synthesize directly PTMA based nano-objects in suspension in aqueous medium by copolymerizing it with a hydrophilic polymer block using a PISA process. This strategy was developed as an alternative to the principal project, which was in collaboration with Armes et al. from the University of Sheffield in United Kingdom and for which the samples synthesized by them do not give conclusive results in electrochemistry. Herein, we report the RAFT polymerization induced self-assembly of the 2,2,6,6-tetramethylpiperidin-4-yl methacrylate (TMPM) monomer which is the precursor of the PTMA. Two types of water-soluble macro-CTAs are synthesized, *i.e.* the thermo-responsive poly[oligo(ethylene glycol) methyl ether methacrylate] (POEGMA) (Fig.3a) and the cationic poly[(4-methacryloyloxy)-2,2,6,6-tetramethylpiperidinium chloride] ($PTMPM^+Cl^-$) (Fig. 3b). This PISA process leads to the formation of micellar nano-objects with a PTMPM core and either a POEGMA or a $PTMPM^+Cl^-$ corona. After the oxidation step to transform PTMPM into PTMA, the redox properties of redox-active

polymer based nano-objects are confirmed through cyclic voltammetry measurements.

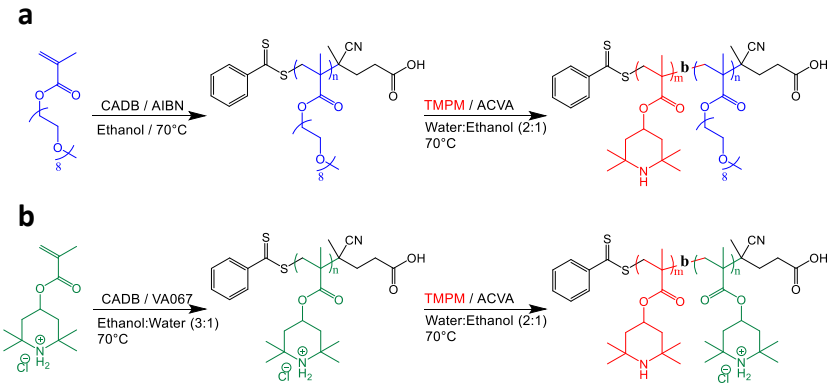

Figure 3. Polymerization process of **(a)** POEGMA-*b*-PTMPM (called diblock 1 and diblock 2) and **(b)** $PTMPM^{+}$-*b*-PTMPM (called diblock 3) via RAFT-PISA.

6.2 Synthesis of Macro-CTAs

Firstly, the RAFT homopolymerization of TMPM was conducted in order to determine the boundary conditions and parameters to elaborate well-defined block copolymers. During the controlled radical polymerization of TMPM, an aminolysis side reaction takes place, leading to the premature end of chain growth (Fig.4).

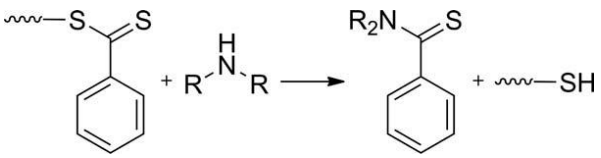

Figure 4. Schematic representation of the aminolysis of thiocarbonylthio CTAs by secondary amines.[26]

Three solutions were found to overcome this issue:[26] (1) the protection of the free secondary amine by protonation, forming the ammonium salt; (2) the use of a polar solvent to stabilize the nucleophilic amine function thanks to an hydrogen bond between the amine and the solvent and (3) the introduction of a large amount of initiator varying from 0.5 to 1 equivalent. In our case, the PTMPM polymerization was carried out, as reported by Schubert et al.,[26] in ethanol at 70 °C with a CTA:initiator molar ratio of 1:1 with a dithiobenzoate (CADB) as chain transfer agent. By fixing these reaction conditions, a conversion up to 90% and a dispersity of 1.18 were reached without further purification (Fig. 5).

Secondly, different macro-CTAs with various lengths were synthesized using the same chain transfer agent and standard RAFT polymerization conditions. POEGMA is known for its water-soluble and thermo-responsive properties, allowing it to be studied for many promising applications in biotechnology and medicine[27] but also in solid polymer electrolytes based batteries.[28] The POEGMA polymerization was performed using CADB as CTA and AIBN as initiator with [CADB]:[AIBN] ratio of 5:1. According to the length of the OEGMA lateral chains, the hydrophilicity degree and the lower critical solution temperature (LCST) of the POEGMA change accordingly.[29] In order to not disturb the initiation of chains, which is carried out at 70°C, the $OEGMA_{475}$ with a LCST of *ca.* 90°C has been selected. Moreover, two lengths of POEGMA macro-CTA chains were synthesized to investigate their impact on the electrochemical results thereafter. In both cases, the monomer concentration [M] was kept at 1 $mol.L^{-1}$ in ethanol. Another macro-CTA3 was synthesized, namely $PTMPM^{+}Cl^{-}$. The ammonium salt lateral groups of $PTMPM^{+}Cl^{-}$ are ionized in a polar solvent with a high dielectric constant such as water, making this polyelectrolyte a good hydrophilic block. Its polymerization was conducted in the same way as for POEGMA macro-CTAs. Only the AIBN initiator was replaced with VA067 and water was added to ethanol (water:ethanol 1:3 vol:vol) to ensure complete solubilization of the monomer (Fig. 6).

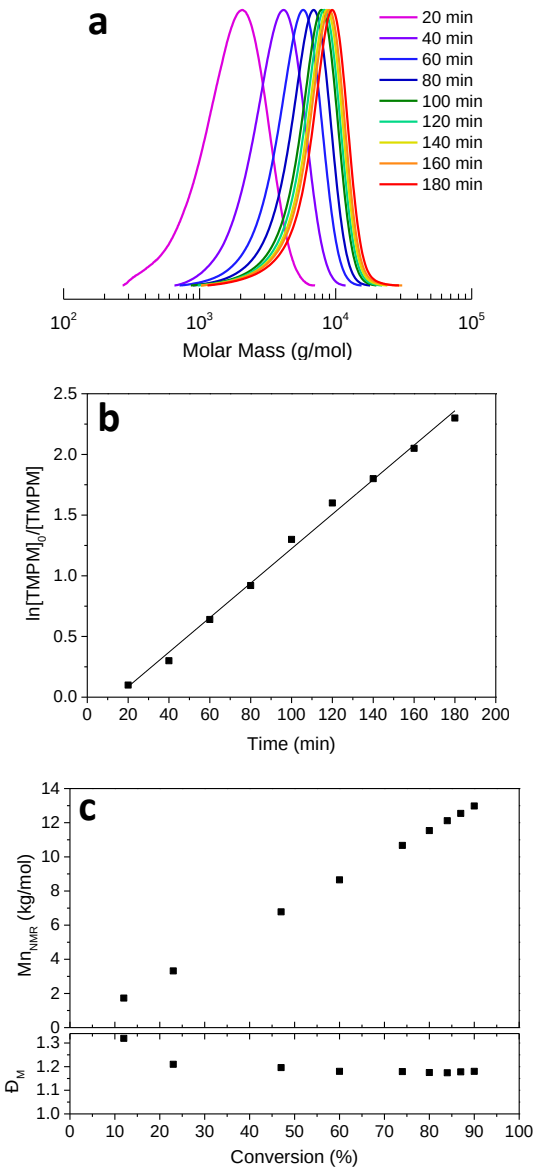

Figure 5. Kinetic study of PTMPM homopolymerization. **(a)** Evolution of molar mass distribution vs time as measured by SEC. **(b)** Evolution of $\ln[TPMPM]_0/[TPMPM]_t$ vs time. **(c)** Evolution of the number-averaged molar mass and the dispersity index vs conversion.

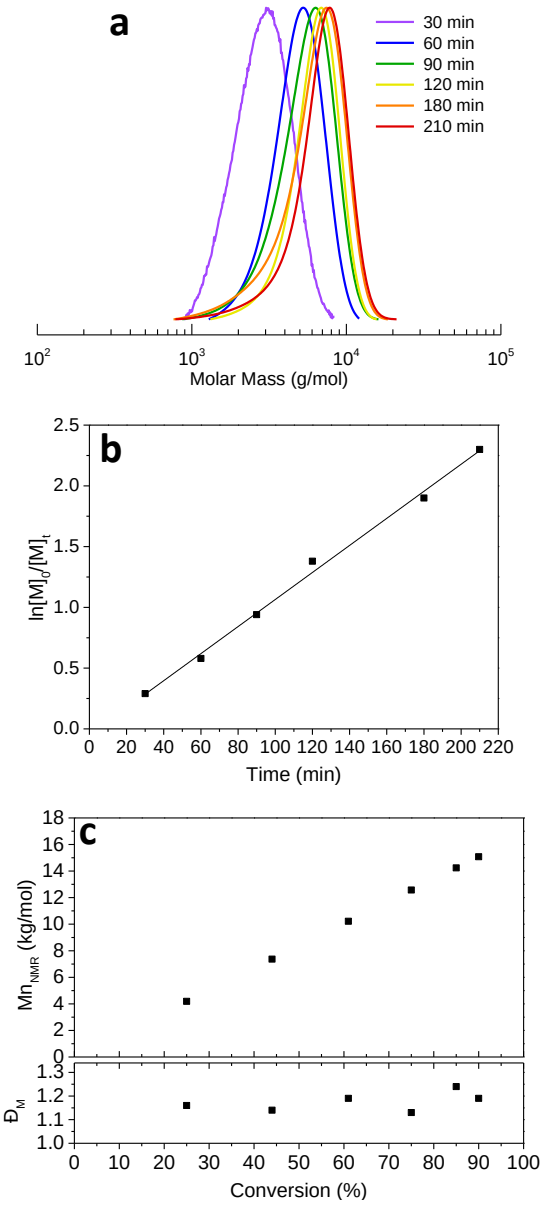

Figure 6. Kinetic study of PTMPM^{+}Cl^{-} homopolymerization. (a) Evolution of molar mass distribution vs time as measured by SEC. (b) Evolution of ln[TPMPM^{+}Cl^{-}]$_0$/[TPMPM^{+}Cl^{-}]$_t$ vs time. (c) Evolution of the number-averaged molar mass and the dispersity index vs conversion.

The obtained macro-CTA1, macro-CTA2 and macro-CTA3 display an average molar mass (Mn) of 7600 g.mol^{-1}, 17100 g.mol^{-1} and 9200 g.mol^{-1} respectively, as determined by ^{1}H-NMR. Additionally, the SEC analysis was performed and macro-CTA1 and macro-CTA2 were injected in SEC with N,N-dimethylformamide + 2.5 mM NH_4PF_6 as eluent while macro-CTA3 was deprotonated into PTMPM prior to injection in the SEC with chloroform/triethylamine/isopropanol (94/4/2) as eluent. The three macro-CTAs display low dispersities (Đ) of 1.11, 1.13 and 1.13 respectively, indicating a well-controlled polymerization.

6.3 RAFT-PISA of TMPM monomer

The next step consists in the direct formation of the block copolymer nano-objets at the same time that the polymerization of the core forming block, more precisely during the polymerization of the insoluble PTMPM block. The TMPM monomer has the ability to be molten at 70°C. Thus, the PISA process has been carried out at this temperature in order to obtain a dispersion of molten TMPM droplets in water selected as polymerization medium. Then, the presence of a hydrophobic CTA segment from CADB at the end of the hydrophilic macro-CTAs chains (containing either POEGMA or PTMPM^{+}) could promote interaction with hydrophobic TMPM molecules and could participate to its copolymerization, subsequently forming nano-objects. However, the polymerization of the TMPM in the molten state in water did not lead to good results. Moreover, since we are using a water-soluble initiator (ACVA), the PISA process should occur via an emulsion mechanism. However, the too high hydrophobicity of TMPM in the molten droplet could impede such an emulsion process due to a too low solubility of TMPM in the aqueous phase. Therefore, the PISA of TMPM monomers was carried out in a mixture of water:ethanol (2:1). Ethanol was selected for two reasons: firstly, in order to favor the formation of well-defined amphiphilic block copolymers by solubilizing TMPM in the polymerization medium and secondly in order to prevent the aminolysis side reaction, as previously observed for the TMPM homopolymerization.

It is obvious that increasing the length (or the weight amount) of the PTMA block in the synthesized diblock copolymers should lead to better electrochemical properties in terms of the amount of reversibly stored electrical energy.[30] However, this increase of the length of the hydrophobic block could lead to the sedimentation of the nano-objects due to too short hydrophilic stabilizing blocks. It is well known that the size and the morphology of the final particles strongly depend of the relative molar masses of the hydrophilic and hydrophobic blocks, for which a so-called hydrophilic fraction p = Mn(hydrophobic)/Mn(hydrophilic) needs to be taken into account.[23] Herein, our first strategy is to increase the length of both blocks (hydrophilic and hydrophobic) while maintaining the hydrophilic fraction p between 0.3 and 0.5 (diblock 1 and diblock 2 in Table 1). Such a value for p should lead to worm-like nano-objects in which the amount of redox-active PTMA chains in the micellar core is higher compared to the spherical micelles. Our second idea is the use of a polyelectrolyte as highly hydrophilic block, here $PTMPM^+$ (diblock 3 in Table 1). In this case, the high hydrophilic character of the stabilizing block could allow a lower amount of it in the final diblock copolymer and in turn will maximize the amount of electroactive PTMA in the micellar nanostructures. Moreover, it will be possible to reach higher p (close to 1 for diblock 3 in Table 1) and thus to explore other possible complex morphologies. For the diblock 3, a redistribution of the charges is possible. In fact, before the oxidation of TMPM units into TMA units, charges can move between $TMPM^+$ and TMPM units.

Diblock	**$Mn_{(hydrophilic)}$[a]**	**$Mn_{(hydrophobic)}$[a]**	***p*[b]**
1 = $POEGMA_{16}$-*b*-$PTMPM_{17}$	7600	3800	0.50
2 = $POEGMA_{36}$-*b*-$PTMPM_{34}$	17100	7700	0.45
3 = $PTMPM^+_{35}$-*b*-$PTMPM_{40}$	9200	9000	0.98

[a] *Molar mass determined by ^1H NMR.*

[b] *Hydrophilic fraction p = Mn(hydrophobic)/Mn(hydrophilic)*

Table 1. Summary of diblock copolymers characteristic features.

In general for PISA syntheses, the upper limit of solid concentration is of ca. 50 wt.% solids.[17] Unfortunately in our case, it is impossible to reach this concentration. The macro-CTA are too viscous and at this concentration, the medium is frozen and is not homogeneous. It is possible to decrease the concentration of macro-CTA in order to increase the targeted DP of the core-forming block. However, a precipitation of nano-objects occurs in our case if the DP of the hydrophobic block increases and the DP of the hydrophilic block decreases. That why, for all systems, the copolymerization was conducted at relatively high solid concentration (26 wt. %) and at full conversion, highlighting the other advantages of PISA.[24] At the end of the PISA process, samples were withdrawn, dried and subjected to ^{1}H-NMR and SEC analyses by solubilizing them in their respective solvents. Fig.7a shows the ^{1}H-NMR spectrum of $POEGMA_{16}$-*b*-$PTMPM_{17}$ (diblock 1, the numbers in subscript representing the average degree of polymerization of the respective polymer block as determined from the NMR spectrum). The absence of vinyl peaks indicates a full consumption of the monomers. A peak shifting to higher molar mass is observed in SEC (Fig. 7b) proving that the copolymerization did take place.

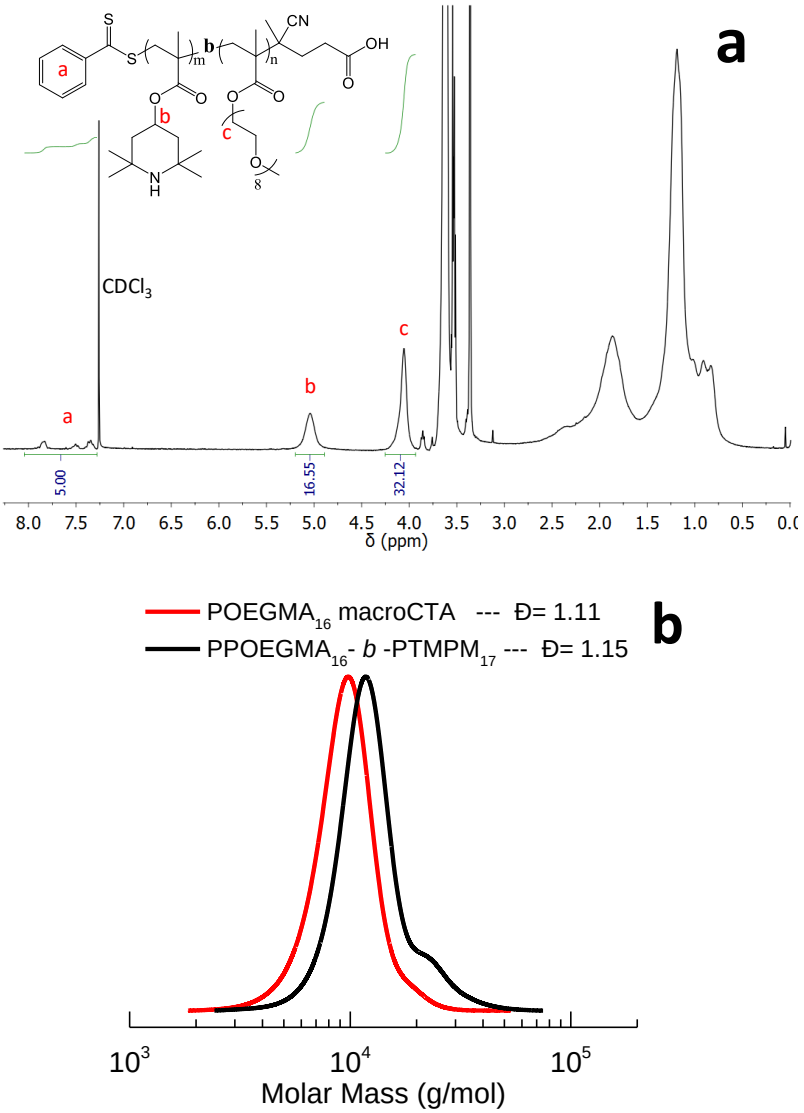

Figure 7. (a) ^{1}H-NMR spectrum of diblock 1 in deuterated DMSO **(b)** SEC curves of macro-CTA (red) and of diblock 1 (black).

These observations are similar for the two other synthesized diblock copolymers (Fig. 8). For the $POEGMA_{16}$-*b*-$PTMPM_{17}$, a shoulder is observed at high molar mass indicating the presence of another population with different chain lengths (Fig. 7b). This shoulder is less pronounced for $POEGMA_{36}$-*b*-$PTMPM_{34}$ (Fig. 8) which may be due to a better control of the RAFT PISA polymerization for longer targeted chains.

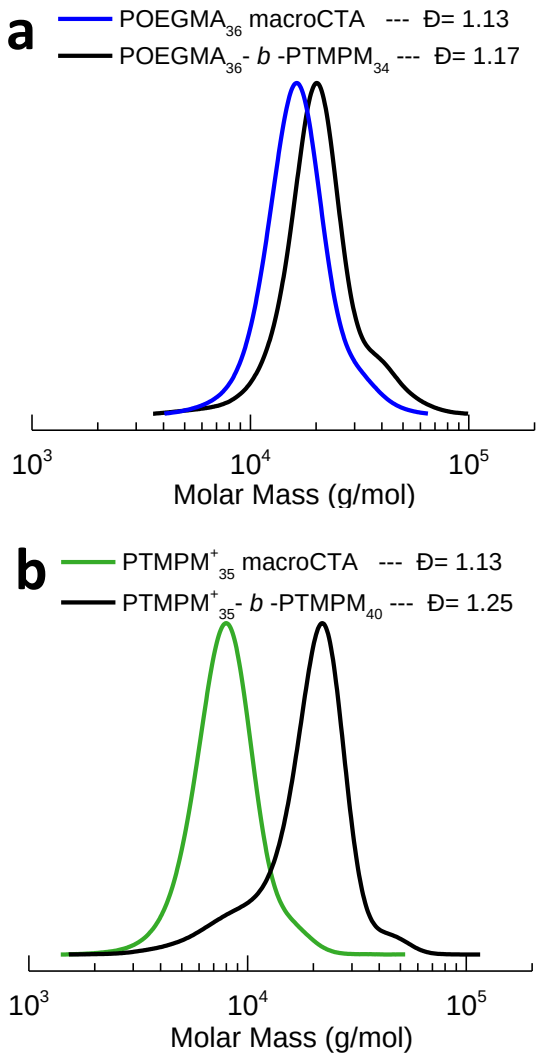

Figure 8. SEC curves of **(a)** diblock 2 with its respective macro-CTA and **(b)** diblock 3 with its respective macro-CTA.

6.4 Morphology of the resulting nanostructures

To visualize the nano-objects resulting from the RAFT PISA process, transmission electron microscopy (TEM) analysis was conducted. Aliquots were taken from the crude block copolymer solutions and water was added in one time to freeze the medium and to reach diluted solutions at 0.2 wt. % of block copolymers. Fig. 9a, b and c reveal representative TEM images for $POEGMA_{16}$-*b*-$PTMPM_{17}$, $POEGMA_{36}$-*b*-$PTMPM_{34}$ and $PTMPM^{+}{}_{35}$-*b*-$PTMPM_{40}$, respectively.

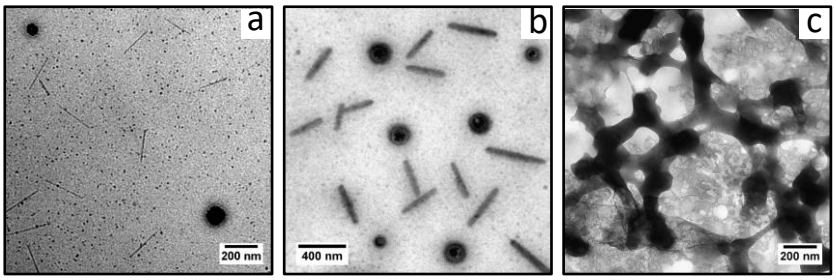

Figure 9. Typical TEM images of **(a)** diblock 1 **(b)** diblock 2 and **(c)** diblock 3. All were diluted at 0.2 wt. %.

Diblock 1 is mainly forming spherical micelles with an average diameter of 28 nm (Fig. 9a). These spherical micelles coexist with a minority of rod-like micelles with a similar diameter of 28 nm, suggesting that the latter originate from the merging of spherical micelles. A few bigger spherical particles with a diameter of *ca.* 140 nm are also observed. They could originate from the second population of block copolymers with a higher molar mass that was previously underlined by SEC analysis. For diblock 2, cylindrical micelles are clearly observed as well as vesicles with average diameters of 200 nm (Fig. 9b). These shapes and sizes could be understood while considering the higher chain lengths in diblock 2 compared to diblock 1 as well as the value of *p* located at the boundary between cylindrical and vesicles for diblock 2. Although the value of *p* for diblock 1 is also located at the boundary between cylindrical micelles and vesicles (Table 1), no vesicles were detected for this sample. Concerning diblock 3, an

interconnected morphology is observed (Fig. 9c). For this sample, the value of *p* is close to 1 (Table 1), indicating the formation of a lamellar microstructure. Those lamellae could lead in solution either to vesicles or to more intricate interconnected structures as observed in our case in Figure 9c.[31] Of course, this structure could also be due to the redistribution of the charges occurring between $TMPM^+$ and TMPM units.

6.5 Electrochemical testing

After the oxidation of PTMPM followed by dialysis purification, micellar nano-objects with PTMA blocks in the core were obtained at a concentration of 10 wt. % in water:ethanol mixture (2:1). It should be noted that the micellar morphologies depicted in Fig. 9 were not affected by the transformation of the PTMPM blocks into PTMA ones after the oxidation reaction (data not shown). Cyclic voltammetry (CV) tests were performed on these micellar solutions, with sodium chloride (0.5 $mol.L^{-1}$) as supporting salt electrolyte (Fig. 13 in Experimental section). Cyclic voltammetry is the most widely used analytical technique in order to provide information about electrochemical reactions. The principle is to measure the current passing over a sweeping potential range, in our case between 0.3 and 1.1 V vs Ag/AgCl reference electrode. For all systems, the mass transfer was performed according to the mechanism of diffusion. No electric field (migration) or physical forces (convection) were applied. This means that the redox-active species moved spontaneously from the bulk to the electrode surface. Fig. 10a, b and c present cyclic voltammograms (CVs) of diblock 1, diblock 2 and diblock 3, respectively.

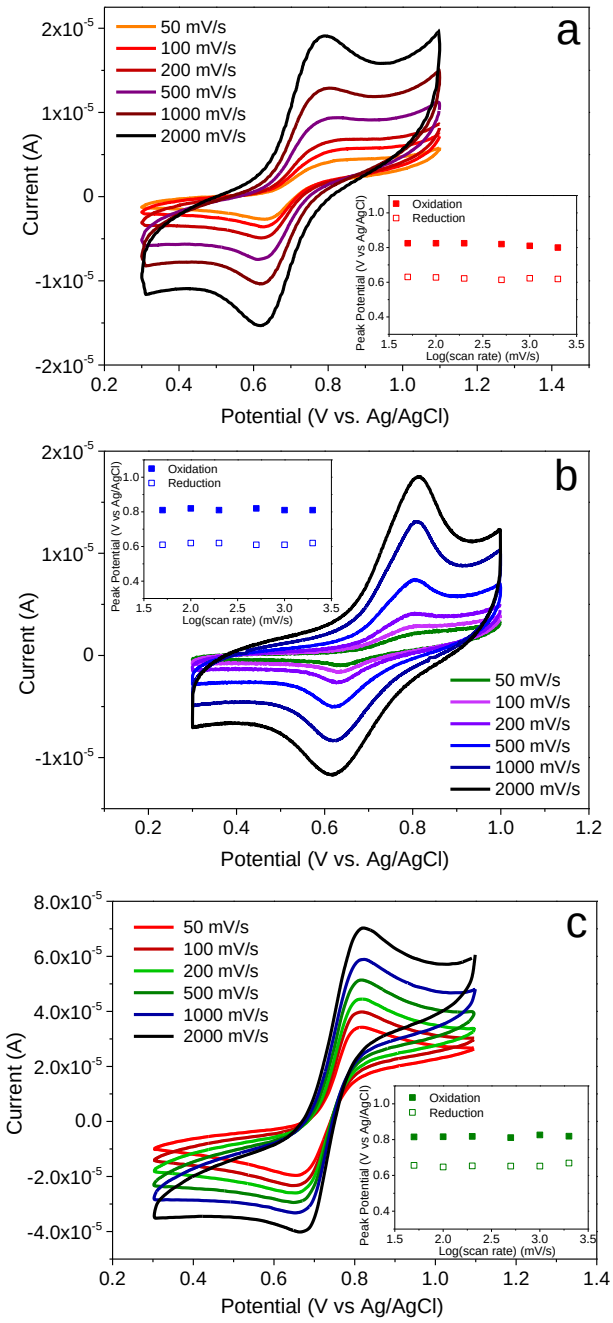

Figure 10. Cyclic voltamograms with different scan rates v (50, 100, 200, 1000 and 2000 mV/s) for **(a)** diblock 1, **(b)** diblock 2 and **(c)** diblock 3 after oxidation. The solutions are comprising 10 wt %

polymer in water:ethanol mixture (2:1) with NaCl as supporting salt electrolyte (0.5 mol/L). The insets are Ep^{ox} and Ep^{red} versus log (v).

These CVs were performed at different scan rates: 50, 100, 200, 500, 1000 and 2000 mV/s. The insets display the oxidation and the reduction peaks potentials (Ep^{ox} and Ep^{red}) *vs.* the logarithm of the scan rate (log v). A familiar "duck" shape is observed for the three systems. Moreover, the redox potential, $E° = (Ep^{ox} + Ep^{red})/2$ is estimated at 0.72 V *vs.* Ag/AgCl for diblock 1 and diblock 2 and at 0.74 V vs Ag/AgCl for diblock 3. These results are ascribed to the reversible redox couple: nitroxide radical/oxoammonium cation and confirms the reversible electrochemical activity of our micellar nano-objects although the PTMA redox-active blocks are located into the micellar cores and not exposed in the micellar corona.[32,11]

All the investigated diblocks present, in the range of 50-2000 mV/s, values of Ep^{ox} and Ep^{red} peak potentials that are constant and independent of the scan rate (insets in Fig. 10). Furthermore, the peak separation potential, $\Delta Ep = \left| Ep^{ox} - Ep^{red} \right|$ is not of 59/n mV (with n corresponding to the number of charge carrier e^- or ion) as expected for reversible systems, but it keeps lower than 200 mV, indicating a quasi-reversible behavior of the redox couple in water:ethanol medium.

Fig. 11 plots the currents for the oxidation and reduction peaks (Ip^{ox} and Ip^{red}) versus the square root of the scan rate ($v^{1/2}$) for each diblock. For diblock 1 (Fig. 11a), Ip^{ox} and Ip^{red} increase linearly as a function of the square root of the scan rate. Moreover, the slope of log(Ip) vs f(log$v$) is below 0.5 (inset in Figure 11) and the peak current ratio (Ip^{ox}/Ip^{red}) is close to 1 for all scan rates. These observations indicate that the redox process of PTMA is a quasi-reversible and that the charge transfer at the electrode surface is controlled by diffusion.[33] Therefore, the PTMA based nano-objects do not adsorb at the working electrode surface during the redox process of TEMPO groups.

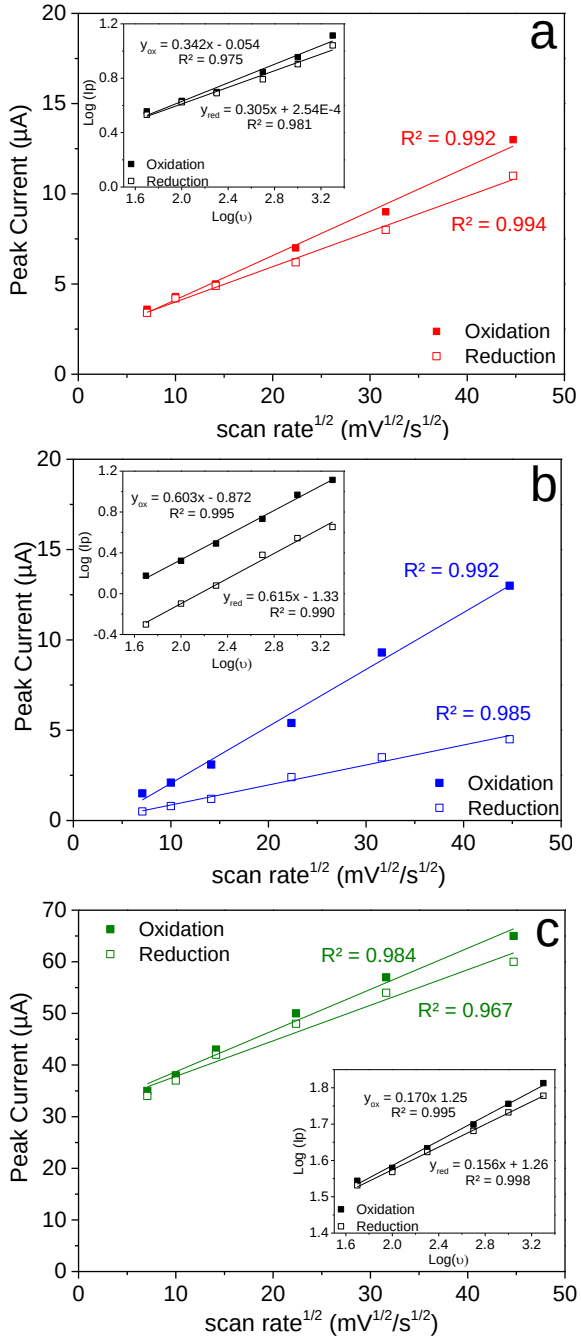

Figure 11. Dependence of Ip^{ox} and Ip^{red} on the square root of the scan rate ($v^{1/2}$) for **(a)** diblock 1, **(b)** diblock 2 and **(c)** diblock 3 after

oxidation. The insets display the dependence of log(Ip^{ox}) and log(Ip^{red}) on the log(scan rate).

Moreover, these observations also indicate that the concentration (C in mol.cm^{-3}) and the diffusion coefficient of the redox species (D in cm².s^{-1}), as well as the stoichiometric number of exchanged electrons (n) and the working electrode area (A in cm²), are related to the peak current Ip according to the Randles-Sevcik equation:

$$Ip = 2.69\ \text{x}10^5 n^{3/2}\, A\, D^{1/2}\, v^{1/2} C$$

According to this equation, the higher the concentration of redox-active species, the higher is the peak current Ip. For diblock 2 (Fig. 11b), Ip^{ox} and Ip^{red} also increase linearly with the square root of the scan rate. However, the slope of log(Ip) vs f(log$v$) is between 0.5 and 1, corresponding to charge transfer by diffusion and adsorption respectively. In the case of $POEGMA_{475}$ based nano-objects, the lengths of the POEGMA hydrophilic block as well as the PTMA hydrophobic block were increased from diblock 1 to diblock 2 (Table 1). It is thus possible that the length of the POEGMA blocks disturbs the PTMA redox process, and that a longer POEGMA coronal block results in the adsorption of part of the nano-objects at the working electrode surface. Additionally, the Ip^{ox}/Ip^{red} ratio is greater than 1 at each scan (average of 2.7), due to the low generated Ip^{red} values. While the oxidation of nitroxide radicals into oxoammonium cations is performed correctly at any scan rate, the system has difficulties to reduce into nitroxide radicals. This observation could be explained by the stability difference between the PTMA cation and the PTMA radical in water. In fact, we suppose that the cationic form is relatively stable in aqueous media, while it is the opposite for the radical one, which is known as to be insoluble in water. Therefore, the long $POEGMA_{36}$ blocks do not sufficiently stabilize the hydrophobic PTMA blocks.[11]

Concerning diblock 3, PTMA can be oxidized and reduced reversibly, by diffusion (Fig. 11c). In fact, the peak current increases linearly with the scan rate, the slope of log(Ip) vs f(log$v$) is below 0.5 and the Ip^{ox}/Ip^{red} ratio is close to 1. Moreover, the measured current values are 6 times higher than the current values obtained for the $POEGMA_{475}$ based nano-objects. This can be firstly explained by the

greater concentration of redox species due to the longer hydrophobic PTMA chains, which is correlated to the Randles-Sevcik equation. Secondly, the $PTMPM^{+}Cl^{-}$ blocks have no impact on the PTMA redox processes and stabilize efficiently the system during the electrochemical process, in contrast with the situation observed for diblock 2.

6.6 Rheological testing

For application in flow electrochemical systems, the viscosity of the suspension electrodes is an important parameter to take into account because it influences the quality of the pumping that is related to the generated energy. Thus, rheological measurements were realized in order to study the viscosity of the investigated PTMA-containing nano-objects. Fig. 12 plots the viscosity versus the shear rate for the diblock 2 and diblock 3 nano-objects.

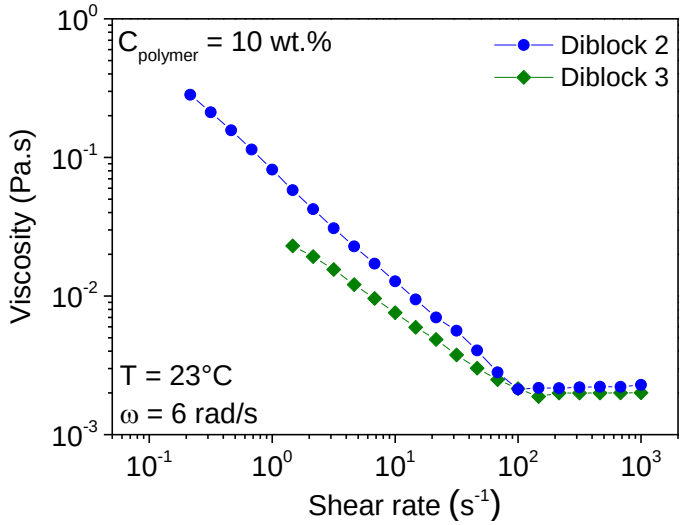

Figure 12. Steady shear viscosity of diblock 2 (blue) and diblock 3 (green) after oxidation at T = 23°C, ω = 6 rad/s and $C_{polymer}$ = 10 wt%.

For both systems, the viscosity decreases when the shear rate increases until 10^2 s^{-1}, indicating a shear-thinning behavior. In fact, those materials are considered as non-Newtonian systems due to their complex flow behavior. The viscosity stabilizes and becomes constant between 10^2 and 10^3 s^{-1}, which is characteristic of a Newtonian behavior. This combination of shear-thinning and Newtonian behaviors can be explained as follows. While increasing the shear rate, the diblock copolymers composing the nano-objects disassemble into free copolymer chains in solution (from 10^{-1} to 10^2 s^{-1}). These chains will eventually stretch and orient with each other towards the flow direction (from 10^2 to 10^3 s^{-1}).[34] Below a shear rate of 10^2 s^{-1}, the decrease of the viscosity is accentuated for diblock 2 with a slope of -0.79 which is consistent with the values reported in the literature for shear-thinning polymers.[35] For diblock 3, a slope of -0.58 is noted. This difference can be explained by the fact that these two diblocks self-assemble into different morphologies, have different chains length and have different chemical composition leading to different interactions. Indeed, ionic interactions are present in diblock 3 and not in diblock 2. This could explain why the viscosity of diblock 3 decreases less sharply than for diblock 2 while increasing the shear rate until 100 s^{-1}. For both solutions analyzed at the same polymeric concentration (10 wt. %), the respective viscosities are lower than 1 Pa.s. However, the POEGMA containing diblock 2 solution is slightly more viscous than the $PTMPM^+Cl^-$ containing diblock 3 solution over the entire range of the shear rate measurements although a higher viscosity in water is expected for the polyelectrolyte based system. This might be due to the bulkiness of the POEGMA hydrophilic block in which the dangling POEGMA segments create a comb-like architecture for the hydrophilic block. Those segments could act as sticky points and could explain the increased viscosity compared to diblock 3 in which the hydrophilic block has a perfect linear architecture. Moreover, it is noteworthy to mention that these diblocks have been analyzed in the presence of NaCl electrolyte in water. Hence, the polyelectrolyte ionic interactions can be significantly weakened or screened in the presence of salt, which can also contribute to the low viscosity of the diblock 3 with respect to diblock 2. Finally, it would have been interesting to do more rheological measurements to deepen the research. Unfortunately, the low concentration does not allow it.

6.7 Conclusion

In this chapter, we have investigated the synthesis of PTMA based nano-objects in suspension in water as precursors of catholytes to be used in flow-assisted electrochemical systems (FAES). Contrary to other investigations reported in the literature, the RAFT polymerization induced self-assembly (PISA) was here employed to produce nano-objects simultaneously with the copolymerization of amphiphilic chains containing hydrophobic PTMA precursor (*i.e.* PTMPM) as core block. Hydrophilic polymers such as POEGMA and $PTMPM^{+}Cl^{-}$ were used as stabilizers, as macro-CTAs and as corona blocks during the PISA.

We have demonstrated that it is possible to avoid the aminolysis side reaction, reported to occur during the controlled radical polymerization of TMPM, and to synthesize nano-objects with RAFT-PISA by carefully tuning experimental parameters. In fact, a large amount of initiator was used to avoid aminolysis by speeding up the polymerization. A good polar solvent (*i.e.* ethanol) for TMPM and PTMPM was added to water in order to promote the control of the RAFT-polymerization. Unfortunately, we were not able to get well-defined nano-objects because of (1) the choice of hydrophilic blocks, (2) the relatively high solid concentration (26 wt. %) and (3) the choice of the hydrophilic fraction p = Mn(hydrophobic)/Mn(hydrophilic) value which was located at the boundary between two types of morphology.

We have demonstrated by cyclic voltammetry measurements that the PTMA units could be oxidized and reduced in all investigated samples, although they are located in the micellar core and thus less accessible than in the micellar corona. However, the reversibility of the redox process of PTMA depends on the nature and on the length of the hydrophilic block used in order to stabilize the oxidized and reduced forms of the redox polymer core blocks.

With the help of rheological measurements (realized by Dr. Flanco Zhuge), we have observed that the investigated systems display rather low viscosities and a shear thinning behavior in a specific shear-rate domain that makes them suitable for application in flow electrochemical systems.

6.8 Experimental section

- Materials

The 2,2,6,6-tetramethylpiperidin-4-yl methacrylate (TMPM, TCI), polyethylene glycol)methyl ether methacrylate ($OEGMA_{475}$, Aldrich) monomers and the 4-Cyano-4-(phenylcarbonothioylthio)pentanoic acid (CADB, 97%, Aldrich) chain transfer agent (CTA) were used as received. The 2,2'-Azobis(isobutyronitrile) (AIBN, 98%, Aldrich) and 4,4'-Azobis(4-cyanovaleric acid) (ACVA, 98%, Aldrich) initiators were purified by recrystallization in methanol before use.

- Instrumentation

^{1}H Nuclear magnetic resonance (NMR). ^{1}H NMR spectra were recorded either on a 300 MHz Bruker Avance II. The polymers were analyzed in deuterated DMSO or $CDCl_3$.

Size exclusion chromatography (SEC). Average molar masses (Mn and Mw) and dispersities (Đ) were measured on two Agilent SEC systems. One is equipped with an Agilent 1100/1200 pump (25 °C, eluent: chloroform/triethylamine/isopropanol (94/4/2), flow rate: 1 mL.min^{-1}), an Agilent differential refractometer and two PSS SDV columns (1000 Å and 10000 Å). The calibration was performed using polystyrene standards. The other one is composed of two PSS Gram columns (100 Å and 1000 Å) connected to a Waters 410 differential refractometer, with N,N-dimethylformamide + 2.5 mM NH_4PF_6 as eluent (35 °C, 1 mL.min^{-1}). Poly(ethylene glycol) standards were used for calibration. Therefore, the M_n, M_w, $Đ$ are obtained in polystyrene equivalents.

Transmission electron microscopy (TEM). TEM images were recorded using a LEO 922 OMEGA transmission electron microscope operating at 120 kV and equipped with a Gatan 1 k CCD camera. Diluted copolymer solutions (c.a. 0.2 % w/w) were dropped on carbon-

coated copper grids and dried overnight at room temperature prior to analysis. The grids were exposed to ruthenium (IV) oxide[36] vapor for a few minutes in order to improve contrast.

Electrochemical measurements. The cyclic voltammetry (CV) tests were performed using a Parstat 3000 with a three-electrode setup equipped with a glassy carbon disk-working electrode, a platinum wire counter electrode, an Ag/AgCl reference electrode and sodium chloride (0.5 mol.L^{-1}) as supporting salt electrolyte (Fig.13).

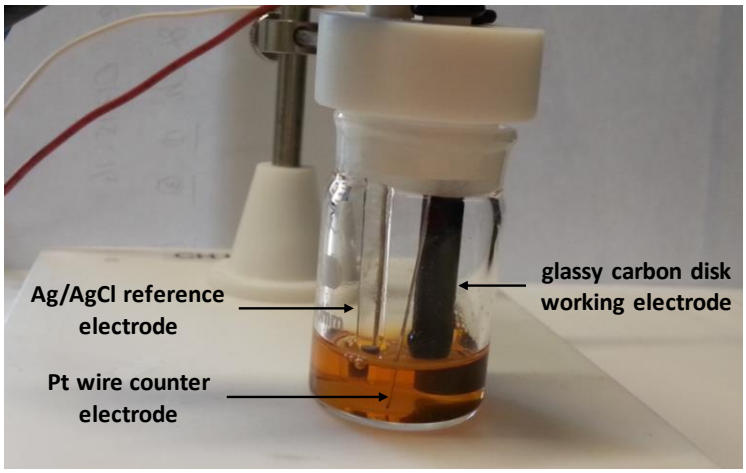

Figure 13. Three-electrode setup employed for the electrochemical characterization of PTMA based nano-objects.

Rheology. Rheological measurements were performed using a strain-controlled Ares (TA Instruments) rheometer equipped with a heat exchanger. Measurements were carried out at ambient temperature, using the Couette cuvette with a 25 mm bob and a 27 mm cup size. The gap was adjusted until the upper surface of the bob is 1 to 2 mm below the surface of the sample and not lower than 5 mm below the upper surface of the cup. Normal forces were checked to be relaxed prior any measurement. Steady rate sweep tests were then conducted at shear rates ranging from 10^{-2} to 10^{3} s^{-1}.

- Synthesis

4-(Methacryloyloxy)-2,2,6,6-tetramethylpiperidinium (TMPM) chloride. TMPM chloride was obtained following a previously reported synthetic strategy.[26]
^{1}H-NMR (300 MHz, $CDCl_3$), δ (ppm): 4.71 (d, 2H, CH_2O), 2.49 (t, 1H, CH≡C), 1.90 (s, 6H, $Br(CH_3)_2C$).
^{13}C-NMR (300 MHz, $CDCl_3$), δ (ppm): 171 (1C, C_{quat}-$\underline{C}O_2$), 77 (1C, HC≡$\underline{C}$-CH_2), 76 (1C, H$\underline{C}$≡C), 55 (1C, ≡C-$\underline{C}H_2$-O-), 52.5 (1C, Br-$\underline{C}_{quat}$), 31 (2C, $(\underline{C}H_3)_2$-C_{quat}).

General procedure for RAFT macro-CTA. $OEGMA_{475}$ monomer (12 g, 25 mmol), CADB RAFT agent (176 mg, 0.63 mmol), and AIBN (20.7 mg, 0.13 mmol, CTA/initiator molar ratio = 5) were solubilized in ethanol (1 mol/L) and purged with nitrogen in a flask sealed with a rubber septum. The solution was placed in a preheated oil bath at 70°C, under nitrogen. Once the targeted conversion rate was reached, the polymerization was quenched by cooling in liquid nitrogen and was exposed to air. The crude polymer was purified by dialysis (SpectraPor membrane, MWCO of 6-8 kDa) against ethanol:water (4:1 vol:vol) during 3 days. After removing solvent, the polymer was dried under vacuum at 40°C overnight, yielding a pink viscous liquid. The macro-CTAs were analyzed by ^{1}H-NMR and SEC in their respective solvents.

General procedure for RAFT - PISA. TMPM monomer (240 mg, 1.06 mmol), $POEGMA_{36}$ macro-CTA (523 mg, 0.036 mmol), and ACVA (9.95 mg, 0.035 mmol, macro-CTA/initiator molar ratio = 1) were solubilized (at a concentration of 0.5 mol/L in function of TMPM) in a 2:1 vol:vol water:ethanol mixture and purged with nitrogen in a flask sealed with a rubber septum. The solution was placed in a preheated oil bath at 70°C, under nitrogen. The polymerization was quenched by cooling in liquid nitrogen and was exposed to air, when full conversion rate was reached (*i.e.* after 120 min). The copolymers were analyzed by ^{1}H-NMR and SEC without any purification in their respective solvents.

Procedure for the oxidation of PTMPM blocks.[11] The crude copolymer solutions were diluted at 18 wt. % in water:ethanol (2:1 vol:vol) and mixed with sodium tungstate dihydrate (0.03 eq). Hydrogen peroxide (6 eq) was slowly added to the mixtures. The temperature was slowly increased to 40 °C. After 48h of stirring, the copolymers were purified by dialysis (SpectraPor membrane, MWCO of 6-8 kDa) against deionized water, yielding solutions at ca. 10 wt. % of polymer.

Bibliography

1 A. Z. Weber, M. M. Mench, J. P. Meyers, P. N. Ross, J. T. Gostick and Q. Liu, *J. Appli. Electrochem.*, 2011, **41**, 1137–1164.

2 J. Winsberg, T. Hagemann, T. Janoschka, M. D. Hager and U. S. Schubert, *Angew. Chem. Int. Ed.*, 2017, **56**, 686–711.

3 K. B. Hatzell, M. Beidaghi, J. W. Campos, C. R. Dennison, E. C. Kumbur and Y. Gogotsi, *Electrochim. Acta*, 2013, **111**, 888–897.

4 M. Duduta, B. Ho, V. C. Wood, P. Limthongkul, V. E. Brunini, W. C. Carter and Y. M. Chiang, *Adv. Energy Mater.*, 2011, **1**, 511–516.

5 K. B. Hatzell, M. Boota and Y. Gogotsi, *Chem. Soc. Rev.*, 2015, **44**, 8664–8687.

6 Z. Qi and G. M. Koenig, *J. Vac. Sci. Technol. B, Nanotechnol. and Microelectron. Mater. Process. Meas. Phenom.*, 2017, **35**, 40801.

7 K. Nakahara, S. Iwasa, M. Satoh, Y. Morioka, J. Iriyama, M. Suguro and E. Hasegawa, *Chem. Phys. Lett.*, 2002, **359**, 351–354.

8 H. Nishide, S. Iwasa, Y. J. Pu, T. Suga, K. Nakahara and M. Satoh, *Electrochim. Acta*, 2004, **50**, 827–831.

9 S. Muench, A. Wild, C. Friebe, B. Häupler, T. Janoschka and U. S. Schubert, *Chem. Rev.*, 2016, **116**, 9438–9484.

10 A. Vlad, N. Singh, J. Rolland, S. Melinte, P. M. Ajayan and J. F. Gohy, *Sci. Rep.*, 2014, **4**, 1–7.

11 T. Janoschka, S. Morgenstern, H. Hiller, C. Friebe, K. Wolkersdorfer, B. Haupler, M. D. Hager and U. S. Schubert, *Polym. Chem.*, 2015, **6**, 7801–7811.

12 J. Winsberg, T. Janoschka, S. Morgenstern, T. Hagemann, S. Muench, G. Hauffman, J. F. Gohy, M. D. Hager and U. S. Schubert, *Adv. Mater.*, 2016, **28**, 2238–2243.

13 T. Janoschka, N. Martin, U. Martin, C. Friebe, S. Morgenstern, H. Hiller, M. D. Hager and U. S. Schubert, *Nature*, 2015, **527**, 78–81.

14 G. Hauffman, Q. Maguin, J. P. Bourgeois, A. Vlad and J. F. Gohy, *Macromol. Rapid Commun.*, 2014, **35**, 228–233.

15 J. Winsberg, S. Muench, T. Hagemann, S. Morgenstern, T. Janoschka, M. Billing, F. H. Schacher, G. Hauffman, J. F. Gohy, S. Hoeppener, M. D. Hager and U. S. Schubert, *Polym. Chem.*, 2016, **7**, 1711–1718.

16 B. Charleux, G. Delaittre, J. Rieger and F. D'Agosto, *Macromolecules*, 2012, **45**, 6753–6765.

17 S. L. Canning, G. N. Smith and S. P. Armes, *Macromolecules*, 2016, **49**, 1985–2001.
18 R. Arshady, *Colloid. Polym. Sci.*, 1992, **270**, 717–732.
19 J. Rieger, W. Zhang, F. Stoffelbach and B. Charleux, *Macromolecules*, 2010, **43**, 6302–6310.
20 Y. Li and S. P. Armes, *Angew. Chem. Int. Ed.*, 2010, **49**, 4042–4046.
21 X. Zhang, J. Rieger and B. Charleux, *Polym. Chem.*, 2012, **3**, 1502–1509.
22 E. R. Jones, M. Semsarilar, P. Wyman, M. Boerakker and S. P. Armes, *Polym. Chem.*, 2016, **7**, 851–859.
23 S. J. Holder and N. A. J. M. Sommerdijk, *Polym.Chem.*, 2011, **2**, 1018–1028.
24 N. J. Warren and S. P. Armes, *J. Am. Chem. Soc.*, 2014, **136**, 10174–10185.
25 D. Zehm, L. P. D. Ratcliffe and S. P. Armes, *Macromolecules*, 2013, **46**, 128–139.
26 U. S. S. T. Janoschka, A. Teichler, A. Krieg, M.D. Hager, *J. Polym. Sci. Part A Polym. Chem.*, 2012, **50**, 1394–1407.
27 J. F. Lutz, *J. Polym. Sci. Part A Polym. Chem.*, 2008, **46**, 3459–3470.
28 A. V. and J.-F. G. J. Rolland, J. Brassinne, J.-P. Bourgeois, E. Poggi, *J. Mater. Chem. A*, 2014, **2**, 11839–11846.
29 U. S. S. C. R. Becer, S. Hahn, M. W. M. Fijten, H. M. L. Thijs, R. Hoogenboom, *J. Polym. Sci. Part A Polym. Chem.*, 2008, **46**, 7138–7147.
30 M. J. M. and Z. J. K.Zhang, Y. Hu, L. Wang, J. Fan, *Polym. Chem.*, 2017, **8**, 1815–1823.
31 N. S. Cameron, M. K. Corbierre and A. Eisenberg, *Can. J. Chem.*, 1999, **77**, 1311–1326.
32 T. Suga, Y. J. Pu, K. Oyaizu and H. Nishide, *Bull. Chem. Soc. Jpn*, 2004, **77**, 2203–2204.
33 N. Elgrishi, K. J. Rountree, B. D. McCarthy, E. S. Rountree, T. T. Eisenhart and J. L. Dempsey, *J. Chem. Educ.*, 2018, **95**, 197–206.
34 M. Khatibi, N. Potokin and R. W. Time, *Annu. Trans. Nord. Rheol. Soc.*, 2016, **24**, 117–126.
35 T. Schweizer, J. van Meerveld and H. C. Öttinger, *J. Rheol. (N. Y. N. Y).*, 2004, **48**, 1345–1363.
36 L. A. Fielding, J. A. Lane, M. J. Derry, O. O. Mykhaylyk and S. P. Armes, *J. Am. Chem. Soc.*, 2014, **136**, 5790–5798.

Conclusions and Perspectives

The main concern of this thesis was to design new polymeric materials for either the cathode (chapters 2, 3 and 6) or the electrolyte (chapters 4 and 5) exhibiting enhanced ionic conductivities. To reach this specific goal, different strategies have been studied in this work. As far as the cathode is concerned, ionically conducting groups have been introduced as crosslinking nodes of redox polymer networks (chapter 2) with the hope that those networks will lead to gel-like cathode swollen by the liquid electrolyte and exhibiting enhanced ionic conductivities (chapter 3). In chapters 4 and 5, we have focused on another compartment of the battery: the electrolyte. More precisely, we have investigated copolymers incorporating cyclic carbonates as side-groups in order to obtain solid polymer electrolytes exhibiting high conductivity but also high lithium ions transference numbers. In chapter 6, we have designed original micellar nano-objects with a core formed by a redox polymer. Those micelles could be further used as catholytes for redox-flow batteries. Again, for this last topic, the idea was to impart a good ionic conductivity to the catholyte solution by allowing easy ionic exchanges between the liquid electrolyte and the nanosized micellar cores containing the redox polymer. Finally, all these investigations were realized to better understand the correlation between the structure of materials used in batteries and their electrochemical properties.

The first phase of this work focused on the ion doping of the PTMA active material based cathode, by incorporating triazolium cation groups, mimicking ionic liquids (ILs), within the PTMA tridimensional network structure.

The synthesis of this PTMA network containing triazole groups as crosslinking nodes, was developed in one-pot by using the copper(0)-mediated reversible-deactivation radical polymerization simultaneously with the copper(I)-catalyzed azide–alkyne cycloaddition (Chapter 2). We demonstrated the existence of an

equilibrium between the coppers, allowing the smooth progress of the gel formation. The oxidation of the PTMPM gels was realized in soft conditions, conducting to PTMA gels, which exhibited better electrochemical performances. We also demonstrated that the capacities of redox-active gels depended of the oxidation degree of PTMA. Unfortunately, the one-pot synthesis must further be studied in order to control the amounts of the different copper species. In fact, a high amount of Cu(II) is generated during the polymerization, which is problematic for the purification step of gels. Moreover, it was difficult to synthesize gels at large scale or with high molar mass, suggesting a problem with the amount of copper species in the reactional medium. Moreover, the formation of the gels was reproducible only if the atmosphere was controlled and the reagents were pure, which was difficult with the rapid degradation of the AzPMA monomer.

The influence of the triazolium gels on the electrochemical performances was therefore investigated on PTMA gel synthesized by free radical polymerization (Chapter 3). We observed that the nature of the free counter-ions of the triazolium groups influences the electrochemical performances. In fact, we have been able to understand the correlation between the nature of ions, the conductivity values and the electrochemical performances. Contrary to the smaller anions such as I^-, the larger anions such as $TFSI^-$ improve the performances because they can move easily during the charge/discharge of the device due to their delocalized charges. For the future works, it would be interesting to study this system in a full battery. Moreover, most researches focused on nitrogen based ILs such as pyridinium, imidazolium and now triazolium. Thus, the triazolium cation could be replaced by other cations based on phosphonium and sulfonium. We could also envisage a cathode synthesis without destroying the redox-active three-dimensional network, realized during the oxidation step and the slurry preparation.

The second phase of this work focused on solid polymer electrolytes based on cyclic carbonate (cyCB) as pendant groups. They were investigated in order to find an alternative system to the poly(ethylene oxide) (PEO) electrolytes.

The cyCB units were firstly incorporated into fluorinated semi-crystalline copolymers (Chapter 4). We demonstrated that the ionic

conductivity increased when the amount of $LiClO_4$ salt incorporated into the poly(VDF-*co*-MAF-cyCB) increased up to cyCB/Li^+ equals to 5. An ionic conductivity value in the range of 2 x 10^{-4} S/cm was noted at room temperature and a lithium transference number was obtained at 0.68 at 40 °C, for the cyCB/Li^+ = 5. This behavior is different from PEO for which a high addition of lithium salt led to a decrease of the ionic conductivity due to the complexation of ions by the electro-donor oxygen atoms of the PEO. Thus, the presence of carbonate and fluorinated units allowed the lithium salt to be better solubilized and to move easily in the polymer matrix. Unfortunately, the poly(VDF-*co*-MAF-cyCB)/$LiClO_4$ SPE exhibited an electrochemical stability between 1.4 V to 4.9 V vs Li/Li^+, which makes it only compatible with the lithium titanate oxides anodes. Whereas, to obtain a battery with high power and high energy density, the battery potential has to be higher. This means that the potential of the cathode should be as high as possible, that of the anode as low as possible and the electrochemical stability of the electrolyte should cover the full range of battery potential. The investigations conducted on the SPE-Lithium interface have shown a stable electrode-electrolyte interphase (SEI) but only at low current, suggesting a problem with $LiClO_4$. In fact, although this salt is economical and easy to handle, it remains unsafe in battery at high current and at high temperature. Therefore, for the future works, it would be interesting to study the poly(VDF-*co*-MAF-cyCB) with $LiPF_6$ salt for example, which is usually used in commercial electrolytes.

The cyclic carbonate units were finally incorporated into linear amorphous copolymers (Chapter 5). In this chapter 5, the cyclic carbonate acrylate (cyCA) monomer was synthesized and randomly copolymerized with *n*butyl acrylate monomer (*n*BA) by RAFT controlled radical polymerization. We observed that for linear amorphous SPE, the ionic conductivity values do not depend on the T_g of the material or on the proportions of cyCA and *n*BA. However, the ionic conductivity is better for short chains. We concluded that ions are vehiculated by the low molar mass polymers and that a high amount of cyCA is not necessary. We also noted that the poly(cyCA-*r*-nBA)/$LiClO_4$ SPEs exhibited lower ionic conductivity values (data not shown) than the poly(cyCA-*r*-nBA)/LiTFSI SPEs, meaning that the ionic conductivity also depends of the nature of lithium salt. Moreover, the poly(cyCA-*r*-nBA)/LiTFSI SPE containing a high cyCA content

(*i.e.* poly(cyCA$_{37}$-*r*-nBA$_{20}$)/LiTFSI in chapter 5) displayed interesting viscosity, which was compared to a "gel" (*i.e.* "firm texture"). Unfortunately, despite these observations, all the poly(cyCA-*r*-nBA)/LiTFSI SPEs (chapter 5) exhibited ionic conductivity values lower of at least one decade than poly(VDF-*co*-MAF-cyCB)/$LiClO_4$ SPEs (chapter 4), which could be explained by the lack of fluorinated groups. Thus, for the future works, it would be interesting to investigate the ionic interactions occurring for these materials in order to further understand and improve the ionic conduction.

Always with the idea of improving the safety and the performances of batteries, using easy synthesizable organic materials, the final chapter of this thesis focused on the development of PTMA redox active polymer based nano-objects as cathode active materials for water flow-assisted electrochemical systems. The synthesis of these nano-objects was realized by the RAFT polymerization induced self-assembly (PISA) in water:ethanol (2:1 v:v) mixture. It was demonstrated that the redox process of PTMA core blocks was not hindered thanks to the presence of ethanol, whatever the obtained morphologies. Unfortunately, the nature and the length of the hydrophilic block influence the reversibility of PTMA redox processes, as with POEGMA. Moreover, these systems displayed low viscosities with a shear thinning behavior. Thus, PTMA is a valuable and promising candidate for further use in all types of batteries. It would be interesting to study the performances of aqueous redox flow battery based on these PTMA nano-objects. Thus, in function of the obtained results, we could play on the size of nano-object or on the nature of hydrophilic blocks.

Simple syntheses of materials were investigated and realized with success in this thesis (chapters 2, 5 and 6). In addition, impedance measurements were also developed during this thesis. They have allowed the understanding of the ion motions in different environments (chapters 3 and 4). Of course, the cathodes and electrolytes were carefully prepared and characterized in order to get as close as possible of industrial applications (experimental part of each chapters). The development of a hybrid cathode based on an ionic liquid and a redox-active component, which generates an ultra-fast electron transfer, was investigated allowing the improvement of the ion motions within

different compartments of batteries. Moreover, ionic liquids are known to make organic electrolyte based batteries safer. Unfortunately, organic electrolytes remains toxic for the environment and men. All solid-state batteries are therefore considered as excellent alternatives and solid polymer electrolytes were thus investigated in this thesis, with the aim to improve ionic conduction in those bulk polymers. The researches carried out during these four years of thesis allowed us to shed light on the mobility of ions in a bulk polymer. In fact, we found new polymeric materials able to improve the motions of ions and more precisely the motions of lithium cations (*i.e.* transference number). The use of ethylene carbonate containing monomers and fluorinated groups based polymers facilitated the dissociation and the transport of ions thanks to their weak interactions with lithium ions and their high dielectric constant. Of course, the mobility of polymer chains also plays on the ion transport mechanisms. For the future works, it would be interesting to study the influence of different topologies of this polymer on the ionic conductivity.

Refereed publications

O. Bertrand, B. Ernould, **F. Boujioui**, A. Vlad and J.-F. Gohy, *Polym. Chem.*, 2015, **6**, 6067–6072.

F. Boujioui, O. Bertrand, B. Ernould, J. Brassinne, T. Janoschka, U. S. Schubert, A. Vlad and J.-F. Gohy, *Polym. Chem.*, 2017, **8**, 441–450.

F. Boujioui, F. Zhuge, H. Damerow, M. Wehbi, B. Améduri and J.-F. Gohy, *J. Mater. Chem. A*, 2018, **6**, 8514–8522.